Waveguide Quantum Electrodynamics with Superconducting Slow-Light Waveguide Circuits

Thesis by
Vinicius S. Ferreira

In Partial Fulfillment of the Requirements for the
Degree of
Doctor of Philosophy

CALIFORNIA INSTITUTE OF TECHNOLOGY
Pasadena, California

2022
Defended 05/25/2022

Vinicius S. Ferreira
ORCID: 0000-0002-9522-2567

For my mom, who taught me by example how to dream and achieve through resiliency and courage.

ACKNOWLEDGEMENTS

At long last, I am entering my last few weeks as a “student"! This decades long winding academic journey has been anything but straightforward to say the least, where numerous times I had to re-evaluate exactly what I wanted to be, or what I wanted to work on, when it was all said and done. But being here at the conclusion of this journey, about to receive a PhD in a subject matter and field that I have a genuine passion for, and about to embark on a career as a *Quantum*(!) Research Scientist, I can honestly say from the bottom of my heart that I could not be happier. As is the case for most graduate students, this PhD has certainly challenged me and often pushed me outside of my comfort zone over the last six years, but thankfully I had the support of many wonderful colleagues and friends that helped me persevere and become the scientist that I am today. Thus, here I would like to express my deepest gratitude to the people that believed in me and supported me throughout my time at Caltech.

I would first like to thank my advisor Prof. Oskar Painter, for where I am today would not be possible without all the opportunities the research group has afforded me. Oskar, you met me in 2015 as I was just finishing my Bachelors in Chemistry, when admittedly, my background did not necessarily make me the best fit for the group. However, when I was candid with you about that, and expressed that nevertheless I had a passion for quantum physics and I was willing to work hard to learn what I had to learn, you welcomed me with open arms and enthusiasm. You taking that chance on me has changed the entire arc of my career for the better, and allowed me to channel the affinity that I had for quantum mechanics in the classroom into a passionate dedication to applied quantum physics research. From 2012 when I excitedly first learned what a wavefunction was, to being able to generate and manipulate quantum entanglement at will today, is truly a wondrous dream come true. And while my time at Caltech has had its ups and downs, learning to adapt to the rigors of the research group, and to the high standard you expect of your students in our communication, our diligence, and the veracity of the scientific claims we make, has pushed me to become the type of scientist that I can be proud of to be. Indeed, while I learned a lot of physics and experimental know-how during my PhD, this high scientific standard that I now hold myself to is probably the biggest new strength that I acquired during my PhD. And I have no doubt that this newfound strength will serve me well in my next steps after Caltech.

Now, I would like to thank various lab members that overlapped with me during the earlier part of my PhD. To Barry Baker, thank you for being the “joker-in-chief" of the group, and for always bringing a light-hearted demeanor to an environment of otherwise intense focus. You not only kept the labs running smoothly, you also did it while bringing a daily smile to all of our faces. And in all our interactions, the fact that you always had the best interest of “your students" at heart always shone through. To Michael Fang and Andrew Keller, thank you for being the first ones to teach me about Circuit QED, and for getting me started on the right track to ultimately succeed in this field. Andrew, I always appreciated how calm, patient, and kind you were, and it was wonderful to have someone throughout my early days with whom I felt truly comfortable asking my “dumb" questions and learning from. Also, me and Jash will forever be in your debt for the fab training you gave us for one whole continuous month! Michael, I remember how indispensable you were in helping to jump start the research group’s transition to working on superconducting circuits. You brought and disseminated invaluable knowledge and know-how to us at the time, and talking to you often felt like talking to a postdoc during my first year of PhD. The fact that in those early days you taught *all* of us in the lab about superconducting qubits, graduate students and postdocs alike, and had such an outsized impact on the research group as a new graduate student yourself, is nothing short of truly amazing. In addition, I thoroughly enjoyed our many conversations in the office about quantum computing, about life, and about the trials and tribulations of doing a PhD; in general you were a great friend to have in the lab. Honestly, choosing my desk to be in that 270 Watson office during my first year was one of the best decisions of my PhD.

To Mohammad Mirhosseini, thank you for working with me and for the guidance you provided during my first few years in the lab. You were the one to first teach me and introduce me to the concepts in quantum optics, and ultimately our time together helped shape and mold the scientific intuition that informs my approach to research today. Further, when writing my first paper, it was thanks to our discussions during that time and throughout the metamaterial project that helped me understand for the first time where my work fitted in the context of quantum optics literature at large, and what it meant to write a meaningful paper. To Alp Sipahigil, while we unfortunately did not directly work together on a common project, the help you gave me (and Jash) during our measurement run for our metamaterial waveguide project felt at the time genuinely immense. There were so many times that, after just a short 10-20 minute conversation with you, either some concept really “clicked" in my

head for the first time, or I learned how to better think about a measurement I was doing, or I received awesome/actionable advice about what to try next. Sometimes even just a minute of your time was the difference between a productive day and an unproductive day, as sometimes in just those brief minutes you would communicate valuable insights. Because I was still putting things together in my head at that time, oftentimes those measurements were a slog, and it's not an exaggeration to say that it often felt like your advice and insights were like a compass that prevented me from becoming totally lost. Mohammad and Alp, I consider you two to be some of the most remarkable scientists I've ever met, and my academic mindset will forever be shaped by the example you two set for us younger graduate students.

To Jash Banker, from the bottom of my heart, I am so thankful to have had you as a partner during our metamaterial project, and as a friend whom I could lean on when the going got tough. You know more than most how much I struggled at times to not be overwhelmed during those days; and the empathy, patience, and kindness you extended to me at that time meant everything to me. It's one thing to get along well and work well with someone, it's entirely another to feel comfortable in being vulnerable with them. And indeed, you not only were a gracious listener, you also helped show me through advice and example how to better manage the daily pressures/challenges that we both had in common. In all the ways I needed at the time, it felt like you had my back; and that camaraderie was an immensely helpful bright spot during the toughest weeks. And even after we went our separate ways project wise, I truly cherished the enduring friendship and trust that we shared, and you were my go-to person when I wanted/needed to talk to someone in the lab as more like a friend than a work colleague. I hope that you always felt like I had your back as well, and that you know just how much I appreciated the relationship that I had with you!

And now, I would like to thank several lab members that I still have the daily pleasure of interacting/working with. To Mo Chen, discussing science with you and working with you has always been a pleasure; I've always felt that you blend together the awesome traits of being a remarkable scientist while also being very down to Earth. In addition, from getting to know you it is clear that you always have people's best interest at heart, and are even willing to sacrifice your own time and effort sometimes to extend a helping hand. I myself was the recipient of such sacrifice from you at one point; and make no mistake that I felt enormous gratitude that, in addition to caring about your own success, you cared about my success as well. I hope that you

have the chance to set an example for many future students on how one should carry themselves as a academic scientist. To Sherry and Eunjong, it has been a pleasure working alongside you throughout my PhD as the "metamaterial/qubit" people of the group. As we all progressed and learned in parallel, it was always helpful to “compare notes" so to speak. Specially throughout the latter half of my PhD, you two were an invaluable resource to discuss measurement protocols, fab processes and images, hardware questions, and in general to sanity-check ideas. And when there came times for me to learn or try something new, I was often fortunate that you two had blazed that trail sometime in the preceding year or so, and that I could draw from your experience. And to Eunjong, I am so happy that after starting together in 2016, when we often felt over our heads in learning all that there is to learn in circuit QED, that today in 2022 we have made it to the end as thriving scientists. Enjoung and Sherry, you two are some of the brightest and hardest working individuals I’ve ever met, and I can’t wait to see what the future has in store for you science wise.

And to Andreas and Gihwan, while I have so much to say, I would like to first and foremost thank you for deciding to work with me on the cluster state project, and for trusting me to be your mentor. At first the responsibility to ensure your success as well as my own felt daunting, but in resolving to make sure that you two had a good *start* to your PhD, I ended up gaining the best *ending* to my PhD that I could have asked for. At first, in teaching you and mentoring you I found myself gaining more confidence as well. Answering your questions, explaining to you concepts, and seeing you assimilate the knowledge I shared, helped crystallize in my mind the notion of how far I had actually come up until that point in my scientific intuition as well. Moreover, seeing you two not only doing science, but doing science with a smile, specially in the middle of the pandemic, brought a daily smile to my face too. And for a long time, thinking about and optimizing and putting effort into the task at hand of how to best mentor, how to best teach, and how to best provide a nurturing environment for you to flourish and do science in, was the best and most rewarding part of my day. And then one day, in what felt like a blink of an eye, I watched you two start to have phase of explosive, exponential growth, and really take off almost on your own. All of a sudden, rather than looking to me for the next steps, you were equipped to have initiative and to act on it. All of a sudden, rather than answering questions about why the data was so or why the measurement was so, I was the one learning from you two about the contributions to the project I had entrusted to you while I was working on fab or on other aspects of the project. All of a sudden, rather than feeling like our team was one “mentor"

and two “young graduate students," it felt like we three were peers with a common knowledge base but with complimentary individual expertise, all contributing at a high level to the project and intellectually driving it. And I was astonished at the speed of it all. You two came into the measurements on the “final device" as mentees, but by the time we saw that first 2D cluster state density matrix, you two were thoughtful, resourceful, independent, and awesome researchers. Seeing the initial conditions that I painstakingly labored to cultivate for you two, coupled with your innate talent, resulting in this wonderful exponential growth, has truly been the most rewarding, fulfilling, happiest experience of my PhD; and I mean this from the bottom of my heart. Your help was invaluable in successfully finishing this project, and successfully finishing this project was invaluable in helping me secure this awesome next stage of my career; and for that I am truly grateful as well. And one of the best parts of it all was that through these last 2.5 years of great research, a great friendship developed between us as well. Our shared success and my time with you has been the happiest part of my time in the research group, and I look forward to staying in touch and keeping up with all the future growth and success you will undoubtedly enjoy.

Finally, I would also like to thank other previous and current lab members that I have had the pleasure of working or interacting with, including Matt Matheny, Hengjiang (Jared) Ren, Jie (Roger) Luo, Greg McCabe, Mahmoud Kalaee, Brett Berger, Szilard Szoke, Anthony Ardizzi, Christy Jenstad, Pierro Chiappina, Utku Hatipoglu, Sammer Sonar, Christy Jenstad, David Lake, Clai Owens, Steven Wood, and Srujan Meesala. Whether it was talking science, having lunch, or shooting the breeze in the cleanroom while waiting for tools to pump down, you all have colored my experiences at Caltech and helped make it home over the last six years; I wish you all the best in your future endeavors. And as also part of this list, I would like to add a heartfelt shoutout to former lab member and now lifelong friend Anchal Gupta: finding a like-minded close friend such as yourself at Caltech was an amazing stroke of luck that significantly enhanced my Caltech experience. Also, I would like to thank my theory collaborator Hannes Pichler. The conversations we had, at first about the $g_2(\tau)$ of a continuously driven qubit in the presence of time-delayed feedback, and subsequently about making 2D cluster states with time-delayed feedback, also had a helpful role in my research success. Principally, those conversations early on during the cluster state project were paramount in helping me start off that project on the right foot, and certainly helped set me up for success.

I would also like to specially thank two of my most special friends Joshua Douglas and Arian Jadbabaie, whose support during the most difficult periods of the last six years was invaluable in helping me to get through those professional or personal humps. Josh, I could speak for hours on how lucky I feel that I have a decade-plus best friend that intimately understands the hardships I experienced during my childhood, and how it factors into who I am today; you are probably the individual that best knows and understands who I am and where I am coming from in this world. But amazingly, not only do we have similar shared trauma, but we also have similar shared world views, a similar shared approach to tackling challenges by leaning on our tenacity, and shared affinity for science and Cribdom; spending time with you has significantly enriched my hours outside of campus ever since you moved here in 2019. And crucially, your support during 2020 when I was dealing with agonizing personal loss was indispensable to coming out of that year stronger than when I entered it, where you helped to empower me to help myself during that time. Your advice, guidance, and often active mentorship in areas like cooking, running, healthy eating, finances, meditation, and other endeavors, has been nothing short of transformative for my growth as an individual. And truly, by progressing in these other areas of my life, you helped me equip myself to have my most productive research years in 2020-2022. In the perpetual pursuit of trying to be the best version of myself that I can be, there has been no better source over the last few years than your wisdom.

And to Arian, from the bottom of my heart, I want to thank you for being undoubtedly the most emotionally supportive friend I have ever had. It is not an exaggeration to say that I feel exceptionally blessed that you came into my life during the beginning of our PhDs at Caltech; not only because we get along and chill splendidly well, but also because your emotional support during the most difficult periods of the last six years helped me to stay the course while dealing with adversity unprecedented in its kind for myself. You have a knack for listening without judgment, for conveying empathy when hearing other's feelings, and for making others feel comfortable in opening up to you. Hence I allowed myself to be vulnerable with you and lean on you when I desperately needed a close friend, and I am so glad that I did. When I was at my wits end on how to manage my work anxiety, you helped me dispel my old self-sabotaging notions of what it meant to be mentally tough, and helped me find anew a better, more sustainable mental fortitude. And through our conversations, you immensely aided my processing of my emotional grief during those tough 2020 months, and ultimately helped me move on from that period with learned lessons, but

without lingering remorse. And importantly, you granted me the space to cry when I truly needed nothing more than a shoulder to cry on; and that meant everything to me. You were quite literally the most load-bearing pillar of my emotional support structure during these last six years, and I will forever appreciate that continuous support you granted me. I hope to have been an excellent friend to you during your PhD as well, and wish you all the luck in pursuing your passion for science, which is like none other that I have ever seen.

And lastly, and most importantly, I would like to thank my dear mother Lauriana for battling like hell since my birth to give me the love and opportunity that has allowed me to be where I am today. The courage you had to upend our lives in Brazil and come to America, with all the difficulties that this entailed but with all the confidence in the world that we would make it, is nothing short of astounding. And indeed it was not easy for you, and I watched you endure back-breaking work, unrelenting work hours, and the burden of ensuring that we both had enough to eat and a roof over our heads, which specially during the Recession was an inordinate task. But nevertheless, I never saw you waver or lose poise, and you stayed the course and navigated us through financial hardship through every means available to you. I often reflect on that time and marvel that, even though I was aware of the all hardships we faced at the time, I always believed that things would work out because of the strength and fortitude you projected; when you didn't seem scared, I wasn't scared either. And that paragon of resiliency and courage that you demonstrated for me, day in and day out, has had a profound impact on who I am as a person today; and has instilled in me the ability to weather adversity through tenacity, and to be bold in pursuing my dreams. Thanks to your fight I am here today, flourishing and realizing opportunities that we both never even dreamed we could have. And to have done all this for me, to have given me the best possible life that you could have with the limited means that you had, is nothing short of the most beautiful expression of motherly love that I could ask for. And for that, I am forever indebted to you, and you will always have my unconditional love and support. I sincerely look forward to sharing the fruits of *our* labor with you for the rest of your life.

ABSTRACT

Waveguide quantum electrodynamics (QED) refers to the study of quantum emitters (qubits) coupled to a single mode waveguide — a 1D electromagnetic reservoir with a continuum of states. This paradigmatic quantum-optical system can serve as a test-bed for experimental investigations in many-body physics, quantum nonlinear optics, reservoir engineering, non-Markovian physics, quantum networks, and quantum computing. While such a system can be realized in a variety of physical platforms, superconducting quantum circuits are well suited to the study of waveguide QED due their readily available strong light-matter interaction strengths.

Of particular interest is the ability to tailor the dispersion relation and modal properties of the waveguide beyond that of a conventional waveguide with linear dispersion. For example, through periodic modulation of the geometry of a waveguide, or through the fabrication of an array of coupled resonant elements, novel electromagnetic responses can be engineered. These include spectral constriction of the 1D continuum to a transmission band of finite bandwidth, enhanced or suppressed emission rates of quantum emitters into the waveguide that are dependent on their frequencies, and extreme slowing of the velocity of light. Such attributes of dispersive waveguides can be leveraged to substantially enrich the physics and applications of qubit-waveguide systems.

In this thesis, we demonstrate the design, fabrication, and characterization of a slow-light waveguide (SLWG) comprised of an array of coupled lumped-element superconducting microwave resonators, and present on various experiments involving superconducting transmon qubits coupled to the SLWG. We investigate the physics of a qubit strongly coupled to the SLWG reservoir by tuning its frequency across the passband of this waveguide, where we find substantial changes to the qubit emission rate, along with oscillatory energy relaxation of the qubit resulting from the beating of bound and radiative dressed qubit-photon states. Further, upon addition of a reflective boundary to one end of the waveguide, we observe revivals in the qubit population on a timescale 30 times longer than the inverse of the qubit's emission rate, corresponding to the round-trip travel time of an emitted photon.

In addition, we show how we leveraged the ability to induce this non-Markovian time-delayed feedback via the SLWG's long delay to generate multidimensional cluster states of itinerant microwave photonic qubits. By utilizing the SLWG as

a delay line with 240 ns round-trip delay, a single flux-tunable transmon qubit as a quantum emitter, and a second auxiliary transmon as a switchable mirror, we achieve rapid, shaped emission of entangled photon wavepackets, and effect time-delayed feedback within the waveguide between previously emitted photons and the emitter qubit. We leverage these capabilities to generate a 2D cluster state of four photons with 70% fidelity, as verified by tomographic reconstruction of the quantum state. We conclude by discussing directly realizable novel follow-up experiments that involve a continuously driven qubit in the presence of time-delayed feedback, and discuss how our cluster-state generation scheme could be straightforwardly extended to generation of even larger multidimensional cluster states, thereby enabling utilization of such states for quantum information processing techniques in the microwave domain.

PUBLISHED CONTENT AND CONTRIBUTIONS

[1] Vinicius S Ferreira, Gihwan Kim, Andreas Butler, Hannes Pichler, and Oskar Painter. Deterministic generation of multidimensional photonic cluster states with a single quantum emitter. *in Preparation*.
V.F. came up with the concept, planned the experiment, did all the fabrication, and with the help of G.K and A.B, performed the device design, performed the measurements, analyzed the data, and wrote the manuscript.

[2] Vinicius S Ferreira*, Jash Banker*, Alp Sipahigil, Matthew H Matheny, Andrew J Keller, Eunjong Kim, Mohammad Mirhosseini, and Oskar Painter. Collapse and revival of an artificial atom coupled to a structured photonic reservoir. *Physical Review X*, 11(4):041043, 2021. doi: 10.1103/PhysRevX.11.041043.
V.F., together with J.B., came up with the concept and planned the experiment, performed the device design and fabrication, and performed the measurements. V.F. in addition analyzed the data and wrote the manuscript.

[3] Eunjong Kim, Xueyue Zhang, Vinicius S Ferreira, Jash Banker, Joseph K Iverson, Alp Sipahigil, Miguel Bello, Alejandro González-Tudela, Mohammad Mirhosseini, and Oskar Painter. Quantum electrodynamics in a topological waveguide. *Physical Review X*, 11(1):011015, 2021. doi: 10.1103/PhysRevX.11.011015.
V.F. participated in the conception of the project and contributed simulation knowledge.

[4] Mohammad Mirhosseini, Eunjong Kim, Vinicius S Ferreira, Mahmoud Kalaee, Alp Sipahigil, Andrew J Keller, and Oskar Painter. Superconducting metamaterials for waveguide quantum electrodynamics. *Nature communications*, 9(1): 1–7, 2018. doi: 10.1038/s41467-018-06142-z.
V.F., participated in the conception of the project and performed exploratory simulation work.

TABLE OF CONTENTS

Acknowledgements iv
Abstract xi
Published Content and Contributions xiii
Table of Contents xiii
List of Illustrations xvi
Chapter I: Introduction 1
Chapter II: General Background and Key Concepts 6
2.1 Background: Superconducting Circuits 6
2.2 Additional General Concepts 21
Chapter III: Coupled Microwave Resonator Arrays for Metamaterial Slow-Light Waveguides 38
3.1 Slow-Light Metamaterial Waveguide Overview 38
3.2 Capacitively Coupled Resonator Array Waveguide Fundamentals . . 42
3.3 Physical Implementation of Finite Resonator Array 51
3.4 Disorder in the Metamaterial Waveguide 53
Chapter IV: Dynamics of a Quantum Emitter Coupled to a One-Dimensional Structured Reservoir 58
4.1 Introduction 58
4.2 Non-Markovian Spectroscopic Signatures 60
4.3 Non-Markovian Radiative Dynamics 63
4.4 Time-Delayed Feedback 66
4.5 Conclusion 68
Chapter V: Deterministic Generation of Multidimensional Cluster States via Time-Delayed Feedback 70
5.1 Introduction 70
5.2 Results 71
5.3 Conclusion 83
Chapter VI: Outlook 85
Appendix A: Fabrication and Measurement Setups 91
Appendix B: Modeling of Qubit Coupled to Coupled Resonator Array Waveguide - General Model 98
Appendix C: Microwave Design of Coupled Resonator Array Waveguides and Qubit Systems 100
C.1 Dispersion Relation of a Periodic Circuit: Transfer Matrix Analysis . 100
C.2 Metamaterial Waveguide Circuit Design Methods 101
C.3 Sonnet Simulation of Metamaterial Waveguide Resonators and Parameter Extraction 103
Appendix D: Supplementary Information for Chapter 4 110
D.1 Master Equation and Circuit Simulations of Qubit Radiative Dynamics 110

D.2 Circuit Simulations . . . 116
D.3 Modeling of Qubit Coupled to Dispersion-less Waveguide in Front of a Mirror . . . 118
Appendix E: Supplementary Information for Chapter 5 - Device Characterization, Modeling, and Control Methods . . . 122
E.1 Device Characterization . . . 122
E.2 Flux Control for Shaped Photon Emission and Qubit-Photon CZ Gate 133
E.3 Sources of Infidelity During Cluster State Generation . . . 139
E.4 Theoretical Analysis of Qubit-Photon “Gate" Errors . . . 141
Appendix F: Supplementary Information for Chapter 5 - Tomography Methods and Additional Results . . . 144
F.1 Radiation Field Quantum State Tomography . . . 144
F.2 Process Tomography of the Time-Delayed Feedback Operation . . . 155
Appendix G: Heterodyne Measurement of Itinerant Microwave Photons - Additional Details . . . 162
G.1 Heterodyne Measurement . . . 162
G.2 Obtaining Field Moments from Noisy Heterodyne Measurements . . 168
G.3 Insights on Heterodyne Measurement Data for Multipartite Entangled Photonic States . . . 171
Bibliography . . . 177

LIST OF ILLUSTRATIONS

Number *Page*

2.1 Superconducting Circuits 8
2.2 Circuit of Two Capacitively Coupled LC Resonators 15
2.3 Experimentally Measured Readout Voltages 19
2.4 Waveguide QED 23
2.5 Flux Modulation of Qubit Frequency 26
2.6 Measurement-Based Quantum Computing 31
2.7 Dynamics of an Atom Inside a Photonic Bandgap Material 35
3.1 Microwave Coupled Resonator Array Slow-light Waveguide 40
3.2 Long-Range Coupling, Delay, and Bandwidth of Metamaterial Slow-Light Waveguide 46
3.3 Impedance Matching to Output CPW Through Boundary Resonators Taper 51
3.4 Anderson Localization in a 1D Periodic Potential with Finite Disorder 55
3.5 Metamaterial Waveguide Disorder Analysis 56
4.1 Artificial Atom Coupled to a Structured Photonic Reservoir 61
4.2 Non-Markovian Radiative Dynamics in a Structured Photonic Reservoir 64
4.3 Time-Delayed Feedback from a Slow-Light Reservoir with a Reflective Boundary 67
5.1 Deterministic Generation of 2D Cluster States with a Single Emitter Qubit 72
5.2 Emission of Shaped Photon Pulses via Flux-Modulation 75
5.3 Time-Delayed Feedback Between Emitter Qubit and Previously Emitted Photons 79
5.4 Qubit-Photon CZ Gate Quantum Process Tomography 80
5.5 Deterministic Generation of a 4-photon 2D Cluster State 81
5.6 4-photon 2D Cluster State Quantum State Tomography 82
A.1 Measurement Setup - Chapter 3 92
A.2 Measurement Setup - Chapter 4 93
C.1 Microwave Office Taper Simulation 102
C.2 Sonnet Unit Cell Simulation 104
C.3 Sonnet Simulation of a Full Tapered Array 108

C.4 Qubit Coupled to Unit Cell Simulation . . . 109
D.1 Master Equation Numerical Simulations of Qubit-Slowlight Waveguide System . . . 111
D.2 Circuit Simulations of Qubit-Slowlight Waveguide System . . . 116
D.3 Time-Delayed Feedback under Flux Modulation Emission Fits . . . 120
E.1 Single-Ended Coupled Resonator Array Slow-Light Waveguide Characterization . . . 122
E.2 Emitter and Mirror Qubit Characterization . . . 126
E.3 Purcell Filter Waveguide and Readout Characterization . . . 132
E.4 Cryoscope . . . 134
E.5 Pulse Shaping via Flux Modulation of the Emitter Qubit . . . 136
E.6 High-Bandwidth Photon Emission . . . 139
E.7 Theoretical CZ and CNOT Qubit-Photon Gate Fidelities . . . 142
F.1 Absolute Power Calibration via AC Stark Shift of Emitter Qubit . . . 147
F.2 Magnitude of Measurement Moments as a Function of Qubit Excitation Angle . . . 150
F.3 Reconstructed Density Matrices of Various Photonic States . . . 152
F.4 Five-Photon Cluster States . . . 153
F.5 Phase Control of Cluster State . . . 154
F.6 Experimental Pulse Sequence for QPT . . . 158
G.1 Heterodyne Detection of Microwave Fields . . . 163
G.2 Probability Distribution Of Phases of Measured Moments . . . 172

Chapter 1

INTRODUCTION

The development of quantum mechanics in the early twentieth century has had a profound impact in the technological advances of the last ~100 years. By first learning to understand the true physical nature of particles and fields at the microscopic scale, crucial inventions such as the transistor [1], laser [2, 3], atomic clocks, etc., were developed through intimate understanding of quantum mechanical principles. In turn, these inventions fueled the development of technologies such as modern computers, the internet, global positioning systems, and others, which have revolutionized the way we interact and work on a day-to-day basis. However, while the physics underpinning the development of these new technologies was "quantum," their fabrication and control remained "classical," and deterministic quantum control of quantum degrees of freedom eluded scientists for many additional decades.

However, the advent of quantum optics in the 1960s and 1970s, and the ability to isolate and probe single atoms with optical light, afforded a stage in which scientists could begin to attempt to manipulate and control matter at the microscopic quantum level [4–7]. The ensuing unrelenting march to observe and control dynamical processes of individual quantum systems encompassed the development of laser cooling [8], atomic traps [9], cavity quantum electrodynamics (QED) [10, 11], and an ever-increasing understanding and appreciation for the subtleties of light-matter interaction. Today, the ground work laid by pioneering quantum optics experiments has helped usher a new age of unprecedented quantum control, where sophisticated new techniques and tools allow for *routine* generation and measurement of complex quantum states in a variety of experimental systems. Indeed, the maturation of quantum information science as a field has recently even culminated in industry-led efforts to build a practical quantum computer [12–15], where the distinguishing features of quantum mechanics such as quantum entanglement and quantum superposition are no longer merely theoretical constructs, but rather form the backbone for potentially breakthrough technology. And although today there are many potential platforms in which to realize quantum-computing, the study of light-matter interaction nevertheless lies at the heart of nearly all of them.

But while atoms were the first system in which scientists learned to isolate and

control quantum degrees of freedom, effective “qubits" can now also be routinely realized in condensed matter systems such as superconducting circuits, where the same techniques that historically were applied to atoms can now be emulated in superconducting qubits. For example, in direct analogy to “cavity QED" in quantum optics, “circuit QED" was developed in superconducting circuits [16], where the bosonic modes consist of λ-sized isolated sections of microwave coplanar waveguide transmission lines, and the “artificial atoms" consist of Josephson-junction-based superconducting qubits. The important advantage of this approach is that the ability to fabricate superconducting circuits with deep sub-wavelength dimensions allowed for very small effective mode volumes which, as predicted by quantum optics decades prior, confers superbly strong (and engineerable) light-matter coupling in these systems. With typical couplings on the order of $g \sim 100$ MHz, and with qubit $T_2^* = 1/(2\gamma) \sim 100\mu s$ and resonator quality factors of $Q = \omega_r/\kappa \sim 10^6$ demonstrated [17, 18], state-of-the-art cooperativities $C = g^2/(\gamma\kappa)$ in these system can exceed *one billion*. Furthermore, the ability to fabricate arbitrary circuit topologies enables one to engineer a diverse array of Hamiltonians, thereby allowing application of superconducting circuits to various endeavors such as quantum computing, quantum simulation of many-body systems, and naturally, fundamental research of quantum optics and light-matter interaction. Thus, in an unanticipated turn of events, bringing together an ~ Avogadro’s number of degrees of freedom in macroscopic-sized pieces of metal has delivered one of the most versatile qubits to date. This astonishing fact, of course, is thanks to the physics of superconductivity [19], where all internal degrees of freedom of the superconductor become correlated and conspire to yield an effective *single* collective degree of freedom that behaves quantum-mechanically: the superconducting phase ϕ.

And naturally, given that prior studies of quantum optics and quantum-light matter interaction are chiefly responsible for fueling this new “quantum revolution," its continued study is also expected to further contribute to the maturation of quantum technologies. In this vein, we now turn to the particular work of this thesis, which finds itself in a subfield of quantum optics research that is different, yet complimentary, to the field of cavity QED: the field of waveguide quantum electrodynamics (QED). Wveguide QED refers to the study of quantum emitters (qubits) coupled to a single mode waveguide — a 1D electromagnetic reservoir with a continuum of states [20–22]. In contrast to cavity QED, where light-matter interaction is achieved between a qubit and a photon that is spatially confined in all dimensions, in waveguide QED qubits are made to interact with propagating, un-localized photons. This

paradigmatic quantum-optical system can serve as a test-bed for experimental investigations in many-body physics [23, 24], quantum non-linear optics [25], reservoir engineering [26, 27], non-Markovian physics [28–30], quantum networks [31], and quantum computing [32].

Additionally, superconducting circuits are well-suited to the study of waveguide QED. In contrast to atomic-optical systems where the finite atom-waveguide cooperativity is often a limiting factor [33, 34], superconducting circuit QED systems enjoy a strong qubit-waveguide coupling that far exceeds the strength of other dissipative channels. Indeed, there have been several recent waveguide QED experiments with superconducting circuits, including observation of paradgmatic quantum optical phenomena such as Mollow Triplets and Autler-Townes splitting [35, 36], observation of Dicke super-radiance and subradiance [37, 38], demonstration of anti-bunching of fluorescence from a continuously driven qubit [39, 40], observation of the Hong–Ou–Mandel effect [41], “giant artificial atoms" that couple to the waveguide at distances much longer than the wavelength of light [42–45], and generation of non-classical states of light [46–49].

However, these aforementioned waveguide QED experiments mostly employ coplanar waveguides, which have linear dispersion, small propagation delays, and can usually studied be through conventional quantum-optical theoretical approaches that invoke the Born-Markov approximation. Thus, in this thesis, we substantially enrich the physics and applications of superconducting qubit-waveguide systems by tailoring the dispersion relation and modal properties of the waveguide beyond that of a conventional waveguide with linear dispersion. Through the fabrication of an array of coupled resonant elements, we engineer novel electromagnetic responses of the waveguide, and through proof-of principle experiments we demonstrate our dispersive waveguide’s application in the generation of novel multipartite entangled photonic states. In this manner, the work presented in this thesis constitutes a meaningful contribution to the fields of quantum optics and quantum information science.

The outline of this thesis is as follows. First, in Chapter 2, I provide a brief overview of superconducting circuits and other relevant background necessary to understand the physics, technical aspects, and noteworthy attributes of this thesis’ work and its applications. In Chapter 3, I give detailed overview of our approach to constructing a dispersive slow-light waveguide (SLWG) through fabrication of a chain of coupled lumped-element superconducting resonators, where we achieve

a group delay of $\sim$ 55 ns per centimeter over a large bandwidth, low ripple in its transmission, and sharp extinction of transmission outside of the passband. I present on the theory underpinning the novel properties of the SLWG, its design and physical implementation, and its characterization. Successful implementation of this SLWG system constitutes one of the main technical achievements in this thesis' body of work, and it underpins the rest of the experiments we present on.

In Chapter 4, we investigate the non-Markovian physics of a qubit strongly coupled to the SLWG environment through spectroscopic and time-domain measurements. We report on direct observation of dynamical phenomena of the qubit-SLWG system resulting from the beating of their bound and radiative dressed states that are consistent with predictions of theoretical work investigating the atomic-optical physics of structured reservoirs [50–59]; to our knowledge this is the first experimental demonstration of these dynamical phenomena. Further, upon addition of a reflective boundary to one end of the waveguide, we observe time-delayed feedback within the waveguide in the form of revivals in the qubit population at a significantly later time than its initial emission, due to the waveguide's large round-trip delay. We also explore the effects of time-delayed feedback when controlling the emission rate of the qubit to the waveguide via flux-modulation, and observe a crossover between Markovian and non-Markovian qubit emission dynamics.

In Chapter 5, we leverage the attributes and capabilities of our system demonstrated in Chapter 4, chiefly: a SLWG with large delay and finite passband, time-delayed feedback between a qubit and its previously emitted photon, and tunable emission rate of the transmon qubit coupled to the SLWG via flux-modulation, to generate multipartite entangled states of itinerant microwave photons. And principally, we demonstrate an experimental implementation in the microwave domain of a resource-efficient scheme for the deterministic generation of 2D photonic cluster states [60]. By utilizing the SLWG as a delay line with 240 ns round-trip delay, a single flux-tunable transmon qubit as a quantum emitter, and a second auxiliary transmon as a switchable mirror, we achieve rapid, shaped emission of entangled photon wavepackets, and effect time-delayed feedback within the waveguide between previously emitted photons and the emitter qubit. We leverage these capabilities to generate a 2D cluster state of four photons with 70% fidelity, as verified by tomographic reconstruction of the quantum state.

Finally, in Chapter 6 I provide an outlook on future directions that build upon the research presented in this thesis. I do so by discussing follow-up experiments to

the work presented here that are directly realizable, as well as by commenting how straightforward hardware and design improvements could enable more complex experiments, such as the generation of significantly larger cluster states. And lastly, in subsequent chapters I provide ample supplementary information, with the hopes that any future graduate student who would seek to understand or replicate any aspect of my work would be well-equipped to do so!

Chapter 2

GENERAL BACKGROUND AND KEY CONCEPTS

In this Chapter we provide a brief review of superconducting circuits (for a more detailed overview, see Refs. [61–63]), and provide brief descriptions of essential concepts referred to in this thesis.

2.1 Background: Superconducting Circuits

LC Resonator

We start by reviewing the classical description of a linear LC resonant circuit, shown in Figure 2.1a, one of the simplest paradigmatic circuits to consider. The energy of photons stored in this resonator oscillates between the electrical energy of the capacitor C and magnetic energy of the inductor L. In analogy to a classical mechanical resonator, we can associate the electrical energy with the “kinetic energy" and the magnetic energy with the “potential energy," although the opposite association is also a valid (although usually less practical) description.

The energy contained in a circuit element at time t can be described as the *power* absorbed by the element (where power is given by the product of voltage and current) from a time where the circuit was completely at rest to the present time t; we may write this energy as

$$E(t) = \int_{-\infty}^{t} V(t')I(t')dt'. \tag{2.1}$$

To arrive at the Hamiltonian description of the circuit, it is useful to work with the generalized *flux* circuit coordinate, which is given by (see Faraday’s Law)

$$V(t) = \frac{d\Phi(t)}{dt}. \tag{2.2}$$

By using the classical circuit relation $V = LdI/dt$ with Equation 2.1, we obtain the energy of the inductor as $LI^2/2$, and by using Equation 2.2 we obtain this energy in terms of flux as $\Phi^2/2L$. Likewise by using the classical circuit relation $I = CdV/dt$ with Equation 2.1 we obtain the energy of the capacitor as $CV^2/2$, and by using Equation 2.2 we obtain this energy in terms of flux as $C\dot{\Phi}^2/2$. The Lagrangian is

defined as the difference between “kinetic" and ‘potential" energy and thus can be expressed as

$$\mathcal{L} = \frac{C\dot{\Phi}^2}{2} - \frac{\Phi^2}{2L}. \tag{2.3}$$

Further, we obtain the Hamiltonian from the Legendre transform $H = \frac{\partial \mathcal{L}}{\partial \dot{\Phi}}\dot{\Phi} - \mathcal{L} = Q\dot{\Phi} - \mathcal{L}$, where the momentum conjugate to the flux is the charge $Q = \frac{\partial \mathcal{L}}{\partial \dot{\Phi}} = C\dot{\Phi}$. We find:

$$H = \frac{Q^2}{2C} + \frac{\Phi^2}{2L}. \tag{2.4}$$

This Hamiltonian has the same functional form as that of a mechanical harmonic oscillator, with mass $m = C$ and frequency $\omega = 1/\sqrt{LC}$. Promoting the charge and flux coordinates to operators (which satisfy a commutation relation $[\hat{\Phi}, \hat{Q}] = i\hbar$ by virtue of the classical coordinates having an unit-valued Poisson bracket), we may subsequently write

$$\begin{aligned} \hat{Q} &= i\sqrt{\frac{\hbar\omega C}{2}}(\hat{a}^\dagger - \hat{a}) = iQ_{\text{zpf}}(\hat{a}^\dagger - \hat{a}), \\ \hat{\Phi} &= \sqrt{\frac{\hbar}{2\omega C}}(\hat{a}^\dagger + \hat{a}) = \Phi_{\text{zpf}}(\hat{a}^\dagger + \hat{a}), \end{aligned} \tag{2.5}$$

where Q_{zpf} and Φ_{zpf} are the zero-point charge and flux fluctuations of the resonator respectively, and $\hat{a}$ ($\hat{a}^\dagger$) is the annihilation (creation) operator for a photon in the LC resonator. Plugging in Equations 2.5 into Equation 2.6, we arrive at the typical harmonic oscillator Hamiltonian in the second quantization formalism:

$$H = \hbar\omega(\hat{a}^\dagger\hat{a} + 1/2). \tag{2.6}$$

We note that although we refer to excitations in superconducting resonators and superconducting qubits as “microwave photons;" they are technically quantized plasmonic oscillations of the superconducting Cooper pair electron condensate [62].

Josephson Junction and SQUID

The Josephson junction is the paradigmatic non-linear circuit element of superconducting circuits, which we leverage to engineer a non-linearity in a LC resonator.

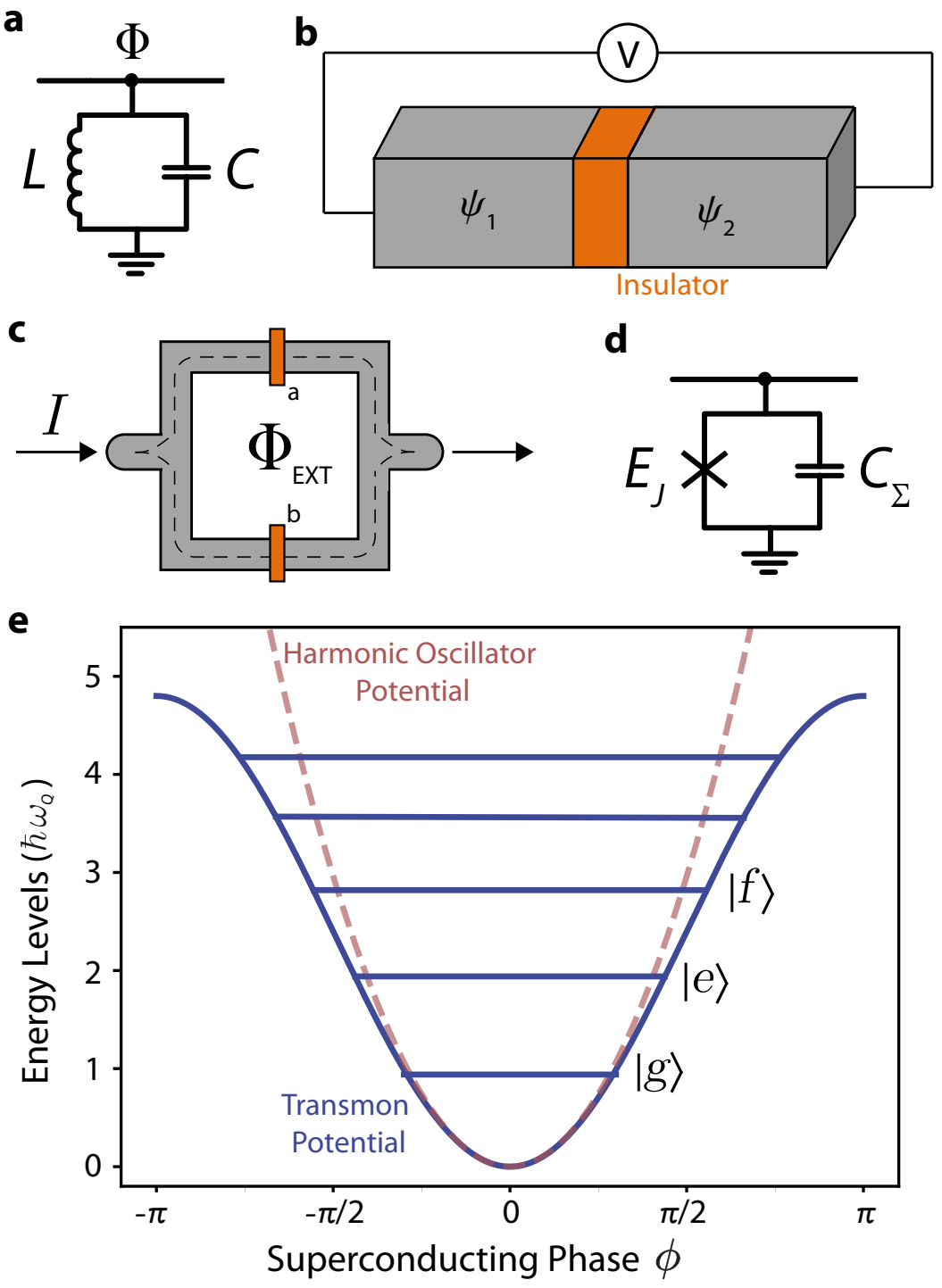

Figure 2.1: **Superconducting Circuits.** **a** Circuit of an LC resonator. **b** Diagram of a Josephson junction, where gray denotes superconductor, and orange denotes insulator. ψ refers to the superconducting quantum state which all Cooper pairs occupy, where $\psi_1 = \sqrt{\rho_1}e^{i\theta_1}$ and $\psi_2 = \sqrt{\rho_2}e^{i\theta_2}$. **c** Diagram of a SQUID, where one junction is denoted as "a," while the other junction is denoted as "b." Φ_{ext} refers to the flux threading the SQUID loop. **d** Circuit of a superconducting transmon qubit. $C_\Sigma = C_J + C_S$, where C_J is the intrinsic capacitance of the junction due to the Coulomb interaction between the superconducting plates, and C_S is any additional shunting capacitance. **e** Anharmonic energy potential of the Josephson junction.

This non-linearity allows us to realize anharmonic oscillators, whose unequal energy level spacing allows us to use these oscilltors as effective “qubits," our “artificial atoms." Following Ref. [64], below we briefly review the physics behind the Josephson effect.

Consider a Josephson junction as shown in Figure 2.1b, composed of two pieces of superconducting metal that are separated by a thin layer layer of insulating material, where the two superconducting regions are connected to the two terminals of a voltage source of voltage V. If the insulating layer is thin enough, there will be some finite probability of tunneling from one superconductor to the other for a Cooper pair. Thus, for a Cooper pair this system is akin to “double-well potential" system, where the tunneling hybridizes the eigenstates of the zero tunneling limit associated with the exclusive occupation of each well. Thus, in order to learn how the tunneling between the superconductors affects the state of a Cooper pair “charge particle" in this Josephson junction system, we may start by defining the state of the Cooper pair on one side as ψ_1, the state of the Cooper pair on the other side as ψ_2, and writing the following standard equations for two quantum mechanical states coupled together:

$$\begin{aligned} i\hbar\frac{\partial\psi_1}{\partial t} &= U_1\psi_1 + K\psi_2, \\ i\hbar\frac{\partial\psi_2}{\partial t} &= U_2\psi_1 + K\psi_1, \end{aligned} \tag{2.7}$$

where K captures the “coupling" between the two superconductors due to the tunneling between them and is characteristic of the junction, and U_1, U_2 is the energy of the Cooper pair in the first and second superconductor, respectively. Due to the voltage source, $U_1 - U_2 = qV$, where $q = 2e$ is the charge of a Cooper pair, and for convenience, we define $U_1 = qV/2$, and $U_2 = -qV/2$.

Moreover, from the standard theory of superconductivity [19] it is known that at zero temperature all electrons in a superconductor pair up into Cooper pairs, due to an effective attractive interaction between electrons when they are embedded in the lattice of positively charged nuclei of the metal atoms. Further, it can be shown that the Cooper pairs are bosonic quasiparticles, and at zero temperature they occupy the same quantum mechanical state; this quantum mechanical state may be written as $\sqrt{\rho}e^{i\theta}$, where ρ is the charge density and ϕ is the well-defined global phase of the wavefunction that all Cooper pairs share. We may thus make the following substitutions in Equation 2.7: $\psi_1 = \sqrt{\rho_1}e^{i\theta_1}$ and $\psi_2 = \sqrt{\rho_2}e^{i\theta_2}$. Equating the real

and imaginary parts in each equation, performing standard algebra, and defining $\theta_2 - \theta_1 = \phi$, we arrive at the following equations:

$$\begin{aligned}
\dot{\rho}_1 &= \frac{2K}{\hbar}\sqrt{\rho_1\rho_2}\sin\phi, \\
\dot{\rho}_2 &= -\frac{2K}{\hbar}\sqrt{\rho_1\rho_2}\sin\phi, \\
\dot{\theta}_1 &= -\frac{K}{\hbar}\sqrt{\frac{\rho_1}{\rho_2}}\cos\phi - \frac{qV}{2\hbar}, \\
\dot{\theta}_2 &= -\frac{K}{\hbar}\sqrt{\frac{\rho_1}{\rho_2}}\cos\phi + \frac{qV}{2\hbar}.
\end{aligned} \tag{2.8}$$

The first two equations can be written as $\dot{\rho}_1 = -\dot{\rho}_2$, and thus correspond to the current from side 1 to side 2. Further, in practice we expect the charge densities for both superconductors to stay the same, and not change, due to the voltage source keeping the potential constant (although current will still flow due to the constant voltage difference). Thus we may say that $\rho_1 = \rho_2 = \rho_0$, and define the current across the junction as

$$I = \frac{2K}{\hbar}\sqrt{\rho_1\rho_2}\sin\phi = I_0\sin\phi, \tag{2.9}$$

where $I_0 = 2K\rho_0/\hbar$ and depends on the microscopic characteristics of the superconductor and of the junction. Through a more involved microscopic derivation [65], one may show that I_0 is the junction critical current, the maximum current the junction can support without incurring dissipation, and it is given by $I_0 = \pi\Delta/2eR_N$, where Δ is the superconducting gap, and R_N is the normal state resistance (i.e., the resistance of the junction if the metal were not superconducting; note that R_N scales inversely with junction area). Furthermore, we can use the other two formulas in Equation 2.8 to relate the phase difference across the junction $\theta_2 - \theta_1$ to the voltage across the junction:

$$V = \frac{\hbar}{2e}\frac{d\phi}{dt}. \tag{2.10}$$

Equations 2.9 and 2.10 together give the two Josephson relations: the voltage and current as a function of the superconducting phase difference across the junction.

We can further extend this analysis to derive the current across two Josephson junctions connected in parallel as shown in Figure 2.1c; this circuit is referred to as

a “Superconducting Quantum Interference Device" (SQUID) and forms the basis for flux-tunable transmon qubits [66]. Calling the two different junctions connected in parallel as “a" and “b," we may define the current across each junction as I_a and I_b, and the phase difference cross the two junctions as ϕ_a and ϕ_b. From electromagnetic theory, it is known that the probability amplitude for a charged particle to go from some beginning point i to some endpoint j along a certain route is proportional to $\exp\left[(iq/\hbar \int_i^j \boldsymbol{A} d\boldsymbol{s}\right]$. Thus, if an electron travels from one end of the SQUID loop to the other through path “a" or path “b," it will acquire the phase

$$\Theta = \phi_a + \frac{2e}{\hbar} \int_a \boldsymbol{A} d\boldsymbol{s} \tag{2.11}$$

or

$$\Theta = \phi_b + \frac{2e}{\hbar} \int_b \boldsymbol{A} d\boldsymbol{s} \tag{2.12}$$

respectively. However, for current flowing in parallel across the two junctions, the phase gained by charges traveling from one end of the SQUID to the other will be the same irrespective of path; thus we may subtract Equations 2.14 and 2.11 to arrive at the relationship between ϕ_a and ϕ_b in a SQUID loop:

$$\phi_b - \phi_a = \frac{2e}{\hbar} \oint_{\text{SQUID}} \boldsymbol{A} d\boldsymbol{s}, \tag{2.13}$$

where $\oint_{\text{SQUID}} \boldsymbol{A} d\boldsymbol{s}$ is the line integral of the vector potential around the SQUID loop. By Stokes theorem, we may equate this line integral to the external magnetic flux through the SQUID loop, giving us the fluxoid quantization condition

$$\phi_b - \phi_a = \frac{2e}{\hbar} \Phi_{\text{ext}} = 2\pi \frac{\Phi_{\text{ext}}}{\Phi_0}, \tag{2.14}$$

where Φ_0 is the magnetic flux quantum $h/2e$. The total current through the SQUID loop will be $I = I_a + I_b = I_0 \sin\phi_a + I_0 \sin\phi_b$; using trigonometric relations, the current is given by

$$I = 2I_0 \left|\cos\left(\pi \frac{\Phi_{\text{ext}}}{\Phi_0}\right)\right| \sin\overline{\phi}, \tag{2.15}$$

where $\overline{\phi} = (\phi_a + \phi_b)/2$. Moreover, note that $\frac{h}{2e}\frac{d\overline{\phi}}{dt} = \frac{1}{2}\left(\frac{h}{2e}\frac{d\phi_a}{dt} + \frac{h}{2e}\frac{d\phi_b}{dt}\right) = V$ for the parallel junction circuit. Thus, the current across the SQUID loop behaves

just like the current across a single junction, with the exception that the critical current is *tunable* via the external flux Φ_{ext} threading the SQUID loop. Thus in all following discussions we make no further distinction between ϕ of a single junction and $\overline{\phi}$ of a SQUID. Intuitively, this phenomenon may be understood by drawing analogy to Young's double-slit experiment, where light coming from two slits can constructively or destructively interfere. The currents across the two arms of the SQUID interfere, and what sets their interference are the phases that the currents acquire through propagation in each arm. What sets that phase is the vector potential *on* the SQUID loop, which in turn is related to the flux *through* the SQUID loop Φ_{ext}. For some Φ_{ext} there is destructive interference, and hence the effective critical current (the maximum current the junction can support) is smaller, while for other Φ_{ext} there is constructive interference and the effective critical current is greater.

Finally, we note that if we plug in Equation 2.10 into Equation 2.2, we obtain $\Phi = \frac{\hbar}{2e}\phi \rightarrow \phi = 2\pi\Phi/\Phi_0$. Thus each time the flux coordinate Φ of the junction changes by one flux quantum, the superconducting phase variable ϕ winds by 2π. Furthermore, by calculating the derivative of the Josephson current, we can see that it is proportional to the voltage: $dI/dt = I_0 \cos\phi \frac{d\phi}{dt} = I_0 \cos\phi \frac{2\pi}{\Phi_0} V$, as is the case for an inductor where $V = LdI/dt$. We thus see that the Josephson junction effectively behaves as a non-linear inductor with inductance $L_J = \Phi_0/(2\pi I_0 cos\phi)$.

Superconducting Qubits

Given that a Josephson junction consists of two parallel metal plates separated by a dielectric, it will also have a capacitance that can be considered to be parallel to its effective "inductance." In addition, large shunting capacitances are typically added in parallel to Josephson junctions in order to realize transmon qubits. Thus, we may generically represent a Josephson junction circuit as depicted in Fig 2.1d. We may obtain the "inductive" energy of the junction (or SQUID) by plugging in Equations 2.10 and 2.9 into Equation 2.1, obtaining $E = -\frac{I_0\hbar}{2e}\cos\phi = -E_J \cos\phi$, where $E_J = \frac{I_0\Phi_0}{2\pi}$. Note that if a SQUID is used instead of a single junction, then E_J is tunable via the the external flux Φ_{ext} threading the SQUID loop (see Equation 2.15). Furthermore, recognizing that the charge $\hat{Q}$ on the capacitor formed by the junction electrodes and other shunting capacitances corresponds to the number of Cooper pairs that have tunneled from one side of the junction to the other, we may define the number operator (for Cooper pairs) $\hat{n} = \hat{Q}/2e$, with the associated charging energy of a single tunneling electron $E_c = e^2/2C_\Sigma$, where C_Σ is the total capacitance in parallel with the junction. We can therefore write the Hamiltonian

of the circuit depicted in Figure 2.1d as

$$H = 4E_c\hat{n}^2 - E_J \cos\hat{\phi}. \tag{2.16}$$

Expanding the Hamiltonian potential energy term into a a Taylor series $-E_J \cos\phi = -E_J\left(1 - \frac{\phi^2}{2} + \frac{\phi^4}{24}\right)$, we obtain the following anharmonic oscillator Hamiltonian (up to a constant term):

$$H = 4E_c\hat{n}^2 + E_J\frac{\hat{\phi}^2}{2} - E_J\frac{\hat{\phi}^4}{24} + O(\hat{\phi}^6). \tag{2.17}$$

We can once again transform the Hamiltonian of Equation 2.17 into a second-quantized Hamiltonian of a harmonic oscillator, albeit this time with the quartic $-E_J\frac{\phi^4}{24}$ perturbation. Writing $\hat{n}$ and $\hat{\phi}$ in terms of $\hat{a}$ and $\hat{a}^\dagger$:

$$\begin{aligned}\hat{n} &= i\left(\frac{E_J}{32E_C}\right)^{1/4}(\hat{a}^\dagger - \hat{a}),\\ \hat{\phi} &= \left(\frac{2E_c}{E_J}\right)^{1/4}(\hat{a}^\dagger + \hat{a})\end{aligned} \tag{2.18}$$

we arrive at the following anharmonic oscillator second-quantized Hamiltonian

$$H = \sqrt{8E_JE_c}\left(\hat{a}^\dagger\hat{a} + \frac{1}{2}\right) - \frac{E_c}{12}(\hat{a}^\dagger + \hat{a}). \tag{2.19}$$

By calculating the energy corrections to the states $|0\rangle$, $|1\rangle$, and $|2\rangle$ via first-order perturbation theory, where the perturbation Hamiltonian is given by $-\frac{E_c}{12}(\hat{a}^\dagger + \hat{a}) \approx -\frac{E_c}{2}\left((\hat{a}^\dagger\hat{a})^2 + \hat{a}^\dagger\hat{a}\right)$ after dropping fast-rotating terms that have an uneven number of $\hat{a}$ and $\hat{a}^\dagger$, we can calculate the anharmonicity η of the superconducting qubit as

$$\hbar\eta = E_{21} - E_{10} = (E_2 - E_1) - (E_1 - E_0) = -E_c, \tag{2.20}$$

while its new renormalized frequency due to the perturbation is $\omega_Q = (E_1 - E_0)/\hbar = (\sqrt{8E_JE_c} - E_c)/\hbar$. We plot the anharmonic energy potential of the transmon qubit, and a comparison to a harmonic potential, in Figure 2.1e.

For transmon qubits, we will have the following typical parameter values: $E_J/\hbar 2\pi =$ 15 GHz, $\eta/2\pi = 250$ MHz, $\omega_Q/2\pi = 5$ GHz, and driving powers commensurate

with qubit Rabi frequencies of $\Omega/2\pi \sim 20$ MHz. The transmon anharmonicity ensures that a drive *resonant* with the first transmon qubit transition is *off-resonance* with other transmon qubit transitions, thereby preventing population of higher transmon levels during driving as would be the case for a linear harmonic oscillator. Hence, the transmon anharmonicity allows us to effectively control this anharmonic oscillator as a two-level system, yielding to us our effective "qubit." We note that the ratio of E_J/E_c is typically chosen to be 50-100, in order to minimize the dependence of ω_Q on offset charges of the transmon island while still maintaining sufficient anharmonicity [66]. Lastly, asymmetric SQUIDs are often used in transmon qubits because they have a smaller tuning curve, and hence their sensitivity to flux noise tends to be smaller (see Figure 2.5 for an example of a tuning curve of a superconducting transmon qubit with an asymmetric SQUID). The E_J of a transmon qubit with an asymmetric SQUID is given by

$$E_J \rightarrow E_{J\Sigma} \left|\cos\left(\pi \frac{\Phi_{\text{ext}}}{\Phi_0}\right)\right| \sqrt{1 + d^2 \tan^2\left(\pi \frac{\Phi_{\text{ext}}}{\Phi_0}\right)}, \tag{2.21}$$

where $E_{J\Sigma} = E_{J1} + E_{J2}$, $d = (E_{J2} - E_{J1})/(E_{J2} + E_{J1})$, and E_{J1} and E_{J2} are the Josephson energies of each junction of the SQUID.

Two Capacitively Coupled LC Resonators

Here we briefly review how to derive the second quantized Hamiltonian of two capacitively coupled LC resonators as shown in Figure 2.2; a typical circuit in circuit QED systems.

By inspection of the circuit in Figure 2.2, we denote the voltage at node 1 as V_1 and the voltage at node 2 as V_2 where, as previously discussed, we may relate a node voltage to the node flux via $V = \dot{\Phi}$. As done before, the energy associated with L_1, L_2, C_1, and C_2 is $\Phi_1^2/2L_1$, $\Phi_2^2/2L_2$, $C_1\dot{\Phi}_1^2/2$, and $C_2\dot{\Phi}_2^2/2$ respectively, while the energy associated with C_g is $C_g(V_1 - V_2)^2/2 = C_g(\dot{\Phi}_1 - \dot{\Phi}_2)^2/2$, where $V_1 - V_2$ is the voltage across C_g. Thus, the Lagrangian of the system may be written as:

$$\mathcal{L} = \frac{C_1\dot{\Phi}_1^2}{2} + \frac{C_2\dot{\Phi}_2^2}{2} + \frac{C_g(\dot{\Phi}_1 - \dot{\Phi}_2)^2}{2} - \frac{\Phi_1^2}{2L_1} - \frac{\Phi_2^2}{2L_2}. \tag{2.22}$$

The conjugate momenta of the Lagrangian are calculated as $Q_1 = \frac{\partial \mathcal{L}}{\partial \dot{\Phi}_1} = C_1\dot{\Phi}_1 + C_g\dot{\Phi}_1 - C_g\dot{\Phi}_2$, and $Q_2 = \frac{\partial \mathcal{L}}{\partial \dot{\Phi}_2} = C_2\dot{\Phi}_2 + C_g\dot{\Phi}_2 - C_g\dot{\Phi}_1$. Solving for $\dot{\Phi}_1$ and $\dot{\Phi}_2$ in terms the node charges Q_1 and Q_2, we obtain $\dot{\Phi}_1 = \frac{Q_1}{C_1+C_g} + \frac{C_gQ_2}{(C_1+C_g)(C_2+C_g)}$, with a

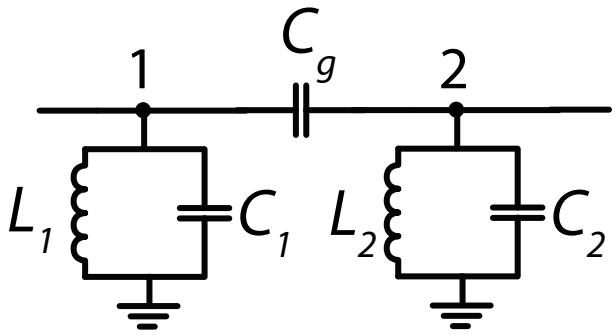

Figure 2.2: **Circuit of Two Capacitively Coupled LC Resonators**. The numbers 1 and 2 refer to the circuit nodes.

similar formula for $\dot{\Phi}_2$. Performing the Legendre transform $\sum_i^2 Q_i \dot{\Phi}_i - \mathcal{L}$, we arrive at the following Hamiltonian of the coupled resonator system:

$$H = \frac{Q_1^2}{2(C_1 + C_g)} + \frac{Q_2^2}{2(C_2 + C_g)} + \frac{\Phi_1^2}{2L_1} + \frac{\Phi_2^2}{2L_2} + \frac{C_g Q_1 Q_2}{(C_1 + C_g)(C_2 + C_g)}. \tag{2.23}$$

We can once again obtain the second quantized form of this Hamiltonian by making the associations $m_i = C_i + C_g$ and $\omega_i = 1/\sqrt{L_i(C_i + C_g)}$ where $i = 1, 2$, promoting the charge and flux coordinates to operators, and defining them in terms of raising and lowering operators

$$\begin{aligned} \hat{Q}_i &= i\sqrt{\frac{\hbar\omega_i m_i}{2}}(\hat{a}_i^\dagger - \hat{a}_i), \\ \hat{\Phi}_i &= \sqrt{\frac{\hbar}{2\omega_i m_i}}(\hat{a}_i^\dagger + \hat{a}_i). \end{aligned} \tag{2.24}$$

Plugging Equations 2.24 into the Hamiltonian of Equation 2.23, we obtain:

$$H = \hbar\omega_1 \left(\hat{a}_1^\dagger \hat{a}_1 + \frac{1}{2}\right) + \hbar\omega_2 \left(\hat{a}_2^\dagger \hat{a}_2 + \frac{1}{2}\right) - \hbar g(\hat{a}_1^\dagger - \hat{a}_1)(\hat{a}_2^\dagger - \hat{a}_2), \tag{2.25}$$

where the effective coupling constant g for two capacitively coupled resonators is given by

$$g = \frac{1}{2}\sqrt{\omega_1 \omega_2}\frac{C_g}{\sqrt{(C_0 + C_1)(C_0 + C_2)}}. \tag{2.26}$$

We thus see that the Hamiltonian consists of a harmonic oscillator portion for each resonator, plus a coupling Hamiltonian H_c. Applying the rotating wave approximation (RWA) to discard fast-rotating terms, we arrive at the familiar “beam-splitter" coupling Hamiltonian

$$H_c = \hbar g(\hat{a}_1^\dagger \hat{a}_2 + \hat{a}_2^\dagger \hat{a}_1). \tag{2.27}$$

It can be verified that in the single-photon manifold if $\omega_1 = \omega_2$, the eigenstates of the system are given by the even and odd symmetric superposition of the states corresponding to a photon in each mode: $|\psi\rangle = \frac{1}{\sqrt{2}}(|01\rangle \pm |10\rangle)$. Note that because g is positive valued, the anti-symmetric odd normal mode of the system is the lower energy eigenmode. This has direct consequences on the dispersion of a periodic chain of coupled resonators, as described in Chapter 3. Finally, note that Equation 2.26 is what is often used in practice to predict couplings between capacitively coupled resonant elements given their simulated circuit parameters.

Dispersive Coupling of Transmon Qubit to a Resonator

Here, we briefly review how to obtain the “dispersive approximation" Hamiltonian of a qubit coupled to a substantially detuned resonator, and the properties of this coupled system. Dispersive coupling of a qubit to a resonator is the predominant method for QND single-shot readout of superconducting qubit states. In addition, we review key practical concepts regarding single-shot qubit dispersive readout in the next subsection.

We start by considering the generalized Jaynes-Cummings Hamiltonian for a multi-level atom interacting with a bosonic mode in the RWA approximation

$$\hat{H} = \hbar \sum_j E_j \left|j\right\rangle \left\langle j\right| + \hbar\omega_r \hat{a}^\dagger \hat{a} + \left(\hbar \sum_i g_{i,i+1} \left|i\right\rangle \left\langle i+1\right| \hat{a}^\dagger + \text{h.c}\right), \tag{2.28}$$

where we consider the limit where $(E_1 - E_0) - \omega_r = \omega_{01} - \omega_r \gg g_{01}$. In order to arrive at the dispersive limit Hamiltonian of the coupled qubit-resonator system, we perform the canonical transformation $\hat{H}_{\text{disp}} = \hat{U}^\dagger \hat{H} \hat{U}$, where $\hat{U} = \exp\left(\hat{S} - \hat{S}^\dagger\right)$, $\hat{S} = \sum_i (g_{i,i+1}/\Delta_i) \left|i+1\right\rangle \left\langle i\right| \hat{a}$, and $\Delta_i = (E_{i+1} - E_i) - \omega_r = \omega_{i,i+1} - \omega_r$. We employ the canonical transformation through the Baker-Campbell-Haussdorf relation:

$e^{\hat{A}}\hat{B}e^{-\hat{A}} = \hat{B} + \left[\hat{A}, \hat{B}\right] + \frac{1}{2}\left[\hat{A}, \left[\hat{A}, \hat{B}\right]\right] + ...$, and discard all fast rotating terms and terms of order $O(1/\Delta_i^2)$. It can be verified that due to the form of operator $\hat{S}$, the Baker-Campbell-Haussdorf expansion with $\hat{A} = \hat{S} - \hat{S}^\dagger$ can be simplified to $\hat{H}_{\text{disp}} = \hat{H} + \left([\hat{S}, \hat{H}] + \text{h.c}\right) - \frac{1}{2}\left(\left[\hat{S}^\dagger, [\hat{S}, \hat{H}]\right] + \text{h.c}\right) + O(1/\Delta_i^2)$. Calculation of these commutators and some serious algebra leads to the following Hamiltonian:

$$\begin{aligned}\hat{H}_{\text{disp}} = \hbar \sum_j E_j \left|j\right\rangle \left\langle j\right| + \hbar\omega_r \hat{a}^\dagger \hat{a} + \hbar \sum_{i=0} \chi_{i,i+1} \left|i+1\right\rangle \left\langle i+1\right| \\ + \hbar\hat{a}^\dagger\hat{a}\left(\sum_{i=1}(\chi_{i-1,i} - \chi_{i,i+1})\left|i\right\rangle\left\langle i\right| - \chi_{01}\left|0\right\rangle\left\langle 0\right|\right) + O\left(\frac{1}{\Delta_i^2}\right),\end{aligned} \tag{2.29}$$

where $\chi_{i,i+1} = g_{i,i+1}^2/\Delta_i$. Further restricting the Hilbert Space to the first two levels of the transmon, we obtain $\hat{H}_{\text{disp}} = \hbar E_0 \left|0\right\rangle\left\langle 0\right| + \hbar(E_1 + \chi_{01})\left|1\right\rangle\left\langle 1\right| + \hbar\hat{a}^\dagger\hat{a}\left(\omega_r + (\chi_{01} - \chi_{12})\left|1\right\rangle\left\langle 1\right| - \chi_{01}\left|0\right\rangle\left\langle 0\right|\right)$. Defining the Pauli matrix $\sigma_z = \left|0\right\rangle\left\langle 0\right| - \left|1\right\rangle\left\langle 1\right|$, and $\tilde{\omega}_Q = \omega_{10} + \chi_{01}$, $\tilde{\omega}_r = \omega_r - \chi_{12}/2$, and $\chi = -(\chi_{01} - \chi_{12})$, after some algebra we obtain the familiar dispersive Hamiltonian

$$\hat{H}_{\text{disp}} = -\frac{\hbar}{2}\tilde{\omega}_Q\hat{\sigma}_z + \hbar\hat{a}^\dagger\hat{a}\left(\tilde{\omega}_r + \chi\hat{\sigma}_z\right), \tag{2.30}$$

where the dispersive shift χ is calculated to be:

$$\chi = -\frac{g_{01}^2}{\Delta_0}\frac{1}{1 + \frac{\Delta_0}{\eta}}, \tag{2.31}$$

where the transmon anharmonicity is $\eta = -E_c/\hbar$. It is evident from Equation 2.30 that the effective frequency of the bosonic mode $\hat{a}$ is dependent on the state of the qubit, where the difference in frequency depending on if the qubit is in its ground or excited state is given by 2χ. Typical parameters for dispersive readout of transmon qubits are $g_{01}/2\pi \sim 50 - 200$ MHz, $\Delta_0/2\pi = 0.8 - 2$ GHz, and $\chi/2\pi = 1 - 5$ MHz.

This analysis reveals several important attributes of a dispersively coupled transmon-resonator system. Firstly, we see that the effective qubit and resonator frequencies are *renormalized* from their bare frequencies due to their coupling to a detuned mode; an effect known as the “Lamb shift." Moreover this Lamb shift, which is on the order of the dispersive shift χ, can be measured in experiment: by driving the resonator coupled to the qubit at various powers, one will see a shift in the resonator

frequency from $\tilde{\omega}_r$ to the bare frequency ω_r for drive powers commensurate with a resonator photon occupation significanty larger than the critical photon number $n_{\text{crit}} = \Delta^2/4g^2$ [16]. Furthermore, the result obtained for χ in Equation 2.31 is different than the one obtained for a bare two level system where $\chi_{\text{TLS}} = -g^2/\Delta$; this can be ascribed to the fact that the transmon has several transitions of different frequencies that each have dispersive coupling to the bosonic mode. Moreover, from Equation 2.29 it can be shown that the effective frequency of the bosonic mode $\hat{a}$ if the qubit is in its second excited state $|2\rangle$ is given by $\omega_r + \chi_{12} - \chi_{23}$, where $\chi_{12} - \chi_{23}$ is on the order of χ but is still different from χ. Thus, the resonator will have different frequencies depending on if the transmon qubit is in either in its ground, excited, or second excited state; which can be leveraged for readout discrimination of its first three levels. Finally, note that the Hamiltonian in Equation 2.30 can be re-written as $\hat{H}_{\text{disp}} = \frac{\hbar}{2}\hat{\sigma}_z\left(-\tilde{\omega}_Q + 2\chi\hat{a}^\dagger\hat{a}\right) + \hbar\tilde{\omega}_r\hat{a}^\dagger\hat{a}$. By inspection of this form of $\hat{H}_{\text{disp}}$ it is evident that photon occupation in the resonator will change the qubit frequency, otherwise known as the “AC Stark-shift" effect, where for each photon the qubit frequency will change by an amount χ. This phenomenon can be leveraged to measure the photon occupation of the resonator.

Qubit Readout via Dispersive Coupling to Readout Resonator

We conclude with a brief discussion about further technical details of dispersive readout of transmon qubits. As discussed, the readout (RO) resonator frequency is different depending on the qubit state; thus if one probes the RO resonator by driving it through some transmission line they will see a state-dependent RO resonator response. By connecting a RO resonator to a transmission line in a way such that drive pulses sent down the transmission line can interact with the RO resonator (see Figure 4.1 for an example), and can subsequently leave the chip for quantum-limited amplification and heterodyne measurement via a digitizer, we may perform dispersive single-shot readout of the qubit state. Through signal processing techniques, this measured state-dependent RO resonator response can be processed into a state-dependent voltage measurement; see Figure E.3d for an example of histograms of single-shot measurements for when the qubit is prepared in its ground state or second excited state. State discrimination then consists of assigning a qubit state for a given measured voltage based on the measurement results of such histograms. Again considering Figure E.3d as an example, if a readout voltage above ≈ 0.1 was measured, we would assign the qubit to have been in its excited state, while if a readout voltage below ≈ 0.1 was measured, we would assign the qubit as having

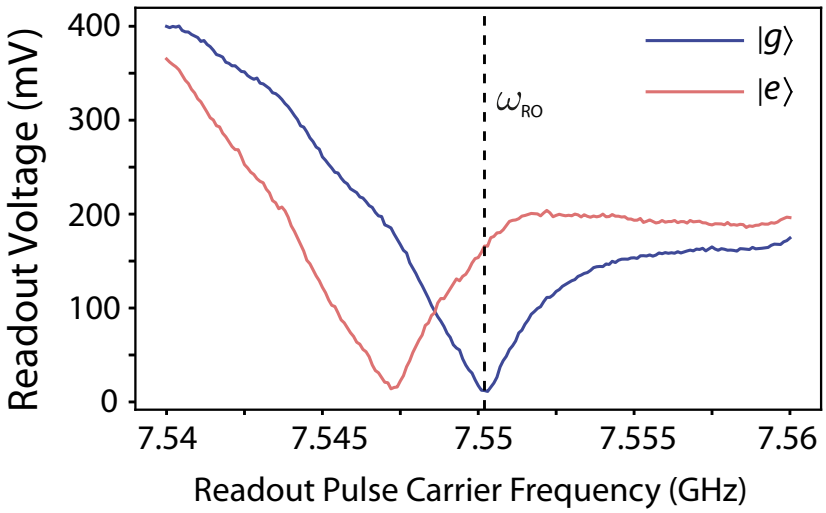

Figure 2.3: **Experimentally Measured Readout Voltages**. State-dependent readout voltages as a function of readout probe frequency, measured for when the qubit is prepared in the $|g\rangle$ state or the $|e\rangle$ state. The readout signal sent is a 600ns square pulse. ω_{RO} here corresponds to the carrier frequency of the readout pulse that yields maximum readout voltage contrast between the two states. The difference in readout voltage at ω_{RO} between the $|g\rangle$ and $|e\rangle$ curves yields the quantity $|V_{\text{diff}}(\omega_{\text{RO}})|$; see main text for more details. The readout resonator in this measurement is side-coupled to its feedline, and transmission through the feedline is what is measured here.

been in its ground state. Additionally, note that measurement of these histograms will be negatively impacted by the non-ideal effects of state preparation errors, such as initial thermal population of the excited state $|e\rangle$, as well as measurement errors such as measurement-induced state transitions or decay of the qubit during readout that leads to misclassification of the qubit state [67, 68].

Two important metrics to consider for single-shot superconducting qubit readout are the readout SNR and readout infidelity. Again referring to Figure E.3d, the readout SNR may be defined as the ratio of the voltage separation between the centroids of the (dominant) Gaussian distributions for the $|g\rangle$ and $|e\rangle$ measurement histograms, to the standard deviation of these Gaussian distributions. The standard deviation is set by the noise in the heterodyne measurement of the drive pulse, where the drive pulse is a coherent state. Thus, this noise will include the intrinsic vacuum fluctuations of the coherent state, as well as added amplifier noise and effects from losses before the first amplifier in the output chain; see Appendix G.1 for more details on the sources and magnitudes of noise in heterodyne measurement of amplified signals.

Meanwhile, the magnitude of voltage separation between the state-dependent Gaussian distributions depend on a combination of other factors. Given that readout pulse signals are typically long enough to drive the RO resonator to steady state,

the effective voltage separation will intrinsically be determined by the difference in complex voltage between the measured spectra of the transmission line used to probe the resonator (either reflection spectra or transmission spectra depending on the measurement modality) *at the carrier frequency* of the readout pulse (see Figure 2.3 for an example of transmission spectra for a readout resonator when the qubit is prepared in either the $|g\rangle$ state or the $|e\rangle$ state). We henceforth refer to this complex voltage difference as $V_{\text{diff}}(\omega_{\text{R0}})$, where ω_{RO} is the carrier frequency of the readout pulse. The resonator's spectral lineshape in turn is related to its decay dynamics, and lineshape's "width" is given by the decay rate κ of the RO resonator. Furthermore, the spectra's dependence on carrier frequency will differ if the qubit is in the $|g\rangle$ state or the $|e\rangle$ state by virtue of the dispersive shift χ of the resonator frequency. Thus, because κ affects the RO resonator lineshape and χ affects the spectra's dependence on carrier frequency, both will impact the overall $V_{\text{diff}}(\omega_{\text{R0}})$. Additionally, the spectra will also be affected by other components in the amplification chain such as filters, impedance mismatches, etc., which in turn will also impact the overall voltage separation. Finally, the readout power used will also affect this voltage separation, where the readout power will effectively *scale* the intrinsic difference in complex voltage between the RO spectra, up to powers commensurate with the critical photon number n_{crit} (above which the dispersive approximation breaks down).

On the other hand, readout infidelity will result from non-ideal effects of dispersive measurement, such measurement-induced state transitions or decay of the qubit during readout, as alluded to earlier. Generally, shorter readout lengths are commensurate with less decay of the qubit during readout, and shorter readout lengths can be achieved with a larger κ (which allows one to "ring up" the RO resonator to steady state faster). Meanwhile, measurement-induced state transitions can be minimized by utilizing readout powers meaningfully below n_{crit}.

Thus, optimization of qubit readout, through maximization of readout SNR and minimization of readout infidelity, must carefully take into account all the interdependent factors discussed above. For example, while a larger κ yields faster readout, which minimizes readout infidelity, it also broadens the RO lineshape width relative to the dispersive shift χ, and can thus decrease the intrinsic difference in complex voltage between the RO spectra. Moreover, while larger readout power may increase the voltage difference between the centers of the Gaussian distributions, it also can induce more measurement-induced state transitions. Further, the choice of g and Δ

that would allow for a large $n_{\text{crit}} = \Delta^2/4g^2$, and thus allow for large readout powers, would also result in a small $\chi \sim g^2/\Delta$, which would result in a smaller $V_{\text{diff}}(\omega_{\text{R0}})$. While for ideal systems optimal relations between some of these parameters have been obtained, system complexity such as Purcell filters (see next paragraph), dispersion, impedance mismatches, additional components in the amplification chain, etc., further complicate this optimization challenge. Thus in practice, one must aim for a reasonable n_{crit} and readout time, pick reasonable g and Δ based on those considerations, and empirically optimize things such as ω_{RO}, readout power, and readout length in experiment.

Finally, we note that although it is possible for the qubit to decay through its readout resonator through the Purcell effect, this decay channel can largely be mitigated through the use of a Purcell Filter. If a passive filter circuit that yields $Z_{\text{ext}}(\omega_Q) \approx 0$ is placed between the RO resonator and its feedline, where ω_Q is the qubit frequency and $Z_{\text{ext}}(\omega)$ is the impedance of the external environment that the RO resonator is coupled to, qubit emission at its frequency ω_Q is effectively blocked [69]. Thus, through the use of an appropriate Purcell filter, one may use a large κ to increase readout speed without incurring reduction in qubit lifetimes. In Appendix E.1 we discuss the design and performance of a Purcell filter comprised of a coupled-resonator array. For further details on signal processing techniques typically used in superconducting qubit dispersive readout, see Refs. [61, 70].

2.2 Additional General Concepts

Waveguide QED

Waveguide quantum electrodynamics (QED) refers to the study of quantum emitters (qubits) coupled to a one-dimensional (1D) single mode waveguide [20–22]. In contrast to cavity QED, where strong light-matter interaction is achieved between a qubit and a photon due to confinement of the photon in a cavity, in waveguide QED qubits are made to interact with propagating, un-localized photons. While light-matter interaction with propagating photons tends to be weak in free-space due to their small scattering cross section, this predicament can be circumvented by restricting the electromagnetic mode profile of the photon's field in the dimensions transverse to its direction of propagation [71]. This confinement to propagation in only one dimension not only increases the light-matter coupling between qubits and propagating photons due to decrease in the mode volume in the propagating photon's transverse dimensions, it also enhances interference effects between photons because light can only propagate to the left or to the right. In this manner, waveguide QED

experiments may enjoy strong-light matter interaction while meaningfully differing from experiments where photons are confined in *all* spatial dimensions, such as cavity QED. Hence, waveguide QED systems enable exploration of novel physics and applications in quantum information science that complement the extensive body of work accomplished in other quantum optical systems. While such a system can be realized in a variety of physical platforms, superconducting quantum circuits are well suited to the study of waveguide QED due their readily available strong light-matter interaction strengths [16].

Strong light-matter interaction in waveguide QED systems can be characterized by the collection efficiency of the emitter's radiation to the desired waveguide channel. In a canonical waveguide QED system where the waveguide has linear dispersion, a light-matter interaction figure of merit known as the *Purcell factor* may be defined as [72]

$$P_{1D} = \frac{\Gamma_{1D}}{\Gamma'}, \tag{2.32}$$

where Γ_{1D} is the emission rate of the qubit into the waveguide, and Γ' quantifies the intrinsic decoherence rate of the qubit. Γ' will have contributions both from the decay of the qubit to other radiative channels Γ_{loss}, as well as dephasing of the qubit Γ_φ, such that $\Gamma' = \Gamma_{\text{loss}} + 2\Gamma_\varphi$. However, if the waveguide's dispersion is significantly non-linear in the vicinity of the qubit frequency, its decay will be non-exponential, and thus its emission into the waveguide will not be characterized by a single "rate." Nevertheless, strong-light matter interaction in waveguide QED systems with dispersive waveguides can still be characterized by the degree of "desired emission" relative to the parasitic damping and dephasing rates.

The Hamiltonian describing the interaction of the qubit with the waveguide continuum may be generically written as ($\hbar = 1$)

$$\hat{H} = \frac{1}{2}(\omega_Q - i\frac{\Gamma'}{2})\hat{\sigma}_z + \int_k \omega_k \hat{a}_k^\dagger \hat{a}_k + \int_k g_k(\hat{\sigma}_- \hat{a}_k^\dagger + \hat{\sigma}_+ \hat{a}_k), \tag{2.33}$$

where ω_k captures the dispersion of the waveguide, and g_k allows for a frequency-dependent coupling of the qubit to waveguide modes with wavevector k. From this Hamiltonian, one may derive generic properties of a single qubit-waveguide system by making the simplifying assumption that $\omega_k = c|k|$ and $g_k = g$. For example, through input-output theory, we may derive the Rabi frequency of a qubit driven by an input coherent drive on the waveguide as [73]:

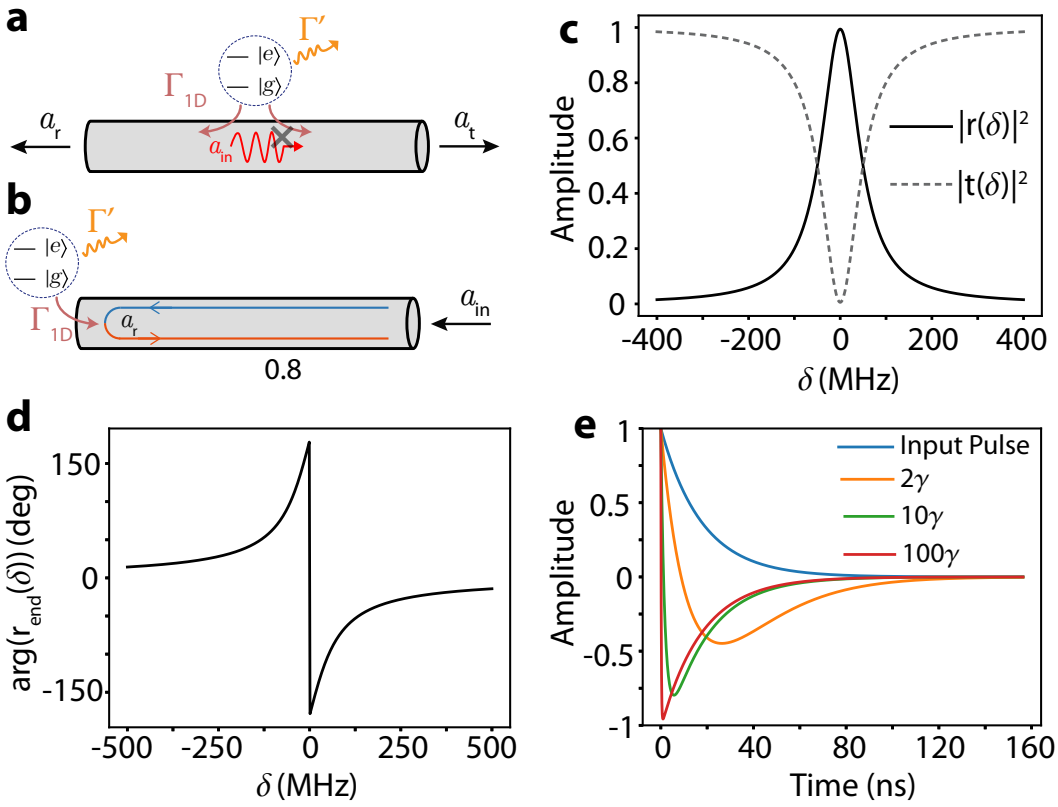

Figure 2.4: **Waveguide QED**. **a, b** Illustrations of typical waveguide QED systems, where a qubit is coupled to a waveguide with emission rate Γ_{1D} and parasitic decoherence rate Γ'. **a** Qubit side-coupled to a waveguide. Qubit emission induced by the incident field $a_t extin$ destructively interferes with the incident field, leading to an extinction of transmission. **b** Qubit coupled to the end of a semi-infinite waveguide. The input field $a_t extin$ scatters off of the qubit when it reaches the end of the waveguide and picks up a scattering phase, which is illustrated by the color change on the drawing. **c** Reflectance $r(\delta)|^2$ and transmitance $|t(\delta)|^2$ of a side-coupled qubit with $\Gamma_{1D}/2\pi = 100$ MHz and $T_2^* = 500$ ns (the parameters of our mirror qubit in the experiment discussed in Chapter 5). In the vicinity of the qubit frequency, the transmitance is negligible. **d** Phase of the reflection coefficient of an end-coupled qubit with $\Gamma_{1D}/2\pi = 140$ MHz, plotted in degrees. **e** Illustration of distortion of a wavepacket with exponential pulse shape $e^{\gamma t/2}$ after scattering on an end-coupled qubit with $\Gamma_{1D} = n\gamma$. Note that although a π phase shift is obtained for all cases, significant distortion of the input pulse shape occurs unless $\Gamma_{1D} \gg \gamma$. Moreover, note that the distortion is significantly smaller for Gaussian-shaped pulses, and here exponential pulses are plotted instead for visualization purposes.

$$\Omega = 2\alpha\sqrt{\Gamma_{1D}/k_n}, \tag{2.34}$$

where $|\alpha|$ is the amplitude of the coherent state drive, $k_n = 2$ for a qubit side-coupled to an infinite waveguide, and $k_n = 1$ for a qubit coupled to the end of a semi-infinite waveguide (which we henceforth refer to as an "end-coupled" qubit). See Figure 2.4a, b for an illustration of a side-coupled qubit and an end-coupled qubit, respectively. Furthermore, for a waveguide QED system with a side-coupled qubit, scattering theory reveals the low-power behavior of the system with a side-coupled qubit to be [72]:

$$r(\delta) = \frac{\Gamma_{1D}/2}{i\delta - (\Gamma_{1D} + \Gamma')/2}, \qquad t(\delta) = 1 + r(\delta), \tag{2.35}$$

where ω is the frequency of an input weak coherent state or single-photon signal onto the waveguide, $\delta = \omega_Q - \omega$, and r and t are the reflection coefficient and transmission coefficient, respectively. On resonance (when $\delta = 0$), the reflectance $|r|^2$ can be calculated from Equation 2.35 to be $|r(0)|^2 = (P_{1D}/(1 + P_{1D}))^2$; see Figure 2.4c for a plot of $|r|^2$ and $|t|^2$. Thus, for a large P_{1D} the side-coupled qubit can act as a nearly perfect *mirror* for propagating single photons, with "mirror efficiency" $\sim |r(0)|^2$. This phenomenon can be attributed to the destructive interference between the incident single-photon signal and the qubit's induced radiation into the forward reaction. This property of a highly-coherent side-coupled qubit was leveraged to realize a switchable mirror for propagating itinerant photons in the experiment discussed in Chapter 5. Note that for high-power coherent states, the behavior of the system is given by:

$$r(\delta) = -\frac{\Gamma_{1D}}{2} \frac{i\delta + \frac{\Gamma_{1D}+\Gamma'}{2}}{\delta^2 + \left(\frac{\Gamma_{1D}+\Gamma'}{2}\right)^2 + \frac{\Omega^2}{2}}. \tag{2.36}$$

For large Ω, saturation phenomena will be observed such as power-broadening, finite transmission on resonance, and incoherent broadend emission by the qubit.

In the case of a qubit coupled to the end of a semi-infinite waveguide, the low-power behavior of the system is given by [74]

$$r(\delta) = 1 - \frac{i\Gamma_{1D}}{\delta + i(\Gamma_{1D} + \Gamma')/2}. \tag{2.37}$$

For negligible Γ' and a resonant signal, we find that $r(\omega_Q) = -1$, indicating that a single-photon signal scattering on the qubit picks up a scattering phase of π. Meanwhile, for detuned signals, we find that the scattering phase approaches 0 with large detuning; see Figure2.4d for a plot of $\arg(r)$ for the end-coupled system. This property of a highly-coherent "end-coupled" qubit was leveraged to realize a CZ gate between a transmon qubit and a propagating itinerant photon. Note that for an itinerant wavepacket of finite-bandwidth with carrier frequency resonant with the qubit frequency, scattering upon the qubit will induce distortion of the wavepacket shape due to the frequency dependence of the scattering phase; see Figure 2.4e for an example for exponential-shaped pulses. However, this distortion can be minimized if $\Gamma_{1D} \gg \sigma$, where σ is the bandwidth of the photon. This distortion directly impacts the fidelity of the CZ gate alluded to (see Ref. [60] for further details), and thus as discussed in Chapter 5 we used Gaussian-shaped photons with bandwidth $\sigma \sim 1/14\Gamma_{1D}$ during realization of the CZ gate.

Note that although the formulas of the preceding discussion would technically be different for a waveguide with non-linear dispersion, the general intuition behind the formulas still generally apply for a dispersive waveguide QED system.

Fundamentals of Flux-Modulation of Qubit Coupled to Finite-Bandwidth Waveguide

In our experiments, we achieve tunable interaction between flux-tunable qubits and the coupled resonator array slow-light waveguides (SLWG) discussed in the introduction via sinusoidal flux modulation of the qubit frequency. For the purposes of the following discussion, consider a SLWG to be a waveguide with a finite-bandwidth passband, and an absence of propagating modes outside of the passband. Flux modulation induces a sideband-mediated interaction with the passband of the SLWG, whose strength is controlled by the amplitude of the flux modulation AC flux drive [75–77], if the sideband frequency lies in the passband of the SLWG.

Here, we briefly review the underlying physics of flux modulation by analyzing the following Hamiltonian of a qubit coupled to a waveguide

$$\hat{H} = \frac{1}{2}\omega_Q(\Phi(t))\hat{\sigma}_z + \int_k \omega_k \hat{a}_k^\dagger \hat{a}_k + g_Q \int_k (\hat{\sigma}_- \hat{a}_k^\dagger + \hat{\sigma}_+ \hat{a}_k), \tag{2.38}$$

where $\omega_Q(\Phi(t))$ is the qubit frequency as a function of the time-dependent flux $\Phi(t)$, ω_k is the frequency of a propagating waveguide mode with wavevector k, g_Q

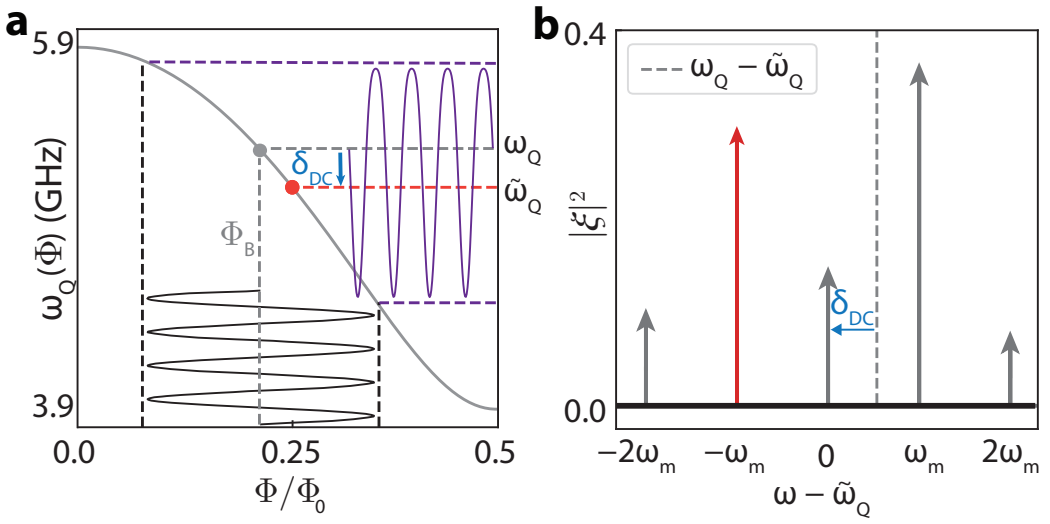

Figure 2.5: **Flux Modulation of Qubit Frequency a** Illustration of flux modulation of a qubit, when the qubit has a static flux bias $\Phi_B = 0.234\Phi_0$ and the AC flux amplitude $\Phi_{AC} = 0.152\Phi_0$, where Φ_0 is the magnetic flux quantum. The gray curve is the qubit tuning curve. The black line depicts typical flux modulation amplitudes in terms of flux quanta, while the purple curve depicts qubit frequency as a function of time under flux modulation. $\tilde{\omega}_Q$ corresponds to the average qubit frequency under flux modulation. **b** Sideband spectrum of a qubit under flux modulation. $|\xi|$ refers to sideband strength. The red colored arrow corresponds to the sideband used to effect emission into the SLWG in the experiment discussed in Chapter 5.

is the coupling of the qubits to the propagating modes, $\hat{\sigma}_+$, $\hat{\sigma}_-$ are the raising and lowering operators of the qubit, and $\hat{a}_k^\dagger$, $\hat{a}_k$ are the raising and lowering operators of mode k. By going into the interaction picture by the unitary transformation $U(t) = \exp[-i\int_0^t \frac{1}{2}\omega_Q(\Phi(t'))\hat{\sigma}_z dt' - it\int_k \omega_k \hat{a}_k^\dagger \hat{a}_k]$, we arrive at the following interaction Hamiltonian

$$\hat{H}_{int} = g_Q \int_k e^{-i(\phi(t)-\omega_k t)}\hat{\sigma}_- \hat{a}_k^\dagger + \text{h.c.}, \tag{2.39}$$

where $\phi(t) = \int_0^t \omega_Q(\Phi(t'))dt'$. Note that setting g_Q to be independent of k is a valid assumption for a qubit coupled to a single unit-cell of an infinite periodic array of coupled resonators [78].

Under sinusoidal modulation of external flux $\Phi(t)$, we can write $\Phi(t) = \Phi_B + \Phi_{AC}\sin(\omega_{\text{mod}}t)$, where Φ_B is the the static flux bias, Φ_{AC} is the AC flux ampltiude, and ω_{mod} is the modulation frequency. The periodicity of the flux signal allows for the $e^{-i\phi(t)}$ term to be expanded by the following Fourier series [79]

$$\hat{H}_{int} = g_Q \int_k \sum_s \xi_s e^{-i(\tilde{\omega}_Q - s\omega_{\text{mod}} - \omega_k)t}\hat{\sigma}_- \hat{a}_k^\dagger + \text{h.c.}, \tag{2.40}$$

where $\tilde{\omega}_Q$ is the average of $\omega_Q(t)$, and ξ_s is the Fourier coefficient of the s-th term, which we refer to as the "sideband amplitude." We note that because qubit tuning curves are non-linear (as depicted in Figure 2.5a), sinusoidal flux modulation will result in an average DC shift to the static qubit frequency $\omega_Q(\Phi_B)$, which is captured by the term $\tilde{\omega}_Q$. Moreover, note that one can obtain the magnitudes of ξ_s by simply taking the Fourier transform of $e^{-i\phi(t)}$, as shown in Figure 2.5b for one set of flux modulation and qubit parameters.

According to the RWA, we expect that only non-fast rotating terms of the Hamiltonian of Equation 2.40 would appreciably contribute to the qubit dynamics; hence we seek terms where $\tilde{\omega}_Q - s\omega_{\text{mod}} - \omega_k \approx 0$. Assuming that the waveguide has a finite bandwidth passband, and that only the first lower sideband ($s = 1$) is resonant with one of the passband modes, we can assume terms involving all other s are fast-rotating terms and discard them. This results in the final Hamiltonian

$$\hat{H}_{mod} = g_Q \xi \int_k e^{-i(\omega_Q^1 - \omega_k)t} \hat{\sigma}_- \hat{a}_k^\dagger + \text{h.c.}, \tag{2.41}$$

where $\omega_Q^1 \equiv \tilde{\omega}_Q - \omega_m$ is the frequency of the first lower sideband, and $\xi \equiv \xi_1$. Thus, $\omega_k = \omega_Q^1$ will be the center frequency of emission, while photon emission will also occur at surrounding frequencies where $\omega_Q^1 - \omega_k$ is small; thus imparting a finite bandwidth to any emitted photon. Note that the resultant Hamiltonian is in an equivalent form as Equation (2.39) up to a renormalization of the effective coupling rate. Thus, we can tune the strength of interaction between a qubit and the SLWG by controlling the sideband amplitude ξ and locating the first lower sideband inside the passband.

Non-Markovianity

While the Schrödinger equation is sufficient to describe the dynamics of theoretical isolated quantum systems, in practice quantum systems one wishes to control will have interactions with an external environment; we call such systems "open quantum systems." In general, these interactions influence the dynamics of open quantum systems, and can result in loss of their energy and information.

The standard approach to the study of open quantum system dynamics typically employs the Born–Markov approximation, which presupposes that future evolution of the system does not depend on past interactions with its environment [80, 81]. More precisely, this approximation assumes that the quantum system and its

environment are initially uncorrelated at $t = 0$, and that the interaction between the system and the environment is sufficiently weak such that 1) system-environment correlations do not manifest and 2) that the environment's state negligibly changes. This assumption can be succinctly expressed as $\rho_{SE}(t) = \rho_S(t) \otimes \rho_E$, where ρ_{SE} is the joint density matrix of the system and the environment, and ρ_S and ρ_E are the individual density matrices of the system and environment, respectively. These assumptions imply short environmental correlation times, and thus memory-less interaction with the environment, which allows one to theoretically predict the behavior of open quantum systems through the familiar Lindblad master equation [82].

However, it is known that this naive approximation can break down, and substantial quantitative and qualitative deviations from the dynamics of quantum Markov processes have been previously observed [83–86]. Such dynamics are referred to as "non-Markovian," implying that they are governed by significant memory effects, which arise in the case of strong system-environment couplings, structured or finite reservoirs, or large initial system–environment correlations. There have been several studies investigating the effects of "non-Markovianity" on the preservation of quantum information and multipartite entanglement [28, 30].

In particular, for non-Markovian systems the following two aspects of Markovian physics no longer hold: that information contained in the system is lost to the environment and never returns, and that any coupling between subsystems mediated by the environment can be approximated as an effective static interaction between them. In the non-Markovian regime there can be backflow of information from the environment back to the system, and if two subsystems couple via the environment one cannot simply trace out the environment's degrees of freedom and still be able to faithfully describe the dynamics.

A more rigorous definition of non-Markovianity was presented in Ref. [81]. First, consider the trace distance between two quantum states D, an often-used distance measure in quantum information theory [87]:

$$D(\rho^1, \rho^2) = \frac{1}{2}||\rho^1 - \rho^2|| \tag{2.42}$$

where $||A|| = Tr\left(\sqrt{A^\dagger A}\right)$. The trace distance has the property that $0 \leq D(\rho^1, \rho^2) \leq 1$, where $D(\rho^1, \rho^2) = 0$ if and only if $\rho^1 = \rho^2$, and $D(\rho^1, \rho^2) = 1$ if and only if ρ^1 and ρ^2 are orthogonal. It can be shown that for Markovian processes, the following

holds for all possible pairs of initial states $\rho_S^1(0)$ and $\rho_S^2(0)$ of an open quantum system at all times t [81]:

$$D\left(\rho_S^1(t), \rho_S^2(t)\right) \leq D\left(\rho_S^1(0), \rho_S^2(0)\right). \tag{2.43}$$

Thus, a quantum process is non-Markovian if there is an initial pair of states $\rho_S^{1\prime}(0)$ and $\rho_S^{2\prime}(0)$ whose trace distance $D\left(\rho_S^{1\prime}(t), \rho_S^{2\prime}(t)\right)$ is non-monotonic, i.e., starts to increase for some time $t > 0$. An increase in the trace-distance in this context is strictly associated with information flow from the environment back to the open quantum system, which is a non-Markovian phenomena. Equation 2.43 is consistent with the typical intuition behind Markovian decoherence, where decoherence results in the system state evolving toward either a mixed state or some specific lower energy dissipated state *irrespective* of its initial state. Note that in principle, if one could perform state tomography of different initial states at different times during their evolution, non-Markovianity could be experimentally assessed for a general quantum system. However, in general there are many competing manners to quantify non-Markovianity which do not necessarily agree [88].

In the work presented in this thesis, we are typically concerned with non-Markovianity in the context of a quantum emitter interacting with a slow-light dispersive waveguide reservoir. It is shown in Ref. [89] that for a qubit with population dynamics $P_{|e\rangle}(t)$, that:

$$\text{if} \quad \frac{dP_{|e\rangle}(t)}{dt} < 0 \quad \forall t \rightarrow \text{the system is Markovian.} \tag{2.44}$$

Thus, non-monotonic population dynamics of a qubit when coupled to a dispersive waveguide is a signature of non-Markovian dynamics.

Measurement-Based Quantum Computation

Conventional approaches to quantum computing entail implementing quantum algorithms by controlling and entangling a large number of matter-based qubits (trapped ions, quantum dots, superconducting qubits, etc.) via unitary quantum gates. At the end of the computation, the quantum information stored in the system of entangled matter-based qubits is converted to classical information, i.e., the result of the computation, through projective measurements on the qubits. However, an alternative approach to quantum computation exists called “measurement-based quantum computation" or “one-way quantum computation" [32, 90]. In measurement-based

quantum computation we start with a resource state of entangled qubits, and perform quantum computation by applying a time-ordered sequence of single-qubit measurements in specific bases to specific qubits. The choice of measurement basis in later measurements generally depends on the outcome of earlier measurements, thus in general there is a feedforward of information during computation (hence the qualifier “one-way"). Thus, the “computational step" here is projective measurements rather than unitary gates, and as the computation progresses, the total initial entanglement in the resource state diminishes. At the end of the computation when all qubits have been measured, the qubit measurement results comprise the result of the computation. See Figure 2.6a, b for an schematic representation of measurement-based quantum computation.

By starting with an universal highly-entangled resource state called the “cluster state," it can be shown that universal quantum computation is possible simply through single-qubit projective measurements on a 2D cluster state, while fault-tolerant quantum computation can be realized through this measurement-based scheme with a 3D cluster state [91]. Furthermore, it can also be shown that this measurement-based scheme incurs additional overhead compared to conventional gate-based quantum computing that is at most polynomial in the number of qubits [92]. Accordingly, there has been significant interest in the photonics community and industry in achieving photonic quantum computing via this measurement-based approach, where optical photons comprise the entangled qubits of the cluster state. Hence, reliably making large cluster states of entangled photonic qubits constitute a large burden of this approach to quantum computation, and is an area of active exceedingly active research [60, 93–98].

A cluster state of photons is simply a lattice of photons where each photonic qubit is entangled to its nearest neighbor; a cluster state can be 1D, 2D, 3D, etc., see Figure 2.6c for an illustration. A cluster state of N photons may be defined as the following quantum state:

$$|\phi\rangle_C = \prod_{(a,b)\in\mathcal{L}_C} CZ_{a.b}\,|+\rangle^{\otimes N}\,, \tag{2.45}$$

where $|+\rangle = \frac{1}{2}(|0\rangle + |1\rangle)$, $CZ_{a,b}$ is a controlled CZ gate between qubit a and qubit b, and $(a, b) \in \mathcal{L}_C$ denotes all pairs of qubits (a, b) that are nearest neighbors in the cluster state lattice, which is denoted by $\mathcal{L}_C$. This state will obey the following set of eigenvalue equations:

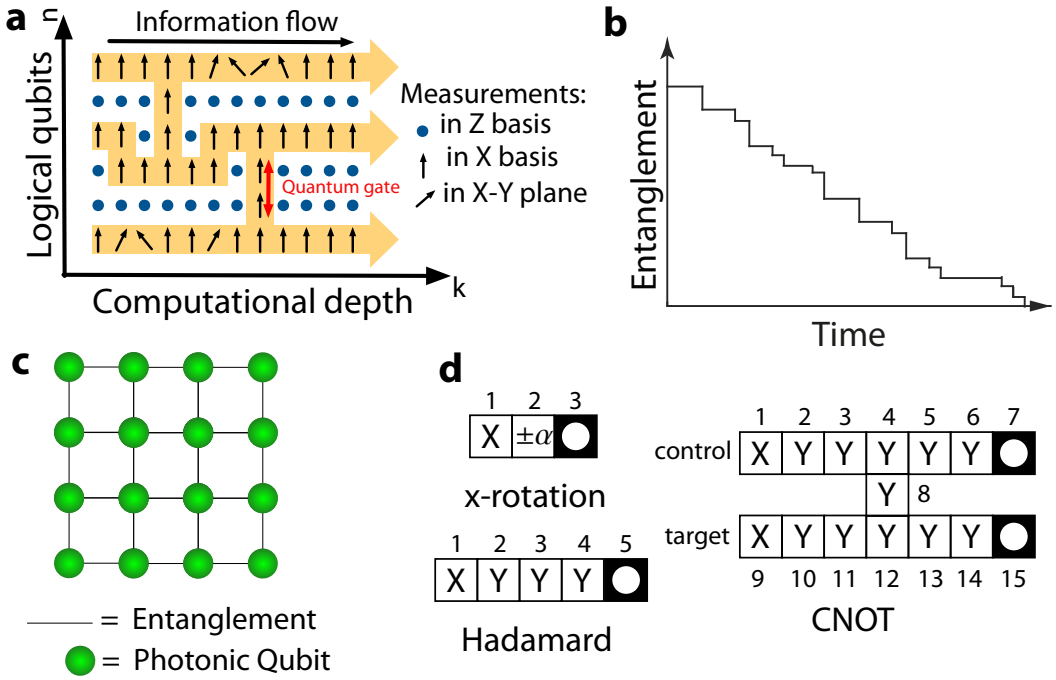

Figure 2.6: **Measurement-Based Quantum Computing**. **a** Schematic of measurement-based quantum computation with a 2D cluster state; this figure is adapted from Ref. [90]. Rows of the cluster state may be regarded as "logical qubits," while information is propagated horizontally through the cluster. Qubits indicated to have been measured in the Z-basis are all unentangled from other qubits and do not participate in computation. The quantum logic carried out is hence dependent on the shape of the cluster state C' containing the remaining entangled qubits. **b** Cartoon illustrating that, as computation is carried out through single-qubit measurements, the initial entanglement contained in the resource state diminishes as entangled qubits are projected into their measured state. Thus, all the entanglement necessary for computation should be initially contained in the resource state. **c** Cartoon illustration of a 2D cluster state. **d** Illustration of measurement sequences for realizing specific quantum gates on the 2D cluster state via the measurement-based approach. Leftmost qubits are the "input qubits" to the gate, and comprise the state of the "logical qubit" prior to the gate. Rightmost qubits (denoted by the black square with a white circle) are the "output qubits," whose states correspond to the states resulting from application of the desired gate on the input qubits.

$$K^{(a)} |\phi\rangle_C = \pm |\phi\rangle_C , \qquad \text{where} \quad K^{(a)} = \sigma_x^{(a)} \bigotimes_{b \in N(a)} \sigma_z^{(b)}, \tag{2.46}$$

and where $N(a)$ denotes all qubits in the neighborhood of qubit a, and the distribution of positive and negative eigenvalues depends on the distribution of qubits on the lattice.

In the following discussion we turn to universal measurement-based quantum computation with 2D cluster states, and reference the reader to Ref. [91] for further discussion of fault-tolerant measurement based quantum computing. As shown in Figure 2.6a, in a 2D cluster state the number of rows may be regarded as the number

of “logical qubits," while the number of columns is related to the circuit depth of the effective quantum circuit being realized through measurement of the photonic qubits. Quantum information is thereby propagated horizontally through the cluster, while vertical entanglement connections in the cluster are utilized to realize effective two qubit gates.

In general, realization of a specific quantum circuit will require a specific graph state C' of nearest-neighbor entangled qubits where only *some* of the qubits in the original cluster state are necessary for computation. Thus, the first step in utilizing the initial cluster state is to disentangle unnecessary qubits from the state by measuring them in the Z-basis, resulting in the desired graph state C'. With the desired state, effective gates on the “logical qubits" may be performed through a sequence of adaptive one-qubit measurements.

In Figure 2.6d we schematically show the measurement sequences of some common gates, such as an x-rotation, a Hadamard gate, and a CNOT gate, and further detail their measurement sequences below [92]. As alluded to earlier, rows in a cluster state correspond to “logical qubits." Thus, single-qubit gates are realized through measurements on a single row of photonic qubits, while entangling gates will involve multiple rows of qubits. In order to realize an x-rotation “gate" $U_x(\alpha) = \exp(-i\alpha\sigma_x/2)$ on a “logical qubit" corresponding to a row of the cluster state, three photonic qubits are required. Qubit 1 (the first leftmost qubit) will contain the input “qubit state" $|\psi_{\text{in}}\rangle$ to the gate, i.e., qubit 1 contains the state of the logical qubit established through all preceding measurements. The first qubit is measured in the x-basis, and we denote its measurement result by s_1. Qubit 2 will then be measured in the basis specified by the following equation (where $j = 2$):

$$\mathcal{B}_j(\varphi_j) = \left\{ \frac{|0\rangle + e^{i\varphi_j}|1\rangle}{\sqrt{2}}, \frac{|0\rangle - e^{i\varphi_j}|1\rangle}{\sqrt{2}} \right\}, \tag{2.47}$$

where $\varphi_2 = (-1)^{s_1}(-\alpha)$. It can be shown that qubit 3, which is the output qubit, will have the state $|\psi_{\text{out}}\rangle = U_\Sigma U_x(\alpha)|\psi_{\text{in}}\rangle$, where $U_\Sigma = \sigma_x^{s_2}\sigma_z^{s_1}$ is a “byproduct operator." Thus, we see that the effective rotation angle realized depends on the outcome of the measurement on qubit 1 (s_1). This is an example of the “information feedforward" alluded to earlier: in order to realize $U_x(\alpha)$ deterministically, the basis of measurement of qubit 2 depends on the measurement result of qubit 1, thus measurement of qubit 1 must be done before measurement of qubit 2. Addidionally, in general effective “gates" performed in this measurement-based manner are

equivalent to the "ideal gate" concatenated with a byproduct operator that depends on qubit measurement outcomes. Thus, these byproduct operators are intrinsically random. However, by keeping track of the measurement outcomes, one can effectively "commute" these byproduct operators to the end result of the computation, and correct for them in post-processing with the recorded measurement results [92]. In this manner, deterministic quantum logic can be executed in spite of the intrinsic randomness of quantum measurement results. Similarly, to realize an arbitrary rotation $U_{\text{Rot}}(\alpha, \eta, \xi) = U_x(\xi)U_z(\eta)U_x(\alpha)$ 5 qubits are needed, and they are measured in bases $\mathcal{B}_1(0), \mathcal{B}_2(-\alpha(-1)^{s_1}), \mathcal{B}_3(-\eta(-1)^{s_2}), \mathcal{B}_4(-\xi(-1)^{s_1+s_3})$, where the qubits are measured one after the other since their measurement basis depends on the results of preceding measurements.

In order to realize a Hadamard gate, qubits 1-4 must be measured in the X,Y,Y, and Y bases respectively, albeit for this specific gate all measurements can be performed simultaneously. Once again qubit 1 contains the input qubit state $|\psi_{\text{in}}\rangle$, and qubit 5 is the output qubit such that $|\psi_{\text{out}}\rangle = U_\Sigma H |\psi_{\text{in}}\rangle$, where $U_\Sigma = \sigma_x^{s_1+s_3+s_4}\sigma_z^{s_2+s_3}$. To realize a CNOT gate, measurements on two cluster state rows will be performed, in addition to a measurement on an intervening qubit between the rows, in order to entangle two "logical qubits" of the cluster state. An schematic of the required measurements is shown in Figure 2.6d; here qubit 1 and qubit 9 are the input control and target qubits respectively, qubit 7 and qubit 15 are the output control and target qubits respectively, and all measurements can be performed simultaneously as well. Note that since in this discussion we have briefly reviewed how to perform arbitrary single-qubit gates and a two-qubit gate, it is evident that universal quantum computation is possible with this measurement-based approach.

In the experiments in Chapter 5 we experimentally demonstrate deterministic generation of a 2D cluster state of itinerant microwave photons; thus paving the way for exploration of measurement-based quantum computation in the microwave domain.

Overview of Early Literature on an Atom Coupled to a Bandgap Material

Spontaneous photon emission by a quantum emitter into the fluctuating quantum-electrodynamic vacuum is an emblematic example of the dynamics of an open quantum system, characterized by memory-less exponential decay and a Lamb shift of the emitter's transition frequency [99]. However, these dynamics are altered upon constriction of the electrodynamic vacuum's mode density, as demonstrated by the appearance of coherent vacuum Rabi oscillations when the radiation field is

constricted to a single mode [100]. Between the limits of boundless vacuum and a single mode field, the rich dynamics that arise when an emitter is coupled to a radiation field with a bounded continuous spectrum, as typically found in dispersive media, became the subject of strong theoretical interest during the late 80s and 90s [50–59]. We briefly review some of this work below.

From the pioneering works in cavity QED, it was already apparent to the quantum-optics community that the spontaneous decay and Lamb shift of an atom were dependent on the geometry and associated mode structure of its environment. For example, an atom's decay rate could be enhanced if placed inside a high Q resonant cavity, while it could be suppressed if placed inside a detuned cavity [101]. Nonetheless, while modulation of the atom's decay rate by a cavity is possible, theoretically in the $t \to \infty$ limit the atom will eventually fully decay to the environment, as is the case for an atom in free-space.

However, pioneering quantum-optics works theoretically demonstrated that a drastically different situation arises if the atom is placed in an environment where its electromagnetic mode spectrum exhibit gaps in frequency, which are henceforth called bandgaps. They found that because there are no modes with frequencies inside the bandgap for radiation to propagate in, an atom whose transition frequency falls deep in the bandgap will never decay, even in the $t \to \infty$ limit.

Furthermore, the dynamics of an atom with frequency in the vicinity of the "band-edge" of a photonic bandgap (PBG) was also an area of strong interest. It was found that due to the singular nature of the density of states (DOS) at the bandedge of a PBG material, the resulting dynamical behavior of the atom is *fundamentally different* from that of an atom in a cavity or free-space. This fundamental difference may be understood to stem from the many-body nature of a PBG material that leads to such a singular DOS. Note that a singular DOS precludes application of the Born-Markov approximation, thus rendering master equation approaches inapplicable to the study of atoms in PBG materials.

More specifically, pioneering works by Sajeev John and others investigated the behavior of an atom placed in a material where a bandgap is realized by modulation of the refractive index, which forbids propagation of radiation at certain frequencies due to Bragg scattering. In their earlier work [52], they directly solve the time-independent Schrödinger equation with a Hamiltonian similar to the one in in Equation 2.33 ($\Gamma' = 0$), with the ω_k and g_k one could expect in an isotropic PBG material. By solving for the eigenenergies through complex-analysis mathematical

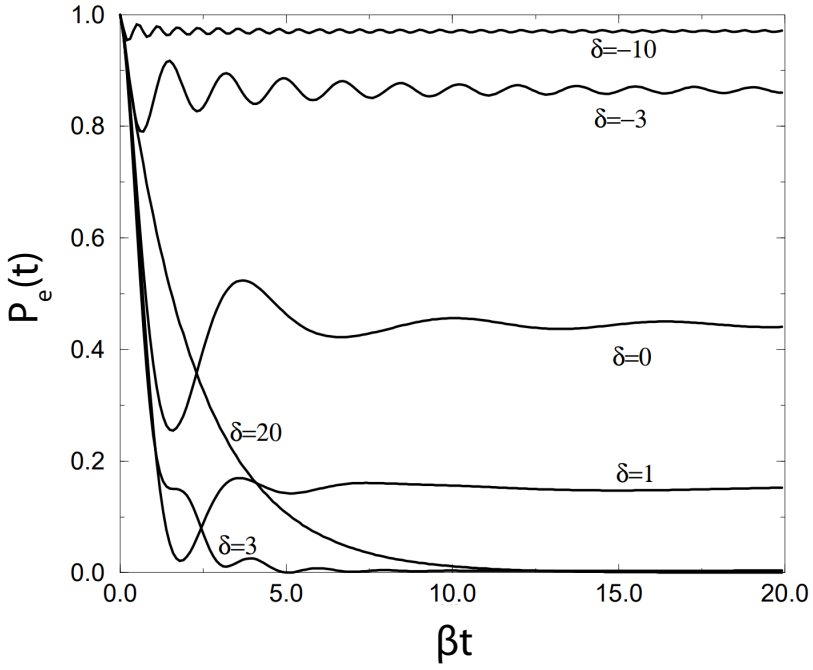

Figure 2.7: **Dynamics of an Atom Inside a Photonic Bandgap Material**. Dynamics of an initially excited atom inside a photonic bandgap material (PBG) for various values of the detuning from the bandedge $\delta = (\omega_Q - \omega_b)/\beta$, where ω_b is the frequency of the bandedge and 2β is the difference in energy between the bound and radiative dressed states when $\delta = 0$ (i.e., the resonant frequency splitting by the bandedge). We bring particular attention to the $\delta = 1$ curve, where it is evident that finite population trapping occurs even though the qubit is *outside* the bandgap, where the DOS is finite. Figure adapted from Ref. [58].

methods, they found that in the vicinity of the bandedge, the bandedge splits the transition of the atom into a non-radiative atom-photon bound state in the bandgap, and a radiative state outside of the bandgap. Because there are no electromagnetic modes in the bandgap, the photonic component of the atom-photon bound state remains bound to the qubit and is not lost into the continuum; thus the atom can be considered to be self-dressed by its own localized radiation. Note that, unlike the case of an atom coupled to a cavity, the dressed states resultant from the splitting of the atom by the bandedge are *fundamentally* different from one another, due to the properties of the dressed states discussed. In Chapter 3.2 we go through a similar derivation, where we also demonstrate that the bound state has an exponentially localized photonic wave function.

Additionally, in a follow-up work [55], they directly solve the time-dependent Schrödinger equation with the same Hamiltonian (albeit in the rotating frame of the atom), and with the following ansatz for the state of the system in the single-photon manifold:

$$|\psi\rangle = c_e(t)\,|e, \text{vac}\rangle + \sum_k c_k(t)\hat{a}_k^\dagger\,|g, \text{vac}\rangle\,e^{-i\Delta_k t}, \tag{2.48}$$

where $\Delta_k = \omega_k - \omega_Q$. Through their analytical methods, they derive equations of motion for the population of an initially excited atom as a function of its detuning from the bandedge $\delta = \omega_Q - \omega_b$, where ω_b is the frequency of the bandedge; we plot dynamics calculated from their equations of motion for several values of δ in Figure 2.7. In the vicinity of the bandedge they find non-exponential oscillatory decay dynamics as well as finite population trapping in the $t \to \infty$ limit, where the frequency of oscillations and the amount of trapped population depends on δ. Far from the bandedge, they recover the expected dynamics of exponential decay when ω_Q is far from the bandgap, and no decay when ω_Q is deep in the bandgap.

These phenomena can be understood by considering the dynamical interplay of the dressed radiative and bound states. The initial state of the system $|e, \text{vac}\rangle$, where the qubit is excited and there are no photons in the PBG material, is not an eigenstate of the system, but is rather a superposition of the dressed bound and radiative eigenstates of the system. The observed interaction dynamics of the qubit with the PBG material thus originate from interference of the dressed states during time-evolution, which leads to oscillatory behavior in the qubit population analogous to vacuum-Rabi oscillations. The frequency of these oscillations is thus set by the difference in energy between the dressed states. Moreover, the amplitude of these oscillations decays with time because the energy in the radiative dressed state component of the initial superposition state is lost into the waveguide as the emission propagates away. However, the energy in the bound dressed state component of the initial superposition state does not decay even in the $t \to \infty$ limit, which results in the finite population trapping observed in the dynamics. The fraction of the initial excitation that remains trapped in the bound state depends on δ, which sets the relative magnitudes of the different dressed states in the initial superposition state. Note that even for atom frequencies outside the bandgap (with moderate detunings from the bandedge), some degree of population trapping in the $t \to \infty$ limit occurs.

The most remarkable aspect of the behavior of an atom coupled to a PBG material is the formation of a stable, non-radiative atom-photon bound state *due to hybridization of the atom with the structured continuum of modes*. The formation of this bound state, and thus some degree of finite population trapping, is observed even for atom frequencies outside the bandgap where the DOS is finite. This behavior is

fundamentally distinct from the behavior of conventional open quantum systems, where hybridization with a continuum leads to dissipation and full loss of energy in the $t \rightarrow \infty$ limit, and where the strength of decay typically depends on the value of the DOS at the transition frequency of the atom. Due to the physical nature of the structured reservoir, it retains memory of the atom's past interactions with it, thus leading to this distinctly non-Markovian behavior of the atom-PBG system. Hence, it was recognized by Sajeev John and others that the behavior of an atom in a PBG material constituted a new paradigm in the study of open quantum-optical systems, which led to its further detailed study for decades to come [56, 57, 78, 102, 103].

In the experiment described in Chapter 4, where we couple a superconducting transmon qubit to a SLWG that has a finite passband (and accordingly has "bandgaps" outside of the passband), we demonstrate experimental observation of this canonical behavior of an atom coupled to a structured reservoir that has been thus far described. To our knowledge, this is the first time that these physical phenomena have been observed in dynamical measurements. Thus, our results constitute a substantial contribution to this field of quantum optics in structured reservoirs.

Chapter 3

COUPLED MICROWAVE RESONATOR ARRAYS FOR METAMATERIAL SLOW-LIGHT WAVEGUIDES

In this Chapter we present the theory, design principles, and characterization of an all-electrical slow-light waveguide (SLWG) consisting of a chain of coupled lumped-element superconducting resonators, fabricated out of aluminum patterned on a silicon substrate. We demonstrate that this compact, low-loss microwave waveguide has sharp bandedges, and a passband with group delay of 55 ns per centimeter over an 80 MHz bandwidth. *This slow-light waveguide system forms the basis for all subsequent experiments in this thesis*. This Chapter starts with an overview of the design principles of this slow-light waveguide, as well as characterization data for a SLWG test device (without qubits). We then delve deeper into various aspects of the SLWG system's theory and design, as well as further characterization analysis of the SLWG test device.

3.1 Slow-Light Metamaterial Waveguide Overview

In prior work studying superconducting qubit emission into a photonic bandgap waveguide [104], we employed a metamaterial consisting of a coplanar waveguide (CPW) periodically loaded by lumped-element resonators. In that geometry, whose circuit model simplifies to a transmission line with resonator loading in parallel to the line, one obtains high-efficiency transmission with a characteristic impedance approximately that of the standard CPW away from the resonance frequency of the loading resonators, and a transmission stopband near resonance of the resonators. The spectral characteristics of the metamaterial in Ref. [104] were studied via spontaneous emission lifetime and lamb-shift measurements of a weakly coupled superconducting qubit, which revealed information about the local DOS at the qubit frequency that were consistent with the metamaterial's engineered dispersion. In contrast, here we seek a waveguide with high transmission efficiency, slow-light propagation within a transmission passband, and considerably stronger qubit coupling to the waveguide's guided modes. The stronger coupling renders the Born approximation inapplicable in such a system, where the effect of the qubit's interaction with the photonic reservoir takes on significantly more complexity than simply a decay rate dependent solely on the DOS at the qubit's frequency. Furthermore,

the increased propagation delay gives rise to non-Markovian memory effects in the waveguide-mediated interactions between qubits, for which the waveguide degrees of freedom can no longer be be traced out, as in Ref. [38] for instance.

Large delay per unit area can be obtained by employing a network of sub-wavelength resonators, with light propagation corresponding to hopping from resonator-to-resonator at a rate set by near-field inter-resonator coupling. This area-efficient approach to achieving large delays is well-suited to applications where only limited bandwidths are necessary. However, realizing such a waveguide system in a compact chip-scale form factor requires a modular implementation that can be reliably replicated at the unit cell level without introducing spurious cell-to-cell couplings. In optical photonics applications, this sort of scheme has been realized in what are called coupled-resonator optical waveguides, or CROW waveguides [105, 106]. Here we employ a periodic array of capacitively coupled, lumped-element microwave resonators to form the waveguide. Such a resonator-based waveguide supports a photonic channel through which light can propagate, henceforth referred to as the passband, with bandwidth approximately equal to four times the coupling between the resonators, J. The limited bandwidth directly translates into large propagation delays; as can be shown (see Section 3.2), the delay in the resonator array is roughly ω_0/J longer than that of a conventional CPW of similar area, where ω_0 is the resonance frequency of the resonators.

An optical and scanning electron microscope (SEM) image of the unit cell of the metamaterial slow-light waveguide used in this work are shown in Figure 3.1a. The cell consists of a tightly meandered wire inductor section (L_0; false color blue) and a top shunting capacitor (C_0; false color green), forming the lumped-element microwave resonator. Note that these delineations between inductor and capacitor are not strict, and that the meandered wire inductor (top shunting capacitor) has a small parasitic capacitance (parasitic inductance). The resonator is surrounded by a large ground plane (gray) which shields the meander wire section. Laterally extended 'wings' of the top shunting capacitor also provide coupling between the cells (C_g; false color green). Note that at the top of the optical image, above each shunting capacitor, we have included a long superconducting island (C_q; false color green); this is used in the next section as the shunting capacitance for Xmon qubits. Similar lumped-element resonators have been realized with internal quality factors of $Q_i \sim 10^5$ and small resonator frequency disorder [104], enabling propagation of light with low extinction from losses or disorder-induced scattering [107]. The

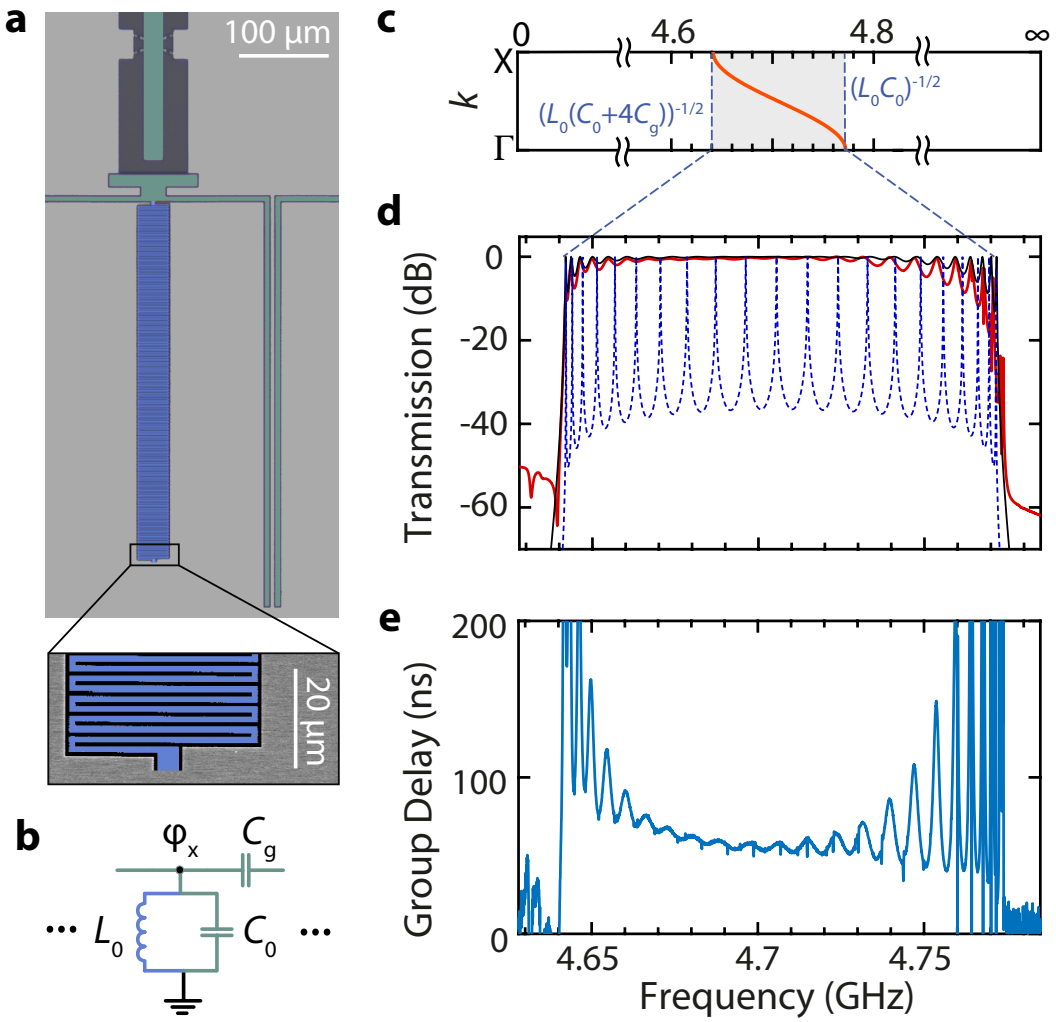

Figure 3.1: **Microwave Coupled Resonator Array Slow-light Waveguide.** **a** Optical image of a fabricated microwave resonator unit cell. The capacitive elements of the resonator are false-colored in green, while the inductive meander is false colored in blue. The inset shows a false colored SEM image of the bottom of the meander inductor, where it is shorted to ground. **b** Circuit diagram of the unit cell of the periodic resonator array waveguide. **c** Theoretical dispersion relation of the periodic resonator array. See Section 3.2 for derivation. **d** Transmission through a metamaterial slow-light waveguide spanning 26 resonators and connected to 50-Ω input-output ports. Dashed blue line: theoretical transmission of finite array without matching to 50-Ω boundaries. Black line: theoretical transmission of finite array matched to 50-Ω boundaries through two modified resonators at each boundary. Red line: measured transmission for a fabricated finite resonator array with boundary matching to input-output 50-Ω coplanar waveguides. The measured ripple in transmission is less than 0.5 dB in the middle of the passband. **e** Measured group delay, τ_g. Ripples in τ_g are less than $\delta\tau_g = 5$ ns in the middle of the passband.

waveguide resonators shown in Figure 3.1a have a bare resonance frequency of $\omega_0/2\pi \approx 4.8$ GHz, unit cell length $d = 290$ μm, and transverse unit cell width $w = 540$ μm, achieving a compact planar form factor of $\bar{d}/\lambda = (\sqrt{dw})/(2\pi v/\omega_0) \approx 1/60$, where v is the speed of light in a CPW on an infinitely thick silicon substrate.

The unit cell is to a good approximation given by the electrical circuit shown in Figure 3.1b, in which the photon hopping rate is $J \propto C_g/C_0$ [108]. We chose a ratio of $C_g/C_0 \approx 1/70$, which yields a delay per resonator of roughly 2 ns. Note that we have achieved this compact form factor and large delay per resonator while separating different lumped-element components by large amounts of ground plane, which minimizes spurious crosstalk between different unit cells. Analysis of the periodic circuit's Hamiltonian and dispersion can be found in section 3.2, where the dispersion is shown to be $\omega_k = \omega_0/\sqrt{1 + 4\frac{C_g}{C_0}\sin^2(kd/2)}$. Figure 3.1c shows a plot of the theoretical waveguide dispersion for an infinitely periodic waveguide, where the frequency of the bandedges of the passband are denoted with the circuit parameters of the unit cell.

For finite resonator arrays, care must be taken to avoid reflections at the boundaries that would result in spurious resonances (see Figure 3.1d, dashed blue curve, for example). To avoid these reflections, we taper the impedance of the waveguide by slowly shifting the capacitance of the resonators at the boundaries. In particular, we modify the first two unit cells at each boundary, but in principle, more resonators could have been modified for a more gradual taper. Increasing C_g to increase the coupling between resonators, and decreasing C_0 to compensate for resonance frequency changes, effectively impedance matches the Bloch impedance of the periodic structure in the passband to the characteristic impedance of the input-output waveguides [109]. In essence, this tapering achieves strong coupling of all normal modes of the finite structure to the input-output waveguides by adiabatically transforming guided resonator array modes into guided input-output waveguide modes. This loading of the normal modes lowers their Q such that they spectrally overlap and become indistinguishable, changing the DOS of a finite array from that of a multi-mode resonator to that of finite-bandwidth continuum with singular bandedges. Further details of the design of the unit cell and boundary resonators can be found in section 3.3.

Using the above design principles, we fabricated a capacitively coupled 26-resonator array metamaterial waveguide. The waveguide was fabricated using electron-beam deposited aluminum (Al) on a silicon substrate and was measured in a dilution refrig-

erator; transmission measurements are shown in Figure 3.1d, e, and further details of our fabrication methods and measurement set-up can be found in Appendix A. We find less than 0.5 dB ripple in transmitted power and less than 10% variation in the group delay ($\tau_g \equiv -\frac{d\phi}{d\omega}$, $\phi = \arg(t(\omega))$, where t is transmission) across 80 MHz of bandwidth in the center of the passband, ensuring low distortion of propagating signals. Qualitatively, this small ripple demonstrates that we have realized a resonator array with small disorder and precise modification of the boundary resonators. More quantitatively, from the transmitted power measurements we extract a standard deviation in the resonance frequencies of $3 \times 10^{-4} \times \omega_0$ (see section 3.4). Furthermore, we achieve ≈ 55 ns of delay across the 1 cm metamaterial waveguide, corresponding to a slow-down factor given by the group index of $n_g \approx 650$. We stress that this group delay is obtained across the center of the passband, rather than near the bandedges where large (and undesirable) higher-order dispersion occurs concomitantly with large delays.

3.2 Capacitively Coupled Resonator Array Waveguide Fundamentals

Band Structure Analysis

We consider a periodic array of capacitively coupled LC resonators, with unit cell circuit diagram shown Figure 3.1b. The Lagrangian for this system can be constructed as a function of node fluxes ϕ_x of the resonators, and is written as,

$$L = \sum_x \left[\frac{1}{2} C_0 \dot{\phi}_x^2 + \frac{1}{2} C_g (\dot{\phi}_x - \dot{\phi}_{x-1})^2 - \frac{{\phi_x}^2}{2L_0} \right]. \tag{3.1}$$

Since we seek traveling wave solutions to the problem, it is convenient to work with the Fourier transform of the node fluxes, defined as

$$\phi_k = \frac{1}{\sqrt{M}} \sum_{x=-N}^{N} \phi_x e^{-ikxd}, \tag{3.2}$$

where $M = 2N + 1$ is the total number of periods of a structure with periodic boundary conditions, d is the lattice constant of the resonator array, and k are the discrete momenta of the first Brillouin zone's guided modes and are given by $k = \frac{2\pi m}{Md}$ for integer $m = [-N, N]$. Using the inverse Fourier transform,

$$\phi_x = \frac{1}{\sqrt{M}} \sum_k \phi_k e^{ikxd}, \tag{3.3}$$

we arrive at the following k-space Lagrangian

$$L = \sum_k \left[\frac{1}{2} C_0 \dot{\phi}_k \dot{\phi}_{-k} + \frac{1}{2} C_g \dot{\phi}_k \dot{\phi}_{-k} \left| 1 - e^{-ikd} \right|^2 - \frac{\phi_k \phi_k}{2L_0} \right], \tag{3.4}$$

where we note that $\left|1 - e^{-ikd}\right|^2$ is equivalent to $4 \sin^2 (kd/2)$. The canonical node charges Q_k of the system will be given by the conjugate "momenta" of the node fluxes:

$$Q_k = \frac{\partial L}{\partial \dot{\phi}_k} = \dot{\phi}_{-k} \left(C_0 + 4C_g \sin^2 (kd/2) \right). \tag{3.5}$$

We can invert this relationship (and make use of that fact that $\sin^2(kd/2) = \sin^2(-kd/2)$) to obtain the Hamiltonian via the standard Legendre transformation $H = \sum_k \dot{\phi}_k Q_k - L$, yielding

$$H = \sum_k \left[\frac{1}{2} \frac{Q_k Q_{-k}}{\left(4C_g \sin^2 (kd/2) + C_0 \right)} + \frac{\phi_k \phi_{-k}}{2L_0} \right]. \tag{3.6}$$

Promoting charge and flux to quantum operators and utilizing the canonical commutation relation $\left[\hat{\phi}_k, \hat{Q_{k'}}\right] = i\hbar\delta_{kk'}$, we define the following creation and annihilation operators:

$$\begin{aligned} \hat{a}_k &= \sqrt{\frac{m_k \omega_k}{2\hbar}} \left(\hat{\phi}_k + \frac{i}{m_k \omega_k} \hat{Q}_{-k} \right), \\ \hat{a}_k^\dagger &= \sqrt{\frac{m_k \omega_k}{2\hbar}} \left(\hat{\phi}_{-k} - \frac{i}{m_k \omega_k} \hat{Q}_k \right), \end{aligned} \tag{3.7}$$

where $m_k = \left(C_0 + 4C_g \sin^2 (kd/2) \right)$. The resulting dispersion relation, ω_k, plotted in Figure 3.1c is given by,

$$\omega_k = \frac{\omega_0}{\sqrt{1 + 4\frac{C_g}{C_0} \sin^2(kd/2)}}, \tag{3.8}$$

where $\omega_0 = 1/\sqrt{L_0 C_0}$, and $\left[\hat{a}_k, \hat{a}_{k'}^\dagger\right] = \delta_{kk'}$. Expressing the flux and charge operators in terms of $\hat{a}_k, \hat{a}_{k'}^\dagger$ and substituting them into Equation (3.6), we recover the second-quantized Hamiltonian in the diagonal k-space basis

$$\hat{H} = \sum_k \hbar\omega_k \left(\frac{1}{2} + \hat{a}_k^\dagger \hat{a}_k\right). \tag{3.9}$$

Note that, given the translational invariance of the capacitively coupled resonator array circuit, it was expected that the the Hamiltonian would be diagonal in the Fourier plane-wave basis (Bloch Theorem).

Also note that, for two capacitively coupled LC resonators, their coupling $J = \frac{\omega_0}{2}(C_g/(C_0 + C_g))$ is positive-valued [108] due to the fact that the anti-symmetric odd mode of the circuit is the lower energy eigenmode. This results in positive-valued photon hopping terms in the Hamiltonian, which directly lead to a maximum in frequency at the Γ point and opposite directions of the phase velocity and group velocity in the structure, as observed in other dispersive media [110–112].

Comparison to Tight-Binding Model

In the limit $C_0 \gg C_g$, the dispersion is well approximated to first order by a tight-binding model with dispersion given by $\omega_k = \omega_p + 2J\cos(kd)$, where $J = \omega_0(C_g/2C_0)$ is approximately the nearest-neighbor coupling between two resonators of the resonator array, and $\omega_p = (\omega_0 - 2J)$ is the center of the passband. The difference in the two dispersion relations reflects the coupling beyond nearest-neighbor that arises due to the topology of the circuit, in which any two pairs of resonators are electrically connected through some capacitance network dependent on their distance. The magnitude of these interactions is captured in the Fourier transform of the dispersion. Consider the Fourier transform for the annihilation operator of the (localized) mode of the individual resonator located at position x,

$$\hat{a}_k = \frac{1}{\sqrt{M}} \sum_x \hat{a}_x e^{-ikxd}. \tag{3.10}$$

Substituting Equation (3.10) into Equation (3.9), we arrive at the following real-space Hamiltonian,

$$\hat{H} = \hbar \sum_x \sum_{x'} V(x - x')\hat{a}_x^\dagger \hat{a}_{x'}, \tag{3.11}$$

where $V(x-x')$ is the distance-dependent interaction strength between two resonators located at positions x and x', and is simply given by the Fourier transform of the dispersion relation,

$$V(x-x') = \frac{1}{M}\sum_k \omega_k e^{-ikd(x-x')}. \tag{3.12}$$

For example, substituting the tight-binding dispersion $\omega_k = \omega_p + 2J\cos(kd)$ into Equation (3.12) yields $V(x-x') = \omega_p\delta_{x,x'} + 2J\left(\delta_{x-x',1} + \delta_{x-x',-1}\right)$, which, upon substitution into Equation (3.11), recovers the tight-binding Hamiltonian with only nearest-neighbor coupling.

In Figure 3.2a we plot the magnitudes of nearest neighbor ($x - x' = 1$), next-nearest neighbor ($x - x' = 2$), and next-next-nearest neighbor ($x - x' = 3$) couplings in the capacitively coupled resonator array as a function of C_g/C_0, calculated numerically via the discrete Fourier transform of the dispersion relation. It is evident that for small C_g/C_0 the nearest neighbor coupling overwhelmingly dominates.

Qubit Coupled to Passband of a Waveguide

The Hamiltonian of a transmon-like qubit coupled to the metamaterial waveguide via a single unit cell, where only the first two levels of the transmon ($|g\rangle, |e\rangle$) are considered, can be written as ($\hbar = 1, d = 1$),

$$\hat{H} = \omega_{ge}|e\rangle\langle e| + \sum_k \omega_k \hat{a}_k^\dagger \hat{a}_k + \frac{g_{\mathrm{uc}}}{\sqrt{M}}\sum_k \left(\hat{a}_k^\dagger \hat{\sigma}^- + \hat{a}_k \hat{\sigma}^+\right), \tag{3.13}$$

where ω_k is given by Equation (E.1). For an infinite array, the time-independent Schrödinger equation $\hat{H}|\psi\rangle = E|\psi\rangle$ has two types of solutions in the single-photon manifold: there are scattering eigenstates, which have an energy within the passband, and there are bound states that are energetically separated from the passband continuum. We demonstrate this in the following analysis. First, we substitute into $\hat{H}|\psi\rangle = E|\psi\rangle$ the following ansatz for the quantum states of the composite qubit-waveguide system, i.e., for dressed states of the qubit,

$$|\psi\rangle = c_e|e, \mathrm{vac}\rangle + \sum_k c_k \hat{a}_k^\dagger |g, \mathrm{vac}\rangle, \tag{3.14}$$

where $|\mathrm{vac}\rangle$ corresponds to no excitations in the waveguide. Doing this substitution and subsequently collecting terms, we arrive at the following coupled equations for c_e and c_k:

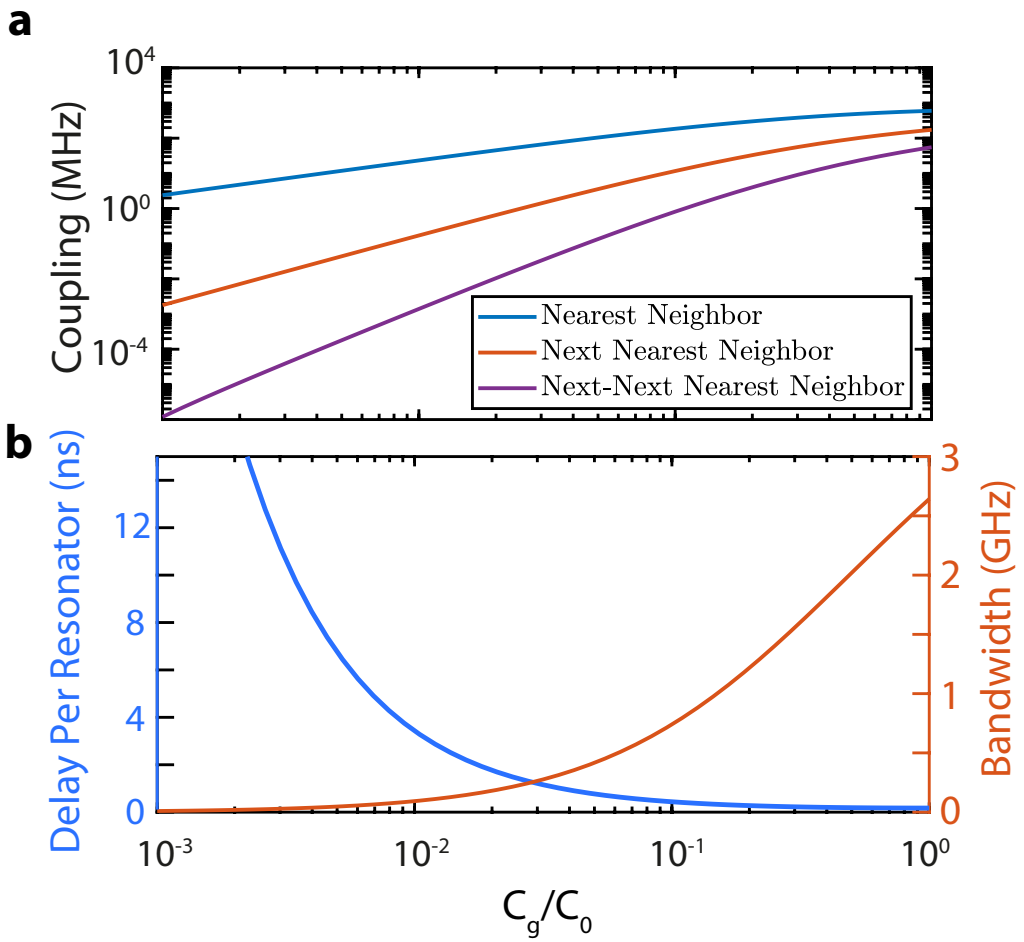

Figure 3.2: **a** Magnitude of nearest neighbor, next-nearest neighbor, and next-next-nearest neighbor inter-resonator couplings in an (infinite) capacitively coupled resonator array as a function of C_g/C_0 ratio. The bare resonator frequency was chosen to be 4.8GHz. **b** Magnitude of delay per resonator and bandwidth of the passband as a function of C_g/C_0 ratio. The bare resonator frequency was again chosen to be 4.8GHz, and the calculated delays are for frequencies in the middle of the passband.

$$c_e = \frac{g_{\text{uc}}}{\sqrt{M}} \sum_k \frac{c_k}{E - \omega_{ge}}, \tag{3.15}$$

$$c_k = \frac{g_{\text{uc}}}{\sqrt{M}} \frac{c_e}{E - \omega_k}. \tag{3.16}$$

By further assuming that the waveguide supports a continuum of modes (which is appropriate for a finite tapered waveguide, as described in Section 3.1), the sum can be changed into an integral $\sum_k \to \frac{1}{\Delta_k} \sum_k \Delta_k \to \frac{1}{\Delta_k} \int_{-\pi}^{\pi} \mathrm{d}k$, where $\Delta_k = 2\pi/M$. In this continuum limit, E can be found by first substituting Equation (3.16) into Equation (3.15) and subsequently dividing both sides by c_e, which yields the following transcendental equation for E,

$$E = \omega_{ge} + \frac{1}{2\pi}\int \mathrm{d}k \frac{g_{\mathrm{uc}}^2}{E - \omega_k}, \tag{3.17}$$

where the integral on the right-hand side of Equation (3.17) is known as the "self-energy" of the qubit [55, 57, 58]. Note that in the opposite limit of a single resonator (where ω_k takes on a single value and the density of states $\frac{\partial\omega}{\partial k}$ becomes a delta–function at that value), Equation (3.17) yields the familiar Jaynes-Cummings splitting $\sqrt{\delta^2 + g_{\mathrm{uc}}^2}$.

Computation of the self-energy for E such that $E > \omega_k$ or $E < \omega_k \ \ \forall k$, i.e., for energies outside of the passband, yields real solutions for Equation (3.17). On the other hand, for energies E inside the passband, the self-energy integral contains a divergence at $E = \omega_k$ for real E while there is no divergence if E is allowed to be complex with an imaginary component; thus Equation (3.17) has complex solutions when $\mathrm{Re}(E)$ is inside the passband. While a Hermitian Hamiltonian such as the one in Equation (3.13) by definition does not contain complex eigenvalues, it can be shown that the magnitude of the imaginary component of complex solutions of Equation (3.17) gives the decay rate of an excited qubit for a qubit dressed state with energy in the passband. For further details we suggest Refs. [52, 57, 58] to the reader. Thus, the existence of complex solutions of Equation (3.17) reflects the fact that qubit dressed states with energy in the passband are radiative states that decay into the continuum, characteristic of open quantum systems coupled to a continuum of modes. In contrast, the dressed states with (real) energies outside of the passband do not decay, and are known as qubit-photon bound states in which the photonic component of the dressed state wavefunction remains bound to the qubit and is not lost into the continuum.

For further analytical progress, we consider only the upper bandedge, and make the effective-mass approximation. This approximation is tantamount to assuming the dispersion is quadratic, such that $\omega_k \approx \omega_0 - Jk^2$, which is obtained in the limit of small C_g/C_0 (where ω_k is well approximated by the tight binding cosine dispersion) and small k (where $\cos(k)$ to second order is approximately $1 - k^2/2$). This approximation is appropriate when ω_{ge} is close to the upper bandedge, where the qubit is dominantly coupled to the Γ-point $k = 0$ modes close to the bandedge due to the van Hove singularity in the DOS, and when the lower bandedge is sufficiently detuned from the qubit. Complimentary analysis for the lower bandedge can also be done in the same manner. For a more detailed derivation, see Refs. [51, 52, 57, 78, 113].

Under the effective-mass approximation, the self-energy integral in Equation (3.17) can be easily analyzed by taking the bounds of integration to infinity, and is calculated to be $g_{\mathrm{uc}}^2/2\sqrt{J(E-\omega_0)}$. For $\omega_{ge} = \omega_0$, Equation (3.17) then has the following two solutions:

$$E_b = \omega_0 + (g_{\mathrm{uc}}^4/4J)^{1/3}, \tag{3.18}$$

$$E_r = \omega_0 - e^{i\pi/3}(g_{\mathrm{uc}}^4/4J)^{1/3}. \tag{3.19}$$

These two solutions are indicative of a splitting of the qubit transition frequency by the bandedge into two dressed states: a radiative state with energy E_r in the passband and a bound state with energy E_b above the bandedge. The magnitude difference between the dressed state energies is $2(g_{\mathrm{uc}}^4/4J)^{1/3}$, which is the frequency of coherent qubit-to-photon oscillations for an excited qubit at the photonic bandedge.

For the remainder of the analysis, we focus on the qubit-photon bound state of the system. The wavefunction of the bound state with energy E can be obtained by first substituting Equation (3.16) into Equation (3.14), which yields

$$|\psi_E\rangle = c_e\left(|e\rangle + \frac{g_{\mathrm{uc}}}{\sqrt{M}}\sum_k \frac{1}{E-\omega_k}\hat{a}_k^\dagger\,|g,\mathrm{vac}\rangle\right). \tag{3.20}$$

The qubit and photonic components of the bound state can be calculated from the normalization condition of $|\psi_E\rangle$,

$$|c_e|^2\left(1 + \frac{1}{2\pi}\int \mathrm{d}k\left|\frac{g_{\mathrm{uc}}}{E-\omega_k}\right|^2\right) = 1. \tag{3.21}$$

By assuming $E > \omega_0$, the integral in Equation (3.21) is calculated to be equal to $g_{\mathrm{uc}}^2/4\sqrt{J(E-\omega_0)^3}$, which yields the following magnitude for the qubit component of the bound state,

$$|c_e|^2 = \left(1 + \frac{1}{2}\frac{E-\omega_{ge}}{E-\omega_0}\right)^{-1}, \tag{3.22}$$

whereas the photonic component is simply $\int \mathrm{d}k|c_k|^2 = 1 - |c_e|^2$. We can thus see that when $E \approx \omega_{ge} \neq \omega_0$, the qubit is negligibly hybridized with the passband modes and $|c_e|^2 \approx 1$. On the other hand, as $\omega_{ge} \to \omega_0$ we have $|c_e|^2 \to 2/3$,

indicating that the bound-state photonic component contains half as much energy as the qubit component when the qubit is tuned to the bandedge.

We can also obtain the real-space shape of the photonic bound state by inserting Equation (3.10) into Equation (3.20), where for a continuum of modes in k-space we arrive at the following photonic wavefunction,

$$\sum_x e^{-|x|/\lambda} \hat{a}_x^\dagger \left|g, \text{vac}\right\rangle , \tag{3.23}$$

up to a normalization constant, where $\lambda = \sqrt{J/(E-\omega_0)}$ and the qubit is assumed to reside at $x = 0$. We thus find an exponentially localized photonic wavefunction for the bound state. The localization length λ increases as J increases, indicating that the bound state becomes more delocalized across multiple resonators as the strength of coupling between the resonators in the waveguide increases, whereas λ diverges as the $E \to \omega_0$, which is associated with full delocalization of the bound-state as its energy approaches the continuum of the passband.

Group Delay

Lowering the ratio C_g/C_0 effectively lowers the photon hopping rate J between resonators, and can thus be chosen to significantly decrease the group velocity of propagating modes of the structure, albeit at the cost of decreased bandwidth of the passband modes. The group delay per resonator may be obtained from the inverse of the group velocity $\frac{\partial \omega_k}{\partial k}$, while the bandwidth can be calculated to be equal to $\omega_0 \left(1 - 1/\sqrt{1+4C_g/C_0}\right)$; both are plotted in Figure 3.2b. Note that although the group velocity approaches zero near the bandedge, a traveling pulse at the bandedge frequency would experience significant distortion due to the rapidly changing magnitude of the group velocity near the bandedge. At the center of the passband where the dispersion is nearly linear, however, it is possible to have propagation with minimal distortion.

Hence, in order to effectively use the coupled resonator array as a delay line, the coupling should be made sufficiently high such that the bandwidth of propagating modes (where the dispersion is also nearly linear) is sufficiently high, and the effect of resonator frequency disorder due to fabrication imperfections is tolerable. After the resonator coupling constraints have been met, the desired delay may be achieved with a suitable number of resonators. It is thus evident that the ability to fabricate resonators of sub-wavelength size with minimal frequency disorder is critical to

the effectiveness of implementing a slow-light waveguide with a coupled resonator array.

An appropriate metric to compare the performance of the resonator array as a delay line against dispersionless waveguides is to consider the delay achieved per area rather than per length, in order to account for the transverse dimensions of the resonators. In addition, typical implementations of delay lines with CPW geometries commonly require a high degree of meandering in order to fit in a packaged device; thus the pitch and turn radius of the CPW meandered trace also must be taken into account when assessing delay achieved per area. However, by making certain simplifying assumptions about the resonators it is possible to gain intuition on how efficient the resonator array is in achieving long delays compared to a dispersionless CPW. For the unit cell resonators implemented throughout (see Figure 3.1), the capacitive elements of the resonator are electrically connected to one end of the meander while the opposite end of the meander is shunted to ground. This geometry is therefore topologically similar to a $\lambda/4$ resonator, and consequently the lengths of the meander and a conventional $\lambda/4$ CPW resonator will be similar to within an order of magnitude for conventional implementations (here λ is the wavelength of the CPW resonator mode).

Thus, by approximating that a single resonator of the array occupies the same area as a $\lambda/4$-section of CPW, a direct comparison between the delays of the two different waveguides can be made. In the tight-binding limit, the group delay per resonator in the middle of the passband is approximately equal to $1/2J$, where J is the coupling between two resonators of the array. Hence, for N resonators ${}^{\text{array}}/^{\text{CPW}} = \frac{N/2J}{N\lambda/4v} \sim \omega_0/J$, where τ_d is group delay and v is the group velocity of light in the CPW. Hence, the resonator array is more efficient as a delay line when compared to conventional CPW by a factor of approximately ω_0/J (assuming group velocity is approximately equal to phase velocity in the CPW). In practice, this factor will also depend on the particular geometrical implementations of both kinds of waveguide. For example, for the resonator array described in Figure 3.1, $\omega_0/J \approx 120$ and = 55 ns delay was achieved in the middle of the passband for a resonator array of area $A = 6\,\text{mm}^2$. This constitutes a factor of 60 (500) improvement in delay per area achieved over the CPW delay line in Ref. [114] (Ref. [115]).

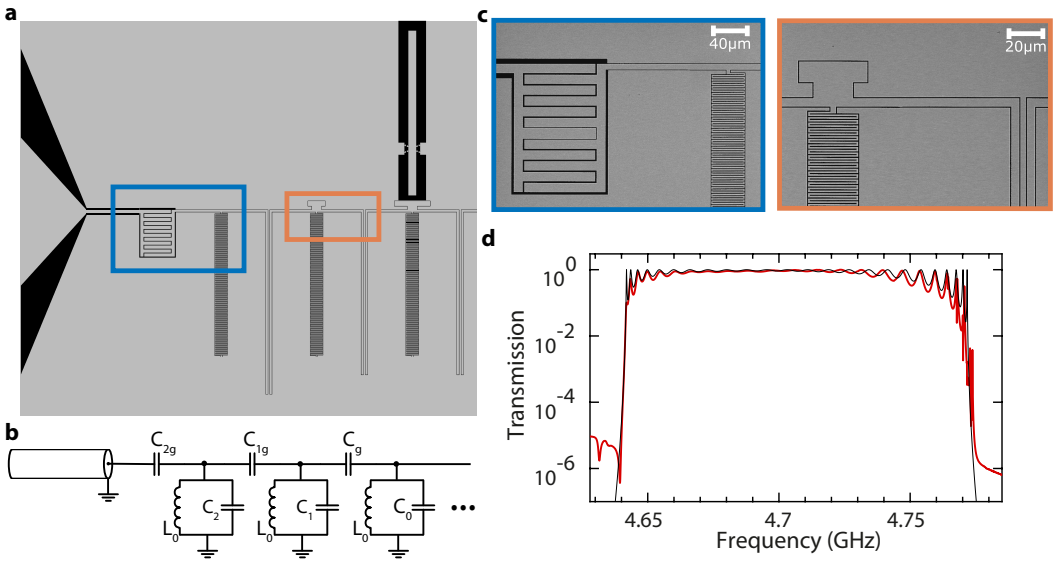

Figure 3.3: **a** CAD diagram showing the end of the finite resonator array, including the boundary matching circuit (which in this case includes the first two resonators) and the first unit cell. **b** Corresponding circuit model of the end of the finite resonator array. **c** Zoomed-in SEM images of the first (left) and second (right) boundary-matching resonators. **d** Transmission spectrum of the full resonator array consisting of 22 unit cells and 2 boundary-matching resonators on either end of the array (for a total of 26 resonators). Measured data is plotted as a red curve and the circuit model fit is plotted as a black curve. Fit model parameters are given in the text.

3.3 Physical Implementation of Finite Resonator Array

Geometrical Design of Unit Cell

As shown in Figure 3.1, the unit cell of the resonator array in this work includes a lumped-element resonator formed from a tightly meandered wire with a large “head" capacitance, and “wing" capacitors which, in addition to providing the majority of the capacitance to ground, are used to couple between resonators in neighbouring unit cells. The meandered wire has a 1 μm pitch and a 1 μm trace width for tight packing. From the top of the meander inductor is the head capacitor and a pair of thin metal capacitor strips which extend to the lateral edges of the unit cell (the wing capacitors). The ground plane in between the resonators’ meander inductor and their lateral wing capacitors acts as an electrical “fence", restricting the meander from coupling to neighboring resonators via stray capacitance or mutual inductance. This ensured that the bulk of the coupling between resonators was from the resonators’ wing capacitive elements, thereby facilitating theoretical analysis of the structure using a simple single resonator per unit cell model. Furthermore, we included ground metal between the thin metal capacitor traces of neighbouring unit cell wing capacitors. In this way, the ground planes above and below the resonator array are tied together at each unit cell boundary, thereby suppressing the influence

of higher-order transverse, slot-line modes of the waveguide.

In addition, anticipating integration with Xmon qubits, we incorporated into our unit cell design a Xmon shunting capacitance to ground, along with pads for facile addition of Josephson Junctions. This ensured that the addition of a qubit at a particular unit cell site in the resonator array minimally affected the capacitive environment surrounding that unit cell, and prevented the breaking of translational symmetry of the resonator array due to the addition of qubits. The capacitance between the Xmon capacitor and the rest of the unit cell was designed to be ~ 2 fF, yielding a qubit-unit cell coupling of $g_{\mathrm{uc}} \sim J$.

Matching of the Finite Resonator Array to Input-Output CPWs

It has been previously shown that for a finite coupled cavity array, low-ripple transmission at the center of the passband is possible by appropriate variation of the inter-resonator coupling coefficients for a few of the resonators adjacent to the ports, effectively matching the finite periodic structure to the input-output ports [116]. In the case of capacitively coupled electrical resonators, modifying the coupling capacitance in isolation results in a renormalization of the resonance frequency and thus constitutes a scattering center for propagating light. Thus, concurrent modification of both the coupling capacitance and the shunt capacitance to ground for the boundary resonators is necessary to achieve low-ripple transmission in the middle of the passband, as previously shown in filter design theory [117]. By constraining the total capacitance in each modified resonator to remain constant (and keeping the inductance constant), the total number of parameters to adjust in order to achieve low ripple transmission is merely equal to the chosen number of resonators to be modified, resulting in a low-dimensional optimization problem. A filter design software such as Microwave Office can be used to provide initial guesses on the optimal circuit parameters with high accuracy, which can then be further optimized.

In Section 3.1 we present results on matching of a resonator array spanning 26 resonators to 50-Ω CPWs via modification of two resonators at each of the array-CPW boundaries. The geometrical design of the boundary resonators is shown in Figure 3.3. The number of boundary resonators to modify (2) was chosen as a compromise between device simplicity and spectral bandwidth over which matching occurs. In principle, however, more resonators could have been used for matching of the finite structure to the ports in order to decrease the ripples in the transmission passband near the bandedges. Referring to the notation in Figure 3.3b, the targets for

the unit cell resonator and boundary resonator elements extracted from Sonnet [118] electromagnetic simulations were C_{2g} = 89 fF, C_{1g} = 8.9 fF, C_g = 6.47 fF, C_2 = 269 fF, C_1 = 351 fF, C_0 = 353 fF, and geometric inductance L_0 = 2.92 nH. The individual capacitive and inductive elements have parasitic inductance and capacitance, respectively, and thus were not simulated separately. Rather, circuit parameters for the three different resonators were extracted by simulating the whole resonator circuit. We extracted the circuit element parameters from these simulations by numerically obtaining the dispersion for an infinite array of each of the three types of resonators via the $ABCD$ matrix method [109]. This yielded ω_0 and C_g/C_0; C_g was obtained from the B parameter of the $ABCD$ matrix (which contains information on the series impedance of the unit cell circuit). We found this method of extracting parameters from simulation to give much higher accuracy when compared to other approaches, such as simulating unit cell elements separately.

Figure 3.3d shows a plot of the measured transmission spectrum of the fabricated 26 unit cell slow-light waveguide based upon the above design and presented in Section 3.1 (c.f., Figure 3.1). A circuit model fit to the measured transmission spectrum yields the following circuit element parameters for boundary and central waveguide unit cells: C_{2g} = 87.5 fF, C_{1g} = 7.3 fF, C_g = 5.05 fF, C_1 = 352.1 fF, C_2 = 275.5 fF, C_0 = 353.2 fF, and geometric inductance L_0 = 3.151nH. Based upon this model fit, we were thus able to realize good correspondence (within 3%) between design and measured capacitances to ground, while extracted coupling capacitances are systematically lower by approximately 1.5 fF. We attribute the systematically smaller coupling to stray mutual inductance between neighboring meander inductors, which tends to lower the effective coupling impedance between the resonators. The slightly larger fit inductance compared to design is to be expected as the kinetic inductance of the meander trace was not included in simulation. According to Ref. [119], for a 1 μm trace width and 120 nm-thick aluminum wire, the expected increase in the total inductance due to kinetic inductance is approximately 5% of the geometric inductance, in reasonable correspondence to the measured value.

3.4 Disorder in the Metamaterial Waveguide

Fluctuations in the bare resonance frequencies of the lumped-element resonators making up the metamaterial waveguide breaks the translational symmetry of the waveguide, and effectively leads to random scattering of traveling waves between different Bloch modes. The interference between the randomly rescattered waves can be shown to lead an exponential reduction in the probability that a propagating pho-

ton traverses across the entire length of the waveguide. Furthermore, if the strength of scattering is large relative to the photon hopping rate, Anderson localization of light occurs where photons are completely trapped within the waveguide[107]; see Figure 3.4. Thus, the aforementioned strategy for constructing a slow-light waveguide from an array of weakly coupled resonators is at odds with the inherent presence of fabrication disorder in any practically realizable device. Therefore, a compromise must be struck between choosing an inter-resonator coupling low enough to provide significant delay, but high enough such that propagation through the metamaterial waveguide is not significantly compromised by resonator frequency disorder.

Figure 3.5a shows numerical calculations of the transmission extinction in the metamaterial waveguide as a function of σ/J, where σ is the resonator frequency disorder. This analysis was performed for a 50 unit cell waveguide, with $C_0 = 353.2$ fF, $C_g = 5.05$ fF, and $L_i = 3.101$ nH $+ \delta_i$. Here, L_i is the inductance of the i^{th} unit cell and δ_i are random inductance variations in each unit cell that give rise to a particular resonator frequency disorder, σ. These L_i were calculated by: (i) determining the resonator frequencies of each unit cell by drawing from a Gaussian distribution with mean ω_0 and variance σ^2, and (ii) solving for the corresponding inductances given the resonator frequencies and a fixed C_0. Note that we modeled the disorder as originating from inductance variations, rather than C_0 or C_g variations, based on the fact that earlier work showed that disorder in superconducting microwave resonators was primarily due to variations in kinetic inductance [121]. As we see in Figure 3.5a, in order for the average transmission to drop by less than 0.5dB (10%), the normalized resonator frequency disorder must be less than $\sigma/J < 0.1$.

In order to quantify the resonator frequency disorder in our fabricated resonator array one can analyze the passband ripple in transmission measurements [121] (c.f., Figure 3.1d, e). Given that the effect of tapering the circuit parameters at the boundary is to optimally couple the normal modes of the structure to the source and load impedances, the ripples in the passband are merely overlapping low-Q resonances of the normal modes. Therefore, we can extract the normal mode frequencies from the maxima of the ripples in the passband, which will be shifted with respect the to normal mode frequencies of a structure without disorder.

Furthermore, the mode spacing is dependent on the number of resonators and, in the absence of disorder, follows the dispersion relation shown in Figure 3.1c where the dispersion is relatively constant near the passband center and starts to shrink near the bandedges. In the presence of disorder, however, this pattern breaks down

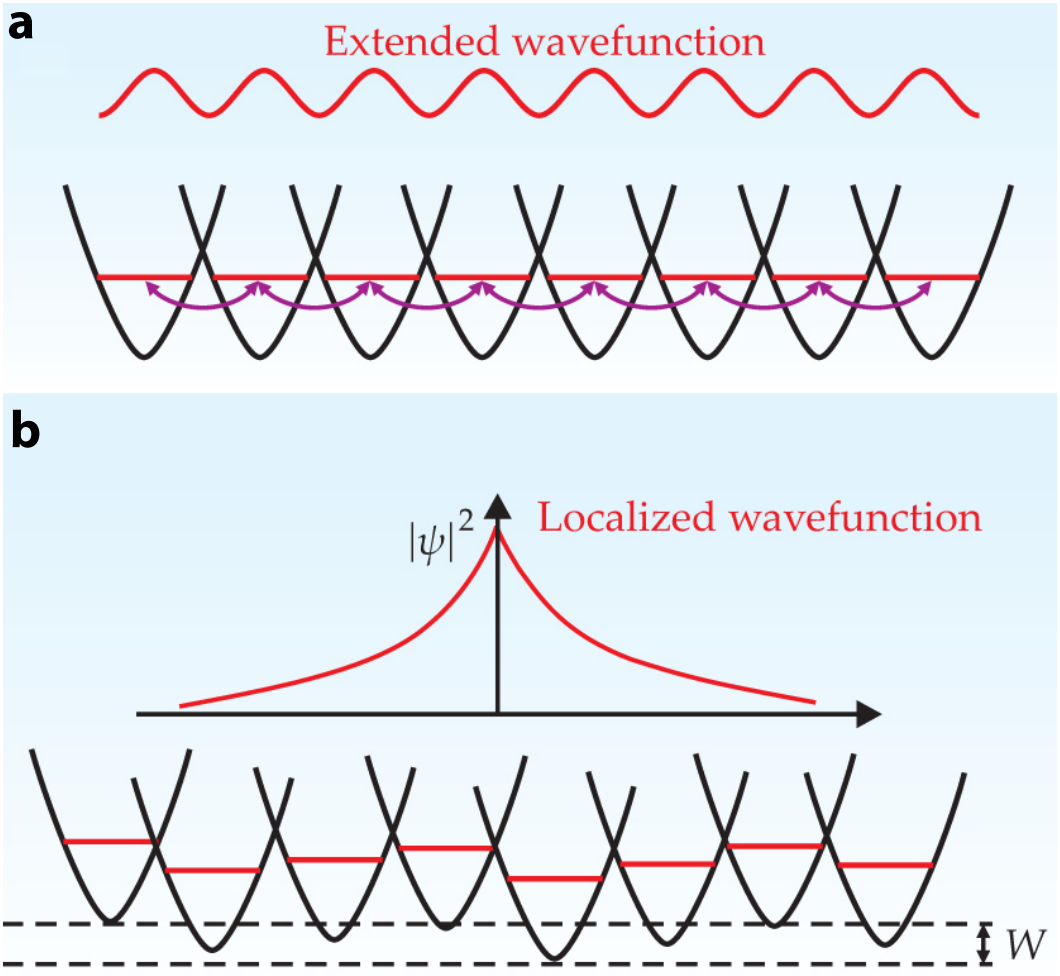

Figure 3.4: **Anderson Localization in a 1D Periodic Potential with Finite Disorder.** **a** Perfectly periodic potential of nearest-neighbor coupled lattice sites. For a particle in this potential, one obtains freely propagating waves as the solution of the Schrödinger equation, as per the Bloch Theorem. **b** Disordered potential of nearest-neighbor coupled lattice sites, with disorder W. Due to destructive interference between randomly scattered waves, one obtains an exponentially localized wavefunction in space as the solution of the Schrödinger equation. Note that in 1D, some degree of localization happens irrespective of how small W is, because even small potential fluctuations will cause some degree of scattering. Figure adapted from Ref. [120].

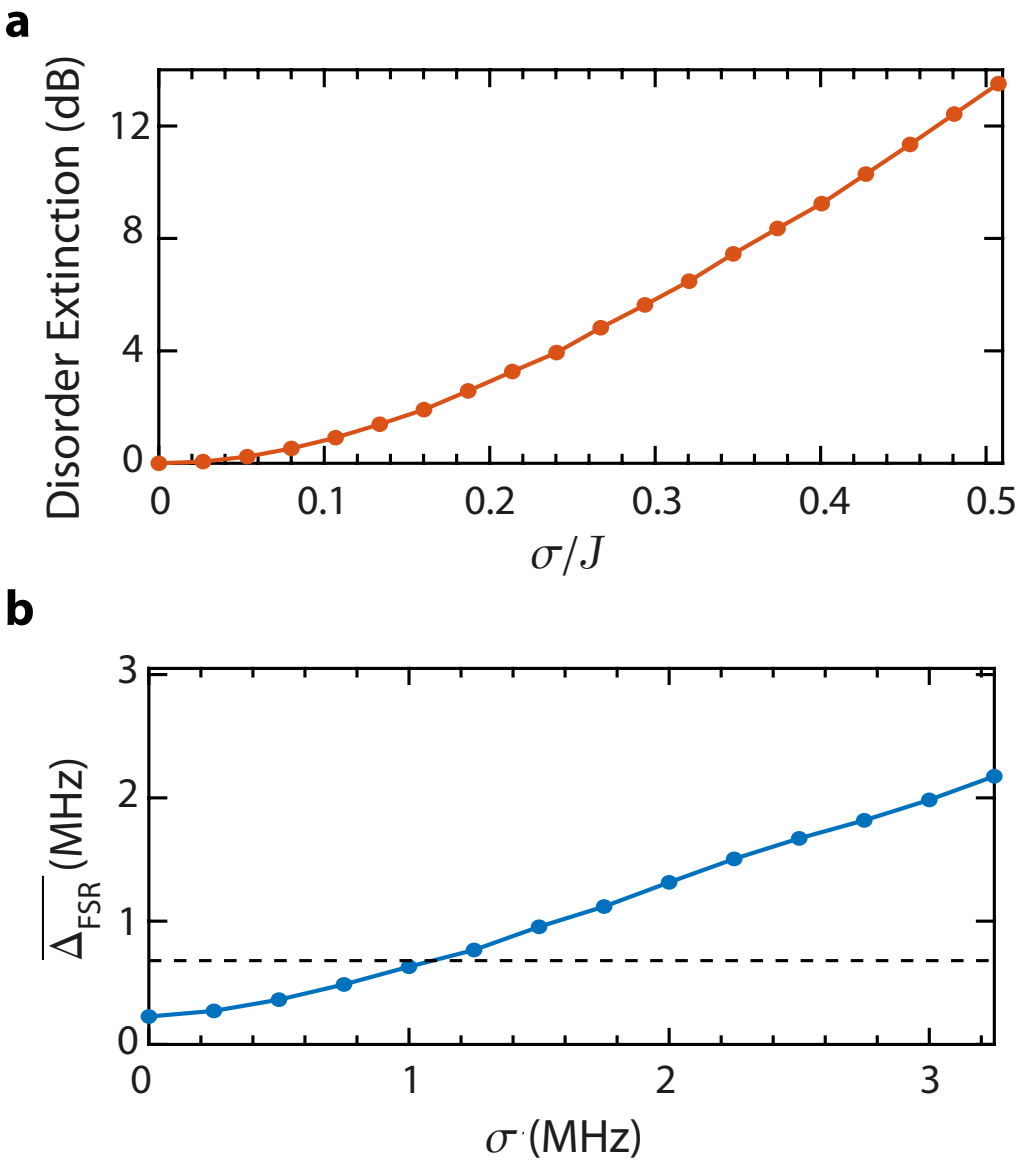

Figure 3.5: **a** Numerically calculated extinction as a function of disorder. Here, σ is the disorder in the bare frequencies of the (unit cell) resonators making up the metamaterial waveguide and J is the coupling between nearest-neighbor resonators in the resonator array. 50 unit cells were used in this calculation, which included taper-matching sections at the input and output of the array that brought the overall passband ripple to 0.01dB. For a given disorder strength, σ, disorder extinction was calculated by taking the mean of the transmission across the passband for a given disorder realization, and subsequently averaging that mean transmission over many disorder realizations. Note that the calculated values depend on the number of unit cells. **b** Numerically calculated variance in normal mode frequency spacing as a function of disorder. See text for details on the method of calculation of $\overline{\Delta_{\mathrm{FSR}}}$. Dashed line indicates the experimentally measured Δ_{FSR}, which was extracted from the data shown in Figure 3.1d.

as the modes become randomly shifted. Our approach was therefore as follows. Starting with the fit parameters presented in section 3.3, we simulated transmission through the metamaterial waveguide for varying amounts of resonator frequency disorder, σ. For each level of disorder we performed simulations of 500 different disorder realizations, and for each different disorder realization we computed the standard deviation in the free spectral range of the ripples, Δ_{FSR}. This deviation in free spectral range was then averaged over all disorder realizations for each value of σ, yielding an empirical relation between $\overline{\Delta_{\mathrm{FSR}}}$ and σ.

The numerically calculated empirical relation between variation in free spectral range and frequency disorder is plotted in Figure 3.5b. Note that the minimum of $\overline{\Delta_{\mathrm{FSR}}}$ at $\sigma = 0$ is set by the intrinsic dispersion of the normal mode frequencies of the unperturbed resonator array. As such, in order to yield a better sensitivity to disorder we chose to only use the center half of the passband in our analysis where dispersion is small. From the data in Figure 3.1d, we calculated the experimental Δ_{FSR}. Comparing to the simulated plot of Figure 3.5b, this level of variance in the free spectral range results from a resonator frequency disorder within the array at the 1 MHz level (or 2×10^{-4} of the average resonator frequency), corresponding to $\sigma/J \approx 1/30$. We have extracted similar disorder values across a number of different metamaterial waveguide devices realized using our fabrication process.

Chapter 4

DYNAMICS OF A QUANTUM EMITTER COUPLED TO A ONE-DIMENSIONAL STRUCTURED RESERVOIR

4.1 Introduction

Spontaneous emission by a quantum emitter into the fluctuating electromagnetic vacuum, and the corresponding exponential decay of the emitter excited state, is an emblematic example of Markovian dynamics of an open quantum system [99]. However, modification of the electromagnetic reservoir can drastically alter this dynamic, introducing “non-Markovian" memory effects to the emission process, a consequence of information back-flow from the reservoir to the emitter [83, 84, 86, 122]. A canonical example of this, considered in early theoretical work [50–52], is the behavior of a quantum emitter whose natural emission frequency lies close to the gap edge of a photonic bandgap material [53, 54] where a sharp transition of the photonic density of states (DOS) occurs. Inside the bandgap the emitter sees a reservoir devoid of electromagnetic states, while just outside of the bandgap lies a continuum of states. This structure of the photonic bandgap reservoir leads to a strong dressing of the emitter, and a resulting emission dynamics modified by the interplay between bound and radiative emitter-photon resonant states [55–59].

More recently, theoretical studies have explored how a structured reservoir with non-Markovian memory alters the entanglement within a quantum system coupled to such a reservoir [28–30]. This has led to the paradigm of reservoir engineering, where non-Markovianity is a quantifiable resource for quantum information processing and communication. Theory work from this quantum information perspective has shown that long-lived reservoir correlations can be used for the generation and preservation of entanglement [26, 27] and quantum control [123] of a quantum system, enhancement of the capacity of quantum channels [124], and the synthesis of exotic many-body quantum states of light from single emitters [60].

In practice, observation of non-Markovian emission phenomena can be achieved by strongly coupling an emitter to a single-mode waveguide — a one-dimensional (1D) reservoir with a continuum of states. Waveguides which break continuous translational symmetry, or which host resonant elements within the waveguide, are of particular interest in this regard owing to the structure in their spectrum [125–

127]. For example, an array of coupled resonant elements leads to a constriction of the 1D continuum of guided modes to a transmission band of finite bandwidth, with sharp transitions in the photonic DOS occurring at the bandedges as in a photonic bandgap material.

Spectral constriction of the waveguide continuum, and the concomitant frequency dispersion, can also result in the slowing of light propagation which enables observation of additional non-Markovian phenomena. For instance, by placing a reflective boundary (mirror) on one end of a slow-light waveguide, a fraction of the emitter's radiation can be fed back from the waveguide reservoir to the emitter at significantly delayed timescales [89, 128, 129]. The non-Markovian regime is reached when $\Gamma_{1D} > 1$, where Γ_{1D} is the emitter's emission rate into the waveguide and is the round-trip travel time of an emitted photon. Theoretical studies have shown that such non-Markovian delayed feedback in a 1D waveguide reservoir can lead to revivals in excited-state population of an emitter as it undergoes spontaneous emission decay [89, 130–135], realization of stable bound states in a continuum (BIC) [136, 137], and enhanced collective effects including multipartite entanglement and superradiant emission from emitters interacting via a common waveguide channel [30, 138–142]. This deceptively simple mechanism of time-delayed feedback can also be used for the generation of multi-dimensional photonic cluster states by a single emitter, and has been proposed as a means for generating the universal resource states necessary for measurement-based quantum computation [60].

Superconducting microwave circuits incorporating Josephson-junction-based qubits [143, 144] represent a near-ideal test bed for studying the quantum dynamics of emitters interacting with a 1D continuum [37, 145]. In comparison to solid-state and atomic optical systems [146–149], superconducting microwave circuits can be created at a deep-sub-wavelength scale, giving rise to strong qubit-waveguide coupling far exceeding other qubit dissipative channels. This has enabled a variety of pioneering experiments probing qubit-waveguide radiative dynamics, employing waveguide spectroscopy [42, 102, 103, 129], time-dependent qubit measurements [38, 104, 114, 150], and analysis of higher-order field correlations [39, 151]. Recent experiments have also explored the coupling of superconducting qubits to acoustic wave devices, demonstrating the capability of these systems to produce significant time-delayed feedback and remote entanglement of qubits [42, 150].

In this work, through the addition of strongly coupled Xmon-style superconducting qubits [66, 152] to a microwave metamaterial slow-light waveguide, we are able to

realize a quantum emitter-reservoir system operating deep within the non-Markovian limit. Spectroscopic measurement of the coupled system shows the emergence of dressed qubit-photon resonant states near the bandedges of the constricted passband of the waveguide [51, 52, 102]. Using non-adiabatic tuning of the qubit emission frequency, we also measure the time-dependent dynamics of the qubit excited-state population when it is resonant at different points across the bandgap and passband of the waveguide. We directly observe non-exponential, oscillatory radiative decay of the qubit, which modeling indicates is a result of the interference of the pair of bound and radiative dressed qubit-photon states that exist on either side of the bandedge of the slow-light waveguide [55]. Further, by terminating one-end of the slow-light waveguide with a reflective boundary, we explore the effects of time-delayed feedback on the qubit emission as it emits into the passband of the slow-light waveguide. In this regime, we observe multiple, well-resolved revivals in the qubit excited state population, and explore the cross-over between Markovian and non-Markovian emission dynamics through in situ tuning of the qubit coupling to the waveguide.

4.2 Non-Markovian Spectroscopic Signatures

In order to study the non-Markovian radiative dynamics of a quantum emitter, a second sample was fabricated with a metamaterial waveguide similar to that in the previous section, this time including three flux-tunable Xmon qubits [152] coupled at different points along the waveguide (see Figure 4.1a—c). Each of the qubits is coupled to its own XY control line for excitation of the qubit, a Z control line for flux tuning of the qubit transition frequency, and a readout resonator (R) with separate readout waveguide (RO) for dispersive read-out of the qubit state. The qubits are designed to be in the transmon-limit [66] with large tunneling to charging energy ratio (see Refs. [104, 153] for further qubit design and fabrication details). As in the test waveguide of Figure 3.1, the qubit-loaded metamaterial waveguide is impedance-matched to input-output 50-Ω CPWs. In order to extend the waveguide delay further, however, this new waveguide is realized by concatenating two of the test metamaterial waveguides together using a CPW bend and internal impedance matching sections. The Xmon qubit capacitors were designed to have capacitive coupling to a single unit cell of the metamaterial waveguide, yielding a qubit-unit cell coupling of $g_{\mathrm{uc}} \approx 0.8J$.

In this work only one of the qubits, Q_1, is used to probe the non-Markovian emission dynamics of the qubit-waveguide system. The other two qubits are to be used in a

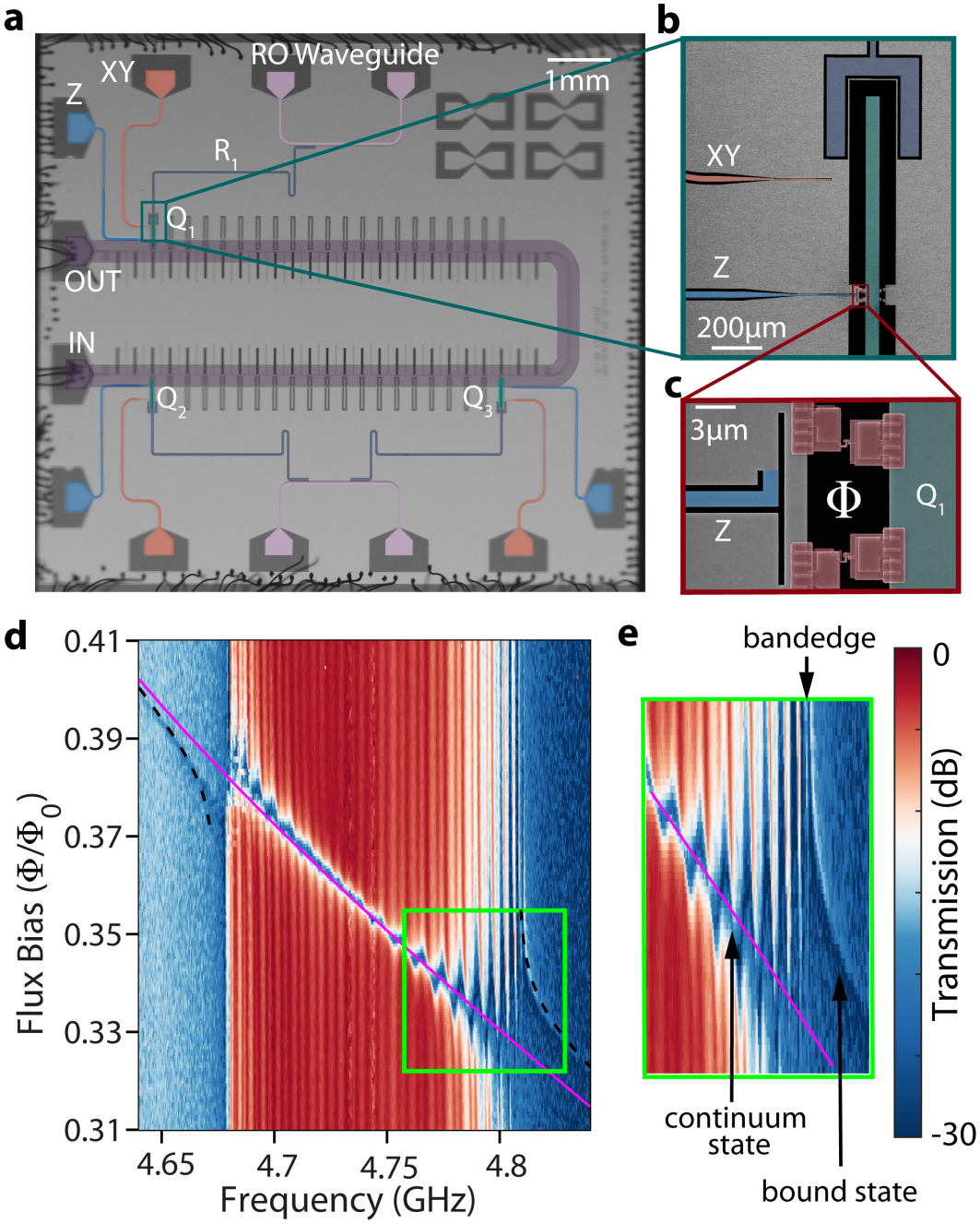

Figure 4.1: **Artificial Atom Coupled to a Structured Photonic Reservoir. a** False-colored optical image of a fabricated sample consisting of three transmon qubits (Q_1,Q_2,Q_3) coupled to a slow-light metamaterial waveguide composed of a coupled microwave resonator array. Each qubit is capacitively coupled to a readout resonator (false color dark blue) and a XY control-line (false color red), and inductively coupled to a Z flux-line for frequency tuning (false color light blue). The readout resonators are probed through feed-lines (false color lilac). The metamaterial waveguide path is highlighted in false color dark purple. **b** SEM image of the Q_1 qubit, showing the long, thin shunt capacitor (false color green), XY control-line, the Z flux-line, and coupling capacitor to the readout resonator (false color dark blue). **c** SEM zoom-in image of the Z flux-line and superconducting quantum interference device (SQUID) loop of Q_1 qubit, with Josephson Junctions and its pads false colored in crimson. **d** Transmission through the metamaterial waveguide as a function of flux. The solid magenta line indicates the expected bare qubit frequency in the absence of coupling to the metamaterial waveguide, calculated based on the measured qubit minimum/maximum frequencies and the extracted anharmonicity. The dashed black lines are numerically calculated bound state energies from a model Hamiltonian of the system; see Appendix D.1 for further details. **e** Zoom-in of transmission near the upper bandedge, showing the hybridization of the qubit with the bandedge, and its decomposition into a bound state in the upper bandgap and a radiative state in the continuum of the passband.

separate experiment, and were detuned from Q_1 by approximately 1 GHz for all of the measurements that follow. At zero flux bias (i.e., maximum qubit frequency), the measured parameters of Q_1 are: $\omega_{ge}/2\pi = 5.411$ GHz, $\eta/2\pi = (\omega_{ef} - \omega_{ge})/2\pi = -235$ MHz, $\omega_r/2\pi = 5.871$ GHz, and $g_r/2\pi = 88$ MHz. Here, $|g\rangle$, $|e\rangle$, and $|f\rangle$ are the vacuum, first-excited, and second-excited states of the Xmon qubit, with ω_{ge} the fundamental qubit transition frequency, ω_{ef} the first-excited state transition frequency, and η the anharmonicity. ω_r is the readout resonator frequency, and g_r is the bare coupling rate between the qubit and the readout resonator.

As an initial probe of qubit radiative dynamics, we spectroscopically probed the interaction of Q_1 with the structured 1D continuum of the metamaterial waveguide. These measurements are performed by tuning ω_{ge} into the vicinity of the passband and measuring the waveguide transmission spectrum at low power (such that the effects of qubit saturation can be neglected). A color intensity plot of the measured transmission spectrum versus flux bias used to tune the qubit frequency is displayed in Figure 4.1d. These spectra show a clear anti-crossing as the qubit is tuned toward either bandedge of the passband (a zoom-in near the upper bandedge of the passband is shown in Figure 4.1e). As has been shown theoretically [55, 56], in the single excitation manifold the interaction of the qubit with the waveguide results in a pair of qubit-photon dressed states of the hybridized system, with one state in the passband (a delocalized “continuum" state) and one state in the bandgap (a localized “bound" state). This arises due to the large peak in the photonic DOS at the bandedge (in the lossless case, a van Hove singularity), the modes of which strongly couple to the qubit with a coherent interaction rate of $\Omega_{\mathrm{WG}} \approx (g_{\mathrm{uc}}^4/4J)^{1/3}$, resulting in a dressed-state splitting of $2\Omega_{\mathrm{WG}}$. This splitting has been experimentally shown to be a spectroscopic signature of a non-Markovian interaction between an emitter and a photonic crystal reservoir [102, 103]. Further details and discussion can be found in section 3.2 and Appendix D.1.

The dressed state with frequency in the passband is a radiative state which is responsible for decay of the qubit into the continuum [52]. On the other hand, the state with frequency in the gap is a qubit-photon bound state, where the qubit is self-dressed by virtual photons that are emitted and re-absorbed due to the lack of propagating modes in the waveguide for the radiation to escape. This bound state assumes an exponentially shaped photonic wavefunction of the form $\sum_x e^{-|x|/\lambda}\hat{a}_x^\dagger |\mathrm{vac}\rangle$, where $|\mathrm{vac}\rangle$ is the state with no photons in the waveguide, $\hat{a}_x^\dagger$ is the creation operator of a photon in unit cell at position x (with the qubit located at $x = 0$), and $\lambda \approx \sqrt{J/(E_b - \omega_0)}$

is the state's localization length. In the theoretical limit of an infinite array, and in absence of intrinsic resonator and qubit losses, the qubit component of the bound state does not decay even though it is hybridized with the waveguide continuum; a behavior distinct from conventional open quantum systems. Practically, however, intrinsic losses and the overlap between the bound state's photonic wavefunction and the input-output waveguides will result in decay of the qubit-photon bound state.

4.3 Non-Markovian Radiative Dynamics

In complement to spectroscopic probing of the qubit-reservoir system, and in order to directly study the population dynamics of the qubit-photon dressed states, we also performed time-domain measurements as shown in Figure 4.2. In this protocol (illustrated in Figure 4.2a) we excite the qubit to state $|e\rangle$ with a resonant π-pulse on the XY control line, and then rapidly tune the qubit transition frequency using a fast current pulse on the Z control line to a frequency (ω'_{ge}) within, or in the vicinity of, the slow-light waveguide passband. After an interaction time τ, the qubit is then rapidly tuned away from the passband, and the remaining qubit population in $|e\rangle$ is measured using a microwave probe pulse (RO) of the read-out resonator which is dispersively coupled to the qubit. The excitation of the qubit is performed far from the passband, permitting initialization of the transmon qubit whilst it is negligibly hybridized with the guided modes of the waveguide. Dispersive readout of the qubit population is performed outside of the passband in order to minimize the loss of population during readout. Note that, as illustrated in Figure 4.2a, the qubit is excited and measured at different frequencies on opposite sides of the passband; this is necessary to avoid Landau-Zener interference [154].

Results of measurements of the time-domain dynamics of the qubit population as a function of ω'_{ge} (the estimated bare qubit frequency during interaction with the waveguide) are shown as a color intensity plot in Figure 4.2b. In this plot we observe a 400-fold decrease in the $1/e$ excited state lifetime of the qubit as it is tuned from well outside the passband to the middle of the slow-light waveguide passband, reaching a lifetime as short as 7.5 ns. Beyond the large change in qubit lifetime within the passband, several other more subtle features can be seen in the qubit population dynamics near the bandedges and within the passband. These more subtle features in the measured dynamics show non-exponential decay, with significant oscillations in the excited-state population that is a hallmark of strong non-Markovianity in quantum systems coupled to amplitude damping channels [88, 155].

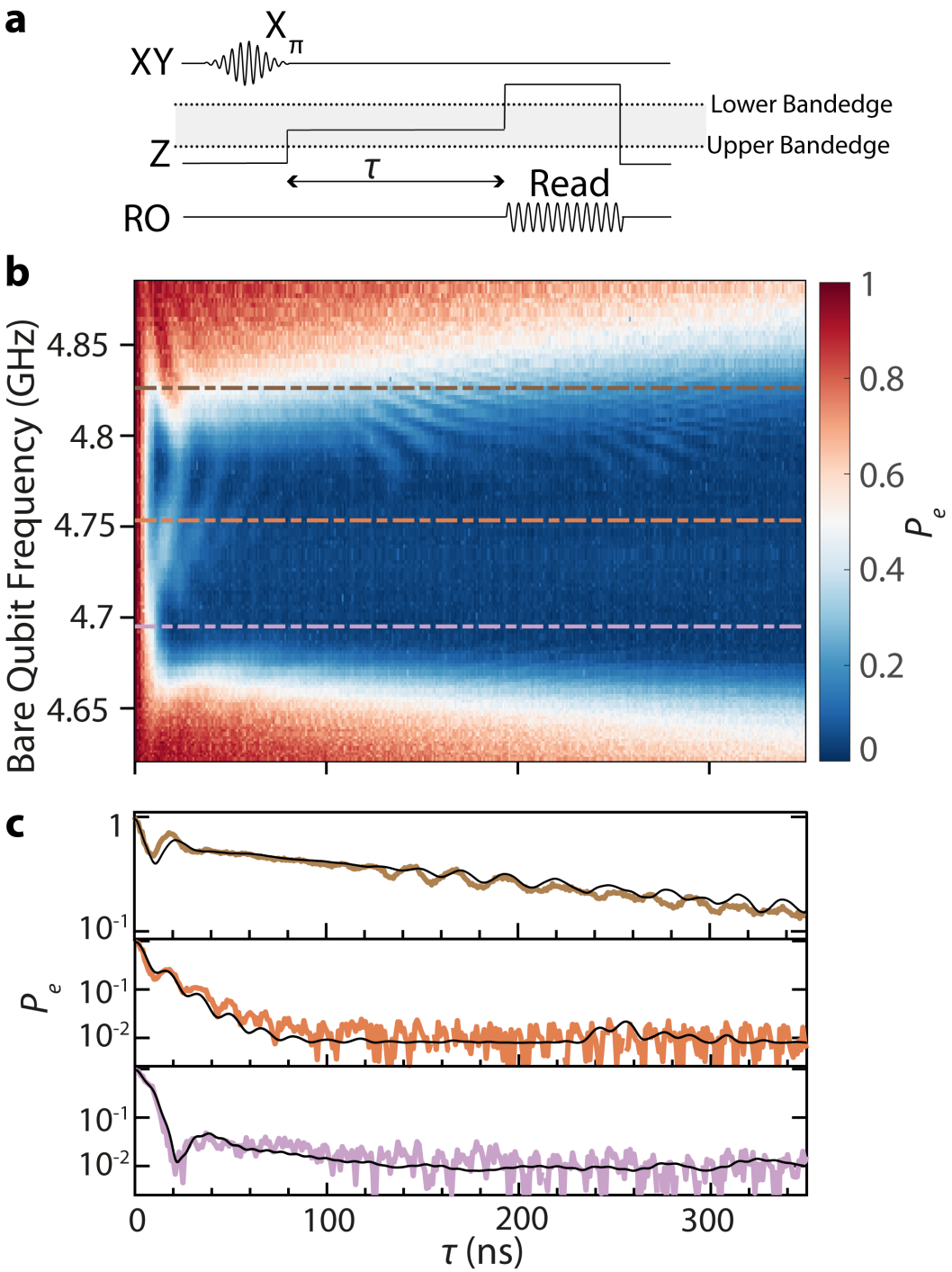

Figure 4.2: **Non-Markovian Radiative Dynamics in a Structured Photonic Reservoir.** **a** Pulse sequence for the time-resolved measurement protocol. The qubit is excited while its frequency is 250 MHz above the upper bandedge, and then it is quickly tuned to the desired frequency (ω'_{ge}) for a interaction time τ with the reservoir. After interaction, the qubit is quickly tuned below the lower bandedge for dispersive readout. **b** Intensity plot showing the excited-state population of the qubit versus interaction time with the metamaterial waveguide reservoir as a function of the bare qubit frequency. **c** Line cuts of the intensity plot shown in (**b**), where the color of the plotted curve matches the corresponding horizontal dot-dashed curve in the intensity plot. Solid black lines are numerical predictions of a model with experimentally fitted device parameters and an assumed 0.8% thermal qubit population (see Appendix D.1 for further details).

The observed qubit emission dynamics in this non-Markovian limit are best understood in terms of the qubit-waveguide dressed states. Fast (i.e., non-adiabatic) tuning of the qubit in state $|e\rangle$ into the proximity of the passband effectively initializes it into a superposition of the bound and continuum dressed states. The observed early-time interaction dynamics of the qubit with the waveguide then originate from interference of the dressed states, which leads to oscillatory behavior in the qubit population analogous to vacuum-Rabi oscillations [156]. The frequency of these oscillations is thus set by the difference in energy between the dressed states. The amplitude of the oscillations, on the other hand, quickly decays away as the energy in the radiative continuum dressed state is lost into the waveguide.

All of these features can be seen in Figure 4.2c, which shows plots of the measured time-domain curves of the qubit excited-state population for bare qubit frequencies near the top, middle, and bottom of the passband. Near the upper bandedge frequency we observe an initial oscillation period as expected due to dressed state interference. Once the continuum dressed state has decayed away, a slower decay region free of oscillations can be observed (this is due to the much slower decay of the remaining qubit-photon bound state). Finally, around $\tau \approx 115$ ns, there is an onset of further small-amplitude oscillations in the qubit population. These late-time oscillations can be attributed to interference of the remaining bound state at the site of the qubit with weak reflections occurring within the slow-light waveguide of the initially emitted continuum dressed state. The 115 ns timescale corresponds to the round-trip time between the qubit and the CPW bend that connects the two slow-light waveguide sections.

In the middle of the passband, we see an extended region of initial oscillation and rapid decay, albeit of smaller oscillation amplitude. This is a result of the much smaller initial qubit-photon bound-state population when tuned to the middle of the passband. Near the bottom of the passband we see rapid decay and a single period of a much slower oscillation. This is curious, as the dispersion near the upper and lower bandedge frequencies of the slow-light waveguide is nominally equivalent. Further modelling has shown this is a result of weak non-local coupling of the Xmon qubit to a few of the nearest-neighbor unit cells of the waveguide. Referring to Figure 3.1c, the modes near the lower bandedge occur at the X-point of the Brillouin zone edge where the modes have alternating phases across each unit cell, thus the extended coupling of the Xmon qubit causes cancellation effects which reduce the qubit-waveguide coupling at the lower frequency bandedge. Further detailed numerical

model simulations of our qubit-waveguide system via a tight-binding model and a circuit model, as well as the correspondence between the observed dynamics and the theory of spontaneous emission by a two-level system near a photonic bandedge [55], are given in Appendix D.1.

4.4 Time-Delayed Feedback

In order to further study the late-time, non-Markovian memory effects of the qubit-waveguide dynamics, we also perform measurements in which the end of the waveguide furthest from qubit Q_1 is terminated with an open circuit, effectively creating a “mirror" for photon pulses stored in the slow-light waveguide reservoir. As illustrated in Figure 4.3a, we achieve this in situ by connecting the input microwave cables of the dilution refrigerator to the waveguide via a microwave switch. The position of the switch, electrically closed or open, allows us to study a truly open environment for the qubit or one in which delayed-feedback is present, respectively (see Appendix A for further details).

Performing time-domain measurements with the mirror in place and with the qubit frequency in the passband, we observe recurrences in the qubit population at one and two times the round-trip time of the slow-light waveguide that did not appear in the absence of the mirror (see Figure 4.3b). The separation of timescales between full population decay of the qubit and its time-delayed re-excitation demonstrates an exceptionally long memory of the reservoir due to its slow-light nature, and places this experiment in the deep non-Markovian regime [89]. The small recurrence levels as they appear in Figure 4.3b are not due to inefficient mirror reflection, but rather can be explained as follows. Because the qubit emits towards both ends of the waveguide, half of the emission is lost to the unterminated end, while the other half is reflected by the mirror and returns to the qubit. In addition, the exponentially decaying temporal profile of the emission leads to inefficient re-absorption by the qubit and further limits the recurrence (see, for instance, Ref. [157, 158] for details). These two effects can be observed in simulations of a qubit coupled to a dispersionless and loss-less waveguide (pink dotted line; for more details, see Ref. [131] and Appendix D.3). The remaining differences between the simulation and the measured population recurrence (blue solid line) can be explained by the effects of propagation loss and pulse distortion due to the slow-light waveguide’s dispersion.

We also further probed the dependence of this phenomenon on the strength of coupling to the waveguide continuum by parametric flux modulation of the qubit

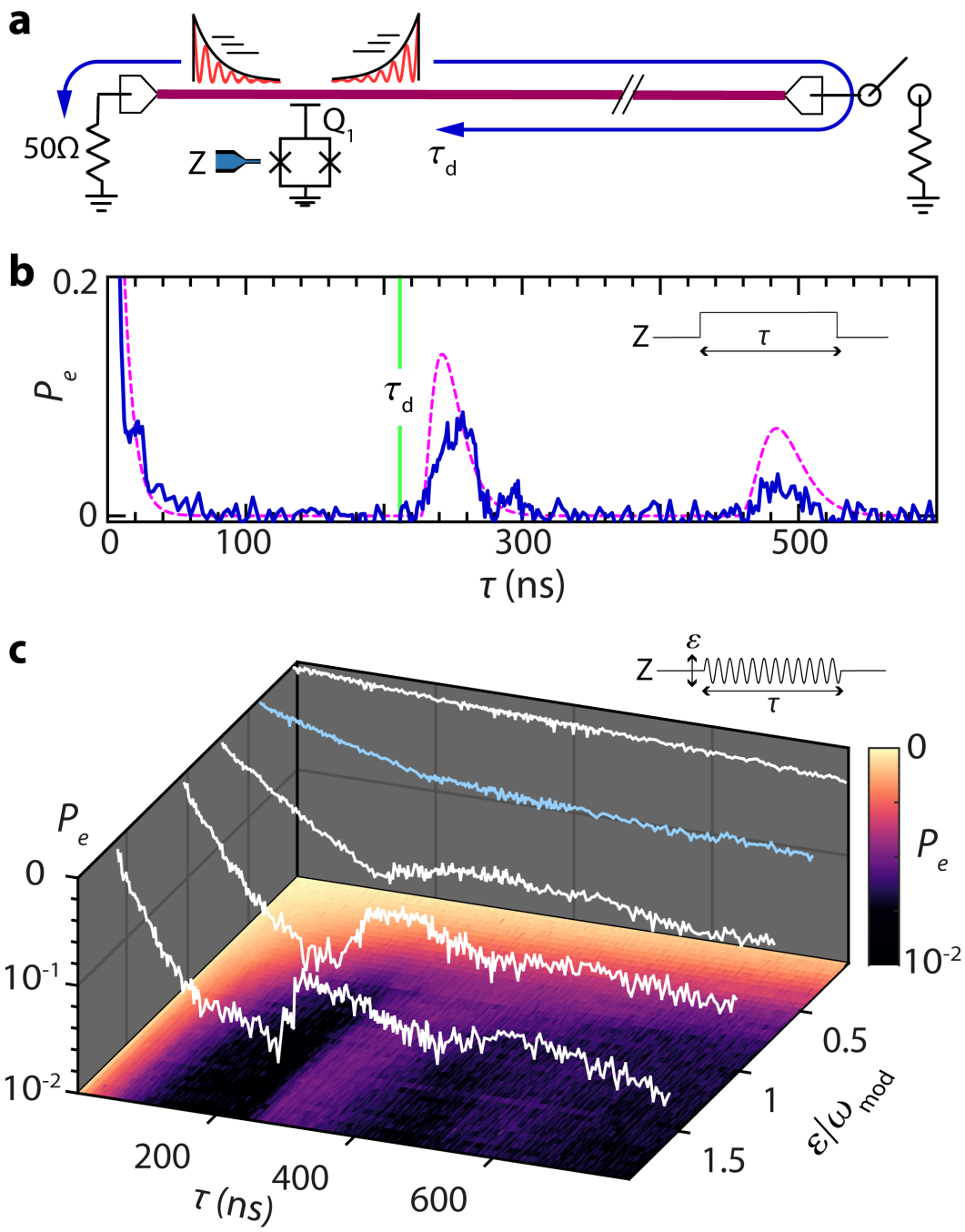

Figure 4.3: **Time-Delayed Feedback from a Slow-Light Reservoir with a Reflective Boundary** **a** Illustration of the experiment, showing the qubit coupled to the metamaterial waveguide which is terminated on one end with a reflective boundary via a microwave switch. **b** Measured population dynamics of the excited state of the qubit when coupled to the metamaterial waveguide terminated in a reflective boundary. Here the bare qubit is tuned into the middle of the passband. The onset of the population revival occurs at $\tau = 227$ ns, consistent with round-trip group delay () measurements at that frequency, while the emission lifetime of the qubit is $(\Gamma_{1D})^{-1} = 7.5$ ns. The magenta curve is a theoretical prediction for emission of a qubit into a dispersionless, lossless semi-infinite waveguide with equivalent and Γ_{1D} (see Appendix D.3 for details). **c** Population dynamics under parametric flux modulation of the qubit, for varying modulation amplitudes, demonstrating a Markovian to non-Markovian transition. When the modulation index $(\epsilon/\omega_{\text{mod}})$ is approximately 0.4 we have $\Gamma_{1D}(\epsilon) = 1/$; the corresponding dynamical trace is colored in blue.

transition frequency [159] when it is far detuned from the passband. This modulation creates sidebands of the qubit excited state, which are detuned from ω_{ge} by the frequency of the flux tone ω_{mod}. By choosing the modulation frequency such that a first-order sideband overlaps with the passband, the effective coupling rate of the qubit with the waveguide at the sideband frequency was reduced approximately by a factor of $\mathcal{J}_1^2[\epsilon/\omega_{\text{mod}}]$, where ϵ is the modulation amplitude and $\mathcal{J}_1$ is a Bessel function of the first kind ($\epsilon/\omega_{\text{mod}}$ is the modulation index). Keeping a fixed ω_{mod}, we observe purely exponential decay at small modulation amplitudes. However, above a modulation amplitude threshold we again observe recurrences in the qubit population at the round-trip time of the metamaterial waveguide, demonstrating a continuous transition from Markovian to non-Markovian dynamics (see Appendix D.3 for further comparisons between this data and the theoretical model of Ref. [131]).

4.5 Conclusion

In conclusion, by strongly coupling Xmon qubits to a 1D structured photonic reservoir consisting of a metamaterial slow-light waveguide, we are able to probe the non-Markovian dynamical regime of waveguide quantum electrodynamics. In this regime, we observe non-exponential qubit spontaneous decay near the bandedges of the slow-light waveguide, attributable to interference resulting from the splitting of the qubit state into a radiative state in the passband and a bound state in the bandgap region of the metamaterial waveguide. Moreover, by placing a reflective boundary on one end of the waveguide, we observe recurrences in the qubit population at the round-trip time of an emitted photon, as well as a Markovian to non-Markovian transition when varying the qubit-waveguide interaction strength.

The demonstrated ability to achieve a true finite-bandwidth continuum with time-delayed feedback opens up several new research avenues for exploration [128, 130–142, 160]. As a straightforward extension of the current work, one may probe the qubit-waveguide-mirror system in a continuous, strongly-driven fashion, and use tomography to study photon correlations in the output radiation field [128]. This output field, with expected photon stream of high entanglement dimensionality, has a direct mapping to continuous matrix product states which can used for analog simulations of higher-dimension interacting quantum fields [46, 160]. With technical advancements in the tomography of microwave fields [151, 161], and realization of single-microwave-photon qubit detectors [162–164], the basic tools for characterization of these entangled photonic states and their quantum many-body-system

analogues are now available. And looking forward even further, additionally leveraging the multi-level structure of transmon-type qubits, by situating ω_{ef} in the passband and ω_{ge} in the gap, enables high-fidelity generation of 2D cluster states for device parameters already achieved in this work [60]. We therefore expect our results to find applications in future studies of non-Markovian open quantum systems, studies of many-body physics, and measurement-based quantum computation with microwave photons.

Chapter 5

DETERMINISTIC GENERATION OF MULTIDIMENSIONAL CLUSTER STATES VIA TIME-DELAYED FEEDBACK

5.1 Introduction

Quantum entanglement is generally regarded as a necessary resource for exceeding classical performance limits in tasks such as quantum computing, quantum communication, and quantum metrology [31, 165–168]. In the optical domain, where photons are the ubiquitous carriers of quantum information, multi-partite entangled states are key resources for various quantum computation and networking protocols [169, 170]. Of particular importance are multi-dimensional cluster states, a subset of the family of entangled graph states, which are highly flexible resource states necessary for measurement-based quantum computing [32, 90, 91, 171], and well suited for tackling many paradigmatic metrological problems [172, 173], as well as decoherence protected preservation and teleportation of quantum information [174–177].

However, reliable generation of cluster states of photonic qubits by conventional optical means remains an outstanding challenge due to reliance on probabilistic photon entanglement heralding schemes and a large number of optical components [95, 178, 179]. Thus, there has been significant interest in achieving generation of such multi-dimensional cluster states by deterministic, resource-efficient means. Notable among these are schemes that involve sequential emission of entangled photons via control of only one or a small number of quantum emitters [93, 180]. Note that while sequential emission from a single coherent emitter is sufficient to generate 1D cluster states, higher dimensional cluster states require more emitters or an additional memory element. A promising approach is based on delay lines generating a time-delayed feedback mechanism, expanding the class of cluster states that can be generated with a single emitter [60, 181–184].

Superconducting circuit QED systems are a natural fit to implement such protocols. In contrast to atomic-optical systems where the finite atom-waveguide cooperativity is often a limiting factor [33, 34], superconducting circuit QED systems enjoy a strong qubit-waveguide coupling that far exceeds the strength of other dissipative channels due to the ease of creating microwave circuits at a deep subwavelength scale

[16]. Indeed, there has been significant progress over the last decade in leveraging superconducting qubits to generate, manipulate, and measure non-classical states of light, including 1D cluster states [39, 41, 46–48, 161]. However, to date, deterministic generation of higher dimensional photonic cluster states via a single quantum emitter remains largely unexplored, and generation schemes involving time-delayed feedback have yet to be tackled.

Thus in this work, we go beyond the previous state-of-the-art by using time-delayed quantum feedback, via a slow-light waveguide, for the generation of multipartite entangled photonic states, thereby achieving generation of a 2D cluster state of microwave photons. Our system consists of two superconducting flux-tunable transmon qubits coupled to the two ends of a slow-light waveguide that serves as a delay line. One qubit serves as our quantum emitter, generating shaped photon pulses with durations as short as 30 ns. The other qubit serves as a switchable mirror for selective reflection of emitted photons. In conjunction with the slow light waveguide this mirror allows us to introduce a time-delayed feedback mechanism, which is essential to our multidimensional entanglement generation scheme (following the proposal in Ref. [60]).We characterize the time-delayed feedback between the emitter qubit and previously emitted photons through quantum process tomography, and certify via quantum state tomography the generation of a 2D cluster state of four photons with a fidelity of 70%. Finally, we comment on how straightforward hardware and design improvements could increase the size of generated cluster states by an order of magnitude, and allow for the generation of 3D cluster states. Thus, our demonstrated results pave the way for deterministic, resource-efficient synthesis of multi-dimensional photonic quantum resource states, and their use in quantum information science.

5.2 Results

Cluster State Generation Protocol: We first discuss the general scheme we use to generate multidimensional cluster states on a conceptual level. Our approach is based on the proposal in Ref. [60], and is illustrated in Figure 5.1a. In our scheme we couple a quantum emitter to the terminated end of a single-ended, low-group velocity waveguide. This quantum emitter has two stable states $|g\rangle$ and $|e\rangle$, as well as a radiative state $|f\rangle$ which is highly damped to the waveguide and decays to the $|e\rangle$ state.

Starting with the emitter in the $|g\rangle$ state, the protocol first involves the generation

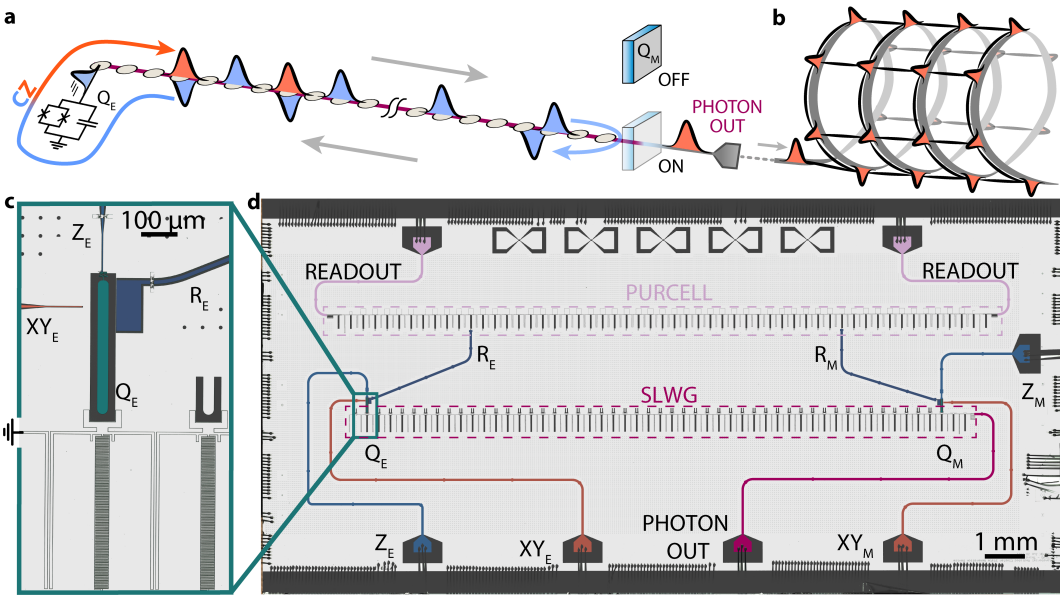

Figure 5.1: **Deterministic Generation of 2D Cluster States with a Single Emitter Qubit. a,** General scheme for generation of 2D cluster states of photons via a single quantum emitter qubit and time-delayed feedback. The qubit is made to emit a pulse train of nearest-neighbor entangled photons (colored blue) into a delay line. Via control of a switchable mirror, each emitted photon pulse is reflected at the end of the delay line for re-scattering (blue to orange color change) by the emitter qubit. In the device used in this work, superconducting transmon qubits are used as both the quantum emitter (Q_E) and the switchable mirror (Q_M), and an array of weakly coupled resonators comprise a slow-light waveguide, which serves as a single-ended delay line. **b,** Visualization of the resulting entanglement structure. **c, d** False-color optical images of the device, comprising a slow-light waveguide (SLWG) and two transmon qubits (false color green), with each qubit coupled to a readout resonator (false color dark blue), a XY control-line (false color red), and a Z fast flux-line (false color light blue). The readout resonators are probed through a coupled resonator array Purcell filter connected to CPW feed-lines (false color lilac). The emitted photons exit the slow-light waveguide and device via a CPW feedline (false color dark purple).

entanglement between the emitter and a photon mode using two coherent pulses: a first $\pi_{ge}/2$ pulse generates an equal superposition of the $|g\rangle$ and $|e\rangle$ state, then a π_{ef} pulse transfers the amplitude from the $|e\rangle$ state to the $|f\rangle$ state, which subsequently decays back to the $|e\rangle$ state by emission of a photon into the waveguide. This leaves the emitter and the first emitted photon in the maximally entangled state $|\psi\rangle = (|g\rangle|0\rangle_1 + |e\rangle|1\rangle_1)/\sqrt{2}$. Repeating this 2-pulse control sequence leads to sequential emission of a train of entangled photonic time-bin qubits with a nearest-neighbor entanglement structure equivalent to the one of a 1D cluster state [93, 180] into the slow-light waveguide (illustrated in Figure 5.1a as the blue colored pulses).

This train of sequentially-emitted pulses is then reflected back toward the emitter by a switchable mirror at the other end of the delay line. After a full round-trip the photons thus scatter from the quantum emitter and pick up a state-dependent

scattering phase (illustrated in Figure 5.1a as a color change in the pulses from blue to orange). Specifically, if the emitter qubit is in state $|e\rangle$, the returning photon is resonantly coupled to the $|e\rangle \rightarrow |f\rangle$ transition, and acquires a scattering phase of π. However, if the emitter qubit is in state $|g\rangle$, then the returning photon is not resonant with any transition, and no scattering phase is acquired. Thus, this scattering process effectively implements a controlled CZ gate between the emitter qubit and the returning photonic qubit of the form $|g\rangle\langle g| \bigotimes \mathbb{I} + |e\rangle\langle e| \otimes \sigma_z$.

This combination of the sequential emission process and the state-dependent scattering process allows us to synthesize the 2D cluster state: through judicious control of the switchable mirror and emitter qubit, we ensure that all sequentially emitted photons scatter from the emitter qubit exactly once and thereafter are allowed to leave the waveguide. The resulting entanglement structure of the outgoing photon pulse train is that of a 2D cluster state with shifted periodic boundary conditions, as illustrated in Figure 5.1b (see [60] and Appendix F.1 for a quantum circuit representation of this protocol). Nearest-neighbor entanglement in this photonic pulse train is derived from the sequential emission of photons representing one of the two dimensions, whereas entanglement along the other dimension results from the time-delayed scattering process. Importantly, the extent of the second dimension is set by the number of photon pulses that can be generated during one round trip time τ_d, highlighting the role of the time-delayed feedback.

Device Description: Inspired by this proposal, we fabricated the device shown in Figure E.1c, d in order to achieve a practical realization of this scheme. We implement the requisite delay line as a single-ended slow-light waveguide (SLWG), which is comprised of a periodic coupled resonator array of 52 resonators [185]. The output port of the SLWG is connected to a coplanar waveguide (CPW) through which emitted itinerant photons leave the device for amplification and subsequent measurement at the digitizer (see Appendix A for details on the measurement output chain of the device). The round-trip delay of the slow-light waveguide is $\tau_d = 240$ ns. The resonator array is terminated at one end via a capacitance between the leftmost unit cell and the ground plane. At the other end of the resonator array the last two boundary resonators are modified relative to the unit cells in order to effectively match the Bloch impedance of the periodic structure to the characteristic impedance of the output CPW (for further details and design principles of this resonator array slow-light waveguide, see Ref. [185] and Appendix A). The resulting transfer function of such a slow-light waveguide is that of a flat “passband"

of finite bandwidth for guided modes, and a sharp extinction of transmission outside of the passband due to the sharp decline in the photonic density of states (DOS) of the periodic structure occurring at the bandedges. The width of the passband is $4J$, where J is the coupling between unit cells in the resonator array; in our device $J/2\pi = 34$ MHz (giving a passband width of 136 MHz) and the passband center frequency is $\omega_p/2\pi = 4.82$ GHz.

On the terminated end of the slow-light waveguide we couple the emitter qubit Q_E, while at the other end of waveguide we couple another qubit Q_M. The mirror qubit is effectively side-coupled to the slow-light waveguide, allowing it to act as a high-reflectivity mirror for single photons if the ratio between its decay rate into the waveguide and its decoherence rate into other channels, Γ_{1D}/Γ', is sufficiently high [186]. Each qubit is coupled to its own XY control line for single-qubit control, a Z control line for rapid flux tuning of the qubit transition frequency, and a CPW readout resonator (R) coupled to a Purcell filter for dispersive readout of the qubit state (the Purcell filter in this work is also comprised of a coupled resonator array; for more details, see Appendix A). At zero flux bias, the transition frequency between Q_E's ground state (denoted $|g\rangle$) and first excited state (denoted $|e\rangle$) is $\omega^E_{ge}/2\pi = 6.21$ GHz, and the transition frequency between the first excited state and second excited state (denoted $|f\rangle$) is $\omega^E_{ef}/2\pi = 5.93$ GHz, with associated anharmonicity of $\eta^E/2\pi = (\omega^E_{ef} - \omega^E_{ge})/2\pi = -273$ MHz. The center frequency of the Q_E readout resonator at this bias is $\omega^E_r/2\pi = 7.67$ GHz, and its induced dispersive shift $2\chi^E$ is given by $\chi^E/2\pi = 2.1$ MHz. The same quantities parameterizing the mirror qubit at its zero flux bias are given by $\omega^M_{ge}/2\pi = 6.44$ GHz, $\eta^M/2\pi = -280$ MHz, $\omega^M_r/2\pi = 7.47$ GHz, and $\chi^M/2\pi = 3.4$ MHz (see Appendix A for further qubit characterization details).

Crucially, due to the finite width of the slow-light waveguide passband and its sharp bandedges, it is possible to tune the $|e\rangle \rightarrow |f\rangle$ transition frequency into resonance with ω_p and achieve large emission rates of the $|f\rangle$ state, while simultaneously protecting the $|e\rangle$ state from decay if the $|g\rangle \rightarrow |e\rangle$ transition frequency is situated outside the passband of the waveguide (where the DOS of the periodic structure is negligible). In our system we naturally achieve this configuration, where our anhamonicity $\eta^E/2\pi$ of ~280 MHz allows us to situate the $|e\rangle \rightarrow |f\rangle$ transition frequency inside the passband of 136 MHz width, while maintaining the $|e\rangle \rightarrow |g\rangle$ outside the passband. Thus, with these parameters, the first three levels of the transmon comprise the aforementioned necessary ladder level structure for cluster

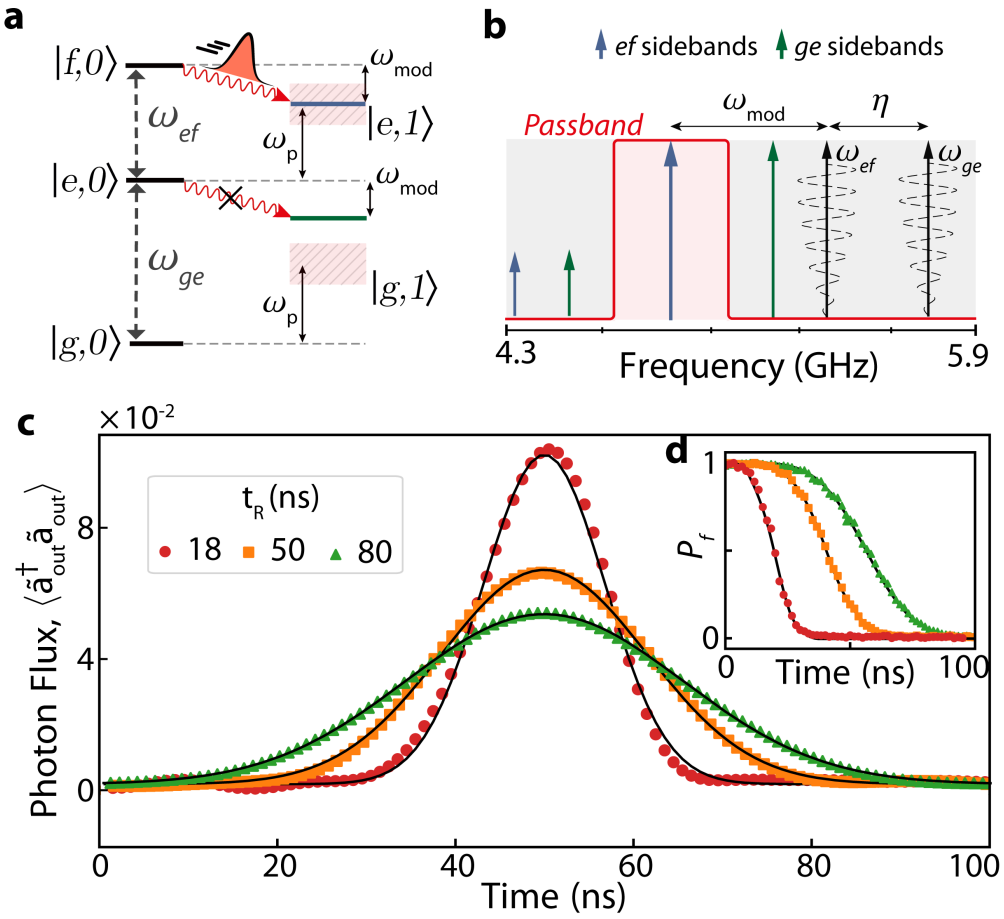

Figure 5.2: **[Emission of Shaped Photon Pulses via Flux-Modulation. a** Effective level diagram of the qubit-waveguide system, showing the photon emission process. In the $|i,n\rangle$ notation, i denotes the state of the transmon emitter qubit, and n denotes the number of photons in the slow-light waveguide; additionally, ω_m is the flux-modulation frequency, and ω_p is the center frequency of the waveguide's passband. When $\omega_{ef} - \omega_{\text{mod}} = \omega_p$, the qubit's levels assume a three-state ladder system where only the $|f\rangle$ state is selectively damped to the slow-light waveguide. **b** Simplified frequency spectrum of the emitter qubit under flux-modulation, where η is the qubit anharmonicity. The flux-modulation waveform is depicted as a dashed black line; the waveform's modulated amplitude directly maps to a modulated emission rate into the waveguide that allows for shaped emission of photon pulses. **c** Measured photon flux $\langle a^{\dagger}{}_{\text{out}} a_{\text{out}} \rangle$ (dots) of shaped emitted pulses, in normalized units. Black lines are Gaussian fits. **d** Measured $|f\rangle$ population during shaped emission. Black lines are the scaled integral of the Gaussian fits of subfigure **c**.

state generation. We stress that the sharp bandedges of the waveguide allow us to engineer remarkably large emission rates of $\Gamma_{1D}^{ef}/2\pi = 2\Gamma_{1D}^{ge}/2\pi \approx 140$ MHz for Q_E, while strongly suppressing decay of the $|g\rangle \rightarrow |e\rangle$ transition to single kHz rates, even though η is comparable to Γ_{1D}^{ge}.

Shaped Photon Emission: For generation of 2D cluster states as we have described, it is crucial to be able to control the shape of emitted photon pulses. This allows us to mitigate the effects of the waveguide's residual dispersion near ω_p, and to improve the fidelity of the CZ gate after a photon round trip. For this it is necessary to control the photon pulse shape as well as its bandwidth, reducing it to less than Γ_{1D}^{ef} (see Ref. [60] for more details). We shape the pulse of the emitted photons by a tunable qubit-waveguide interaction strength for Q_E via parametric flux modulation of the qubit frequency [75–77]. Specifically, we apply an AC flux drive to the SQUID loop of Q_E with frequency ω_{mod}, which generates a series of sidebands, spaced by ω_{mod}, for each transition of the transmon qubit (for more details, see Appendix E.2).

By judiciously choosing the qubit frequency and modulation frequency such that $\omega_{ef} - \omega_{\text{mod}} = \omega_p$, while $\omega_{ge} - \omega_{\text{mod}}$ lies outside the passband due to the anharmoniciy of the qubit, we can ensure that only a first-order sideband of the $e - f$ transition overlaps with the passband. Meanwhile, all other relevant qubit transition frequencies and their sidebands do not fall into the passband. Thereby we achieve photon emission into the waveguide from the $|f\rangle$ state through the first order $e - f$ sideband, while retaining protection of the $|g\rangle$ and $|e\rangle$ levels. This is shown schematically in Figure 5.2a, b: where in Figure 5.2a we illustrate this emission process through a level diagram, whereas in Figure 5.2b we show a simplified frequency spectrum of the particular configuration of qubit frequencies and sideband frequencies used in our experiment. By choosing $\omega_{ge}/2\pi = 5.55$ GHz and $\omega_{\text{mod}}/2\pi = 450$ MHz, we situate the lower first sideband of the $|e\rangle \rightarrow |f\rangle$ transition at $\omega_p/2\pi = 4.823$ GHz, while all other sidebands and bare qubit transition frequencies are sufficiently detuned from the passband as to negligibly contribute to qubit emission, as verified by separate measurements.

We thereby achieve shaped emission by continuously varying the amplitude of the flux modulation AC drive during the emission time, which varies the strength of the aforementioned emission sideband and thus allows us to achieve arbitrary time-dependent modulation of Q_E's emission rate $\Gamma_{1D}^{ef}(t)$ (see Appendix E.2 for further details on how we achieve pulse shaping of emitted photons in this manner). With this capability we achieve shaped emission of Gaussian-shaped photons with ex-

cellent accuracy, as demonstrated in Figure 5.2c, which henceforth constitutes our photonic time-bin qubits. We plot the measured photon flux of three emitted Gaussian pulses with different bandwidths (along with their respective fits), demonstrating the flexibility in our shaped emission scheme (photon flux is plotted in normalized units, see Appendix F.1 for further details). This emission is also achieved with high-efficiency, and thus enables deterministic high-fidelity preparation of entangled photonic states (see Appenddix F.1 for more details).

Further, in Figure 5.2d, we plot Q_E's population dynamics during emission, as well as the integral of the photon fluxes plotted in Figure 5.2c which, in the absence of waveguide-induced distortion, would coincide with the measurement of the population dynamics of Q_E. We find excellent agreement between the two, indicating that the effects of the slow-light waveguide dispersion are minimal for Gaussian pulses. Finally, we stress that our large Γ_{1D} allows high-efficiency emission of pulses that are tightly confined to a time-bin window of length as small as 30 ns, which not only is an important attribute to achieve in order to increase the size of generated cluster states given a fixed τ_d, but also demonstrates significant improvement in emission speed of shaped photons over previous shaped emission demonstrations in circuit QED systems[187–190].

Qubit-Photon CZ Gate Implementation: In addition to high efficiency shaped photon preparation, we also demonstrate a high fidelity CZ gate between Q_E and previously emitted photonic qubits, which is effected by the time-delayed feedback. In Figure 5.3a we show an schematic of the process, where an itinerant photon emitted by Q_E propagates through the waveguide, is reflected by Q_M, and propagates back toward Q_E, whereupon photon scattering on Q_E realizes the CZ gate. Afterward, the photon propagates back toward the output, and is allowed to leave the slow-light waveguide by suitable Q_M control. The fast flux control sequence necessary to implement this process is shown in Figure 5.3b. An amplitude modulated AC pulse on the Z_E line induces photon emission, while a square pulse is initiated in the Z_M line at a time $t = \tau_d/2$, the single-trip time of the waveguide (see Appendix E.2 for details on flux-line distortion compensation). The square pulse amplitude is chosen such that ω_{ge}^M is tuned to the center of the passband, which reflects the emitted itinerant photon. At $t = \tau_d$, a square pulse is initiated on the Z_E line, which tunes ω_{ef}^E to the center of the passband in order to re-scatter the reflected photon and realize the CZ gate. Note that while a flux-modulation sideband is used to emit the photon, decay rates induced by the sideband are at maximum less than 50% the intrinsic Γ_{1D}^{ef} of

the qubit. Thus it is more suitable to rapidly tune the qubit frequency rather than modulate it to re-scatter the photon, given that larger Γ_{1D} increases the fidelity of the time-delayed feedback induced CZ gate (see Ref. [60] for more details).

In Figure 5.3c, d we illustrate the actions of reflection by Q_M and photon re-scattering by Q_E on an emitted photon. In Figure 5.3c we show the emitted photon's measured photon flux at the digitizer with the square pulse on the Z_M line turned on or turned off. With the Z_M square pulse turned on, the photon's arrival at the digitizer is delayed by τ_d, while negligible photon flux is measured at all prior times, demonstrating that the Q_M reflects the itinerant photon with high efficiency. Note that the magnitude of the photon flux when the Z_M square pulse is turned on is lower than when the pulse is turned off due to the additional 0.6 dB loss incurred by the itinerant photon during its round-trip. Furthermore, in Figure 5.3d we show the emitted photon's average measured *field* when Q_E is prepared in either the $|g\rangle$ state or the $|e\rangle$ state (where the phase of the field is referenced to the measurement in which Q_E is in the $|g\rangle$ state). It is evident that the sign of the real part of the re-scattered photon's complex field changes when the state of Q_E is changed from $|g\rangle$ to $kete$ (while the imaginary part of the re-scattered photon's complex field is negligible). This corresponds to a state-dependent π difference in the phase of the photon, as desired for the CZ gate implementation.

In addition, we perform quantum process tomography in order to demonstrate the quantum character of the CZ gate. The tomography procedure is shown in the top left of Figure 5.4: different input photonic states are first prepared via suitable Q_E control, followed by qubit preparation into Q_E's different cardinal states. The CZ gate is then performed for each photon/qubit state combination, after which single shot measurements of both the qubit state and the photon field are carried out. The single-shot measurements of the time-dependent photon field, obtained via heterodyne detection of the field after suitable amplification, are post-processed to field quadratures I and Q of the photonic qubit, and are thereupon correlated with single-shot qubit readout measurements (for further details on the single-shot measurement of the field quadratures of the photonic qubits, see Appendix F.1). Joint qubit-photon moments $\langle (a^\dagger)^n a^m \sigma_i \rangle$ are calculated from the processed single-shot data, which are finally used to reconstruct the process matrix χ_{CZ}, show in Figure 5.4; we calculate a process fidelitiy of $\mathrm{Tr}\left(\sqrt{\sqrt{\chi_{CZ}}\chi_{\mathrm{ideal}}\sqrt{\chi_{CZ}}}\right)^2$ of 90%. We attribute most of the infidelity to dephasing and state preparation and measurement (SPAM) errors, given that a similar measurement of the $\mathbb{I} \bigotimes \mathbb{I}$ process matrix yields a process

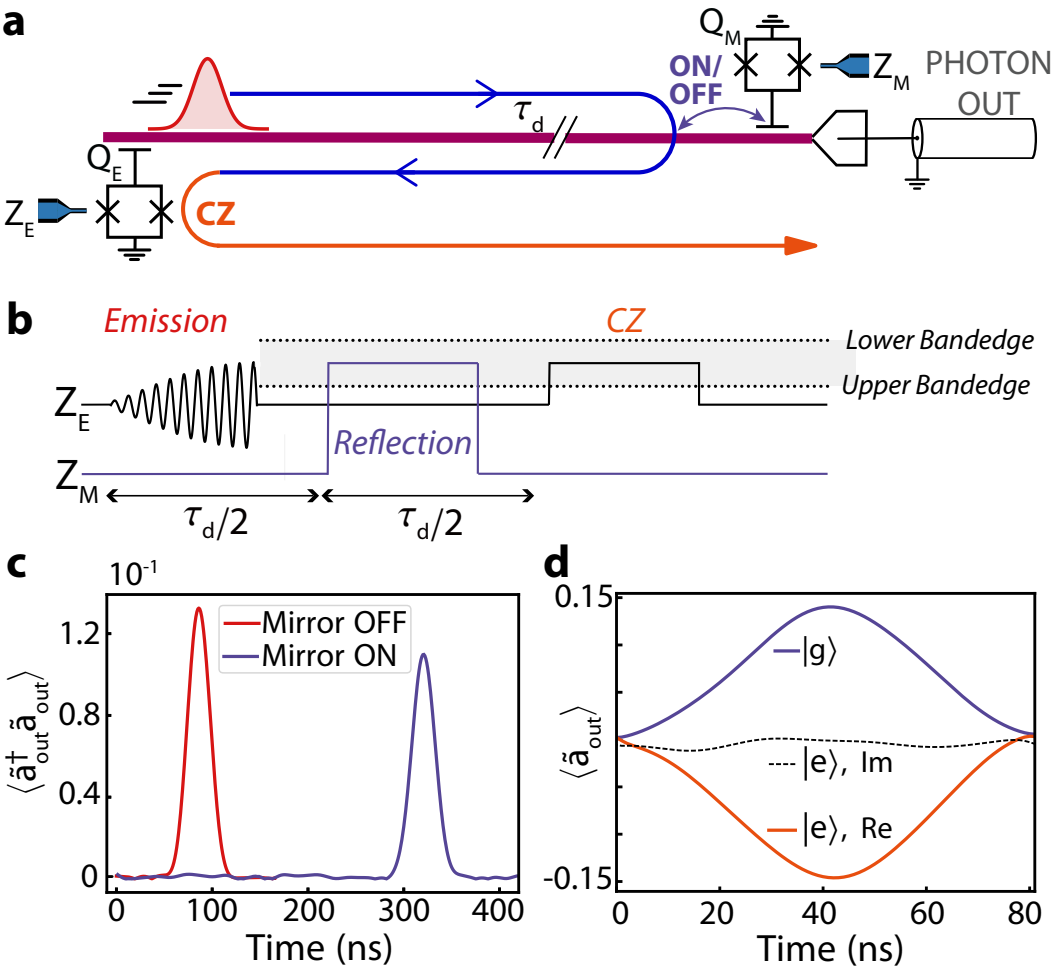

Figure 5.3: **Time-Delayed Feedback Between Emitter Qubit and Previously Emitted Photons. a,** Illustration of the time-delayed feedback process that realizes the CZ gate between Q_E and its emitted photon, where the photon undergoes a round-trip through the slow-light waveguide and re-scatters on Q_E. **b,**. Z-control of the qubits that implements the CZ gate. Both square pulses on Z_M and Z_E tune their respective qubit frequencies to the middle of the passband. **c,** Measured photon flux of qubit emission with the Z_M square pulse for mirror reflection ON vs OFF. **d,** Measured $\langle a_{\text{out}} \rangle$ of the reflected pulse after it re-interacts with Q_E , where Q_E is prepared in either the $|g\rangle$ or the $|e\rangle$ state. The complex phase of $\langle a_{\text{out}} \rangle$ in both cases is normalized to the phase of the measurement where Q_E is prepared in the $|g\rangle$ state.

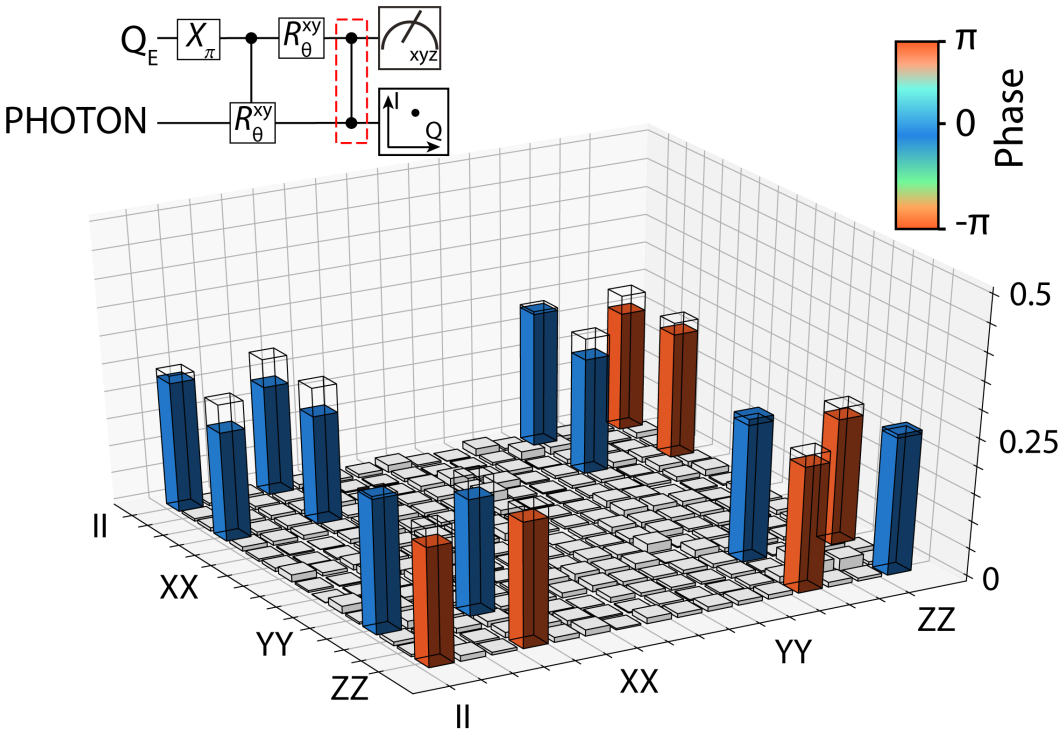

Figure 5.4: **Qubit-Photon CZ Gate Quantum Process Tomography.** Quantum Process Tomography of the Pauli process matrix χ_{CZ} of the CZ gate between Q_E and its emitted photon, demonstrating a 90% fidelity relative to the ideal gate; the procedure for performing the tomography is shown on the top left.

fidelity of 92.5% (for further details of the process tomography, see Appendix F.2).

2D Cluster State Preparation: Finally, with our high-efficiency shaped photon preparation and high-fidelity CZ gate, we demonstrate generation of a 2D cluster state of four microwave photons. In Figure 5.5a, we show the full Q_E control we used to generate the cluster state, which results in the entangled state schematically shown in Figure 5.5b. The control sequence essentially consists of four cycles of the aforementioned operation that generates a 1D cluster state: a $\pi_{ge}/2$ pulse followed by a π_{ef} pulse and flux modulation induced photon emission. Additionally, the first emitted photon is reflected by Q_M and re-scatters on Q_E in between the fourth $\pi_{ge}/2$ and π_{ef} pulses, thus entangling photon 1 to photon 4 once photon 4 is emitted. Notably, before the last π_{ef} pulse we also apply a π_{ge} to Q_E in order to disentangle it from the photonic state upon its final emission. Also, we emit photon 1 with a lower bandwidth than other photons in order to maintain the high fidelity of the CZ gate between photon 1 and Q_E, while photons 2, 3, and 4 are emitted more rapidly (within a 30ns time window) in order to more efficiently use the fixed τ_d delay available. The measured photon flux of the individual time-bin photonic qubits is

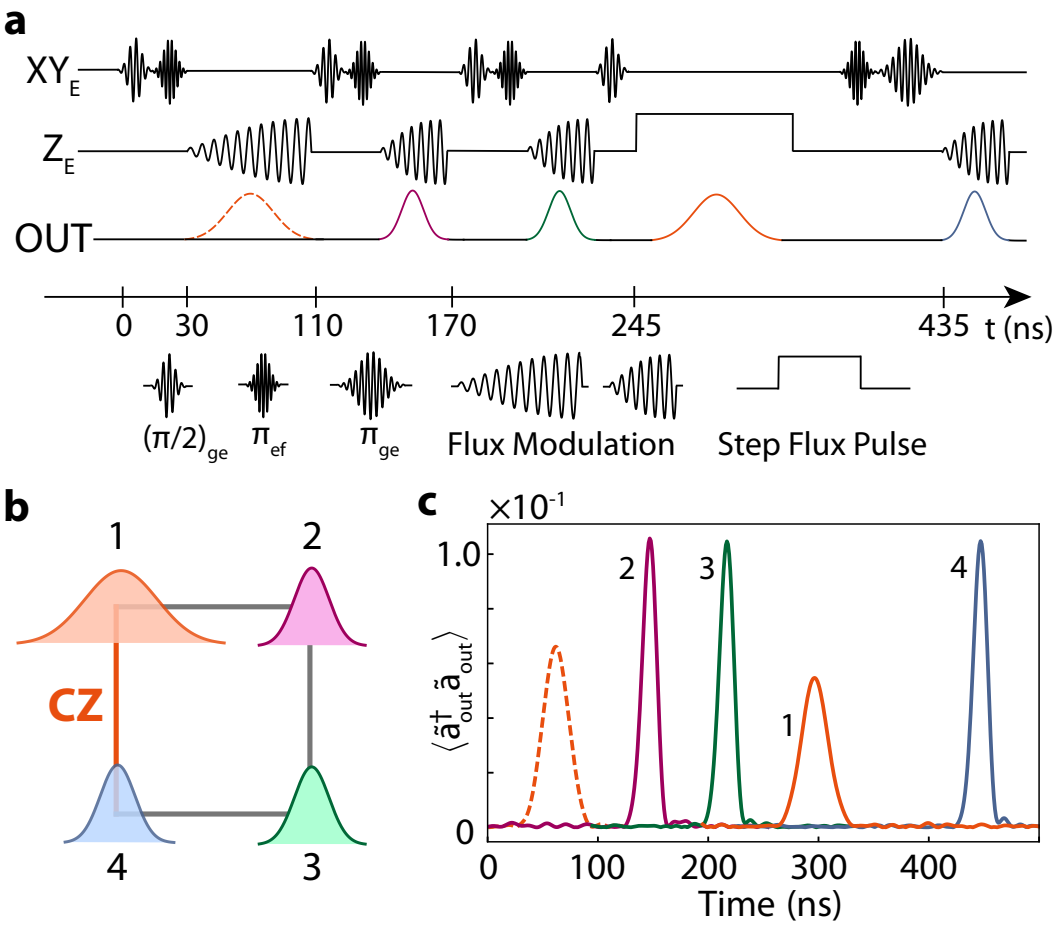

Figure 5.5: **Deterministic Generation of a 4-photon 2D Cluster State a** Pulse sequence of Q_E control lines, and illustration of outgoing photon flux from Q_E. Depiction of Z_M line control can be found in Figure 5.3. Photons 1, 2, 3, and 4 are represented by the colors orange, purple, green, and blue, respectively. **b** Illustration of the generated entangled state. "CZ" signifies the entanglement that arises due to the CZ gate between Q_E and photon 1. **c** Photon flux of individual time-bin photonic qubits. The dotted orange line corresponds to the photon flux of the first emitted photon in the absence of reflection by the mirror qubit, and is only shown for illustration purposes.

shown in Figure 5.5c, where their position in time corresponds to their arrival time at the digitizer.

In order to tomographically reconstruct the generated state, we once again obtain the single-shot field quadratures I_i and Q_i of each photonic time-bin qubit, and obtain their correlations through calculation of all joint moments of the photonic fields. With the moments, we obtain the density matrix ρ of the generated state through a maximum likelihood (MLE) algorithm, shown in Figure 5.6 (for a detailed description of the photonic state tomography process, refer to Appendix F.1). When compared to the ideal expected density matrix ρ_{ideal} shown in Figure F.5b, we observe excellent agreement between the phase pattern of the density

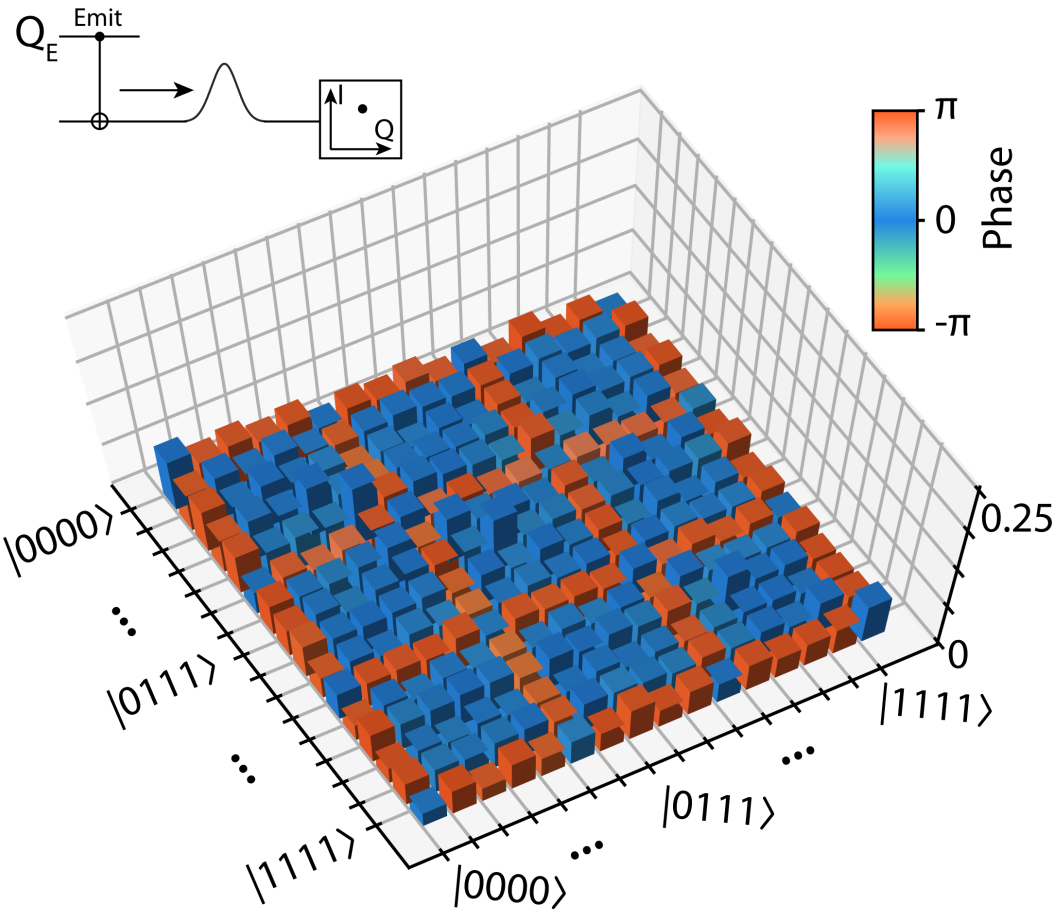

Figure 5.6: **4-photon 2D Cluster State Quantum State Tomography.** Density matrix ρ of the generated 2D cluster state obtained from photonic quantum state tomography. The height of the bars represents the magnitudes of the elements of ρ, while the color of the bars represents the phases of the elements of ρ. The fidelity of the generated state $F = \mathrm{Tr}\left(\sqrt{\sqrt{\rho}\rho_{\mathrm{ideal}}\sqrt{\rho}}\right)^2$ is 70%.

matrix elements, qualitatively indicating that we have achieved the desired entanglement structure of the state shown in Figure 5.5b. Further, each photon has a finite weight-three stabilizer operator $\sigma_x^i \bigotimes_{j\in N(i)} \sigma_z^j$ expectation value, where $N(i)$ are the nearest neighbors of photon i (assuming the connectivity of Figure 5.5b), with calculated values $0.73, 0.73, 0.8, 0.75$, consistent with a square entanglement connectivity rather than a linear entanglement connectivity.

We calculate a fidelity $F = \mathrm{Tr}\left(\sqrt{\sqrt{\rho}\rho_{\mathrm{ideal}}\sqrt{\rho}}\right)^2$ of 70% between the generated and ideal state, indicating achievement of genuine four-partite entanglement and successful implementation of the protocol of Ref. [60]. This is in good agreement with our estimated state fidelity limit of 76%, which we calculate from contributions to preparation infidelity that include the dephasing of Q_E (the primary source of infidelity), the round-trip loss suffered by photon 1, and measured qubit preparation

and control errors (see Appendix E.3 for more details).

5.3 Conclusion

In conclusion, we successfully implemented a resource-efficient protocol for generation of multidimensional cluster states by utilizing a single superconducting qubit as a source of entangled photons, and a coupled resonator array as a slow-light waveguide for time-delayed feedback. We accomplished this by achieving rapid, shaped emission of single photons, as well as by implementing a high-fidelity CZ quantum gate between Q_E and previously emitted photons through the controllable time-delayed feedback of our system. This allowed us to generate a 2D cluster state of four microwave photons, attaining a good state fidelity of 70% (95% CI [69.1%, 70.4%]).

There are numerous avenues for straightforward improvements to our implementation of the cluster state generation protocol that would enable generation of significantly larger cluster states (which we discuss in detail in Chapter 6). By simply improving the dephasing times of the qubit ($T_2^* = 561$ ns in this work) and the quality factors of the unit cell resonators (approximately $\sim 90,000$) to state of the art values [191–193], the major sources of infidelity we incurred could already be dispensed with. Furthermore, potentially increasing the anharmonicity η of the qubit through different qubit design [17, 194, 195] would enable even larger Γ_{1D}, allowing for a high-fidelity CZ gate with high-bandwidth photons and even more rapid emission of shaped photon pulses. The round-trip delay τ_d could also be increased by either further reducing the footprint of our unit cell resonators, for example by leveraging compact high kinetic inductance superconducting resonators [196, 197], or by incorporation of acoustic delay lines [42, 150, 198], increasing the possible size of generated cluster states even further.

Not only would these discussed improvements substantially increase the size of generated 2D cluster states, they would also allow for generation of more complex graph states such as 3D cluster states. Our time-delayed feedback-based scheme for generating 2D cluster states can be easily extended to generate 3D cluster states by simply adding another time-delayed feedback event with a different delay for every photon [181, 182] (which is achievable simply by incorporation of another mirror qubit), where each photon would then be re-scattered by the emitter qubit twice at different times. Indeed, as a preliminary demonstration of this capability, in Appendix F.1 we demonstrate generation of a 5 photon cluster state where we

implemented the time-delayed feedback process twice for one photon, which was necessary for achieving its resultant entanglement connectivity. Generation of 3D cluster states would constitute a hitherto unachieved accomplishment, and would allow for the exploration of fault-tolerant measurement-based quantum computation [91]. We therefore expect our results to not only broaden conventionally optics-based approaches for quantum information science to the microwave domain, but also bolster them by leveraging the rich circuit QED toolbox.

Chapter 6

OUTLOOK

The results presented in this thesis encompass the design and fabrication of a finite-bandwidth SLWG comprised of a coupled-resonator array in a circuit QED system, and its use in various waveguide QED experiments. These experiments included investigation of the physics of a qubit strongly coupled to the SLWG reservoir by tuning its frequency from the bandgap of the waveguide to the passband of the waveguide, as well as demonstration of non-Markovian time-delayed feedback in the system due to the large round-trip delay τ_d of the waveguide. In addition, in another experiment we demonstrated generation of multidimensional cluster states of itinerant microwave photons by leveraging our demonstrated time-delayed feedback, as well as other advantageous properties of the SLWG.

These demonstrated results pave the way for several research avenues, chiefly among them being generation of larger cluster states and their use in a proof of principle measurement-based quantum computation demonstrations, as well as different waveguide QED experiments that make use of our demonstrated non-Markovian time-delayed feedback. In addition, our coupled-resonator array system modality may find use in more conventional circuit QED applications, such as our coupled-resonator array Purcell filter. In the following discussion, I briefly touch upon these different research avenues.

Scaling the Size of the Cluster State

Although there were limiting technical issues in the experiment described in Chapter 5, we believe there is a straight forward path for mitigation of these issues, and realistic strategies for extending our generation scheme to synthesis of much larger cluster states. Firstly, we are confident that there is ample room to reduce the excessive flux noise in our setup to state-of-the-art values [199]. Additionally, while our reliance on flux modulation for tunable coupling between Q_E and the SLWG necessitates operation at “flux sensitive" qubit frequencies, the use of tunable couplers [200, 201] between Q_E and the SLWG would allow operation at Q_E’s “sweet spot" frequencies, thereby increasing its resilience to flux noise. Given that $T_2^* \sim 100\mu$s has been reported for transmon qubits in the past, we expect that the deleterious effects of dephasing could be nearly fully dispensed with. If even

more emitter coherence were to be required, the use of an error-corrected “logical qubit," with emission via an ancilla qubit, could be utilized to fully suppress emitter decoherence based errors.

Furthermore, the 0.7 dB round-trip loss of our waveguide is another serious limiting factor to our fidelity, and arises due to the limited Q of our unit cell resonators, which we estimate to be $90,000$. However, microwave superconducting resonators with $Q > 1,000,000$ have been fabricated in numerous previous works [191–193]. Thus, with fabrication or materials improvement that have already been demonstrated, the waveguide loss could realistically be substantially reduced. We note that while our current compact unit cell design has sharp corners that likely induce strong electric fields that couple to TLS, this effect could be mitigated with different geometrical design or material improvement.

Moreover, while the SLWG's dispersion hinders the use of higher bandwidth Gaussian photon pulses due to dispersion-induced broadening, our tunable coupling capability or dispersion engineering allows for use of well-established [202, 203] or novel [204] dispersion mitigation techniques. By compensating for the dispersion through signal pre-distortion, or via dispersion-cancelling elements post-SLWG propagation, one could ensure that photon pulses arriving for re-scattering or for measurement are well-confined in time, thus alleviating the problem of overlapping broadened pulses. Such techniques would in principle enable even faster emission of photon pulses, and thus would allow for better utilization of limited round-trip delays.

Furthermore, achieving higher anharmonicity of Q_E would allow for realization of even larger Γ_{1D}, without compromising qubit coherence, than what was already achieved in this work. Increasing Γ_{1D} would allow for even more rapid emission of shaped photon pulses, as well as less residual $|f\rangle$ population after emission, and a high fidelity CZ gate with high bandwidth photons. Analysis in Ref. [60] shows that higher Γ_{1D} improves the fidelity of CZ gates, due to decreased “dispersion" of the Q_E induced reflection phase near Q_E's resonance frequency that is commensurate with the broadening of Q_E's lineshape. This reduced “dispersion" of the reflection phase results in the overall phase gained by the photon pulse during re-scattering to be closer to π, and reduces the distortion of the photon pulse imparted by the re-scattering process (which improves mode-matching efficiency). Limited anharmonicity η of Q_E is the main limiting factor to the magnitude of Γ_{1D}, as a Γ_{1D} significantly larger than η would lead to more substantial leakage of the $|e\rangle$ popu-

lation into the SLWG. However, by using a different superconducting qubit design that has higher anharmonicity than the transmon [17, 194, 195], the magnitude of Γ_{1D} could be substantially increased without compromising other aspects of cluster state generation. Also, achieving higher anhamonicity would allow for a larger waveguide passband, which would lower higher-order dispersion (albeit at the cost of less delay per resonator).

Additionally, the round-trip delay could be substantially increased in several ways. One straightforward way is simply by increasing the number of unit cells of the SLWG. Although that would increase the size of the device, which could introduce spurious box modes to the sample, recent advances in microwave packaging techniques could ameliorate the impact of larger device size [205, 206]. Furthermore, the unit cell size could be reduced by leveraging compact high kinetic inductance superconducting resonators [196, 197], allowing for more delay per area. And looking forward even further, incorporation of an acoustic delay line into our system could allow for longer round-trip delays without additional dispersion or susceptibility to microwave packaging box modes [42, 150, 198], increasing the possible size of generated cluster states even further.

We stress that in addition to increasing cluster state size, cluster state dimensionality could be increased to 3D by coupling of another mirror qubit somewhere along the delay line rather than at the end, which would impart the ability to perform time-delayed feedback with two different delays. The ability to perform two time-delayed feedback events with two different delays is the pre-requisite to generating 3D cluster states via sequential photon emission and time-delayed feedback [181, 182], because it allows for sufficient non-nearest neighbor entanglement between photons of the emitted pulse train such that the entanglement topology is that of a 3D cluster state. While this extension of our scheme would necessitate significantly larger delays, we believe achieving such delays is possible. Thus, we believe there is a viable path to measurement-based quantum computation with microwave photons via photonic resource state generation as we have described. We conclude by observing that, even if the size of generated photonic states were to hit some practical limitation, there are other measurement-based quantum computation schemes, such as fusion-based quantum computation [207], that only require the repeated synthesis of smaller photonic resource states which are later “fused" into larger photonic states via linear optical elements. Our cluster state generation scheme would be well suited to be incorporated into such approaches, and could provide a “bridge" toward the goal of

photonic resource state generation via linear optical elements.

Finally, we note that previous works [181, 182] have performed analysis of errors in cluster state generation in the context of fault-tolerant quantum computing. They find that for a gate error rate of $\sim 10^{-3}$ (where "gates" in this context includes Q_E single qubit gates, photon emission, and the qubit-photon CZ gate) and delay line losses of $\sim 3 \cdot 10^{-5}$ dB/ns, one can achieve a fault-tolerance "break-even" point where the logical error rate is lower than the gate error rate, and beyond which logical errors are exponentially suppressed as delay line loss is decreased. State-of-the-art single-qubit gates can routinely achieve such gate error rates of 10^{-3}, while photon emission should in principle also achieve such error rates if there is enough time for full emission from the $|f\rangle$ state, and sufficient protection of the $|e\rangle$ state. Furthermore as mentioned in the main text, although our reported CZ gate fidelity was 90 %, we are able to ascribe most of that infidelity to SPAM errors via separate measurements. From separate simulations, we expected a 97 % fidelity for the CZ gate, and this fidelity could be increased further simply by increasing the Γ_{1D} of the emitter qubit. In addition, while necessary delay line losses are around ~ 100 times smaller than our current losses in our experiment, recent and future advances in superconducting circuit fabrication are expected to allow for 100 times (or more) lower losses in superconducting resonators [208]. Thus, we foresee that with realistic device and fabrication improvements, generating 3D cluster states for fault-tolerant measurement based quantum computation with negligible logical error rates should be feasible. Further, while single-shot photon measurements along arbitrary basis would also be necessary for quantum computation with itinerant microwave photons, such single photon detection could be achieved with a "detector" qubit. With such a detector, an itinerant photon's state would be mapped to the detector qubit state's via suitable time-dependent control of the detector qubit's coupling to the waveguide, as demonstrated in previous works [209, 210]; the "detector" qubit could then be measured in an arbitrary basis. Lastly, we also note that with different photon qubit encodings, different generation and measurement protocols are also possible.

Continuous Wave Experiments in the Presence of Time-Delayed Feedback

While many interesting waveguide QED experiments with superconducting qubits coupled to regular transmission line coplanar waveguides have been accomplished over the last several years, long delays and time-delayed feedback have the potential to enrich the physics hitherto explored in these systems. While there are many interesting experiments involving time-delayed feedback proposed in the lit-

erature, experiments involving correlation measurements of the fluorescence from a continuously driven qubit in the presence of time-delayed feedback present a nice complement to the "pulsed" experiments discussed in Chapter 5. Realizing such proposals with our superconducting qubit-SLWG systems would in principle be a direct extension of the work presented in this thesis, and thus constitute natural follow-up experiments to the work presented here.

For example, in the experiment proposed in Ref. [128], probing a waveguide QED system with a qubit in front of a distant mirror in the continuous, strongly driven regime would reveal remarkably different properties of its steady-state field as compared to a Markovian system without time-delayed feedback. Firstly, the output power spectrum of the qubit's fluorescence would differ from a Mollow Triplet, and would develop many additional "interference peaks" due to the coherence of photons emitted toward and away from the mirror, which results in the interference of signals whose emission time is separated by the round-trip delay τ_d. Moreover, the second-order correlation function $g_2(t)$ would contain long-time correlations, including anti-bunching at $g_2(\tau_d) < 1$, in contrast to the usual $g_2(t)$ of fluorescence of a driven atom that exhibits an antibunching dip only at the vicinity of $t = 0$. $g_2(\tau_d) < 1$ corresponds to a reduced probability of detecting two photons separated in time by τ_d, which can be understood by considering that since photons are emitted in a superposition of states corresponding to propagation toward and away from the mirror, detection of photons emitted away from the mirror at time $t = t'$ precludes detection of photons emitted toward the mirror at time t', which would consequently arrive at the detector at a later time $t = t' + \tau_d$. This phenomenon may be described as the *anti-bunching of photons emitted towards and away from the mirror at the same time*. Furthermore, depending on the round-trip phase φ picked up by a photon emitted toward the mirror, $g_2(t = 0)$ can change from an anti-bunching dip $g_2(0) < 1$ to a bunching peak $g_2(0) > 1$, corresponding to an increased probability of detecting two photons *at the same time*. In spite of the qubit only being limited to emitting one photon at a time, $g_2(0) > 1$ may occur in this system with time-delayed feedback because photons emitted toward the detector at time t' may constructively interfere with photons that were emitted toward the mirror at an earlier time. Note that observation of non-Markovian phenomena in $g_2(t)$ correlation measurements have hitherto been unexplored, and thus offer an exciting new follow-up research direction. Also, we encourage the reader to see Ref. [140] for a proposed experiment that would measure the $g_2(t)$ for a waveguide QED system consisting of a driven waveguide coupled to two qubits separated by a very long propagation delay, where

the non-Markovianity of the system again leads to properties of the transmitted field different than that expected for a Markovian system.

Additionally, the output field of a continuously driven qubit, which consists of a stream of strongly correlated photons, has a direct mapping to matrix-product states, which can be leveraged for analog quantum simulation of interacting quantum fields [160, 211]. Via this mapping, analog variational quantum simulation of a 1D quantum field was realized via fluorescence of a tunable waveguide QED system, see Ref. [46] for more details. Nevertheless, while there is strong interest in simulating higher-dimensional interacting quantum systems via analog quantum simulation methods, simulation of interacting 1D systems are typically tractable through classical means. However, by incorporating time-delayed feedback into a system such as the one presented in Ref. [46], the entanglement dimensionality of the continuous output stream of correlated photons can be increased beyond 1D. This would allow for analog simulations of two-dimensional interacting quantum fields, rather than one-dimensional fields, and would hence constitute a significant advancement in analog quantum simulation of interacting quantum systems.

Finally, we note that there has been several demonstrations and technical advancements in measuring correlation functions of the output from continuously driven quantum circuit QED systems [39–41]. Thus the proposed experiments described here are tractable with our SLWG system in conjunction with conventional circuit QED control and measurement set ups.

Appendix A

FABRICATION AND MEASUREMENT SETUPS

Device Fabrication

The devices used in the work presented in this thesis were fabricatedvia the techniques described in detail in Ref. [70]. A brief summary follows below.

Our devices were fabricated on silicon substrates [525 μm thickness, > 10kΩ-cm resistivity]. Our first aluminum (Al) layer consisting of the ground plane, CPWs, metamaterial waveguide, and qubit capacitor is fabricated as follows. After standard solvent cleaning of the substrate, we spin resist and pattern it by electron-beam lithography. After resist patterning, we clean the exposed substrate surface with oxygen plasma and BOE, followed by electron-beam evaporation of 120 nm aluminum at a rate of 1 nm/s. A liftoff process is performed in n-methyl-2-pyrrolidone at 80 °C for 2.5 hours (with 10 minutes of ultrasonication at the end) to yield the aforementioned metal structures.

The Josephson junctions were fabricated using double-angle electron beam evaporation of 60 nm and 120 nm of Al (at 1 nm/s) on suspended Dolan bridges, with an intervening 20 minute oxidation and a subsequent 2 minute oxidation at 10 mbar, followed by liftoff as described above. Note that prior to the double-angle evaporation, the sample was cleaned by an oxygen plasma treatment and a HF vapor etch.

Furthermore, in order to electrically connect the evaporated Josephson junctions to the first Al layer, a 6 min argon ion mill was performed to locally remove surface aluminum oxide around the areas of overlap between the first Al layer and the Josephson junctions, which was followed by evaporation of an additional “bandage” layer of 140 nm Al that electrically connected the metal layers. Note that if any “patches" were necessary to connect spuriously disconnected/broken metal structures (as was the case for the fabrication of the device shown in Figure 5.1), these patches were concomitantly fabricated together with the “bandage" layer. Finally, airbridges (used in the device shown in Figure 5.1) were fabricated by grayscale electron-beam lithography on a trilayer resist stack. After development and 2 hours of resist reflow at 105 ∘C, electron-beam evaporation of 200 nm Al was performed at a rate of 1 nm/s following 6 min of Ar ion milling.

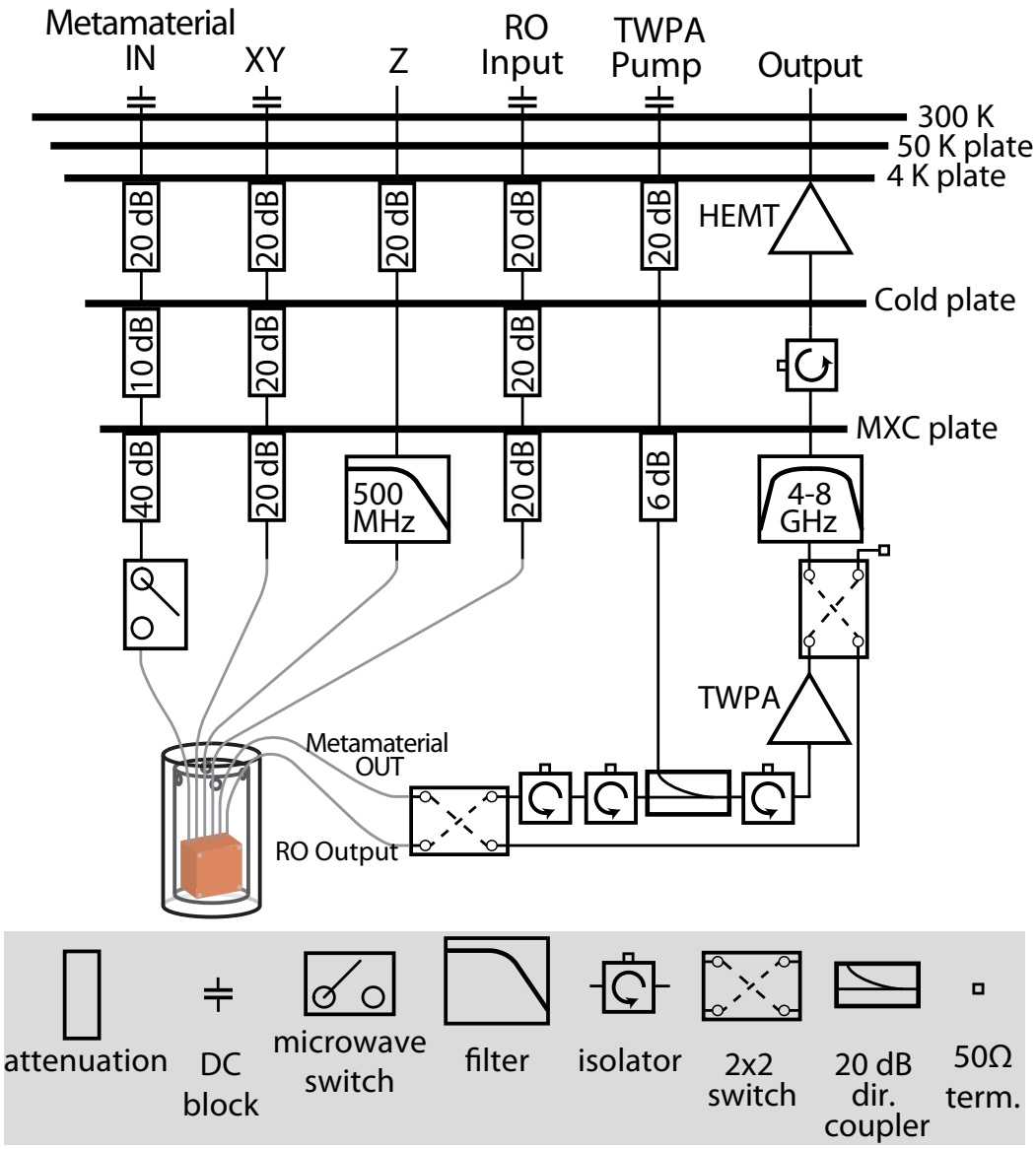

Figure A.1: **Schematic of the measurement chain inside the dilution refrigerator.** See Appendix A text for further details (“dir." is shorthand for “directional," and “term." is shorthand for “termination"). See Figure 4.1 for electrical connections at the sample.

Measurement Setup

Schematics of the fridge wiring used in the work discussed in Chapters 4 and 5 are shown in Figs. A.1 and A.2, respectively. Measurements were performed in a 3He/4He dry dilution refrigerator, with a base fridge temperature at the mixing chamber (MXC) plate of $T_{MXC} \sim 10$ mK. Devices are wirebonded to a CPW printed circuit board (PCB) with coaxial connectors, and are housed inside a small copper box that is mounted to the MXC plate of the fridge. The packaged devices are enclosed in two layers of magnetic shielding to suppress effects of stray magnetic

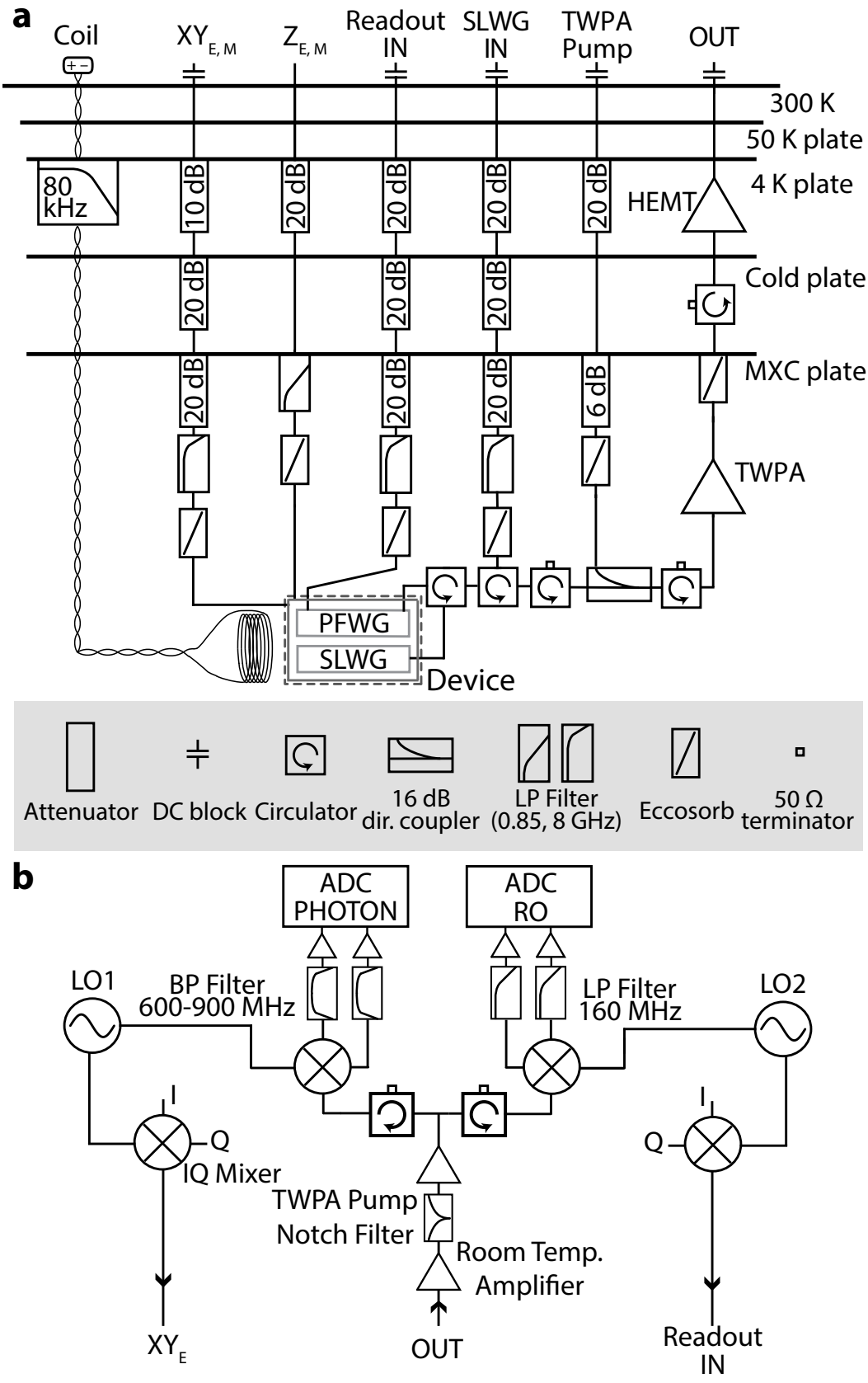

Figure A.2: **Measurement Setup.** **a** Schematic of the measurement wiring inside the dilution refrigerator. See Appendix A text for further details ("dir." is shorthand for "directional," "LP" is shorthand for "Low Pass," and "BP" is shorthand for "Band Pass"). See Figure 5.1 for electrical connections at the sample. **b** Simplified diagram of measurement wiring outside the dilution refrigerator.

fields.

Attenuators are placed at several temperature stages of the fridge to provide thermalization of the coaxial input lines and to reduce thermal microwave noise at the input to the sample. Our gigahertz microwave input lines have significantly more attenuation than our fast flux Z lines for reasons explained in Ref. [212]. In addition, fast flux lines are filtered by a < 1 GHz low-pass filter below the MXC plate, which suppresses thermal noise photons at higher frequencies while still maintaining short rise and fall times of square flux pulses, as well as allowing transmission of AC flux drives. Outside the fridge, all inputs to the dilution refrigerator are low-pass filtered and attenuated such that the noise levels from the electronic sources are reduced to a 300 K Johnson-Nyquist noise level.

Our amplifier chain for our measurements consists of a quantum-limited traveling-wave parametric amplifier (TWPA) [213] as the initial amplification stage, followed by a high mobility electron transistor (HEMT) amplifier mounted at the 4K plate. We use superconducting NbTi cables to minimize loss from the MXC plate to the 4K plate. For operation of the TWPA, a microwave LO pump signal is added to the amplifier via the coupled port of a ~ 20 dB directional coupler, with its isolated port terminated in 50-Ω. We include two isolators between the directional coupler and the sample in order to shield the sample from the strong TWPA pump, as well as an isolator in between the TWPA and the directional coupler in order to suppress any standing waves between the two elements due to spurious impedance mismatches. Our isolators consist of 3 port circulators with the third port terminated in 50-Ω. Note also that all 50-Ω terminations are thermalized to the MXC plate in order to suppress thermal noise from their resistive elements.

We calibrate our TWPA by continuously driving one of the input lines, and measuring the output from the output line with a spectrum analyzer for a wide frequency range; thus with the spectrum analyzer measurement we can measure both the gain and the noise floor. We then run sweeps of TWPA pump power and pump frequency in order to obtain the optimal operating point that best improves SNR by maximizing the ratio of signal power increase to noise power increase. We typically choose the frequency of the continuous tone to be at a measurement frequency of interest; this measurement can be done at multiple different input tone frequencies in order to maximize TWPA SNR at different frequencies. In practice, we have found that some TWPA parameters that maximize gain also lead to large increases in amplifier added noise, and thus are not the optimal points that maximize SNR. This is why

we do spectrum analyzer measurements rather than VNA measurements (which do not give information on noise floor increases) for TWPA calibration.

Chapter 4 Measurement Setup Details

In addition to the attenuation schemes already discussed, the 40 dB attenuation of the “Metamaterial IN" line at the MXC plate includes a 20 dB thin-film “cold attenuator" [214] to ensure a more complete reduction of thermal photons in the metamaterial waveguide. Moreover, in between the TWPA and HEMT amplifiers, we have included a reflective bandpass filter (thermalized to the MXC plate) to suppress noise outside of 4–8 GHz.

We also employed microwave switches in our measurement chain in order to provide in situ experimental flexibility in the following manner. As discussed in Chapter 4, in between the “Metamaterial IN" chain and the metamaterial waveguide we have placed a Radiall R573423600 microwave switch. By electrically opening the switch, we can establish an open circuit at the end of the waveguide furthest from Q_1, effectively creating a mirror for emission from Q_1 and thereby inducing time-delayed feedback.

In addition, in order to utilize our amplifier chain for either spectroscopic or time-domain measurements within the same cool-down, we employed Radiall R577432000 2x2 microwave switches for selective routing of the outputs of the metamaterial waveguide or the readout waveguide to the amplification chain. With our switch configuration, we ensured that when routing the readout waveguide output to the amplification chain, the metamaterial waveguide output was connected to a 50-Ω termination. This allowed us to maintain a 50-Ω environment at the metamaterial output at all times, and thereby ensured that the metamaterial waveguide remained an open quantum system due to its coupling to the 50-Ω continuum of modes. By employing two 2x2 switches instead of one, we had the ability to bypass the TWPA amplifier if desired, although ultimately the TWPA was used when collecting all measurement data presented in Figs. 4.1–4.3.

For spectroscopic measurements, the “Metamaterial IN” and “Output” lines were connected to the input and output of a ZNB20 Rohde & Schwarz vector network analyzer (VNA), respectively. For time-domain measurements, GHz excitation and readout pulses were generated by upconversion of MHz IF in-phase (I) and quadrature (Q) signals sourced from a Keysight M320XA arbitrary waveform generator (AWG), utilizing a Marki IQ-4509 IQ mixer and a LO tone supplied by a BNC

845 microwave source. Following amplification, output readout signals were down-converted (using an equivalent mixer and the same LO source) and subsequently digitized using an Alazar ATS9360 digitizer. For all measurements, qubit flux biasing was also sourced from a M320XA AWG, the TWPA pump tone was sourced by an Agilent E8257D microwave source.

Chapter 5 Measurement Setup Details

In addition to the attenuation schemes already discussed, Gigahertz microwave input lines are filtered by an 8 GHz lowpass filter, and all microwave lines have an Eccosorb filter, in order to ensure strong suppression of thermal noise photons at very high frequencies. Moreover, a coil was used for static flux tuning of the qubits; the coil is placed on top of the copper box package. The tuning coil is differentially biased by two DC input lines, with 80 kHz low-pass filters at the 4K stage to further suppress noise photons.

Output signals from the Purcell filter waveguide (PFWG) and slow-light waveguide (SLWG) device lines are merged to a single amplifier chain in the following manner. Their corresponding coaxial lines are connected to a circulator as shown in Figure A.2a, such that signals exiting the SLWG continue directly to the output chain, while signals exiting the Purcell filter are first routed to the SLWG device line and subsequently reflect off of the finite-bandwidth structure, thus finally routing them to the output chain. Note that input signals to the SLWG IN line undergo similar routing in order to arrive at the device.

We show the wiring outside the fridge in Figure A.2b. Following amplification inside the fridge, we further amplify output signals with amplification that is suitable for the dynamic range of our ADC. We note that we use a Micro Lambda Wireless MLBFR-0212 tunable notch filter to reject the TWPA pump signal in order to prevent saturation of the following room temperature electronics. Additionally, we use IF amplifiers (0-1GHz bandwidth) for downconverted signals due to IQ mixer saturation power limits.

Due to their different frequencies, we route SLWG and PFWG signals to different downconversion stages via a 2-way power splitter, followed by a circulator at each branch to prevent crosstalk between the two branches. The “PHOTON" branch is connected to a IQ mixer for downconversion of ~ 4.8 GHz photonic signals, which are then measured by an Alazartech ATS9371 digitizer (ADC PHOTON); measurement of both photonic signal quadratures $I(t)$ and $Q(t)$ comprise the heterodyne

measurement of time-dependent photon signals alluded to in Appendix F.1. Meanwhile, the other branch of the power splitter is also connected to an IQ mixer for downconversion of ~ 7.5 GHz readout signals, which are then measured a Keysight M3102 digitizer (ADC RO). We note that downconversion mixers share LO signals (generated by Rohde & Schwarz SMB100A microwave signal generators) with their upconversion counterparts (where a Zurich HDAWG is used) , in order to ensure phase drift/jitter of LO's during upconversion are cancelled out during downconversion. And crucially, we place additional filters before measurement at the ADC in order to suppress noise outside of the IF measurement band of interest. This not only allows for better utilization of the ADC dynamic range, but also rejects noise at irrelevant Nyquist bands that "fold" over to the bandwidth of measured signals; we note that this effectively improved the n_{noise} of our photon measurement chain by almost a factor of 2 (see Appendix F.1 for more details).

Appendix B

MODELING OF QUBIT COUPLED TO COUPLED RESONATOR ARRAY WAVEGUIDE - GENERAL MODEL

Throughout the work done in this thesis, we perform time-domain measurements involving the interaction of an excited qubit with a coupled resonator array waveguide. In order to analyze the measurement data for the purposes of device parameter extraction, or for further understanding of observed dynamical phenomena, we compare the measurement data to transient time-domain simulations performed in Qutip.

The following general tight-binding model, which we use in all master equation simulations in this thesis, captures the salient attributes of our system of qubits coupled to our coupled resonator array metamaterial waveguides.

$$\hat{H} = \omega_{ge} \left|e\right\rangle \left\langle e\right| + \sum_{x=1}^{M} \omega_x \hat{a}_x^\dagger \hat{a}_x + (J_x \hat{a}_x^\dagger \hat{a}_{x+1} + J_{nnn} \hat{a}_x^\dagger \hat{a}_{x+2} + h.c) + \sum_i g_i \hat{\sigma}_x \left(\hat{a}_i^\dagger + \hat{a}_i\right), \tag{B.1}$$

where M is the number of resonators, ω_x are the frequencies of the individual resonator modes and, as discussed in Section 3.2, in our parameter regime the capacitively coupled resonator array Hamiltonian can be well approximated as a tight-binding Hamiltonian with dominant nearest-neighbor coupling J_x and small ($\sim J/100$) next-nearest neighbor coupling J_{nnn} (which we keep as a constant in the model for simplicity). In our simulations, for all unit cells we set $\omega_x = \omega_p = \omega_0 - 2J$, which is the passband center frequency and constitutes the bare resonator frequency ω_0 renormalized by its coupling to neighboring resonators; however, for the taper resonators we introduce moderate detunings in order to capture the weak reflections within the slow-light waveguide that is typically evidenced by measured data. Further, we include qubit coupling to multiple resonators in the array in our model with couplings g_i, where i indicates resonator position in the array, in order to capture both g_{uc} and the weak non-local coupling of the qubit to a few of the neighboring unit cells that is typically evidenced by the measured data.

Going into the rotating frame of the passband center frequency ω_p and applying the

rotating wave approximation (RWA) to remove counter-rotating terms, we arrive at the following Hamiltonian

$$\hat{H} = \Delta_{ge} \left|e\right\rangle \left\langle e\right| + \sum_{x=1}^{M} \delta_x \hat{a}_x^\dagger \hat{a}_x + (J_x \hat{a}_x^\dagger \hat{a}_{x+1} + J_{nnn} \hat{a}_x^\dagger \hat{a}_{x+2} + h.c) + \sum_i g_i \left(\hat{a}_i^\dagger \hat{\sigma}^- + \hat{a}_i \hat{\sigma}^+\right), \tag{B.2}$$

where $\Delta_{ge} = \omega_{ge} - \omega_p$ and $\delta_x = \omega_x - \omega_p$ It can be shown that the Hamiltonian in Equation B.2 preserves the number of excitations N by noting that the commutator $\left[\hat{H}, \hat{N}\right] = 0$ with $\hat{N} = \sum_{x=1}^{M} \hat{a}_x^\dagger \hat{a}_x + \hat{\sigma}^+ \hat{\sigma}^-$. Consequently, the dynamics of the system can be partitioned into subspaces with fixed excitation number, and for the purposes of modeling dynamical data of a system with initially only one excited qubit and no other excitations, we only need to consider the subspaces of $N = 0, 1$. The Hamiltonian in this reduced subspace can be computed by explicitly evaluating the matrix elements $\left\langle \phi\right| \hat{H} \left|\phi'\right\rangle$ between different states $\{\left|\phi\right\rangle\}$ in the zero- and single-excitation manifold, and subsequently directly used in numerical master equation simulations.

Finally, while the Hamiltonian in Equation B.2 generates the unitary dynamics of the system, the external loading of the system to the input/output 50-Ω waveguides is incorporated into the model via dissipation with rate $\kappa_{50\Omega}$ in the resonators of the array preceding input/output waveguides. This dissipation by input/output waveguides is generated in our master equation simulations via collapse operators which transfer population from the single-excitation states $\left|1_1, 0_2, 0_3, \ldots, 0_M; g\right\rangle$ and $\left|0_1, 0_2, 0_3, \ldots, 1_M; g\right\rangle$ for input and output waveguides respectively, to the (trivial) zero-excitation ground state of the system $\left|0_1, 0_2, 0_3, ..., 0_M, g\right\rangle$. Note that master equation simulations of a qubit's non-Markovian radiative dynamics are only possible here due to the fact that we are explicitly simulating all the photonic degrees of freedom of the slow-light waveguide in addition to the qubit's degrees of freedom. A Lindbladian master equation simulation of solely the qubit's degrees of freedom, with the photonic degrees of freedom traced out, would not capture its non-Markovian radiative dynamics. Moreover, a simulation of the entire qubit-waveguide system is only amenable here due to our restriction of the Hilbert space to its low-energy sector, and would quickly grow intractable if a higher number of excitations were allowed.

Appendix C

MICROWAVE DESIGN OF COUPLED RESONATOR ARRAY WAVEGUIDES AND QUBIT SYSTEMS

The successful fabrication of our coupled resonator array waveguides was predicated on the development of robust design methodologies that achieved translation of simulated (effective) circuit parameters to fabricated (effective) circuit parameters with good accuracy. In this Chapter I briefly summarize some of these design methodologies and their accompanying theory.

C.1 Dispersion Relation of a Periodic Circuit: Transfer Matrix Analysis

The following is a summary of analysis presented in Ref. [109] Considering the unit cell of a periodic circuit as two-port network, there will be a transfer matrix that relates voltages and currents at the input to the network to the voltages and currents at the output to the network; this matrix is commonly called the $ABCD$ matrix. Thus, for the n^{th} unit cell of a periodic circuit, we may write

$$\begin{bmatrix} V_n \\ I_n \end{bmatrix} = \begin{bmatrix} A & B \\ C & D \end{bmatrix} \begin{bmatrix} V_{n+1} \\ I_{n+1}, \end{bmatrix} \tag{C.1}$$

where in general we expect the $ABCD$ matrix elements to be frequency dependent.

We expect a periodic circuit to support propagation of traveling modes due to the Bloch Theorem. In order to find the dispersion relation of these propagating modes, we may assume that for these traveling modes, the voltages and currents at the n^{th} unit cell will differ from the voltages and currents at the $n+1$ unit cell by the traveling mode propagation factor e^{ikd}

$$\begin{bmatrix} A & B \\ C & D \end{bmatrix} \begin{bmatrix} V_{n+1} \\ I_{n+1} \end{bmatrix} = e^{ikd} \begin{bmatrix} V_{n+1} \\ I_{n+1} \end{bmatrix}. \tag{C.2}$$

This constitutes an eigenvalue problem. By using the fact that the determinant of the $ABCD$ matrix $(AD - BC)$ is always equal to 1 for reciprocal networks, the dispersion relation of the periodic circuit can be shown to be given by the following relation:

$$\cos(kd) = \frac{A+D}{2}. \tag{C.3}$$

Finally, note that one may obtain the $ABCD$ matrix of a two-port network from its scattering matrix [109]:

$$A = \frac{(1+S_{11})(1-S_{22})+S_{12}S_{21}}{2S_{21}}, \tag{C.4}$$

$$B = Z_0\frac{(1+S_{11})(1+S_{22})-S_{12}S_{21}}{2S_{21}}, \tag{C.5}$$

$$C = \frac{1}{Z_0}\frac{(1-S_{11})(1-S_{22})-S_{12}S_{21}}{2S_{21}}, \tag{C.6}$$

$$D = \frac{(1-S_{11})(1+S_{22})+S_{12}S_{21}}{2S_{21}}, \tag{C.7}$$

$$\tag{C.8}$$

where Z_0 is the characteristic impedance of the ports. This allows us to obtain the $ABCD$ matrix of a two-port network from the scattering matrix simulation results of Sonnet.

C.2 Metamaterial Waveguide Circuit Design Methods

As discussed in Chapter 3, our metamaterial slow-light waveguide consists of a periodic coupled resonator array, with modified resonators at the boundary of the array for impedance matching of the periodic structure to input/output 50-Ω CPWs. In order to obtain target circuit parameters for our structure, we in practice utilized the AWR Microwave Office software. First, using its built-in iFilter functionality allows one to obtain the circuit parameters for a low-ripple coupled resonator array bandpass filter comprised of 25 resonators with a target center frequency, bandwidth, and fixed resonator inductance. Taking the circuit parameters of the middle resonator as the unit cell parameters of the periodic structure, and the parameters of the last two resonators as the taper cell parameters, already yields good initial parameters for a tapered coupled resonator array with good impedance matching in the middle of the passband. Further optimization of these initial parameters can then be done with Microwave Office's optimization functionality in order to obtain the lowest passband ripple possible with two taper resonators.

With target circuit parameters in place, we then typically design and simulate planar circuits in Sonnet in order to obtain lumped-element microwave resonator geometri-

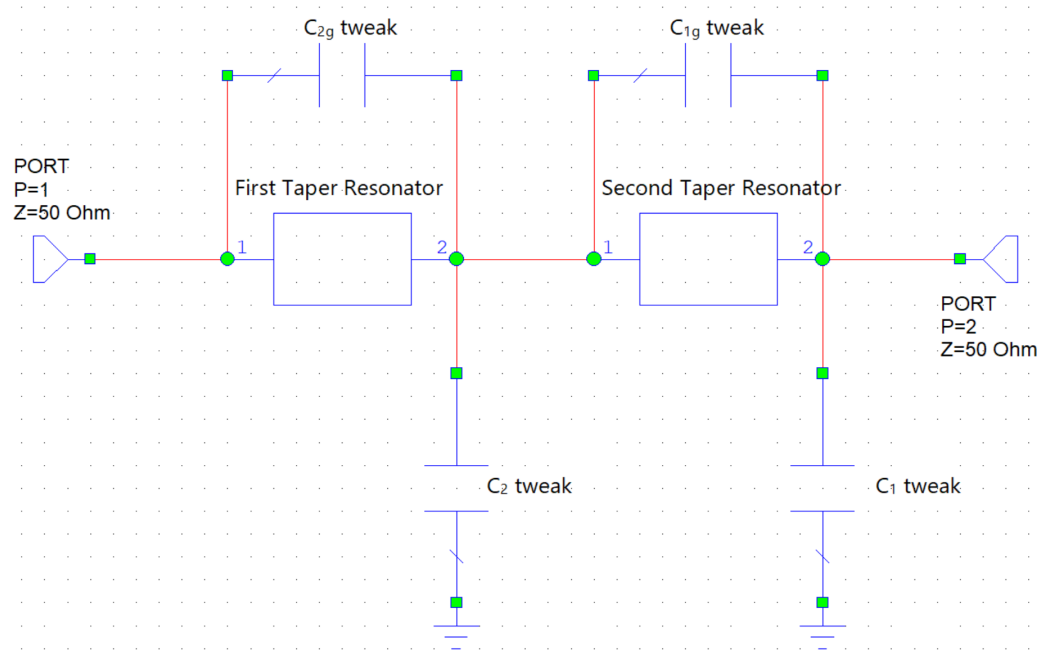

Figure C.1: **Microwave Office Taper Simulation.** Illustration of Microwave Office Simulation of the “taper" section of a coupled resonator array. Here, the simulation results of the first taper resonator and the second taper resonator are “cascaded." This simulation will also eventually be “cascaded" with simulations of the unit cell of the coupled resonator array. The lumped element capacitor values can be adjusted to learn what capacitance values need to be modified in order to improve the simulated transmission of the full array.

cal designs, as is discussed in detail in Section C.3. These simulations are typically performed at the single-resonator level. Scattering parameter simulations results from Sonnet can then be imported into Microwave Office as an effective two-port network. By importing each of the Sonnet simulation results of the unit cell resonator and taper resonators simulations as a two-port network, these “networks" can then be cascaded in Microwave Office to yield a simulation of the transmission through the entire coupled resonator array, based on the planar circuits simulated in Sonnet.

This simulation of the transmission of the full array can then be compared to the ideal transmission of the target coupled resonator array circuit. This comparison allows one to see if any modifications to effective circuit parameters of the simulated resonators need to be made in order to improve transmission characteristics such as ripple. In order to learn which circuit parameters need to changed and by how much, it is convenient to add additional lumped element capacitors to the “cascaded" simulation, as illustrated in Figure C.1. Note that in Microwave Office, these lumped element capacitors can have “negative" capacitances. Thus they can be tuned at

will to change the transmission characteristics of the “cascaded" simulation, and upon reaching the target transmission, their values indicate the change necessary in effective circuit parameters to obtain the target transmission.

Note that while we have described the use of single resonator Sonnet simulations to learn predicted transmission characteristics of the final design, simulations with multiple resonators give spurious results if imported to “cascaded" simulations in Microwave Office. This is because such Sonnet simulations contain additional near-field coupling between the resonators in the simulation, but if the results of such simulations are “cascaded," then near-field coupling between cascaded simulations will not be captured. This inconsistency will lead to flawed transmission simulations.

C.3 Sonnet Simulation of Metamaterial Waveguide Resonators and Parameter Extraction

In our research group, we perform electromagnetic finite-element analysis simulations primarily using Sonnet [118]. Sonnet is a simulation tool well-suited to “quasi-2D" patterned microwave circuits, because it can simulate frequency-dependent scattering parameters very quickly compared to full-field simulation softwares such as Comsol. Sonnet simulations involve defining a microwave network consisting of a “circuit" comprised of patterned metal, as well as “ports" of the microwave network that connect to the circuit. The Sonnet simulation outputs scattering parameters between the defined ports of the network, which contains information about the intervening circuit between the ports.

There are a variety of ways of obtaining effective circuit parameters of a planar circuit comprised of patterned metal in Sonnet. For example, for a circuit consisting of planar inductors and capacitors, one may simulate these elements individually at DC frequencies in order to obtain circuit parameters. Or, for resonators, one may connect to the resonator circuit an ideal circuit element (which Sonnet allows), sweep its value, extract resultant resonance frequencies from Sonnet simulations, and fit to the resultant frequencies in order to extract circuit parameters. However, we found such approaches to be intolerably inaccurate for the design of our metamaterial slow-light waveguides, whose transmission is very susceptible to inaccuracies in circuit parameters. I describe below a simulation/design flow and design principles that yielded fabricated structures with good correspondence to target design parameters.

Firstly, for lumped element resonators such as those illustrated in Figure 3.1a, we found that it was best to simulate as much of the unit cell together as possible, rather

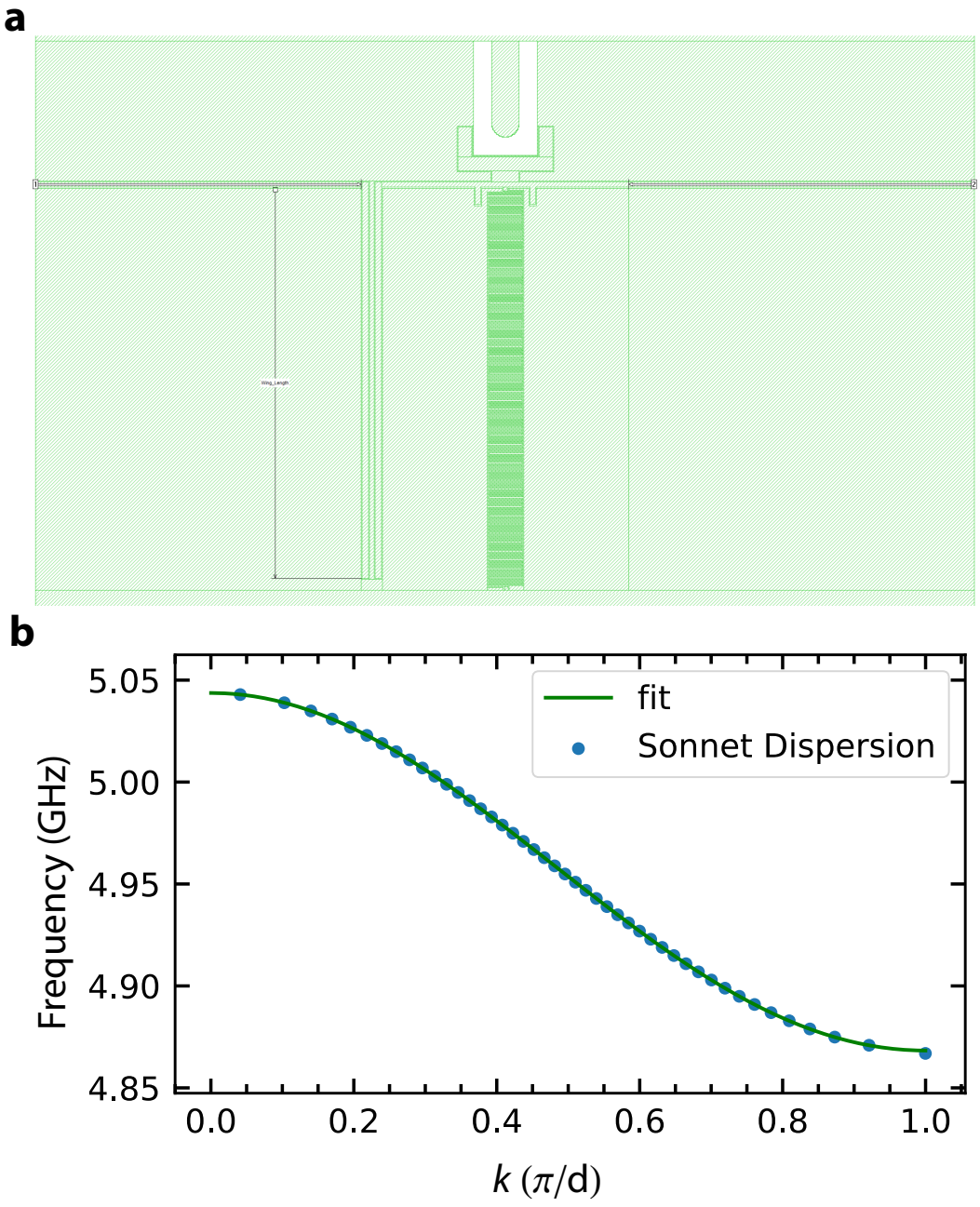

Figure C.2: **Sonnet Unit Cell Simulation.** **a** Illustration of Sonnet simulation for a unit cell of the coupled resonator array. The length of the "wing capacitor" is a simulation geometrical dimension that in practice is varied in order to obtain a desired C_g. Also note that in practice, the box extent is bigger than what is shown here. **b** Plot of the dispersion relation of the unit cell, numerically calculated from the simulation's output scattering parameters. The dispersion relation is fit to Equation 3.8, showing excellent agreement. This fit is used to obtain circuit parameters of the unit cell.

than simulating different components of the unit cell individually. This allowed the simulation to capture the effects of parasitic inductances and capacitances of the different unit cell elements together at once, as well as near-field coupling between the different unit cell elements. This improved the accuracy of the simulation as compared to simulation of the capacitive and inductive elements of the unit cell separately. Moreover, we found that due to these parasitic reactances, simulations at DC frequencies failed to properly capture effective capacitances and inductances at the $\sim$ GHz frequencies of interest; thus we only implemented Sonnet simulations at the frequencies of interest. Further, we found that using ideal lumped element components directly in Sonnet were not accurate due to the details of their implementation (we refer the reader to the Sonnet manual [118] for a detailed discussion of this), and did not use them for the design of the slow-light waveguides.

Thus, for finite-element simulations of our metamaterial waveguide resonators, we will typically employ a simulation similar to what is shown in Figure C.2a. This simulation includes the full meander (which contains the bulk of the inductance) and head capacitance of the unit cell, as well as the coupling capacitance to the previous unit cell. Note that the simulation only contains one “wing capacitor" (from which most of the coupling capacitance between unit cells is derived) such that this “unit cell" can be periodically repeated to yield the full structure. While this simulation does not contain the full capacitance to ground of a single lumped element resonator due to the absence of its other “wing capacitor," this is practically not a problem. In addition, the simulations will have a large simulation “box" compared to the size of the unit cell, such that the effective circuit parameters of the unit cell are not affected by proximity to the simulation box walls. While this necessitates long metal leads from the ports of the simulation to the unit cell circuit, their effect on simulation results can be removed by use of “reference planes" with the ports (we again refer the reader to the Sonnet manual for more details). Furthermore, as discussed in Chapter 3, we note that it was important to have sufficient ground plane surrounding the “wing" coupling capacitors and meanders; otherwise we found that stray capacitance or mutual inductance between neighboring unit cell components were severe enough to thwart simulation of the slow-light waveguide at a single-resonator level.

After obtaining two-port scattering parameters from a simulation such as the one shown in Figure C.2a, we convert the (frequency-dependent) two-port scattering matrix to a (frequency-dependent) $ABCD$ matrix of the unit cell. This allows us

to obtain the effective circuit parameters of the unit cell in the following manner. First, from inspection of Figure C.2b, it is evident that the coupling capacitance of the “wing capacitor" is the only series impedance in the entire planar circuit; everything else can be regarded as a shunt impedance. Due to the absence of any other series impedance, the B matrix element of the $ABCD$ matrix can be shown to directly yield the series impedance, and thus the coupling capacitance C_g, between unit cell resonators [109]. In practice, the extracted coupling capacitance will have some small frequency dependence due to parasitic reactances of the unit cell; thus we typically extract the value at the passband center frequency. Furthermore, from the $ABCD$ matrix we can extract the dispersion relation of the unit cell as discussed in Appendix C.1. By fitting the dispersion relation to Equation 3.8 as shown in Figure C.2b, we can obtain the resonance frequency of the unit cell ω_0 as well as the ratio of C_g/C_0. With these fit parameters and knowledge of C_g, we can obtain the C_0 and L_0 of the unit cell as well. This method is well suited to our needs because these circuit parameters are obtained directly in the context we care about, at the frequencies of interest, via fitting methods that assume a periodic array of the unit cell structure.

For the taper resonators, they will have different coupling geometries to the previous and subsequent resonators, and these different coupling geometries will lead to different contributions to the ground capacitance of the taper resonator. Thus, in order to use the methods above, one must perform a simulation as the one shown in Figure C.2a with each coupling geometry (where the rest of the resonator geometry is maintained the same), and take the average of the obtained C_0 values from both simulations in order to obtain the true C_0.

Furthermore, in order to obtain target circuit parameters, certain geometrical dimensions of the planar circuit will need to be varied (as illustrated in Figure C.2a). We note that in practice, we have typically observed that changes in geometrical dimensions linearly change effective circuit parameters. Thus, by performing two different simulations with two different dimensions, one can approximately learn this linear scaling, and with that, efficiently iterate through simulations to arrive at target circuit parameters.

Finally, once all target circuit parameters have been realized via Sonnet simulations, we found it helpful as a last check to perform simulations of a small coupled resonator array with input/output taper resonators, as shown in Figure C.3. Observing the ripple in the output S_{21} of the simulation allows one to see the effectiveness of the

“taper" matching beyond simulations at the single-resonator level, and if further adjustments to geometrical parameters are necessary. In practice, we typically found that adjusting geometrical parameters for small ripple at the single-resonator level also led to small ripple in the larger simulation of an entire tapered array. However, we found that passband widths of the larger simulation were smaller than predicted passband widths from single-resonator simulations. While mutual inductance between resonators not captured by single resonator simulations could cause this effect, preliminary simulation investigations revealed that the ground connectivity of the lumped element resonators in the structure could have large effects on the passband width as well; further investigations are needed to fully understand this phenomenon. Lastly, the S_{21} of the larger simulation of an entire tapered array would contain resonances outside of the passband that would also be observed in experiment, but were not observed from simulation results of single resonator simulations; preliminary simulation investigation ascribes this effect to the ground connectivity of the structure as well.

In order to extract the capacitive coupling of the qubit to the metamaterial waveguide, we perform the Sonnet simulation illustrated in Figure C.4. We then import the simulation results into Microwave Office, and attach an ideal inductor to port 3 to effectively add inductance to the qubit capacitance island. By using this unit cell/qubit simulation in a “cascaded" simulation of the entire array (with the ideal inductor added), we obtain the simulation of a qubit side-coupled to the metamaterial waveguide. By comparing such a simulation with a similar simulation where the “qubit" is represented by an ideal circuit (with the same lumped element inductance), we can obtain the qubit total capacitance to ground, and its coupling capacitance to the unit cell resonator, by closely matching the two simulation results via modification of the capacitance values of the ideal qubit circuit. Although other methods are in principle possible, this method worked with good accuracy for us.

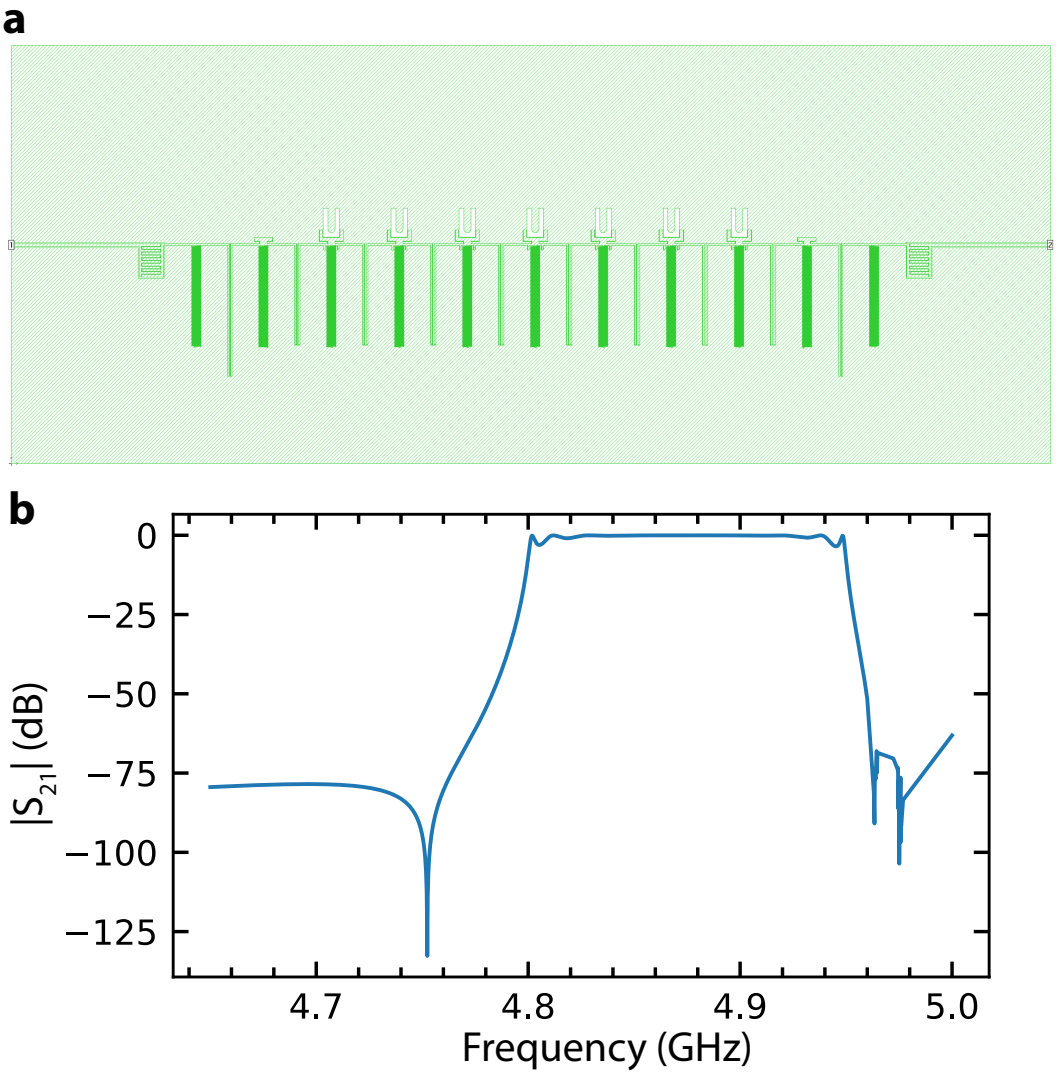

Figure C.3: **Sonnet Simulation of a Full Tapered Array. a** Sonnet Simulation of a Full Tapered Array. Simulations with more resonators require significantly more computational overhead **b** $|S_{21}|$ simulation results.

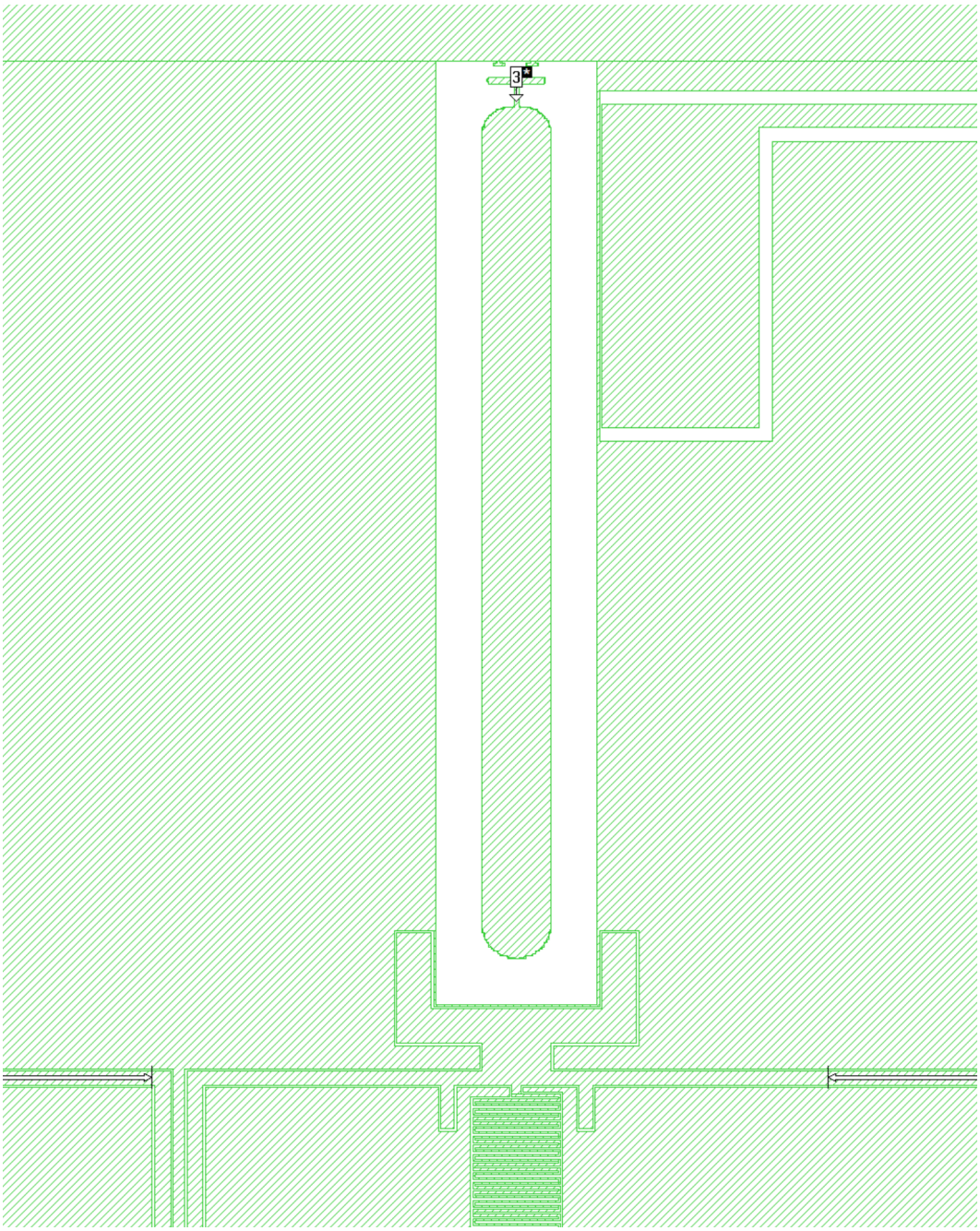

Figure C.4: **Qubit Coupled to Unit Cell Simulation. a** Illustration of Sonnet simulation for a qubit coupled to the unit cell of the coupled resonator array. The full unit cell planar circuit, as well as ports 1 and 2 to the left and right of the unit cell circuit respectively, are not shown in this illustration but are included in the full simulation. Port 3 is used in Microwave Office to connect an ideal lumped element inductor.

Appendix D

SUPPLEMENTARY INFORMATION FOR CHAPTER 4

D.1 Master Equation and Circuit Simulations of Qubit Radiative Dynamics

In this section we present modeling of the interaction between Q_1 and the metamaterial waveguide. Note that, while we observe dynamics that are due to emission and propagation of single-photon radiation field states, which are non-classical states of light, in the single-excitation limit the dynamics of the qubit can also be described by a classical circuit model, where the qubit is represented by a faux resonator. Thus, here we share both viewpoints of analysis, and we employ two separate models to represent our system: a tight-binding model with nearest and next-nearest neighbor coupling which we analyze via a numerical master equation solver, and a classical circuit model (shown in Figure D.2). We find excellent agreement between the two models.

Master Equation Simulations

For our master equation simulations, we employ the model discussed in Appendix B. Referring to Equation B.2 and Figure D.1a, our model assumed the following parameters (2π factors are omitted for readability): $M = 50$, $\delta_1 = \delta_{50} = \delta' = -13.9$ MHz, $\delta_2 = \delta_{24} = \delta_{27} = \delta_{49} = \delta'' - 4.7$ MHz, $\delta_{25} = \delta_{26} = \delta''' = 323$ MHz, $J_1 = J_{24} = J_{26} = J_{49} = J' = 44.1$ MHz, $J_2 = J_{23} = J_{27} = J_{48} = J'' = 32.47$ MHz, $J_{25} = J''' = 349$ MHz, $J_{nnn} = 0.3$ MHz, all other $J_x = J = 32.52$ MHz, all other $\delta_x = 0$, and $\kappa_{50\Omega} = 169.92$ MHz (note that the values of δ''' and J''' are very different from other values in order to accurately capture the circuit of the waveguide's bend section as discussed in Chapter 4). Note that these parameters are consistent with the circuit parameters of the model shown in Figure D.2 that is later discussed. Furthermore, in the model we coupled the qubit to the first, third, and fourth resonators of the array (as opposed to just the third resonator), with couplings $g_1 = 2.2$ MHz, $g_2 = g_{\mathrm{uc}} = 26.4$ MHz, $g_3 = 3.5$ MHz; where all other $g_i = 0$. Physically, the coupling to resonators 1 and 4 was not intentional and was due to parasitic capacitance. We set $g_2 = 0$ in the model because the second metamaterial resonator was not expected to parasitically couple to the qubit as strongly as the first and fourth resonator due to the absence of an interdigitated capacitor or an integrated Xmon shunting capacitance (see Figure 3.3 for images of the second resonator of

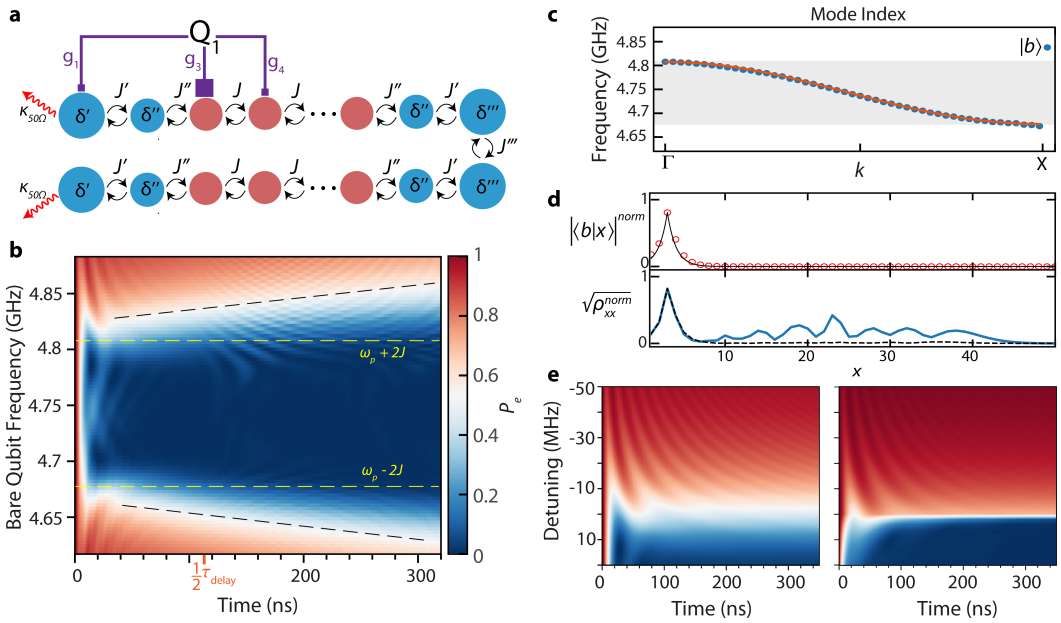

Figure D.1: Master Equation numerical simulations of our qubit-slowlight waveguide system. **a** Diagram of tight-binding model used in simulations. Simulation parameters are described in the text. Note that the next-nearest neighbor coupling J_{nnn}, which is present in the model for all resonators, is omitted from the diagram for readability purposes. **b** Simulation of Figure 4.2b dataset. Bandedges are highlighted in dashed yellow lines, while dashed black lines are guides to the eye. **c** Scatter plot of the eigenenergies of the Hamiltonian in Equation B.2 with $\Delta_{ge}/(2\pi) = 83$ MHz (in the single excitation manifold) offset by ω_p. The orange curve is a plot of the dispersion relation (see Equation E.1). The eigenmode with energy outside of the passband corresponds to the bound state of the system $|b\rangle$ **d** Plot of photonic states of the system as a function of position x. Top panel: plot of the photonic wavefunction of the bound eigenstate of the system $|b\rangle$ in open red dots; "*norm*" indicates that the photonic wavefunction coefficients $\langle x|b\rangle$ are normalized by $\sqrt{\sum_x |\langle x|b\rangle|^2}$, where $|x\rangle$ corresponds to the state $|0_1, 0_2, \ldots, 1_x, \ldots, 0_M; g\rangle$. The solid black line corresponds to a plot of $Ae^{|x-3|/\lambda}$, where $\lambda = \sqrt{J/(E_b - \omega_0)}$ and A is a normalization constant. Bottom panel: plot of the photonic portion of the simulated qubit-waveguide state after $t = 90$ ns. The solid blue line corresponds to a simulation with initial state $|0_1, 0_2, \ldots, 0_M; e\rangle$; the dashed black line corresponds to a simulation with initial state $|b\rangle$. ρ_{xx}^{norm} refers to the scaled density matrix element $\rho_{xx}/\left(\sum_{x=1}^{10} \rho_{xx}\right)$. This particular scaling is chosen because it similarly scales the photonic part of the state within the first 10 resonators of the array, thereby aiding visual comparison between the blue and dashed black curves. **e** Comparison of the dynamics simulated by a modified tight-binding model of a qubit coupled to a metamaterial waveguide (left), and by population equations of motion derived in Ref. [55] (right). Refer to (**b**) for colorbar. Both models assume $g_{\mathrm{uc}}/2\pi = 19$ MHz, as well as $J/2\pi = 33$ MHz. See text for description of modified model. We use $(g_{\mathrm{uc}}^4/4J)^{1/3}$ in place of β for simulations using Equations 2.21—2.28 from Ref. [55].

the metamaterial waveguide). The g_1 and g_4 parasitic couplings were crucial to reproduce some of the subtle features in the measured data; this will be discussed in detail below.

Dynamical Simulations and Eigenenergy Analysis

Figure D.1b shows the simulated dynamics from numerical master equation simulations as a function of Δ_{ge} (note that bare qubit frequency $\omega_p + \Delta_{ge}$ is shown in the plot instead for comparison purposes to Figure 4.2) with initial state $|0_1, 0_2, \ldots, 0_M; e\rangle$. It is evident that there is agreement between Figure D.1b and the measured data in Figure 4.2b, indicating that our model captures the salient dynamical features of our measured data. Furthermore, with the Hamiltonian in Equation B.2, we can numerically calculate its eigenstates and the eigenenergy spectrum; as an example, the spectrum when $\Delta_{ge}/(2\pi) = 83$ MHz is plotted in Figure D.1c. Figure D.1c shows a band of states within the passband, and a state with energy outside of the passband. Because $M = 50$, the Hamiltonian is that of a finite-sized system and the band of states within the passband represents the normal modes of the finite waveguide structure; however, in the presence of input/output waveguides they represent a band of scattering states that support wave propagation between the input/output waveguides. The state with energy outside of the band, however, is the bound eigenstate $|b\rangle$. We calculate bound-state energies as a function of bare qubit frequency Δ_{ge}, and converting bare qubit frequency to the physically applied flux through the SQUID loop used to tune the qubit frequency Φ (via measured qubit minimum/maximum frequencies and the extracted anharmonicity), we numerically obtain the predicted energy of the system's bound eigenstates as a function of flux bias and plot it on Figure 4.1d as dashed black lines. As Figure 4.1d shows, we obtain good quantitative agreement between the prediction of our model and the spectroscopically measured bound-state energies of the qubit-waveguide system.

In our model, the g_3 coupling primarily sets the coupling of the qubit to the metamaterial waveguide. Its magnitude relative to the J between the unit cells, along with the qubit frequency $\omega'_{ge}(\Phi)$, predominantly determines the frequency of oscillations near the bandedge, as well as the decay rate into the waveguide in the passband. In the absence of other parasitic couplings, this decay rate is theoretically determined to be $\sim g_{\mathrm{uc}}^2/v(\omega'_{ge}(\Phi))$ [78], where $v(\omega'_{ge}(\Phi))$ is the group velocity of the metamaterial waveguide at the qubit-waveguide interaction frequency $\omega'_{ge}(\Phi)$. The parasitic coupling g_4, however, is necessary to replicate the asymmetry in the dynamics near the upper and lower bandedges. This is because the lower bandedge modes have an oscillating charge distribution between unit cells, while the upper bandedge modes have a slowly-varying charge distribution across the unit cells (which is typical of 1D tight-binding systems). The parasitic coupling of the qubit to the neighboring

unit cell therefore has the effect of lowering the qubit coupling to the lower bandedge modes due to cancellation effects arising from the opposite charges on neighbouring resonators for lower bandedge modes. On the other hand, coupling of the qubit to the upper bandedge modes which have slowly-varying charge distributions, is enhanced.

In addition, in simulations, the onset of oscillations seen at $\tau \approx 115$ ns could be delayed or advanced by increasing or decreasing the number of resonators in between the qubit and the bend in the metamaterial waveguide model, while it could be removed altogether by removing the bend section. This indicated that these late-time oscillations are a result of spurious reflection of the qubit's emission at the bend, due to the imperfect matching to the 50-Ω coplanar waveguide in between the two resonator rows (which is manifested in this model through parameters δ''' and J'''). Note that this impedance mismatch and reflections are amplified near the bandedges, where the Bloch impedance rapidly changes.

Photonic State Spatial Analysis

In Chapter 4, the observed qubit emission dynamics into the slow-light waveguide are described in terms of the interplay of the qubit-waveguide dressed states; in particular, the bound and continuum dressed states of the qubit-waveguide system. Here we further elucidate this description of our system via our modeling, using the dynamics of the system when the qubit is tuned 18 MHz above the upper bandedge ($\Delta_{ge}/(2\pi) = 83$ MHz) as an illustrative example, corresponding to the brown curve in Figure 4.2c.

Firstly, in Chapter 4 we assert that initializing the qubit in state $|e\rangle$ with its frequency in the proximity of the passband effectively initializes it into a superposition of bound and continuum dressed states. This can be explicitly verified by first numerically calculating the eigenstates and the eigenenergy spectrum of the Hamiltonian, as was done for Figure D.1c. As previously discussed, the state with energy outside of the band is the bound eigenstate $|b\rangle$, and the photonic component of its wavefunction is plotted in the top panel of Figure D.1d. It is evident from Figure D.1d that the photonic component of the bound state wavefuncion is localized around resonator 3, which is the unit cell that the qubit is predominantly coupled to. As discussed in Section 3.2, the bound state is exponentially localized with localization length approximately $\lambda = \sqrt{J/(E_b - \omega_0)}$ where E_b is the energy of the bound state; this theoretical photonic wavefunction is plotted in the top panel of

Figure D.1d with a solid black line, and shows good agreement with the numerically calculated $|b\rangle$ wavefunction plotted in red open dots. Numerically calculating the overlap between the $|0_1, 0_2, 0_3, ..., 0_M, e\rangle$ state and the bound eigenstate yields $|\langle b|0_1, 0_2, 0_3, ..., 0_M, e\rangle|^2 \approx 0.8$, agreeing well with Equation 3.22.

Secondly, in Chapter 4 we also assert that the amplitude of the early-time oscillations quickly dampen away as the energy in the radiative continuum dressed state is quickly lost into the waveguide, while the energy in the bound state remains localized around the qubit, albeit slowly decaying (details of this slow decay are given in the next paragraph). In order to illustrate this point, in the bottom panel of Figure D.1d we plot the photonic portion of the system's state at time $t = 90$ ns, at which point the early-time oscillations have subsided and the qubit can be observed to be slowly decaying. It is evident that while part of the state is delocalized in the array, a significant portion is still localized around the qubit location; this portion corresponds to the bound state portion of the initial state $|0_1, 0_2, 0_3, ..., 0_M, e\rangle$ after time evolution.

Thirdly, in order to understand the slow decay of the qubit following the early-time oscillations, note that a non-negligible proportion of the bound state wavefunction is found on resonator 1, the taper resonator directly coupled to output waveguide, signifying finite overlap between the bound state and the external 50-Ω environment of the output waveguide. This overlap constitutes the dominant intrinsic loss channel for the bound state and leads to its slow decay, which in the $t \rightarrow \infty$ limit results in the full decay of qubit even if its frequency is tuned outside the passband. Near the bandedges, it is this loss that results in a slow population decay as compared to the initial fast dynamics in the data (see top panel of Figure 4.2c for a clear example), and leads to the feature highlighted by dashed black lines in Figure D.1b. This feature would be flat for an infinite-sized resonator array and there would be partial "population trapping" [58] of the qubit in the $t \rightarrow \infty$ limit if its bare frequency was detuned from the passband and there were no other intrinsic loss channels. Note that the g_1 coupling between the qubit and the resonator directly coupled to the 50-Ω port is necessary to quantitatively replicate the slow decay rates of the qubit when its frequency is outside of the passband. In the absence of the g_1 coupling, this overlap was not sufficiently high in the simulations given the coupling of the qubit to the metamaterial waveguide (extracted from separate measurements in the passband). Therefore, this overlap was made larger, while minimizing the increase to the overall coupling of the qubit to the metamaterial waveguide, by incorporating

the small g_1 coupling to the first resonator of the array.

Finally, it can be observed in Figure 4.2b and Figure D.1 that there are differences in both duration and amplitude between the early-time oscillations and the late-time oscillations that occur at $\tau \approx 115$ ns. This is because, when the qubit frequency is near the bandedges, the reflected emission is distorted through its propagation in the metamaterial waveguide due to the significant dispersion near the bandedges. This results in a spatio-temporal broadening of the emitted radiation, which is evident in the bottom panel of Figure D.1d. The frequencies of both sets of oscillations, however, are set by g_{uc} and J as discussed in Chapter 4.

Comparison to Paradigmatic Model of Spontaneous Emission Near the Edge of a Photonic Bandgap

As alluded to in Chapter 4, the early-time oscillations observed in our work are, qualitatively, a generic feature of the interaction between a qubit and a bandedge in a dispersive medium, and not merely an attribute of our specific system. In order to illustrate this point, in Figure D.1e, we further compared the initial oscillations to the theory presented by John and Quang in Ref. [55] of a qubit whose frequency lies in the spectral vicinity of a bandedge. The model assumed for Ref. [55] was that of an atom (qubit) with point dipole coupling to an infinite periodic dielectric environment, whose frequency is in the spectral vicinity of only a single bandedge. Thus, in order to make a comparison to this theory, we changed the model of our system described by Equation B.2 and Figure D.1a in the following manner: (i) we removed the parasitic couplings of the qubit to neighboring unit cells, in order to simplify the coupling to a single-point coupling, (ii) we increased the size of the array and moved the qubit to the middle in order to remove boundary effects from the dynamics, (iii) we reduced the overall coupling of the qubit to the metamaterial waveguide so it predominantly couples to only the bandedge it is least detuned from. Note, however, that the dispersion relation of the waveguide is different than the dispersion assumed in Ref. [55]. Nonetheless, above the bandedge, we see good qualitative agreement between the dynamics modeled both by the modified model and the population equation of motion derived in Ref. [55] (in particular, equation 2.21), with both simulations exhibiting very similar oscillatory decay to what is observed in Figure D.1b and 4.2b. This further confirms our interpretation of the early-time non-Markovian dynamics in Figure 4.2 discussed in Chapter 4: that the non-exponential oscillatory decay is due to the interaction between the qubit and the

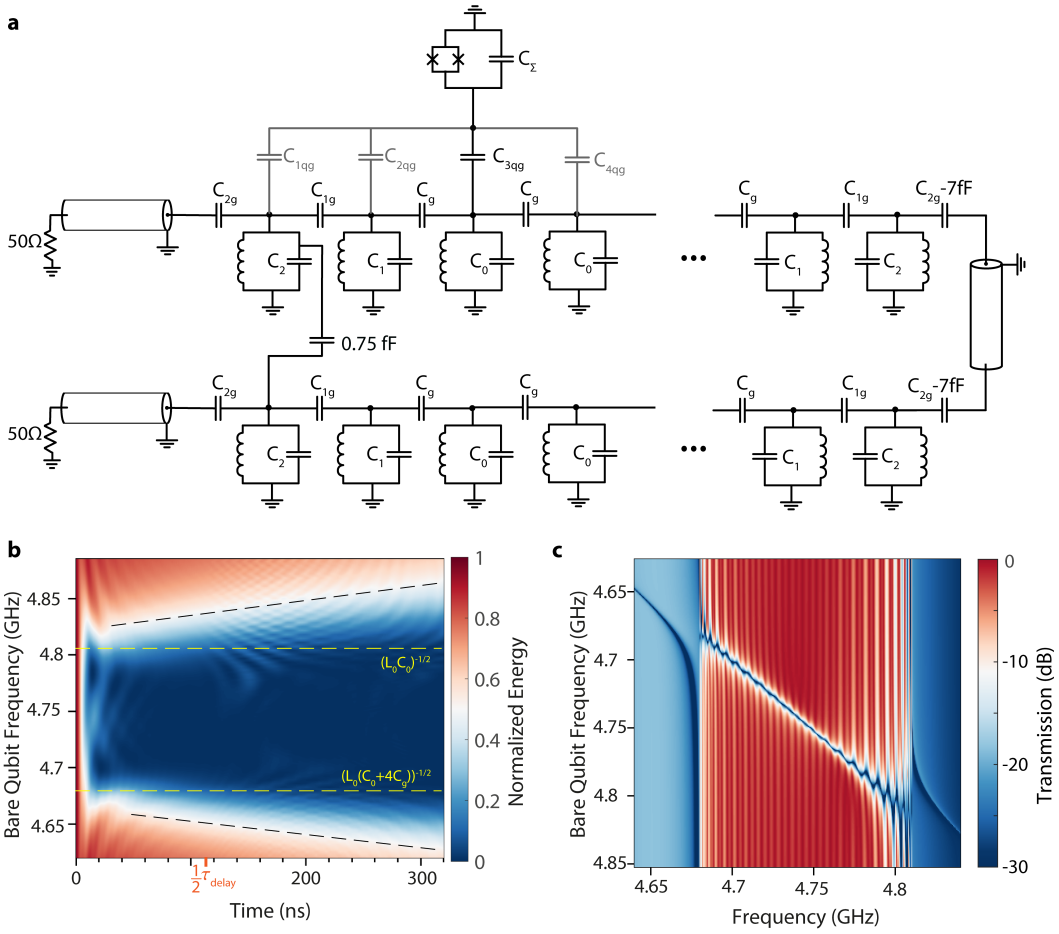

Figure D.2: **a** Full circuit model used in simulations. All inductors were made equivalent, with inductance L_0. Parameters are further discussed in the text. **b** Simulation of Figure 4.2b dataset. Intensity plot is of energy in the faux-qubit resonator normalized by the initial energy; this simulated time-dependent normalized energy corresponds directly to the qubit's excited-state population measurements of Figure 4.2b. Simulation parameters are described in the text. Bandedges are highlighted in dashed yellow lines, while dashed black lines are guides to the eye. **c** Simulation of Figure 4.1d dataset. Circuit model and simulation parameters are described in the text. Simulations were done with the aid of the Microwave Office software package.

strong spike in the density of states at the bandedge.

D.2 Circuit Simulations

In addition to dynamical master equation simulations, we also performed modeling via classical circuit analysis, where the qubit is represented by a linear resonator; this is an accurate representation of the qubit-waveguide system in the single-excitation limit. Time-resolved dynamical simulations were performed with the LTSpice numerical circuit simulation package, while frequency response simulations were performed with Microwave Office and standard circuit analysis. Our model, shown in Figure D.2, assumes the following metamaterial waveguide parameters: $C_{2g} =$

92.5 fF, C_{1g} = 7.8 fF, C_g = 5.02 fF, C_2 = 273 fF, C_1 = 351.2 fF, C_0 = 353.2 fF, and L_0 = 3.099 nH, which were obtained from fitting the transmission through the metamaterial device shown in Figure 4.1a with the qubit detuned away (600 MHz) from the upper bandedge. While in principle there are three independent parameters for every resonator (capacitance to ground, coupling capacitance, and inductance to ground), the set of metamaterial parameters above in addition to the qubit parameters were sufficient to achieve quantitative agreement between simulations and our data.

Our model utilizes a qubit capacitance (excluding the capacitance to the metamaterial waveguide) of C_Σ = 77.8 fF, which, when assuming $E_c \approx -\hbar\eta$, is consistent with measurements of the anharmonicity that was extracted by probing the two-photon transition between the $|g\rangle$ and $|f\rangle$ states. Furthermore, in the model we coupled the qubit to the first, third, and fourth resonators of the array, with capacitive couplings C_{1qg} = 0.16 fF, C_{3qg} = 1.9 fF, and C_{4qg} = 0.25 fF, while C_{2qg} = 0 fF, for reproducing both the dominant and the subtle features in the measured data due to the same reasons described in the preceding discussion.

Time Domain

Figure D.2b shows the simulated dynamics of our circuit model as a function of bare qubit frequency (where the qubit inductance was swept to change the bare qubit frequency). It is evident that there is agreement between Figure D.2b and the measured data in Figure 4.2b, indicating that our circuit model captures the salient dynamical features of our measured data. Moreover, we find excellent agreement between our circuit model and the tight-binding model presented in the preceding discussion, which was expected given that the parameters of the circuit model map nearly directly to the parameters of the tight-binding model. Thus, both models are appropriate for analyzing the data of Figure 4.2, and the insights into the system gained from the tight-binding model in the preceding discussion directly carry over to this circuit model.

Frequency Domain

In addition to time-domain simulations of our circuit model representing the fabricated qubit-waveguide system, in Figure D.2c we plot an intensity color plot of the transmission through the slow-light waveguide as the bare qubit frequency is tuned across the passband using the circuit model (c.f., the corresponding measurement data plotted in Figure 4.1d). Note that in order to capture the background transmission levels as well as the interaction of the qubit with the background transmission,

we included a small direct coupling capacitance of 0.75 fF between the first and last resonators of the array. These two resonators have the largest crosstalk. This is due to the large portion of charge contained in the interdigitated capacitors between the resonators and the input-output waveguides. In simulations without this background transmission, the qubit mode break-up near the bandedge and signatures of the bound-state outside of the passband were significantly weaker.

In addition, the series capacitance of the boundary resonators coupled to the input-output waveguides was made 7 fF higher than the series capacitance of the boundary resonators coupled to the short CPW section in the bend, which is due to the proximity of the large bondpads used to probe the waveguides. Our simulations are in excellent qualitative agreement with the data presented in Figure 4.1d. They also capture the spectroscopic non-Markovian features of our data — the repulsion of the bound state's energy from the bandedge and the persistence of the bound state even when the bare qubit frequency overlaps with the passband (see Refs. [78, 102, 103] for further details).

D.3 Modeling of Qubit Coupled to Dispersion-less Waveguide in Front of a Mirror

In this section we present modeling of the time-delayed feedback phenomenon described in the Chapter 4. Here, we employ a dispersion-less waveguide in our model instead of our slow-light waveguide in order to compare our data to the dynamics of an ideal scenario where pulse distortion and propagation losses are absent. We employ a dispersion-less waveguide with equivalent round-trip delay of = 227 ns to the slow-light waveguide. The theoretical model we use is described at length in Ref. [131]; below we briefly summarize the derivation of the model found in this reference.

Ref. [131] starts with the following Hamiltonian, where the coupling to different waveguide modes is now allowed to vary as a function of k,

$$\hat{H} = \omega_{ge} \left|e\right\rangle \left\langle e\right| + \int dk \omega_k \hat{a}_k^\dagger \hat{a}_k + \int dk g_k \left(\hat{a}_k^\dagger \hat{\sigma}^- + \hat{a}_k \hat{\sigma}^+\right), \tag{D.1}$$

and the same single-excitation ansatz of Equation 3.14, but with time-dependent coefficients $c_e(t)$ and $c_k(t)$ (and where a continuum of modes is already assumed). Following similar analysis to section 3.2, Equations D.1 and 3.14 are substituted into the time-dependent Schrödinger equation $\partial_t \left|\psi(t)\right\rangle = -i\hat{H}\left|\psi(t)\right\rangle$, and after

collecting terms and going into the rotating frame of the qubit, the authors arrive at the following system of coupled differential equations:

$$\dot{c_e}(t) = -i \int dk g_k c_k(t), \tag{D.2}$$

$$\dot{c_k}(t) = -i\Delta_k c_k(t) - i g_k c_e(t), \tag{D.3}$$

where $\Delta_k = \omega_{ge} - \omega_k$. The authors then explicitly integrate Equation D.3 to obtain a solution for $c_k(t)$, and substitute that solution into Equation D.2. In order to evaluate the resultant equation of motion for $c_e(t)$, the authors make the following assumptions: (i) they assume the dispersion is linearized around the qubit frequency such that $\omega_k = \omega_{ge} + v(k - k_0)$, where v is the group velocity, and (ii) $g_k = \sqrt{\Gamma_{1D} v/\pi} \sin k x_0$, where x_0 is the qubit position in the waveguide. The particular form of g_k is chosen by asserting that the field assumes a $\sin kx$ spatial profile such that the field fulfills the boundary condition of being zero at the waveguide termination; thus the field strength at the qubit is $\sin k x_0$. With these expressions for ω_k and g_k, the resultant equation of motion for $c_e(t)$ can be simplified to the following form

$$\dot{c_e}(t) = -\frac{\Gamma_{1D}}{2} c_e(t) + \frac{\Gamma_{1D}}{2} e^{i2k_0 x_0} c_e(t-)\theta(t-), \tag{D.4}$$

where τ_d is the round-trip delay and θ is the heavyside step function; the first term on the right-hand side is responsible for the decay of the qubit, while the second term is responsible for photon re-absorption. Equation D.4 is finally solved via methods described in Ref. [215], yielding the following analytic expression for the dynamics of a qubit excited-state population when coupled to a semi-infinite dispersion-less waveguide:

$$c_e(t) = e^{\Gamma_{1D} t/2} \sum_n \frac{1}{n!} \left(\frac{\Gamma_{1D}}{2} e^{i\phi + \Gamma_{1D}/2} \right)^n \times (t-n)^n \theta(t-n), \tag{D.5}$$

where $\phi = 2k_0 x_0$ is the round-trip phase gained by the propagating emitted pulse.

Substituting $\Gamma_{1D}/(2\pi) = 21$ MHz and $= 227$ ns into Equation D.5, we obtain the magenta curve plotted in Figure 4.3b. As discussed in Chapter 4, our measured dynamics compare favorably to the ideal scenario of no dispersion-induced distortion of the traveling emitted pulse, as well as no propagation losses, captured by the model

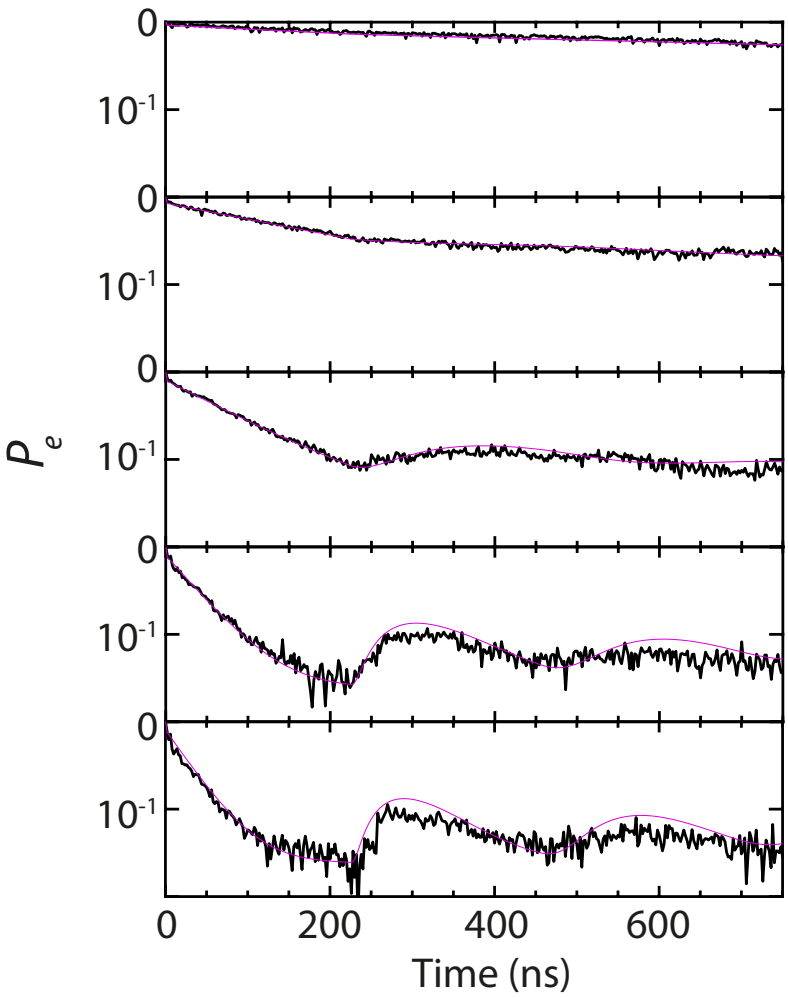

Figure D.3: Replots of the five (white) line cuts of Figure 4.3c, with accompanying theoretical predictions for emission of a qubit into a dispersionless, lossless semi-infinite waveguide. In the theoretical model, was maintained fixed for all simulations, while the qubit emission rate Γ_{1D} and round-trip phase ϕ were allowed to vary as fit parameters to capture the effects of the changing flux-modulation amplitude, which not only changes Γ_{1D} but also causes a residual DC-shift of the average qubit frequency [159], which in turn affects ϕ. Moreover, a thermal qubit population of 2.4% was assumed. From top panel to bottom panel, the fit parameters Γ_{1D} and ϕ are, respectively: $\Gamma_{1D}/2\pi = 0.17$ MHz, $\phi = \pi/2.6$; $\Gamma_{1D}/2\pi = 0.6$ MHz, $\phi = \pi/2.6$; $\Gamma_{1D}/2\pi = 1.8$ MHz, $\phi = \pi/2.1$; $\Gamma_{1D}/2\pi = 5$ MHz, $\phi = \pi/2.6$. Note that the parameter ϕ has negligible effect for dynamics involving large Γ_{1D} where revival events are clearly discernible, and for dynamics involving small Γ_{1D}, ϕ simply modulates the emission rate . However, for intermediate Γ_{1D} such as $\Gamma_{1D}/2\pi = 0.6$ MHz, 1.8 MHz, the shapes of the population dynamics curves are sensitive to ϕ.

discussed above. Thus, the limited recurrence observed can be mostly attributed to emission into the open end of the waveguide, as well as inefficient re-absorption of the emitted wavepacket due to its exponential shape.

In addition, in Figure D.3 we have also plotted similar comparisons between this ideal model of the observed time-delayed feedback phenomenon, and the data shown in

Figure 4.3c. For this comparison, we choose to plot the five line cuts plotted in white in Figure 4.3c, along with comparisons to the theoretical model. The agreement between the two for all five curves is similar to the agreement observed in Figure 4.3b. Quantification of the non-Markovianity of the discussed model under various parameters is presented in Ref. [89]; however, as the reference notes, there are many competing manners to quantify non-Markovianity.

Appendix E

SUPPLEMENTARY INFORMATION FOR CHAPTER 5 - DEVICE CHARACTERIZATION, MODELING, AND CONTROL METHODS

E.1 Device Characterization

Slow-Light Waveguide

As discussed in the 2D cluster state generation protocol proposed in ref [60], one of the dimensions of the resultant cluster state is limited by the number of photons that can be held in the delay line simultaneously, necessitating a delay line with a sufficiently large round trip time τ_d. In this work, we realize such a delay line via implementation of a slow-light waveguide (SLWG), which provides large group delay for time-delayed feedback. In addition, the SLWG also provides spectral constriction of propagating modes to a passband with a finite bandwidth, where the photonic density of states (DOS) sharply decreases at the bandedges and is negligible outside the passband, thus enabling selective emission of the Q_E's $|f\rangle \rightarrow$

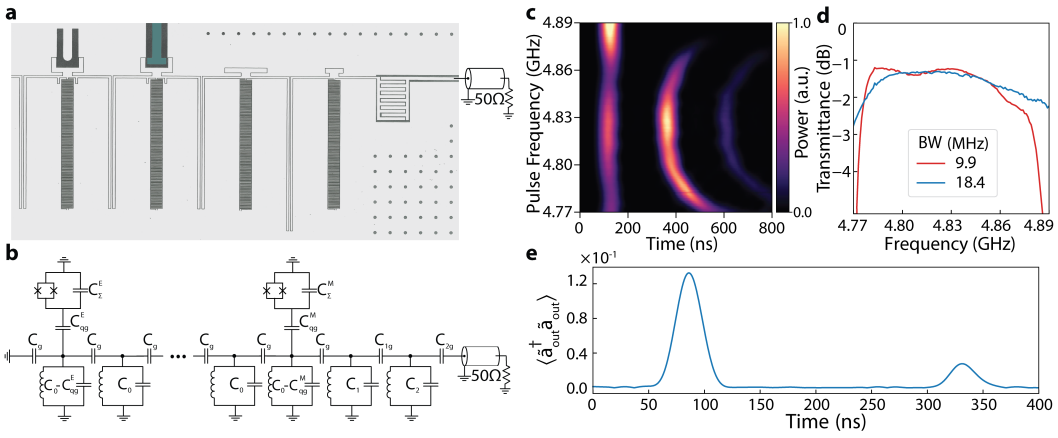

Figure E.1: **Single-Ended Coupled Resonator Array Slow-Light Waveguide Characterization.** **a** False-colored optical image of the end of the slow-light waveguide that is connected to the CPW output waveguide, including the "tapered" boundary matching circuit consisting of the last two resonators. The mirror qubit shunt capacitance is false colored in green. **b** Full circuit model of the slow-light waveguide and coupled qubits. **c** Transient response of slow-light waveguide with narrow-band input pulses of frequencies near around the passband. See Appendix text for further details. **d** Transmittance of the tapered end of slow-light waveguide, calculated from the data in subfigure **c** and a separate measurement of round-trip loss. **e** Photon flux of emitter qubit emission, measured for 400 ns. After one round-trip delay of the slow-light waveguide, the initially non-transmitted portion of the qubit's emitted pulse can be observed.

$|e\rangle$ transition, as discussed in Chapter 5. The SLWG is physically realized as a periodic array of capacitively coupled lumped-element superconducting microwave resonators, with low resonator loss and negligible resonator frequency disorder, as was demonstrated in our prior work [185].

The SLWG is implemented by periodically placing $N = 50$ unit cells across the device as seen in Figure5.1b. At the output side of the SLWG, the Bloch impedance of the SLWG is matched to its output 50 Ω CPW via a “taper section" comprised of two lumped element resonators. Crucially, in order to prevent distortion of Q_E photon emission, at the terminated side of the single-ended SLWG a capacitance to ground via a long capacitive wing is placed at the left of the first unit cell resonator (Figure5.1**c**), thus maintaining the resonance frequency of the first resonator to be the same as the frequency of the other resonators, which ensures monotonic emission from Q_E (as observed in separate modeling).

The corresponding circuit model of the SLWG waveguide coupled to Q_E and Q_M is depicted in Figure E.1b. In the regime of $C_g \ll C_0$, the dispersion of the SLWG is approximately

$$\omega_k = \omega_p + 2J\cos(k), \tag{E.1}$$

where $\omega_0 = 1/\sqrt{L_0 C_0}$ is the resonance frequency of unit cell resonators, $J = \omega_0 \frac{C_g}{2C_0}$, $\omega_p = \omega_0 - 2J$ is the center frequency of the passband, and the passband width is $4J$. To mitigate the deleterious effects in the time-domain shape of emitted photons emerging from the higher-order dispersion [216], a sufficiently large J is required. On the other hand, our requirement for large group delay $\tau_d = \frac{N}{J}$ necessitates a sufficiently small J. In order to balance the conflicting requirements of large delay and manageable dispersion, we chose $J = 33.5$ MHz as a target parameter that corresponds to the round-trip delay of $\tau_d = 237$ ns.

We thus aimed for the following target circuit parameters: $L_0 = 3.1$ nH, $C_0 = 353$ fF, $C_g = 5.05$ fF, $C_1 = 347$ fF, $C_{1g} = 8.6$ fF, $C_2 = 267$ fF, and $C_{2g} = 87$ fF, yielding $J/2\pi = 33.5$ MHz, $\omega_p/2\pi = 4.744$ GHz, and the requisite impedance matching at the boundary. As seen in FigureE.1a, in the taper section the increased coupling capacitances are implemented as longer capacitive wings or interdigitated capacitors, and adjustments to the resonance frequencies are achieved by both shortening the length of the meandered lines and modifying the head capacitances. In addition, the coupling capacitances of Q_E and Q_M to their respective unit cells, as depicted

in Figure5.1c and FigureE.1a, were designed to be 2.41 fF and 5.37 fF, respectively. This yields the qubit-unit cell coupling $g_{uc} = 38.5$ MHz of Q_E and $g_{uc}^M = 85.6$ MHz of Q_M via the following relation:

$$g_{uc} = \frac{C_{qg}^E}{2\sqrt{(C_0 + 2C_g)(C_\Sigma^E + C_{qg}^E)}}\omega_p, \tag{E.2}$$

where g_{uc}^M is obtained by a similar calculation. As discussed in the next subsection of the appendix, these small coupling capacitances lead to large emission rates due to the slow-light nature of the SLWG, where a small group velocity $v_g = \frac{\partial\omega}{\partial k}$ is commensurate with a large density of states $\sim 1/|v_g|$, which enhances emission rates. [78, 217]

In order to characterize the SLWG, we investigated the transmittance of the SLWG boundary for an itinerant pulse by sending coherent Gaussian pulses of variable carrier frequency through the SLWG IN line and measuring their outgoing intensity at ADC PHOTON after they pass through the device. The measurement result, comprising distinct features separated in time that correspond to different reflection events, is shown in E.1c. First, when the pulses arrive at the SLWG boundary, due to the finite reflectance of the taper section, a fraction of the incident pulse is reflected (and thus does not enter the SLWG) and is measured as the first bright feature in FigureE.1c. Next, the transmitted fraction of the pulse propagates through the SLWG, completes a round-trip, and arrives at the SLWG boundary again. While a small fraction of the pulse is again reflected due to finite reflectance, most of the energy transmits through the boundary to constitute the second bright feature in FigureE.1c. Finally, this reflected fraction of the pulse completes a second round-trip, and is found as the last bright feature of in FigureE.1c. Note that this process continues with more round-trips, while the measured data up to the second round-trip is used for analysis.

We estimated the transmittance T of the SLWG boundary via comparing the energy contained in the second bright feature E_2 and the energy contained in the last bright feature E_3, where we define the energy of the "feature" $E = \int |\langle V(t)\rangle|^2 dt$, where $V(t)$ is the measured voltage at the ADC for a particular "feature." As discussed, the pulse corresponding to the last bright feature undergoes an additional incidence at the SLWG boundary and an additional round-trip in the SLWG relative to the pulse corresponding to the second bright feature. Thus, we can compare their energies via the following relation:

$$E_3 = R(1 - L)E_2, \tag{E.3}$$

where $R = 1 - T$ is the reflectance of the boundary, and L is the photon loss during a round trip. By using $L \approx 0.13$, which is obtained from the measurement of Figure 5.3, we estimate transmittance $T \approx -1.2$ dB at the center of the SLWG passband. The transmittance, shown in FigureE.1d, is measured for two different bandwidths of the incident Gaussian pulses, such that the slow pulses (red curve) have approximately the same bandwidth as photon 1 of the generated cluster state (see Figure 5.5) and the fast pulses (blue curve) have approximately the same bandwidth as photon 2—4 of the generated cluster state. The difference of the transmittance between the two cases demonstrates the necessity of adjustment of the power calibration scaling factor G of the output chain according to the bandwidth of the photons (see Appendix F.1 for further details). Note that we measured T via the transient response of the SLWG because the transient response more directly captured the SLWG transmissivity for broadband itinerant signals, as well as because the transient response is less susceptible than the steady-state response to the compounding effects of multiple reflection events due to all impedance mismatches at the output of the SLWG and throughout the OUT line.

Additionally, we directly investigated the effect of reflection at the SLWG boundary on photon pulses emitted from the Q_E. For this measurement, shown in Figure E.1e, a photon pulse with bandwidth of 9.8 MHz is emitted from Q_E prepared in the $|f\rangle$ state via shaped emission. This photon first propagates through the SLWG and is partially transmitted at the tapered boundary due to the finite transmissivity of the taper with transmittance T; this transmitted fraction then arrives at the ADC and the photon flux is measured. Meanwhile, the reflected fraction of the photon undergoes an additional round-trip in the SWLG, and thus arrives at the ADC time $t = \tau_\mathrm{d}$ later, as seen in Figure E.1e. If this returning portion of the photon field interacts with the qubit during subsequent photon emissions, it can lead to qubit control errors as well as an overlap of our desired photon signal with this spurious reflected signal, which leads to measurement errors. Thus, when generating the four-photon 2D cluster state presented in Figure 5.5, and the 5-photon state presented in Figure F.4, we had to ensure that photon emission did not overlap with the returning reflected portion of previously emitted pulses. Thus, for photons emitted after $t = \tau_\mathrm{d}$ into the generation sequence, their emission time was judiciously chosen to avoid this overlap. This is why there is a gap in time between the measured photon flux of photon 1 and photon 4 in Figure 5.5c.

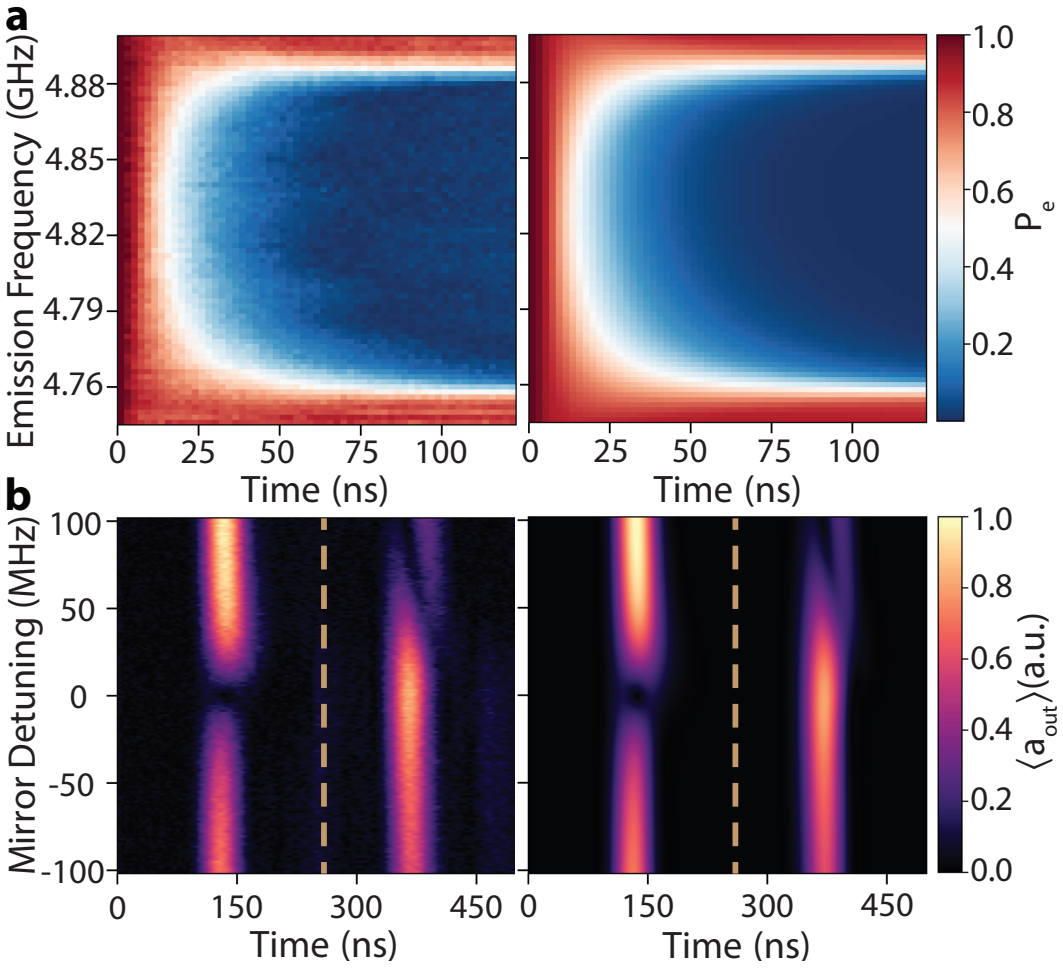

Figure E.2: **Emitter and Mirror Qubit Characterization.** **a** Left: measured emission dynamics of Q_E prepared in $|e\rangle$, where emission to the ground state is induced via flux modulation with $\omega_{\text{mod}} = 450$ MHz. Right: fit to tight-binding model of equation (add eq ref). The fit yields SLWG center frequency of $\omega_p = 4.823$ GHz, Q_E to first unit cell coupling of $g_{uc}/2\pi = 35.16$ MHz, Q_E to second unit cell coupling of $g_{nuc}/2\pi = 2.27$ MHz, and unit cell to unit cell coupling $J/2\pi = 33.96$ MHz. **b** Left: measured averaged field of Q_E emission with different mirror detuning from the center of the passband; right: fit to single-excitation Hamiltonian yielding an effective mirror qubit to unit cell coupling of $g_{uc}^{M}/2\pi = 57$ MHz. In both cases, the mirror is detuned away from the passband after the time indicated by the dashed yellow line.

Qubits

To characterize the system consisting of Q_E and Q_M coupled to our SLWG, we performed multiple dynamical measurements. The central parameters of the system Hamiltonian, ω_p, J, g_{uc}, and g_{uc}^M were obtained via fitting the results from these measurements to the expected results from a time-domain simulation of a model Hamiltonian. In the following paragraphs, we discuss how we performed the measurements, and the simulation methods.

In order to investigate the interaction between Q_E and the SLWG, we measured the decay dynamics of Q_E prepared in $|e\rangle$ interacting with the SLWG, as found in FigureE.2a (left). First, Q_E is prepared in the first excited state $|e\rangle_E$, following which flux modulation of Q_E's transition frequency induces an interaction between a sideband of Q_E and the SLWG. This interaction time (during which the flux modulation is on) is varied, and the sideband frequency is swept across the passband, as indicated on the x- and y-axis of FigureE.2a, respectively. Finally, the interaction is deactivated by turning off the flux modulation, followed by readout of Q_E to measure the remaining population in $|e\rangle_E$. In this experiment, the flux modulation altered the effective qubit-unit cell coupling rate $g_{uc}^{\text{eff}} = \xi g_{uc}$, where ξ is the sideband amplitude. We implemented $\xi = 0.22$ (see Appendix E.2 for details on flux modulation) in order to slow down Q_E's intrinsic emission rate, such that we were able to perform time-resolved measurements of Q_E's dynamics without being restricted by the limited sampling rate of our instruments. However, the resulting decay rate is sufficiently strong such that the population in $|e_E\rangle$ completely decays to ground state when the sideband is resonant with the passband of the SLWG, as seen in FigureE.2a.

The measured decay dynamics are fit to the following tight-binding interaction picture Hamiltonian (a specific instance of the model described in Appendix B):

$$\begin{aligned}\hat{H}^E = &(\omega_1^E - \omega_p)\,|e\rangle\,\langle e|_E + g_{uc}^{\text{eff}}(\hat{\sigma}_+^E \hat{a}_1 + \hat{\sigma}_-^E \hat{a}_1^\dagger) \\ &+ g_{nuc}^{\text{eff}}(\hat{\sigma}_+^E \hat{a}_2 + \hat{\sigma}_-^E \hat{a}_2^\dagger) + J\sum_{x=1}^{50}(\hat{a}_x^\dagger \hat{a}_{x+1} + \hat{a}_x \hat{a}_{x+1}^\dagger),\end{aligned} \tag{E.4}$$

where ω_1^E is the frequency of the sideband Q_E that is resonant with the SLWG, $\hat{\sigma}_+^E$, $\hat{\sigma}_-^E$ are the raising and lowering operators of Q_E, $\hat{a}_x^\dagger$, $\hat{a}_x$ are the raising and lowering operators of the unit cell resonator at position x, g_{nuc} is the parasitic coupling rate of Q_E to the second unit cell resonator, and $\xi = 0.22$ is the sideband amplitude that

renormalizes the following coupling rates to $g_{uc}^{\text{eff}} = \xi g_{uc}$ and $g_{nuc}^{\text{eff}} = \xi g_{nuc}$. Note that g_{nuc}^{eff} accounts for the asymmetry of the decay dynamics at frequencies near the upper bandedge and the lower bandedge of the SLWG that is observed in the data, as discussed in [185]. Also note that the interaction time of Q_E with the SLWG is shorter than τ_{d}, and thus the Hamiltonian terms involving the boundary taper resonators of the SLWG and Q_M can be neglected in this model.

With this Hamiltonian, we simulated the decay dynamics of Q_E initially prepared in $|e\rangle_E$ for various values of ω_1^E, as done in experiment. The fit is performed with ω_p, J, g_{uc}^{eff}, and g_{nuc}^{eff} as fit parameters, yielding $\omega_p = 4.823$ GHz, $J = 33.96$ MHz, $g_{uc} = 35.16$ MHz, and $g_{nuc} = 2.27$ MHz, with the simulated dynamics shown in Figure E.2a (right), demonstrating excellent agreement to the data.

With these parameters, we calculate the intrinsic $\Gamma_{1\text{D}}$ of Q_E when it is tuned to the middle of the passband via the formula $2g_{\text{uc}}^2/J$ [57, 78], where $2J$ is the group velocity (per unit cell) in the middle of the passband, while g_{uc} also corresponds to the coupling of the qubit to each propagating mode of the passband (note that this formula applies to a qubit end-coupled to a waveguide, while for a side-coupled qubit the effective $\Gamma_{1\text{D}}$ is g_{uc}^2/J). The dependence of $\Gamma_{1\text{D}}$ on J is reflective of the slow-light effect on the emission dynamics of the qubit, where a smaller J leads to a smaller group velocity $v_g = \frac{\partial \omega}{\partial k}$, which in 1D systems corresponds to a large density of states $1/\pi|v_g|$. Per Fermi's Golden Rule, a large density of states boosts emission rates for a given coupling [217]. Thus, due to the slow group velocity of the SLWG, we are able to achieve strong emission rates without relying on bulky coupling capacitors of the qubit to the waveguide, and instead achieve sufficient coupling by simply bringing the qubit island within enough proximity to the unit cell of the SLWG. This allows us to hew to the qubit design principles outlined in Ref. [218] that ensure high qubit T_1. Note that we utilize this value of $\Gamma_{1\text{D}}$ for absolute power calibration of measured field amplitudes (see Appendix F.1).

In addition, the interaction of Q_M with an incident photon pulse as a function of Q_M's frequency was also investigated experimentally. The measurements consisted of emitting a Gaussian photon pulse from Q_E with a bandwidth of 9.8 MHz and carrier frequency ω_p via shaped photon emission, followed by rapid tuning of Q_M's frequency to the vicinity of the passband after the photon's one-way propagation time of $t = \tau_{\text{d}}/2$ through the waveguide. This tuning is maintained for the duration of the emitted pulse's interaction with the mirror and then is subsequently turned off. These measurements are performed for various Q_M bias frequencies during the

rapid tuning; the measured average SLWG output photon field $\langle a_{\text{out}} \rangle$ as a function of Q_M frequency (see Appendix F.1 for details on measurement of $\langle a_{\text{out}} \rangle$) is plotted in Figure E.2b (left).

The transmitted fraction of the photon pulse upon the first incidence at the SLWG boundary is measured as the first bright feature at time 140 ns. When Q_M is tuned close to the center of the passband ("Mirror ON"), Q_M scatters the photon pulse with large $\Gamma_{1\text{D}}$ and thus reflects most of the energy, which is observed as the disappearance of the first bright feature near zero detuning in Figure E.2b. The second bright feature corresponds to the fraction of the photon pulse that was reflected at the SLWG boundary, traveled a round-trip through the waveguide, and subsequently exited the SLWG for measurement. Note that the yellow line in Figure E.2b corresponds to the time when the Q_M fast flux bias is turned off; thus turning off the interaction of Q_M with subsequently incident photon fields.

The measured data of Figure E.2b are fit to the expected output photon field, which is simulated with the following model Hamiltonian

$$\begin{aligned} \hat{H}^{EM} &= \hat{H}^E(t) + \Delta^M(t) \left|e\right\rangle \left\langle e\right|_M + g_{uc}^M(\hat{\sigma}_+^M \hat{a}_{50} + \hat{\sigma}_-^M \hat{a}_{50}^\dagger) \\ &\quad + \Delta_1 \hat{a}_{51}^\dagger \hat{a}_{51} + \Delta_2 \hat{a}_{52}^\dagger \hat{a}_{52} + J_1(\hat{a}_{51}^\dagger \hat{a}_{52} + \hat{a}_{51} \hat{a}_{52}^\dagger), \end{aligned} \tag{E.5}$$

where $\Delta^M(t)$, Δ_1, and Δ_2 are the detunings of Q_M, the left taper cell resonator, and the right taper cell resonator from the center of the passband ω_p respectively, σ_+^M, σ_-^M are the raising and lowering operators of Q_M, and J_1 is the photon hopping rate between the taper cell resonators. We replicate the described rapid tuning of Q_M used in the experiment via the Hamiltonian time-dependent term $\Delta^M(t)$. In addition, the external loading of the system to the output 50 Ω waveguide is implemented in the model via a dissipation collapse operator in the last taper resonator with rate $\kappa = 148$ MHz (calculated from circuit parameters of the system). $\hat{H}^E(t)$ corresponds to the Hamiltonian of Equation E.4 where ξ is time-dependent, which allows us to model shaped photon emission. The envelope of output field $|\langle a_{out}(t) \rangle|$ is obtained in the simulation via taking the time derivative of the accumulated population in the zero-excitation ground state. This output field obtained from the simulation is fit to the measured data by utilizing Δ_1, Δ_2, g_{uc}^M, and J_1 as fit parameters, yielding $\Delta_1 = -6$ MHz, $\Delta_2 = -70$ MHz, $g_{uc}^M = 57$ MHz, and $J_1 = 45.4$ MHz. The simulated dynamics, shown in Figure E.2b (right), demonstrates excellent agreement to the data.

In our modeling, the non-zero Δ_1 and Δ_2 fit values account for the asymmetry of the measured photon field at positive detunings of Q_M and negative detunings of Q_M that is observed in the data. Moreover, in our model we do not include parasitic couplings of Q_M to neighboring resonators, and thus any effect of parasitic couplings on the overall Γ_{1D} and reflectance of Q_M are incorporated into the one effective coupling rate g_{uc}^M. We note that the fitted value of g_{uc}^M is consistent with the amount of transmitted energy from an incident photon that Q_M does not reflect, calculated as 0.02 from the data in Figure 5.3c; this corresponds to a “mirror efficiency" of 0.98 as we have defined it.

Purcell Filter

We perform conventional dispersive readout of the state of our qubits by probing $\lambda/4$ coplanar waveguide resonators that are capacitively coupled to the qubits in the dispersive regime. There is an implicit speed-fidelity tradeoff in such readout schemes due to the Purcell decay of the qubit into the readout lines mediated by the readout resonator to which it is coupled. Reducing the Purcell decay without adding auxiliary circuit components requires reducing the dispersive shift of the cavity, thus reducing readout SNR, or the readout resonator decay rate κ, thus reducing readout speed [219]. The common method for bypassing the implicit speed-accuracy tradeoff of such a readout scheme is to add an extra layer of bath engineering via a Purcell filter that modifies the environmental impedance seen by the qubit-resonator system so as to maintain a desirably large κ (for rapid information gain about the qubit state) while simultaneously suppressing decay at the qubit center frequency [206, 219, 220].

A Purcell filter can be modeled by replacing the series impedance of the output CPW seen by the qubit-resonator system with a frequency-dependent environmental impedance $Z_{\text{ext}}(\omega)$. Within such a model the qubit Purcell decay is given by [69]:

$$\gamma_P^{\text{filt}} = \kappa \frac{g^2}{\Delta^2} \frac{\text{Re}\, Z_{\text{ext}}(\omega_q)}{\text{Re}\, Z_{\text{ext}}(\omega_r)}, \tag{E.6}$$

which is just the bare Purcell decay weighted by the ratio of the real impedances of the external load at the qubit and readout resonator frequencies. Thus, by engineering the frequency-dependence of Z_{ext} to be matched to the output CPW at ω_r, while have negligible real part at ω_q, we can surpress Purcell decay while efficiently probing the readout resonator.

A coupled resonator array, such as the one we use to implement the SLWG used in our experiment, can be used as a Purcell filter due to its highly flexible impedance

properties, allowing for a purely imaginary Bloch impedance at frequencies outside of its passband and a purely real Bloch impedance inside [109]. Ideally this allows for complete extinction of qubit Purcell decay by placing ω_Q outside the passband of the array, while maintaining high readout speed by placing ω_r within the passband. In essence, the coupled resonator array has a large nonzero density of states through which the readout resonator can decay if ω_r is within the passband, while having no density of states, and thus no available decay channels, at the qubit frequency [185].

To that end, we engineered a Purcell Filter Waveguide (PFWG) serving as a single Purcell filter for the two readout resonators of both the emitter and mirror qubits. The Purcell filter, which can be seen in Figure E.3a, b, extends between two ports of our device and replaces the usual CPW readout lines to which readout resonators are coupled to on chip. It has the same circuit topology as the SLWG designed for the cluster state generation scheme, comprising 54 lumped-element resonator unit cells coupled to their nearest neighbors capacitively. Referring to the model of Figure E.3b, the following circuit parameters: $L_0' = 1.2$ nH, $C_0' = 323.5$ fF, $C_g' = 19.5$ fF, $C_1' = 315.0$ fF, $C_{1g}' = 27.4$ fF, $C_2' = 218.2$ fF, $C_{2g}' = 126.4$ were targeted for the PFWG using the same principles employed in designing the SLWG.

The transmission spectrum of the PFWG, including the two resonances of the readout resonators, can be seen in Figure E.3 c. The passband of the PFWG is situated from 7.24 GHz to 7.9 GHz so as to safely encompass the resonances of both Q_E and Q_M readout resonators centered at $\omega_{RM} \sim 7.4$ GHz and $\omega_{RE} \sim 7.7$ GHz respectively, while excluding the entire tuning ranges of the qubits and the frequency of a pump tone at ~ 7.95 GHz used for driving a Josephson Travelling Wave Parametric Amplifier (TWPA) for output signal amplification.

The readout resonators are inductively side-coupled to the PFWG by bringing the current antinode of the $\lambda/4$ resonator into close proximity to the grounded end of a unit cell's meander trace, as can be seen in Fig E.3a, for a target resonator decay rate of $\kappa = 10$ MHz. Due to geometric constraints each resonator was coupled to one of the eleventh unit cells of the PFWG counted from its ends. Note that we chose inductive coupling to the PFWG via the current antinode of the resonator because that afforded strong coupling to the PFWG, while still allowing for capacitive coupling to the qubit at the resonator's charge antinode.

The readout-unit cell coupling strength was adjusted in design by changing the distance between the last airbridge of the readout resonator and the current antinode of the resonator near the meander trace of the PFWG unit cell. Moving the airbridge

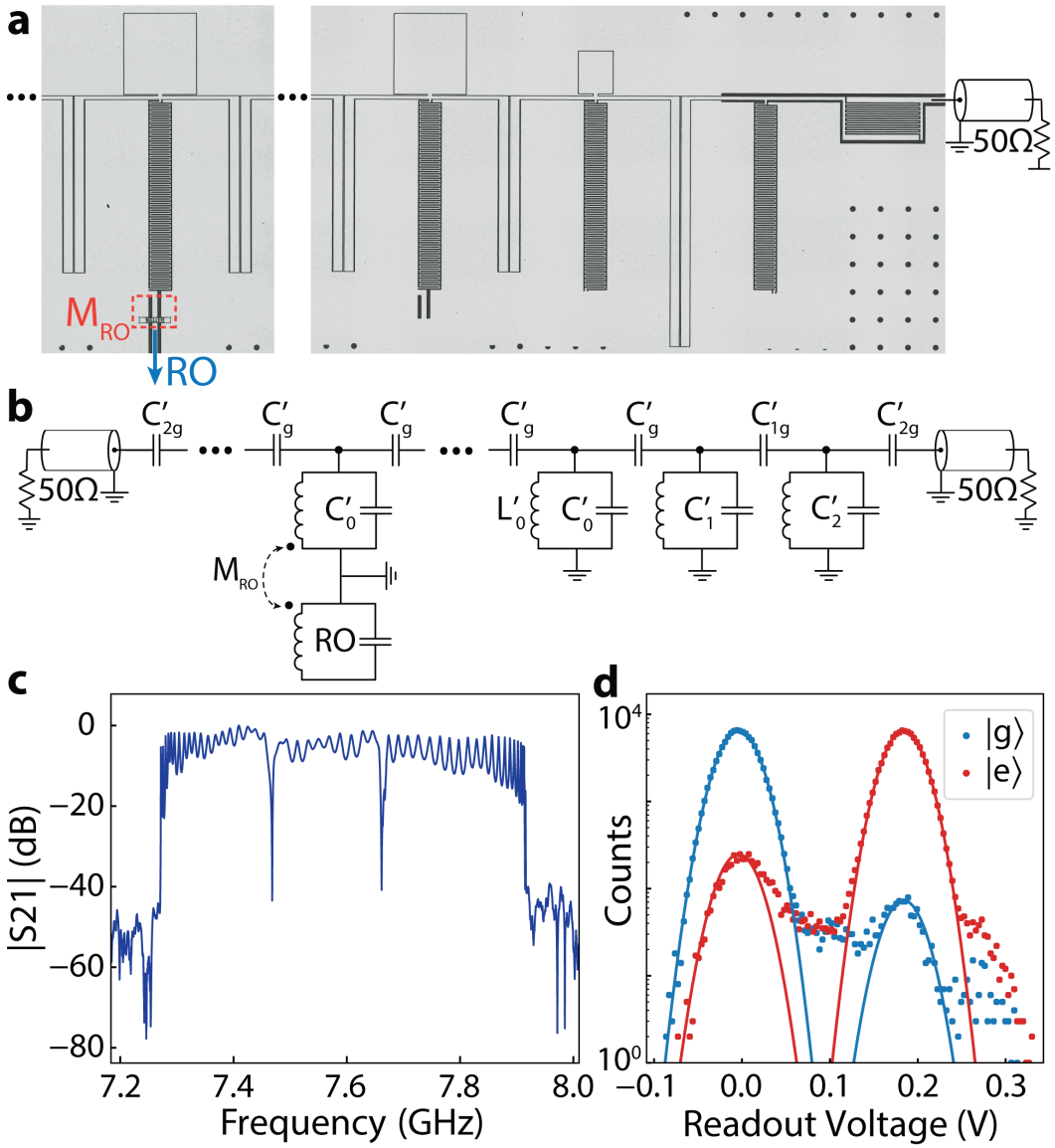

Figure E.3: **Purcell Filter Waveguide and Readout Characterization a** False-colored optical image of the on-chip Purcell filter waveguide. The image on the right depicts one end of the Purcell filter waveguide, while the image on the left depicts the unit cell inductively coupled to one of the CPW readout resonators of the qubits **b** Full circuit model of the Purcell filter and an inductively coupled readout resonator. **c** Transmission spectrum of the full Purcell filter waveguide with two side-coupled readout resonators R_E and R_M. **d** Log-linear raw histogram of single-shot readout measurement results for 100,000 ground-state preparations and 100,000 excited-state preparations. Solid lines are fits to a bimodal normal distribution. Readout fidelity = 97.6% was obtained from this histogram.

closer to the coupling point reduces the overall strength of the inductive coupling, while moving it away increases the strength. We believe the presence of the airbridge screens the extent of magnetic fields generated by the current near the coupling point and thus reduces the overall overlap volume of fields generated by the resonator and the PFWG unit cell. The fabricated resonator decay rate was found to be approximately $\kappa \sim 11$ MHz. Moreover, the dispersive shift of the readout resonator was measured to be $2\chi = 4.2$ MHz for a qubit-readout resonator detuning of $\Delta = 1.45$ GHz, yielding a qubit-resonator coupling strength $g \sim 140$ MHz that agrees well with the design value. The measured Purcell-protected T_1 time of Q_E at its upper sweet spot was measured to be $20\mu s$, which is more than one order of magnitude larger than what would be expected in the absence of a Purcell filter; we believe this T_1 is ultimately limited by sample loss.

In order to optimize Q_E's single shot readout, we first found the readout probe pulse carrier frequency and length that maximized the complex voltage contrast between the readout transmission when Q_E was initialized to either $|g\rangle$ or $|e\rangle$. Due to the distorting effects of the ripples in the PFWG transmission spectrum, the optimal frequency of the readout probe tone was found empirically. We also chose the optimal readout power by maximizing contrast while avoiding any powers that led to spurious features in the 2D single-shot readout signal histograms in the IQ plane (which we attributed to readout-induced qubit transitions). To characterize the readout fidelity we prepared Q_E in either the $|g\rangle$ or $|e\rangle$ state, and measured histograms of demodulated single-shot signals resulting from probing the readout resonator. These histograms were fit to a double-Gaussian model seen in Fig E.3 d. from which a ground-excited discrimination boundary was determined. The readout fidelity with respect to this discrimination boundary was found to be 97.6%; this high single-shot readout fidelity was an important resource for the joint qubit-photon measurements required for the quantum process tomography of the CZ gate used in the cluster state generation protocol.

E.2 Flux Control for Shaped Photon Emission and Qubit-Photon CZ Gate

As alluded to in Chapter 5, sophisticated flux control techniques for dynamical control of the qubit frequency were critical in achieving both shaped photon emission as well as a high-fidelity qubit-photon CZ gate. Below we present a summary of the techniques we employed in order to achieve distortion-free square flux pulses at Q_E and Q_M, and precise control of the time-dependent coupling between Q_E and the SLWG via flux modulation.

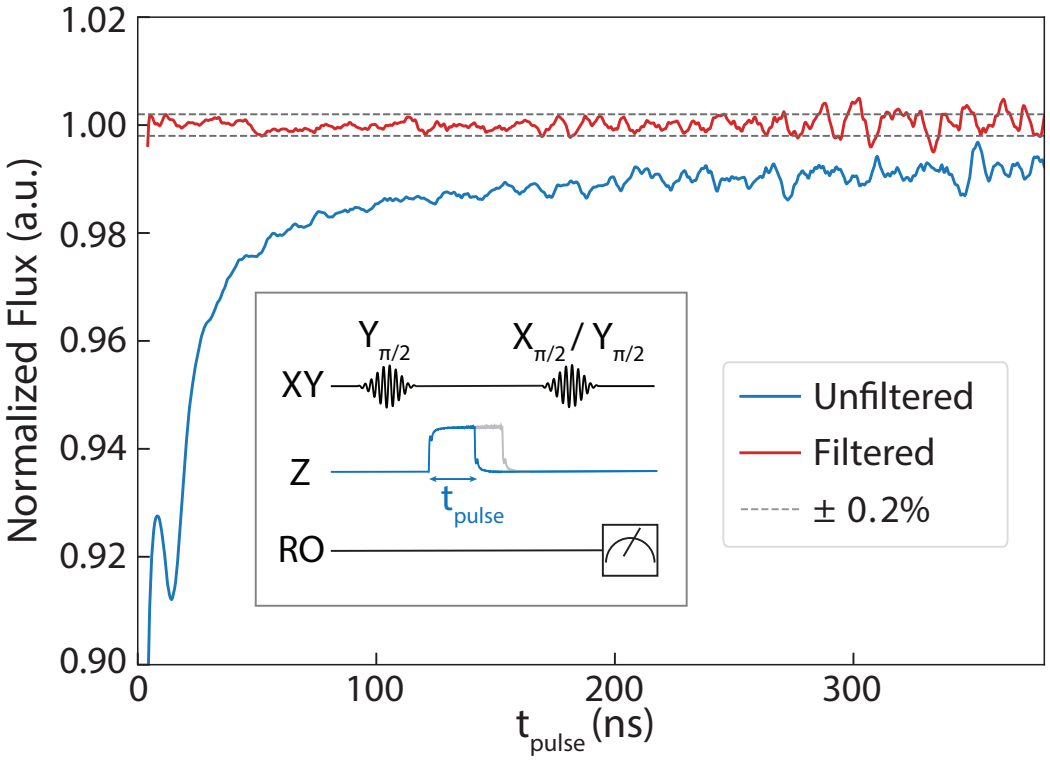

Figure E.4: Reconstructed step response of flux line with and without “Cryoscope" distortion pre-compensation. The pulse sequence used for reconstructing the step response is illustrated as an inset; see Appendix E.2 text for further details.

Distortion Pre-Compensation of Square Flux Pulses

Contributions from dilution refrigerator wiring to signal distortions from flux control lines are often temperature dependent, necessitating techniques for in situ characterization of such distortions via the controlled qubit itself. We used the so-called “Cryoscope" technique [221], consisting of Ramsey-type measurements to reconstruct the step-response of the flux line followed by iterative digital pre-compensation, to mitigate distortion in our Z_E and Z_M lines. With pre-compensation, we achieved a desired flat step response within ±0.2% of error, as depicted in FigureE.4, for both qubits. The qubit measurements undertaken to reconstruct the step response of the flux line are shown in the inset of FigureE.4. We refer the reader to Ref. [221] for a detailed description of the entire “Cryoscope" process, and discuss small modifications to what is presented in Ref. [221] below.

Firstly, we observe that we did not require real-time digital filtering given that our pulse sequences were only ∼ 500 ns in length, and thus chose to use pre-compiled waveforms in order to have more computational flexibility for pre-distortion. Additionally, we note that we observed residual long-time transient responses when

applying pre-compensated flux pulses, as discussed in Ref. [222]. To address this problem, rather than waiting for decay of the transient response, a negative copy of the flux signal is appended at the end of every sequence.

Moreover, when obtaining the reconstructed step response, we found it useful to digitally filter the $\langle X\rangle(t) + i\langle Y\rangle(t)$ data, in order to eliminate data contributions from phase errors in the gates or population offsets, which manifest themselves as spurious features in the spectrum of the data. Moreover, we apply oscillating decaying exponential IIR filters of the form $1+Ae^{-t/\tau_{\mathrm{IIR}}}\cos(\omega_{\mathrm{IIR}}t+\phi_{\mathrm{IIR}})$ in addition to solely decaying exponential IIR filters to achieve better pre-compensation. Finally, for the FIR short-scale precompensation, we mention that it is important to include the smoothing effects of the Savitzky-Golay filter in calculation of the predicted signal from the optimized FIR coefficients.

Photonic Pulse Shaping

As described in Chapter 5, it is important to properly control the time-domain shape of emitted photon pulses in order to ameliorate the effects from the SLWG's non-linear dispersion and to improve the fidelity of the qubit-photon CZ gate. Arbitrary photon pulse shapes can be achieved by controlling the time-dependent decay rate of the Q_E, which necessitates a tunable interaction between Q_E and the SLWG.

For flux-tunable transmon qubits, such tunable interaction can be attained via sinusoidal flux modulation of the qubit frequency (depicted in Figure2.5a) which induces a sideband-mediated interaction with the SLWG whose strength is controlled by the amplitude of the flux modulation AC flux drive [75–77]. In this work, we utilize amplitude modulated AC flux pulses to dynamically control the sideband interaction strength between Q_E and the SLWG, thereby achieving shaped photon pulses. For a review of the theory of flux modulation, we refer the reader to Appendix 2.2, where we note that in that analysis, the two levels of the qubit correspond to the $|e\rangle$ and $|f\rangle$ levels of Q_E that participate in photon emission in our experiment

In order to achieve a desired time-dependent coupling between Q_E and the SLWG, we must achieve the necessary time-dependent sideband strength $\xi(t)$ through control of the AC flux drive amplitude. We are able to accurately predict the necessary AC flux drive amplitudes to achieve desired values of the sideband amplitude ξ by numerical calculation of the "sideband spectrum" of Q_E under flux modulation. Remembering that we are concerned with emission from the $|f\rangle$ state, for this calculation, we require the functional form of the qubit tuning curve $\omega_{ef}(\Phi)$, the

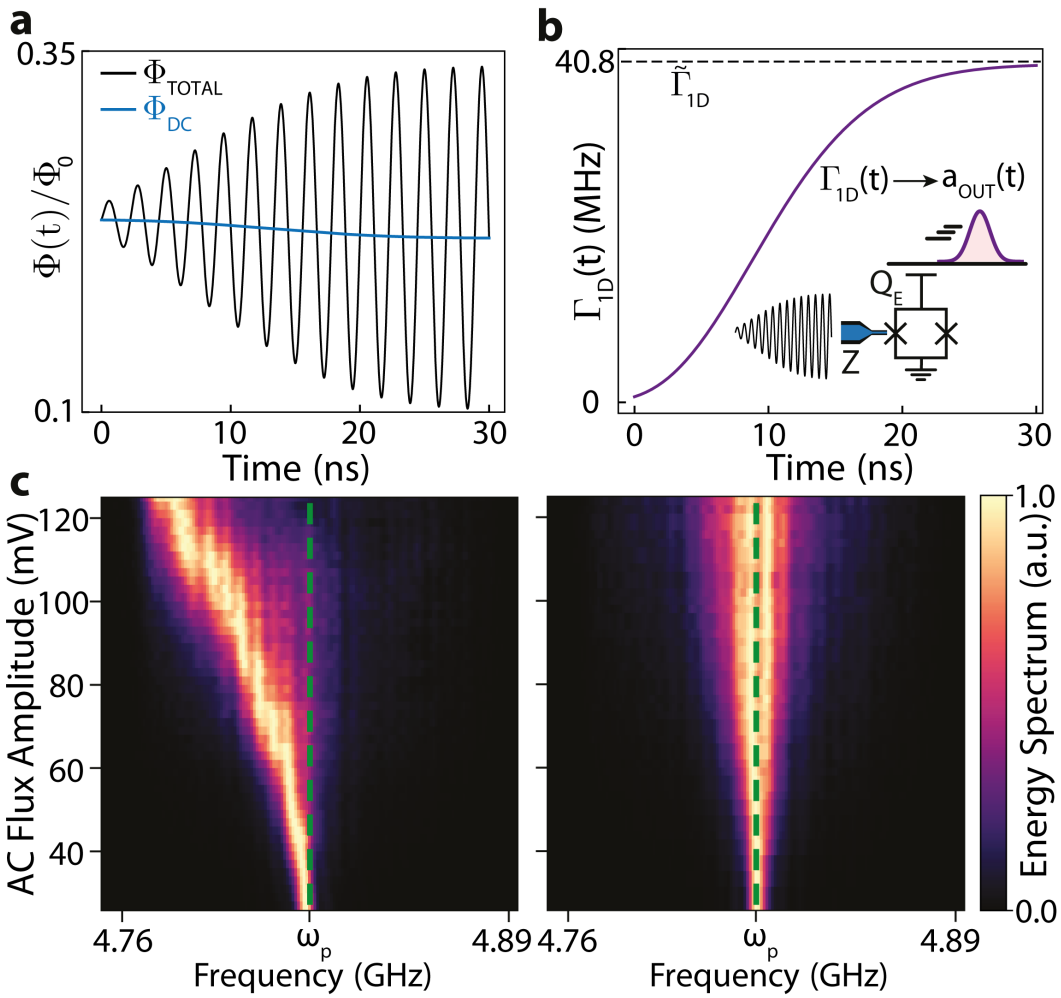

Figure E.5: **Pulse Shaping via Flux Modulation of the Emitter Qubit.** **a** Flux-modulation waveform used in experiment to generate high-bandwidth photons 2, 3, and 4. The blue curve corresponds to a dynamic DC correction that is used to maintain the emission frequency constant; see text for details. **b** Effective $\Gamma_{1D}(t)$ obtained from the flux modulation waveform shown in **a**. **c** Energy spectra of qubit emission for a constant flux modulation amplitude that is swept. Left: energy spectra without DC shift compensation. Right: energy spectra with DC shift compensation, where DC shifts are calculated theoretically assuming an specific insertion loss in the flux line for the used ω_{mod}.

static flux bias Φ_B, and the strength of the sinusoidal flux drive Φ_{AC}. We adopted the analytical form of the transmon tuning curve from ref [79] for accurate calculation of ω_{ef} as a function of Φ, from measurement of the highest qubit frequency, the lowest qubit frequency, and the anharmonicity η at the highest qubit frequency.

The sideband spectrum is calculated via the Fourier Transform of $e^{-i\phi(t)}$ (with an example shown in Figure 2.5b), where the $s = 1$ sideband is highlighted in red. The spectrum yields the different ξ_s, as well as the average "DC shift" of the qubit frequency $\delta_{DC} \equiv \tilde{\omega}_Q - \omega_Q(\Phi_B)$ which depends on both Φ_B as well as Φ_{AC}. We can leverage this DC shift effect to obtain a mapping from AC flux amplitude at the qubit to input AC voltages to the fridge, as illustrated in FigureE.5e. By inducing Q_E emission via flux modulation at various AC input voltages and measuring the carrier frequency of emitted photons, we observe the average DC shift of the qubit frequency via the changing carrier frequency of emitted photons. By comparing the change in photon carrier frequency to numerical predictions of δ_{DC}, we can obtain the scaling factor for converting input AC voltages to Φ_{AC} at the qubit. Meanwhile, note that we obtain a similar scaling factor for converting static DC bias voltages to Φ_B at the qubit via measurements of the qubit tuning curve (note that the two scaling factors are different due to differing DC and AC losses of the flux line).

Thus, we can achieve a desired time-dependent coupling between Q_E and the SLWG via flux modulation, by effecting a time-dependent $\xi(t)$ via some specific $\Phi_{AC}(t)$. However, a time-dependent $\Phi_{AC}(t)$ will also lead to a time-dependent $\delta_{DC}(t)$, which necessitates a "DC correction" signal to maintain the emission frequency constant. Therefore, we obtain the necessary flux drive $\Phi(t) = \Phi_{DC}(t) + \Phi_{AC}\sin(\omega_{\text{mod}}t)$ that achieves a desired $\xi(t)$ while maintaining a constant emission frequency. This is achieved by considering a suitable range of AC flux amplitudes, and obtaining associated Φ_{DC} correction flux biases for each flux amplitude such that for a given Φ_{AC}, overall static qubit bias Φ_B, and the flux amplitude-dependent correction bias Φ_{DC}, the average qubit frequency $\tilde{\omega}_{ef}$ will be equal to $\omega_{ef}(\Phi_B)$; see Figure E.5e (right) for demonstration of this DC correction procedure for various AC flux amplitudes. Then, the sideband amplitudes $\xi(\Phi_B, \Phi_{AC}, \Phi_{DC})$ are numerically calculated for each set of the aforementioned parameter values, with which a desired $\xi(t)$ can be mapped to the necessary $\Phi(t)$ signal; see Figure E.5c,d for an example. Finally, we note that under the flux drive $\Phi(t)$, the time-dependent decay rate $\Gamma_{1D}^{ef}(t)$ of Q_E will be equal to $\Gamma_{1D}^{ef} \cdot |\xi(t)|^2$, where Γ_{1D}^{ef} is the intrinsic decay rate of the $|f\rangle$ state given by $\sim 4g_{uc}^2/J$.

As discussed in Chapter 5, we sought to emit Gaussian-shaped photons for our cluster state generation sequence, as illustrated in Figure 5.2. We observed, both numerically and experimentally, that shaped photons with Gaussian spectra could be emitted by realizing the following sideband amplitude time dependence $\xi(t)$:

$$\begin{aligned} \xi(t) &= \xi_M \mathrm{erf}^2(\frac{t}{t_R} + \delta), \\ \mathrm{erf}(t) &\equiv \frac{2}{\sqrt{\pi}} \int_0^t e^{-t'^2} dt', \end{aligned} \tag{E.7}$$

where t_R scales the erf function with respect to time, ξ_M is the maximum attainable sideband amplitude at a given Φ_B, and the second line defines the erf function whose square increases from 0 and converges to 1 smoothly. The spectral bandwidth of the resultant Gaussian pulse is controlled by t_R, where slow (fast) increase of $\Gamma_{1D}(t)$ due to large (small) t_R leads to small (large) bandwidth. Moreover, the δ parameter shifts the entire function with respect to time, such that it reduces the time needed to reach the maximum sideband amplitude for a given emission time and t_R; this is useful to further suppress residual $|f\rangle$ population after emission for short emission times. This parametrized time dependence is plotted in FigureE.6a.

For the photonic pulses shown in Figure 5.54c, photon 1 was generated by realizing the time-dependent sideband amplitude $\xi(t)$ of equation E.7 with parameters $t_R = 50$ and $\delta = 0$, yielding a Gaussian pulse with 9.9 MHz bandwidth. However, for photons 2, 3, 4 we chose to utilize a finite δ in order to achieve a small $|f\rangle$ residual $|f\rangle$ population for the photons' short 30 ns emission time. In order to obtain the best δ, t_R combination, we modeled and measured experimentally this residual population after photon emission for a range of δ, t_R values, as depicted in FigureE.6b, c (see Appendix E.1 for modeling details). We found that the combination $t_R = 15$ ns, $\delta = 0.33$, suppresses residual $|f\rangle$ state population below 1% and constricts emitted photon pulses to a short time-bin measurement window, and we chose this parameter combination for emission of photons 2, 3, 4 depicted in Figure 5.5c. We note that while higher δ values in general result in less residual $|f\rangle$ population, large δ values also lead to distortions in the emitted Gaussian pulse; thus the parameter choice $t_R = 15$ ns, $\delta = 0.33$ strikes a balance between minimizing residual $|f\rangle$ state population and maintaining the approximately Gaussian shape of the emitted pulse with 17.9 MHz bandwidth.

We also note that we realize fast unconditional reset using flux modulation, where the $|e\rangle$ and $|f\rangle$ state populations are emptied via induced photon emission. First, a

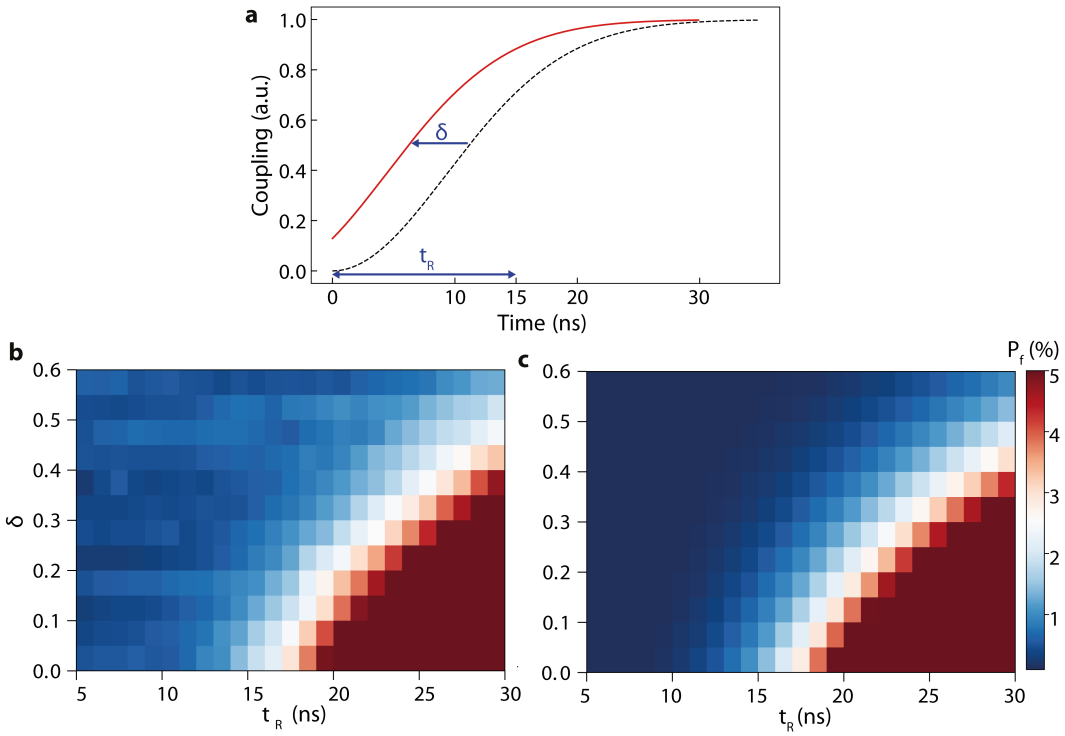

Figure E.6: **High-Bandwidth Photon Emission a** Shape of time-dependent coupling effected by flux modulation, given by the square of the erf function: $\left|\frac{2}{\sqrt{\pi}}\int^{t/t_R+\delta} e^{-t'^2}dt'\right|^2$, where t_R and δ scale and shift the erf function with respect to time, respectively. **b** Residual $|f\rangle$ state population measurement after photon emission via flux modulation with various t_R and δ parameters. **c** Simulation of the experiment done in part **b** using the model of Equation E.4.

constant flux modulation signal that induces emission of $|f\rangle$ to $|e\rangle$ is applied to Q_E. Next, another constant flux modulation signal that induces emission from $|e\rangle$ to $|g\rangle$ is applied to Q_E, bringing it to the ground state. Lastly, we wait approximately 3 μs after this reset before starting qubit control, in order to allow residual emitted fields trapped in the SLWG due to finite taper reflections to fully leave the waveguide. We note that this reset protocol effectively thermalizes Q_E to the SLWG temperature; indeed we confirm via separate measurements that the resultant $|e\rangle$ thermal population is $\sim$ 1% (corresponding to an effective $\sim$ 50 mK temperature). Using this unconditional reset protocol, we generate the 2D cluster state with a conservative repetition rate of 100 kHz.

E.3 Sources of Infidelity During Cluster State Generation

The main source of infidelity in this work was the poor decoherence rate $T_2^* = 561$ ns of Q_E. We ascribe this low T_2^* to excessive flux noise given our robust $T_1 = 34$ μs (and measured T_2^* of over 15 μs at its maximum frequency). The Ramsey decay time-dependence was strongly Gaussian, which suggests that our dephasing is limited by

$1/f$ noise [61, 223]. In order to properly model $1/f$ noise, typical Linbladian master-equation approaches, which assume a Markovian model of decoherence, do not suffice. We thus modeled the effect of $1/f$ noise in our cluster state generation sequence by simulating the state evolution of our joint system of Q_E (here a 3-level system) and photonic qubits under the influence of a $\delta(t)\hat{c}^\dagger\hat{c}$ term in the Hamiltonian, where $\hat{c}$ here is the annihilation operator of Q_E's anharmonic mode, and $\delta(t)$ is a random noise signal with noise power spectral density of $1/f$. The Hamiltonian for state evolution is thus comprised of this $\delta(t)\hat{c}^\dagger\hat{c}$ term, and the time-dependent Hamiltonian that realizes the pulse sequence depicted in Figure 5.5b.

Many different realizations of this noise are generated in the following manner: a random FFT spectrum is generated where each FFT bin is a normally distributed random complex value (and the spectrum is conjugate symmetric), the FFT bins are scaled according to a $1/f$ spectrum, and the inverse FFT is taken to arrive at a random noise signal. We ensure that the generated noise signals are long enough such that the center frequencies of FFT bins are as low as 50 Hz, in order for the resultant time signal to have significant power at very low frequencies. Consequently, we only use small portions of this long noisy time signal as the different realizations of $\delta(t)$ in our simulations (which are confirmed to have a $1/f$ power spectrum). We simulate state evolution of our system under different realizations of $\delta(t)$ and average the resultant states in order to obtain the "average" effect of $1/f$ noise induced dephasing on the system. We confirm that this simulation approach reproduces Gaussian-shaped Ramsey decay as well as the "spin-echo" phenomenon; and with full simulation of our cluster state generation sequence of Figure 5.5b under $1/f$ noise, we determine that our Q_E dephasing results in an infidelity of $\sim 15\%$ for the final 2D cluster state.

Secondly, the second most significant source of infidelity in our generation scheme is the round-trip loss of the slow-light waveguide. As seen in Figure 5.3c, the round-trip loss of the slow-light waveguide corresponds to 13% energy loss for each photon undergoing a round trip. Note that while a limited detection efficiency η_{det} is compensated for in heterodyne based state tomography via the scaling factor G, loss that occurs before the CZ gate, i.e., during state generation, is not considered part of η_{det} and directly contributes to infidelity. We find that our photon loss contributes to $\sim 5\%$ infidelity. Further, we estimate that control and preparation errors, including qubit thermal population (measured to be 1%), residual $|f\rangle$ state population after emission (measured to be 1%), and CZ gate infidelity, contribute another total $\sim$ 4% infidelity. In total, we estimate a 76% fidelity limit for the generated state,

which does not take into account measurement errors or other state preparation errors. This is in good agreement of our measured fidelity of 70%. Finally, we note that while waveguide dispersion was not a serious impediment for the photonic state generation that we have presented, it would limit the use of higher bandwdith photons as compared to what we used.

E.4 Theoretical Analysis of Qubit-Photon "Gate" Errors

The cluster state generation protocol can be theoretically described by the quantum circuit illustrated in Figure F.5. This quantum circuit consists of single-qubit gates for controlling Q_E and qubit-photon gates; where the qubit-photon gates are the CNOT gate and the CZ gate. While in practice the "CNOT gate" consists of excitation from $|e\rangle \rightarrow |f\rangle$ by a single qubit gate and emission from $|f\rangle$, thereby placing a photon in the SLWG, it can still be instructive to consider this process as effectively another "gate."

Following a similar analysis to Ref. [60], we calculate the fidelities of these qubit-photon gates based on experimentally relevant parameters. For the effective CNOT gate (assuming a perfect $|e\rangle \rightarrow |f\rangle$ rotation), the main source of infidelity will be residual population in the $|f\rangle$ state as discussed in Appendix E.2; which essentially can be regarded as a leakage error where the qubit leaves its computational subspace. For the CZ gate, the main source of infidelity will be the wavepacket distortion of the photon after it scatters on Q_E (see Chapter 2.2 for discussion of this phenomenon), as well a scattering phase different than π. The wavepacket distortion will lead to the mode shape of the photon to differ from its true mode-matching function $f(t)$ *when the qubit is in the* $|e\rangle$ *state*. This results in a mode-matching inefficiency that can be regarded as a leakage error where the *photon* leaves its computational subspace; i.e., the subspace spanned by vacuum state and the state with an excitation in the wavepacket mode of interest with shape $f(t)$.

We can calculate the average fidelity of gates that suffer from such leakage error via the formula derived in Ref. [224], where "average fidelity" here corresponds to assessing the "error" of the gate uniformly over all pure initial states in the system Hilbert space. The formula derived is given by

$$F = \frac{1}{d^2 + d}\left[\mathrm{Tr}\left(M_{\mathrm{comp}} M_{\mathrm{comp}}^{\dagger}\right) + \left|\mathrm{Tr}\left(M_{\mathrm{comp}}\right)\right|^2\right], \tag{E.8}$$

where $M_{\mathrm{comp}} = PU_0^{\dagger}UP$, where U_0 is the target gate and U is the effective gate and

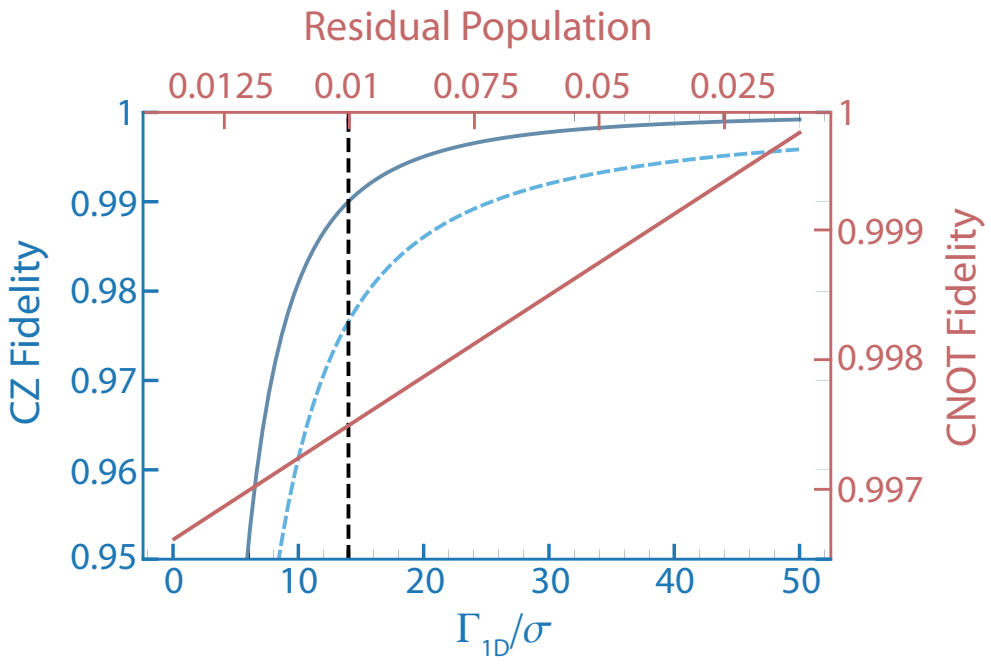

Figure E.7: **Theoretical CZ and CNOT Qubit-Photon Gate Fidelities**. Theoretically calculated qubit-photon CNOT fidelities as a function of residual $|f\rangle$ state population, and theoretically calculated qubit-photon CZ fidelities as a function of Γ_{1D}/σ, where σ is the bandwidth of a Gaussian wavepacket; see Appendix text for more details. The black dashed line indicates the realized values of residual population and Γ_{1D}/σ in our experiment. For the dashed blue curve, the Gaussian wavepacket is truncated outside of 2σ, where for the solid blue curve the Gaussian wavepacket is truncated outside of 4σ. In our experiment, our emission protocol effectively truncated the Gaussian pulse outside of 2σ.

these are defined on the full Hilbert space of the system *including the leakage states*, and P is the projection operator onto the computational subspace. Note that M_{comp} will not be unitary if there is leakage out of the computational subspace, and this property will thus lead to a computed infidelity through Equation E.8.

For the CNOT gate, the $|f\rangle$ state residual population directly gives the magnitude of the leakage. For the CZ gate, the leakage and phase error may be computed by calculating the mode-matching integral $\int dt f^*(t)g(t)$, where $g(t)$ is the resultant distorted wavepacket when the Q_E is in the $|e\rangle$ state. Defining the frequency dependent scattering response of Q_E as $r(\omega)$, we may write in the Fourier basis $g(t) = \int d\omega f(\omega)r(\omega)e^{-i\omega t}$, where $f(\omega)$ is the Fourier Transform of $f(t)$. Further, we note that since the SLWG dispersion is approximately linear in the middle of the passband and our qubit is “end-coupled" to the waveguide, the scattering response $r(\omega)$ will be approximately given by Equation 2.37. Further, given that $\Gamma_{1D} \gg \Gamma'$ in our system, we may assume that $r(\omega) = e^{i\theta_r(\omega)}$, where the magnitude of Q_E's

scattering response is unit-valued for all frequencies. By calculating the overlap integral in the Fourier basis, we arrive at the following result:

$$\int dt f^*(t)g(t) = \int d\omega |\overline{f}(\omega)|^2 e^{i\theta_r(\omega)}, \tag{E.9}$$

where it is evident that the overlap integral is simply the “weighted average" of the scattering phase across the wavepacket's power spectrum. Thus, if the wavepacket's bandwidth is significantly smaller than the “width" of $r(\omega)$, which is set by Γ_{1D}, then this weighted average of the phase will be approximately equal to -1.

In Figure E.7 we plot fidelities for the CZ and CNOT gates that were numerically calculated via Equation E.8. For the CNOT gate we calculate the fidelity as a function of residual population, where for the purposes of this calculation the following CNOT matrix element is given by $\langle 11|\text{CNOT}|10\rangle = \sqrt{1-p_{\text{res}}}$, where p_{res} is the residual population (and all other matrix elements are standard). Further, for the CZ gate we assume a Gaussian wavepacket with width σ, we assume that $r(\omega)$ is given by Equation 2.37, and we calculate the fidelity as a function of Γ_{1D}/σ, where the CZ matrix element $\langle 11|CZ|10\rangle = \int dt f^*(t)g(t)$ (and all other matrix elements are standard). We indicate with a dotted line the expected theoretical gate fidelities given our experimental parameters of $\Gamma_{1D}^{ef}/\sigma \sim 1/14$ and $p_{\text{res}} \sim 0.01$. Moreover, for the CZ fidelity we perform the calculation for a Gaussian pulse that is truncated 2σ away from the mean, and for a Gaussian pulse that is truncated 5σ away from the mean, where outside the truncation window the pulse amplitude is set to 0.

From the plotted curves, it is evident that the CZ gate fidelity has a non-linear dependence on Γ_{1D}, while the CNOT gate has a linear dependence on the residual population, in agreement with Ref. [60]. Further, we note that the infidelities calculated here in general are smaller than the magnitude of leakage, because leakage due to the gate only happens for *some* of the states of the computational subspace (for example, no CZ leakage error occurs if the photon is in the $|0\rangle$ state). Finally, we point out to the reader that although our theoretically expected CZ gate fidelities are only 97% given our experimental parameters, by merely increasing Γ_{1D} by a factor of 3 and minimizing spurious effects of pulse truncation, we can expect a CZ gate infidelity $\sim 10^{-4}$.

Appendix F

SUPPLEMENTARY INFORMATION FOR CHAPTER 5 - TOMOGRAPHY METHODS AND ADDITIONAL RESULTS

F.1 Radiation Field Quantum State Tomography

In order to characterize generated multipartite entangled photonic states, we utilize tomography methods for itinerant microwave photons that were pioneered in Circuit QED systems by Eichler et. al. [161, 225] with suitable modifications when appropriate for us. Below we present a detailed summary of our entire data analysis and tomography procedure. We conclude by presenting additional photonic quantum state preparation and tomography results not presented in Chapter 5. For even further details on our microwave field measurement and tomography techniques, see Appendix G.

Measurement of $\langle a_{\mathbf{out}}(t)\rangle$ and $\left\langle a^{\dagger}{}_{\mathbf{out}}(t)a_{\mathbf{out}}(t)\right\rangle$

The average photon flux $\left\langle a^{\dagger}{}_{\text{out}}(t)a_{\text{out}}(t)\right\rangle$ and average field $\langle a_{\text{out}}(t)\rangle$ of emitted photons are routinely measured in our experiment for the purposes of characterizing our shaped photon emission procedure, characterizing different aspects of our time-delayed feedback process, and obtaining mode matching functions $f(t)$ for the different photonic qubits in order to obtain time-independent statistics from their time-dependent fields (see rest of Appendix text for further details). Measurement of both of these quantities for an emitted photon starts with heterodyne measurement of both quadratures, $I(t)$ and $Q(t)$, of its time-dependent microwave field, via the output chain described in Appendix A. Many measurements are performed and their results are averaged to compute the average field $\langle V(t)\rangle = \langle I(t) + iQ(t)\rangle$ and the the average photon flux $\langle V^2(t)\rangle = \left\langle |I(t)|^2 + |Q(t)|^2\right\rangle$. Note that the calculation of $\langle V^2(t)\rangle$ results in a signal without any carrier frequency, but $\langle V(t)\rangle$ retains the carrier frequencies of $I(t)$ and $Q(t)$ which must be removed by digital demodulation.

Due to spurious DC shifts in the detection set-up, as well as imbalance and LO bleedthrough in the downconversion IQ mixer, the spectrum of $\langle V^2(t)\rangle$ and the demodulated $\langle V(t)\rangle$ will have spurious features outside of the baseband signal. In addition, these band-limited baseband signals will also have significant noise outside of their bandwidth. These undesirable features serve to obscure the time-dependent shape of the baseband signal that we wish to measure, and we remove them through

digital low-pass filtering, with filter bandwidth set to be sufficiently high to capture all of the baseband signal. At this point, the resultant demodulated and filtered $\langle V(t)\rangle$ signal, followed by suitable normalization, can already be used as the mode-matching function $f(t)$, where the normalization is such that $\int |f(t)|^2 dt = 1$.

Further, with an absolute power calibration of our output chain that maps voltage measured at the ADC to field amplitude at the qubit (see subsequent subsection for details on how to obtain this calibration), the digitally processed $\langle V^2(t)\rangle$ and $\langle V(t)\rangle$ signals can be suitably scaled to yield the true $\left\langle {a^\dagger}_{\text{out}}(t) a_{\text{out}}(t)\right\rangle$ and $\langle a_{\text{out}}(t)\rangle$ in units of photon/s and $\sqrt{\text{photon/s}}$, respectively. However, for the purposes of plotting in this manuscript, we presented these quantities in terms of unitless, normalized values $\langle \tilde{a}_{\text{out}}\rangle = \langle a_{\text{out}}\rangle / \tilde{\Gamma}_{1D}^{-1/2}$ and $\left\langle \tilde{a}^\dagger_{\text{out}} \tilde{a}_{\text{out}}\right\rangle = \left\langle {a^\dagger}_{\text{out}} a_{\text{out}}\right\rangle / \tilde{\Gamma}_{1D}$, where $\tilde{\Gamma}_{1D}/2\pi = 40.8$ MHz is the maximum expected emission rate of the $|f\rangle \rightarrow |e\rangle$ transition under flux modulation induced emission (see Appendix E.2 for further details regarding $\tilde{\Gamma}_{1D}$). Thus, these normalized quantities express the time-dependent photon flux and field as a *fraction* of the maximum expected photon flux and field, respectively, for an excited qubit with emission rate $\tilde{\Gamma}_{1D}$ (as an illustrative example, note that for constant flux modulation with flux amplitude that yields $\Gamma_{1D}^{ef}(t) = \tilde{\Gamma}_{1D}$, $\left\langle \tilde{a}^\dagger_{\text{out}} \tilde{a}_{\text{out}}\right\rangle$ at $t = 0$ would be equal to 1).

Absolute Power Calibration

In order to perform quantum-state tomography via heterodyne detection, we need an absolute power calibration that maps voltage measured at the ADC to field amplitude at the qubit's location on the device, given by some conversion factor G. This conversion factor G includes the following contributions: the scaling from the quantum field a to the physical voltage on the device, the gain of the output chain from the first amplifier forward, and the detection efficiency η_{det}. We define η_{det} such that $(1 - \eta_{\text{det}})$ corresponds to the fraction of the itinerant photon's energy that is lost before it reaches the first amplifier (which in our case is a quantum-limited TWPA), either due to the loss or spurious reflections that are suffered by the photon (see Figure E.1e for measurement of such reflections). Generically, G is obtained by measuring a signal at the ADC whose power at the qubit can be independently verified. In our work, we rely on measurement of the AC Stark shift of the qubit frequency induced by an input pulse on the SLWG as our method for power calibration.

The procedure for obtaining G via AC Stark shift measurements is the following.

The qubit frequency ω_{ge} is detuned from ω_p by 740 MHz. A square pulse with carrier frequency ω_p is sent into the SLWG, for varying input powers. This square pulse induces an AC Stark shift Δ^{AC} on the qubit frequency whose magnitude is dependent on the SLWG input power; this Δ^{AC} is measured by determining the resonance excitation frequency of the qubit. The qubit's resonance frequency is measured by applying an excitation pulse to the qubit while the SLWG input pulse is off-resonantly driving the qubit; by sweeping the excitation pulse's frequency, measuring the qubit response, and fitting the resultant lineshape to a Gaussian, we obtain the resonance frequency via the Gaussian's mean. Repeating this procedure for all SLWG input powers, we experimentally obtain the dependence of Δ^{AC} on the power of the SLWG input pulse. Finally, the amplitude of the SLWG input pulse is measured at the ADC for all input powers used.

The power dependence of Δ^{AC} is then fit to the following transmon AC Stark shift model involving five transmon levels [66]:

$$\hat{H} = \sum_{j=0}^{N=4} \left(j\Delta + j(j-1)\eta\right) |j\rangle \langle j| + \frac{\Omega}{2}\left(\sqrt{j+1}\,|j+1\rangle \langle j| + \text{h.c.}\right), \tag{F.1}$$

where $\{j\}$ corresponds to the transmon levels, the SLWG drive frequency is ω_p, $\Delta = \omega_{ge} - \omega_p$, the transmon anharmonicity is $\eta/2\pi = -277$ MHz, and Ω is the Rabi frequency of the SLWG drive. Note that this Hamiltonian is obtained from the full Hamiltonian of a transmon interacting with a classical drive by simply going into the rotating frame of the drive (via the unitary transformation $U = \exp\left[it \sum_j j\,|j\rangle \langle j|\,\omega_p\right]$) and discarding counter-rotating terms. Also note that our model includes multiple transmon levels because the presence of multiple transitions, along with their associated anharmonicities, quantitatively changes the theoretically predicted Δ^{AC}. We found that we needed up to five transmon levels for the theoretically predicted Δ^{AC} to converge for our experimental parameters, whereas beyond five levels changes in the predicted Δ^{AC} were negligible.

For a qubit coupled to a single-ended waveguide, the Rabi Frequency is given by $\Omega = |\alpha|\sqrt{4\Gamma_{1D}}$ [73], where $|\alpha|$ is the field amplitude of the SLWG drive *at the qubit*, and for our slow-light waveguide the qubit's emission rate into the waveguide (at the center of the passband) is given by $\Gamma_{1D} = 2g_{uc}^2/J$ [78]. The parameters g_{uc} and J of our device were obtained through device characterization experiments described in Appendix E.1, and were directly used in this model. From this model Hamiltonian, Δ^{AC} is numerically calculated in the following manner: first, the Hamiltonian is

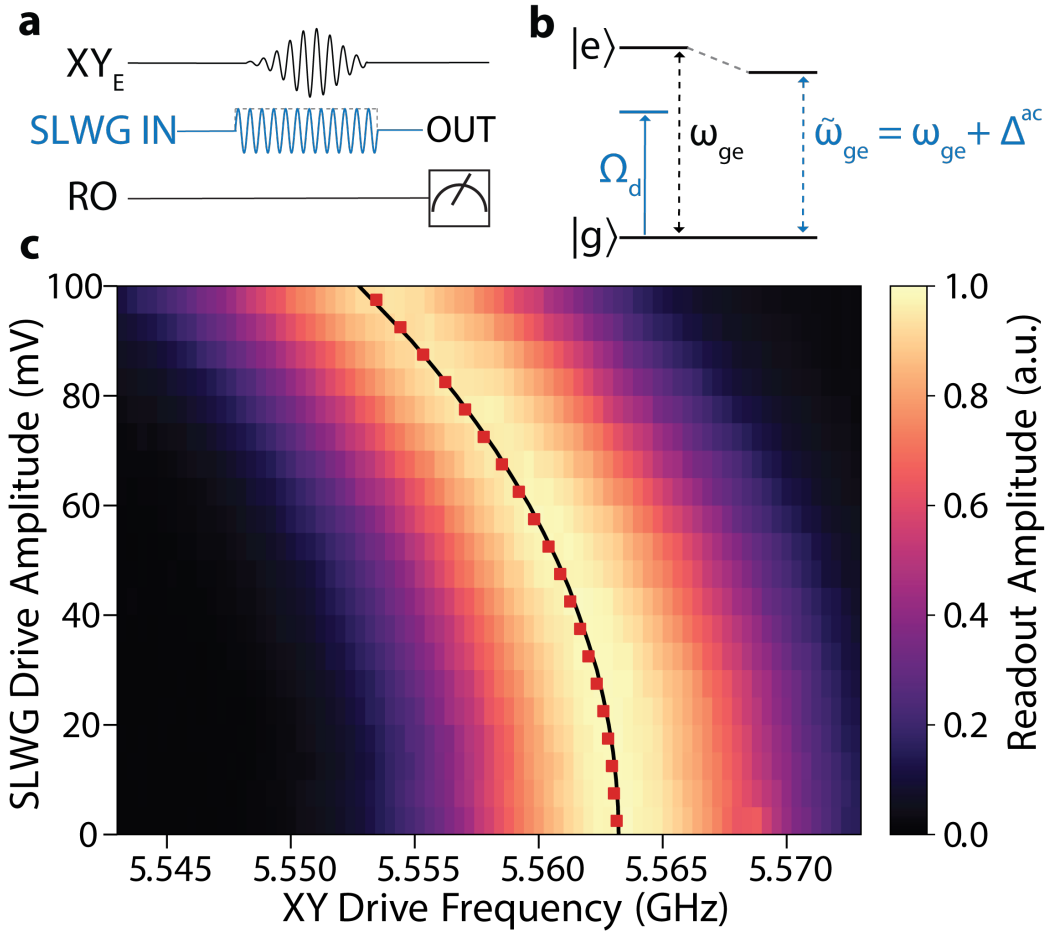

Figure F.1: **Absolute Power Calibration via AC Stark Shift of Emitter Qubit**. **a** Pulse sequence for the AC Stark Shift calibration experiment. An input square pulse with carrier frequency 740 MHz detuned from the qubit ω_{ge} is sent into slow-light waveguide (SLWG) and drives Q_E. Simultaneously, a qubit excitation pulse is sent into the XY_E line and arrives at the qubit at the same time the input SLWG pulse is driving the qubit, for the purposes of determining the resonance frequency of the AC Stark Shifted qubit. This experiment is repeated for multiple SLWG input pulse powers. **b** Level diagram depicting the detuned drive on the qubit from the SLWG, and how that effects an AC Stark Shift of the qubit frequency. **c** AC Stark Shift measurement data. The square markers are the measured qubit frequencies at different SLWG drive amplitudes, while the black line is a fit to a model of the expected qubit frequency due to off-resonant driving. See the Appendix F.1 text for more details.

diagonalized to obtain its eigenenergies. Then, the difference between the energies of the “dressed" ground state and the “dressed" excited state is obtained, and by subtracting Δ from this difference Δ^{AC} is finally obtained.

The fit is performed simply by using $|\alpha| = V_{ADC} \cdot G$ in the model, where V_{ADC} is the amplitude of the SLWG input pulse measured at the ADC. By obtaining Δ^{AC} with G as a fit parameter, the fit of the model to the data is shown as the black curve in Figure F.1c, showing excellent agreement to the data. The obtained fit parameter G was henceforth used to scale all radiation field voltages measured at the ADC. We note that by using a pulsed measurement, rather than a continuous wave (CW) SLWG input tone, the obtained G more accurately captures the contribution of spurious reflections to the overall η_{det} that is experienced by emitted pulses, and is significantly less sensitive to ripples in the output chain transfer function.

Measuring Expectation Values of Radiation Field Moments

The time-independent quantum statistics of emitted photons can be extracted from single shot measurements of their (properly scaled) time-dependent fields by integration with a suitable mode-matching function $f(t)$. This integration $\int f(t) a_{\text{out}}(t) dt = I + iQ = S$ can be shown to yield single-shot measurements of the complex quantity $S = a + h^\dagger$, where a is the mode of interest, and h is the noise mode of the detection chain. By taking many single-shot measurements, one gains access to the statistics of $a + h^\dagger$, and similarly, one can also perform many single-shot “dark" measurements of the noise mode h to obtain its statistics. By calculating the expectation values of moments of $a + h^\dagger$ and h from their single shot measurements, the expectation values of moments of a can thus be obtained, which is sufficient to reconstruct the density matrix of the mode of interest.

The procedure described above can be straightforwardly extended to multiple modes. For our experiment, the mode-matching function $f_i(t)$ for each photonic time-bin qubit is obtained by direct measurement of the average pulse shape $\left\langle a_{i,\text{out}}(t) \right\rangle$. This allows for single-shot measurements of $S_i = a_i + h_i^\dagger$ for every photon, which are then processed into joint moments $\mathcal{S}$ of the form $\left\langle (S_1^\dagger)^{n_1} S_1^{m_1} (S_2^\dagger)^{n_2} S_2^{m_2} \ldots (S_N^\dagger)^{n_N} S_N^{m_N} \right\rangle$. Given that our emitter qubit is a single-photon source, we take $n_i, m_i \in \{0, 1\}$ by assuming that the Hilbert Space of the photonic modes can be restricted to the single-photon manifold subspace. Note that we have experimentally verified the single-photon character of our emitted photons (for each time-bin photonic qubit) via measurements of $\left\langle (a^\dagger)^2 a^2 \right\rangle$ for various prepared photonic states, which are

plotted in Figure F.2. The measured $\left\langle (a^\dagger)^2 a^2 \right\rangle$ moments are close to 0 for all prepared photonic states, corresponding to a vanishing second-order correlation function $g^{(2)}(0)$ at zero time delay.

In turn, the joint photon moments $\left\langle (a_1^\dagger)^{n_1} a_1^{m_1} (a_2^\dagger)^{n_2} a_2^{m_2} ... (a_N^\dagger)^{n_N} a_N^{m_N} \right\rangle \ \forall \ n_i, m_i \in \{0, 1\}$ can be calculated from algebraic formulas involving the measured joint moments $\mathcal{S}$ and the measured moments $\left\langle h_i^\dagger h_i \right\rangle$ under the following simplifying assumptions: the signal modes a_i are uncorrelated from the noise modes h_i, the noise modes h_i are not correlated to one another, and odd-order moments of h_i are taken to be zero. These assumptions are appropriate when the noise modes h_i are in a thermal state, which is typically the case when the main added noise source of the output chain is amplifier noise (note that these assumptions were also verified experimentally). It can be shown that the expectation values of these joint photon moments is sufficient to uniquely reconstruct the density matrix of a multipartite state of N photonic qubits. While algebraic formulas relating the density matrix elements to the joint photon moments can be derived, we instead reconstruct the density matrix of generated photonic states via a maximum-likelihood estimation (MLE) algorithm that uses the obtained joint photon moments as input (for more details, see the next subsection).

MLE

We reconstruct the quantum state of the entangled microwave photons using a maximum-likelihood estimation (MLE) state tomography technique under the following assumptions: (1) the Fock spaces of the bosonic modes representing individual time-bin photonic qubits can be restricted to the single excitation manifold (i.e., the Hilbert space spanned by Fock states $|0\rangle$ and $|1\rangle$), and (2) the distributions of the sample means of the moments of the measured photonic fields are well approximated by normal distributions in the case of many samples (i.e., the statistical central limit theorem holds for the distributions of the means of these moments).

In statistics a likelihood functional $\mathcal{L}(D|H)$ is a function on a set D of observed statistical data sampled from a system which, assuming some underlying parameterization H of the system, returns a value proportional to the probability that the assumed parameterization would result in the observed data. Thus $\mathcal{L}$ encapsulates how “likely" a set of observations is under certain assumptions on the system. Given a dataset of observations D, MLE techniques aim to explore the space of parameterizations of a system to find the one that maximizes a chosen likelihood functional.

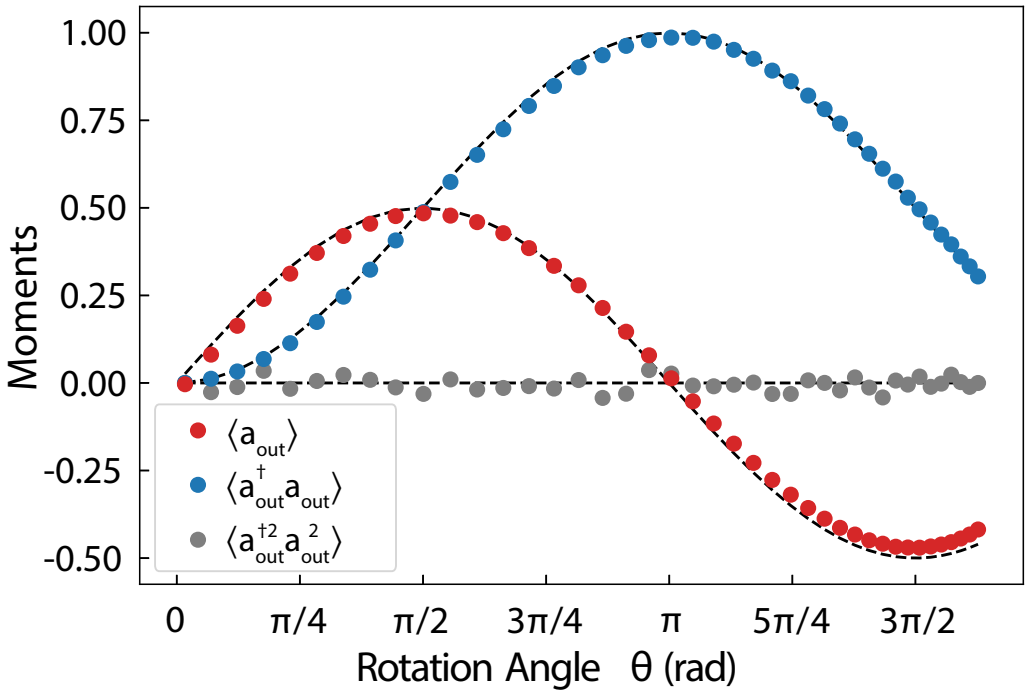

Figure F.2: Magnitude of measured moments $\langle a \rangle$ (red circles), $\langle a^\dagger a \rangle$ (blue circles), and $\langle (a^\dagger)^2 a^2 \rangle$ (gray circles), for emitted photon pulses from Q_E when it is prepared in state $|\psi\rangle_E = \cos(\theta/2)\,|e\rangle + \sin(\theta/2)\,|f\rangle$. Dashed black lines are ideal expected moments given a qubit rotation angle θ.

Our specified goal is to find the quantum state $\hat{\rho}$ of N photons that best approximates the actual photonic state we have prepared with our protocol. Thus to proceed with an MLE approach to this state tomography problem we must identify a dataset D we intend to collect and a likelihood functional $\mathcal{L}(D|\rho)$ over which we will optimize ρ.

To identify a sufficient dataset and associated likelihood functional for MLE state tomography of N entangled photons, note that for a single bosonic mode a constrained to the single excitation manifold, it suffices to know the expectation values $\langle a \rangle$, $\langle a^\dagger \rangle$, and $\langle a^\dagger a \rangle$ to uniquely reconstruct the quantum state of the mode. This is so because linear combinations of these operators along with the identity, when restricted to the Hilbert space of a two-level system, can reconstruct the single-qubit operators σ_x, σ_y, and σ_z whose expectation values uniquely determine an arbitrary single-qubit state. In a similar way, unique reconstruction of the state of a joint system of N bosonic modes each restricted to their single-excitation manifold can be accomplished if all 2^{2N} expectations of the joint moments of the system of the form $\left\langle (a_1^\dagger)^{n_1} a_1^{m_1} (a_2^\dagger)^{n_2} a_2^{m_2} \ldots (a_N^\dagger)^{n_N} a_N^{m_N} \right\rangle \; \forall\, n_i, m_i \in \{0, 1\}$ are known.

Consider $A_j \in \{(a_1^\dagger)^{n_1} a_1^{m_1} (a_2^\dagger)^{n_2} a_2^{m_2} \ldots (a_N^\dagger)^{n_N} a_N^{m_N}\}$ to be one of the 2^{2N} moments

of interest for such an N mode system. If we assume our system to be in the state ρ, then there will be an underlying distribution determined by ρ governing the statistics of measured values of A_j that will have some mean $\mu_j = \mathrm{Tr}\big(A_j\rho\big)$ and variance v_j. By the central limit theorem the sample mean of N measurements of A_j should, for large enough N, respect a normal distribution centered around $\mathrm{Tr}\big(A_j\rho\big)$ with variance v_j/N. This being the case, then the probability $p(\langle\bar{A}_j\rangle|\rho)$ of finding the sample mean of N measurements of A_j to be $\langle\bar{A}_j\rangle$ (we use the bar notation to emphasize that we are talking about a measured statistical value and not a calculated quantum mechanical expectation value), assuming a system state ρ, should obey [226]:

$$p(\langle\bar{A}_j\rangle|\rho) \propto e^{-|\langle\bar{A}_j\rangle - \mathrm{Tr}\left(A_j\rho\right)|^2/(v_j/N)}. \tag{F.2}$$

Assuming the actual variance v_j of the moment is very well approximated by the measured sample variance $\bar{v}_j$, which it should be for large N by the law of large numbers, then v_j can be safely replaced by the measured variance $\bar{v}_j$ in this expression.

Consequently we find that we can define a likelihood functional inspired by (F.2) that takes the form [227]

$$\mathcal{L}(D|\rho) = \prod_{j=1}^{j=2^{2N}} e^{-|\langle\bar{A}_j\rangle - \mathrm{Tr}\left(A_j\rho\right)|^2/\bar{v}_j} \tag{F.3}$$

This functional requires a dataset $D = \{(\langle\bar{A}_j\rangle,\ \bar{v}_j)\}_{j=1}^{j=2^{2N}}$ of measured sample means and variances of all the joint N photon moments considered above.

Because of the monotonically increasing nature of the logarithm, minimizing the negative log-likelihood is equivalent to maximizing the likelihood, and taking the negative of the logarithm of the likelihood yields

$$-\log\mathcal{L}(D|\rho) = \sum_{j=1}^{j=2^{2N}} |\langle\bar{A}_j\rangle - \mathrm{Tr}\big(A_j\rho\big)|^2/\bar{v}_j. \tag{F.4}$$

Intuitively we see that minimizing this negative log-likelihood corresponds to finding the state ρ whose moments minimize the mean-squared error of the measured moments, discounting the error associated with higher variance measured moments more than the error associated with low-variance measured moments. This optimization problem has the form of a quadratic programming problem subject to

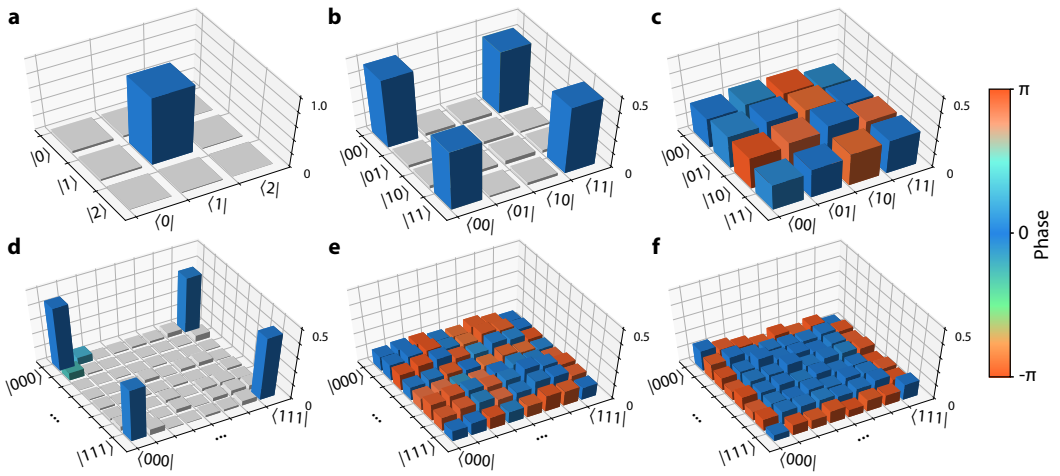

Figure F.3: **Reconstructed Density Matrices of Various Photonic States. a** Reconstructed density matrix of a prepared single-photon Fock state $|1\rangle$. ($F = 97\%$). Only here, the Hilbert space includes the two-photon manifold for a single mode in order to demonstrate the single photon character of photon emission. **b—f**, Reconstructed density matrices of a two-photon GHZ state ($F = 91\%$), a two-photon cluster state ($F = 91\%$), a three-photon GHZ state ($F = 83\%$), a three-photon 1D cluster state ($F = 90\%$), and a three-photon triangular cluster state (where there is all-to-all entanglement connectivity, $F = 73\%$). Note that time-delayed feedback was used to generate the three-photon triangular cluster state. The Hilbert space for each individual mode is truncated to the single-photon manifold. For each state, density matrix elements smaller than 10% of the expected largest density matrix element are colored gray for ease of visualization. Note that global offset phases associated with each photon are adjusted via software in order to arrive at the density matrices plotted here; this amounts to local-Z corrections on the states.

physicality constraints on the quantum state ρ (namely that ρ be trace-one and positive semidefinite):

$$\begin{aligned} \min_{\rho} \quad & -\log \mathcal{L}(D|\rho) \\ \text{s.t.} \quad & \mathrm{Tr}(\rho) = 1 \\ & \rho \succ 0. \end{aligned} \tag{F.5}$$

To perform this optimization over valid states ρ of an N mode system we use the CVXPY python library [228].

Quantum-State Tomography Results

In addition to the quantum-state tomography results of Figure 5.5, we present in Figure F.3 and F.4 reconstructed density matrices for other generated multipartite entangled photonic states (along with their associated fidelities), in order to illustrate the flexibility of our photonic state generation method. We bring particular attention to the 5-photon state illustrated in Figure F.4c, with measured density matrix in

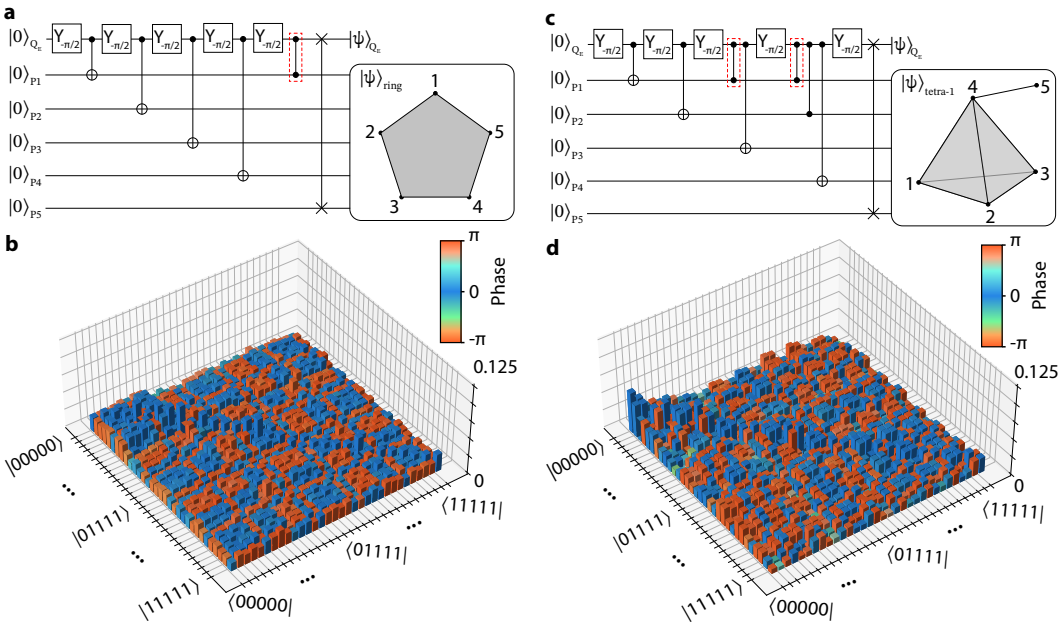

Figure F.4: **Five-Photon Cluster State with Multiple Time-Delayed Feedback Events.** **a** Quantum circuit for the generation of the five-photon cluster state $|\psi_{\text{ring}}\rangle$. In this state, the entanglement structure forms a pentagon, as shown in the diagrams at the end of the quantum circuits. **b** Reconstructed density matrix of the $|\psi_{\text{ring}}\rangle$ state. The fidelity of the generated state is $F = 61\%$. Note that the data for this state was taken in a separate cooldown, and due to techincal reasons, the absolute power calibration we used was acquired from the integrated flux of a prepared single photon state. **c** Quantum circuit for the generation of the five-photon cluster state $|\psi_{\text{tetra}-1}\rangle$. In this state, the entanglement structure of the first four photons (photon 1—4) forms a tetrahedron, and the photon 5 is entangled to photon 4, as shown in the diagram on the right. Two time-delayed feedback events on photon 1 (corresponding the the highlighted CZ gates) entangle photon 1 with both photon 3 and photon 4. **d** Reconstructed density matrix of the $|\psi_{\text{tetra}-1}\rangle$ state. The fidelity of the generated state is $F = 50\%$. Note that the global phases associated with each photon are adjusted via software in order to arrive at the plotted density matrices.

Figure F.4d. In order to generate this state, it was necessary to perform multiple CZ gate operations, including two CZ gate operations for photon 1. Such use of *two* time-delayed feedback events for an emitted photon is the most fundamental prerequisite for extending our 2D cluster state generation scheme to generation of 3D cluster states [91, 181, 182]. Thus, generation of the 5-photon state illustrated in Figure F.4, via multiple time-delayed feedback events, constitutes a preliminary demonstration of the adaptability of our platform for future generation of 3D cluster states of microwave photonic qubits. We also note that the 97% fidelity of the density matrix shown in Figure F.3a of a prepared single-photon Fock state constitutes the quantum efficiency of our Q_E single-photon source (measurement errors notwithstanding), and that the reconstructed density matrix reveals our source's emission has negligible two-photon character.

We conclude this Appendix section by describing some technical details of our

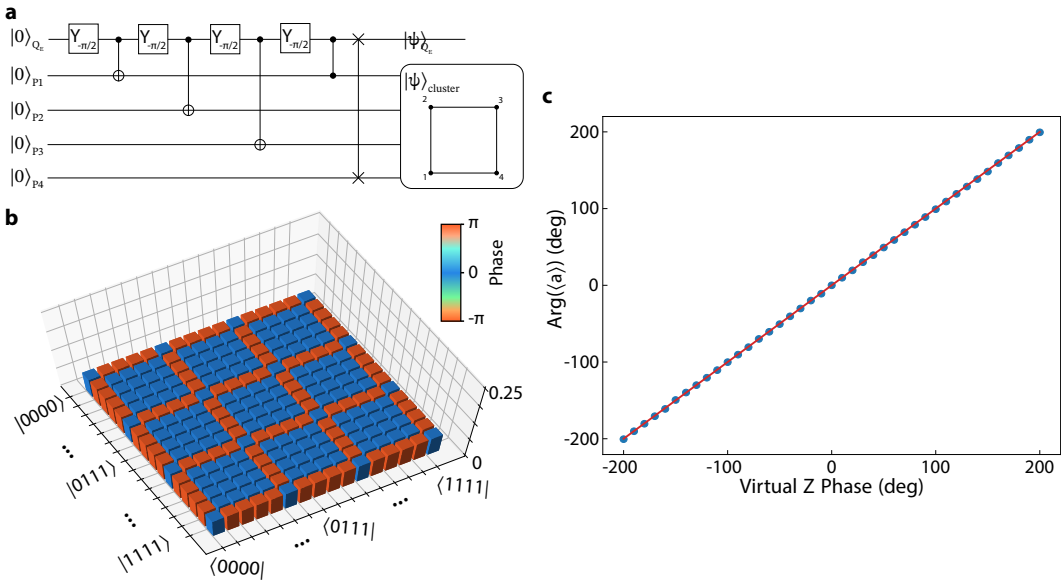

Figure F.5: **Phase Control of Cluster State.** **a** Quantum circuit of cluster state generation protocol, assuming Q_E and photonic states prepared in ground state. **b** Ideal cluster state obtained from the quantum circuit of **(a)**. **c** Measured phase of single photon moment $\langle a \rangle$ as a function of the phase of virtual-Z gates applied to Q_E during generation (blue circles). Red line shows ideal expected phase. Virtual-Z gates applied on Q_E are realized by adding an offset phase to π_{ef} pulses before photon emission.

radiation field tomography measurements that may be of interest to the reader. Firstly, we note that when generating photonic states, lingering gate errors due to the AC Stark shifting of the $|e\rangle \rightarrow |f\rangle$ transition, as well as the use of flux modulation, will result in spurious phases gained by the qubit, which will be imparted onto the phase of emitted photons. This phase, however, is deterministic, and thus can be compensated in hardware by suitable qubit Z-control. For the density matrix presented in Figure 5.5d, these spurious phases were compensated for by the use of Virtual Z-gates [229] when performing π_{ef} pulses before emission of every photon. Thus, we were able to generate the state whose ideal counterpart is shown in Figure F.5b, and the 70% state fidelity quoted in Chapter 5 is calculated with respect to this state. We also note that while these spurious phases correspond to local Z-gates for every photon, which can be removed from the processed tomography data, in practice they could hinder use of such cluster states in quantum information applications. Thus, we chose to demonstrate this additional photon phase control in our generation process, and we stress that the data presented in Figure 5.5d did not have any post-processing phase modification.

In addition, the measured $\left\langle h_i^\dagger h_i \right\rangle$ moments reveal an effective added noise photon

number of $n_{\text{noise}} \approx 3.5$, corresponding to a quantum measurement efficiency of the output chain of $\eta_{\text{meas}} = (1+n_{\text{noise}})^{-1} \approx 0.22$. We note that for heterodyne detection, a finite detection efficiency η_{det} can be shown to be equivalent to added noise in the output chain, and we believe that the majority of n_{noise} can be attributed to losses and spurious reflections before the TWPA (where we estimate a total transmissivity for emitted photon pulses of -5.5dB).

Furthermore, we note that the scaling factor G will be slightly different for photons of different bandwidth. This is due in part to slight differences in the effective transmission coefficient of the tapered end of the SLWG for different bandwidth pulses (see Figure E.1d). Moreover, higher bandwidth pulses will have slightly higher mode-matching inefficiency due to dispersion-induced distortion, which results in a small fraction of the pulse being situated outside of its measurement time-bin window. When generating photonic states we use up to two different bandwidths, and we quantify the difference in their respective G scaling factors by taking the ratio of their measured $\langle a^\dagger a \rangle$ moments when the qubit is fully excited to the $|f\rangle$ state before emission. We find a $\sim 5\%$ difference between the two G scaling factors, which we take into account for calculation of joint photon moments (we use the G obtained from Stark shift measurements for the lower bandwidth photon pulses) .

Finally, for generation of four photon and five photon states, we performed 500 million and 2 billion single-shot measurements, respectively, in order to have sufficient averaging for higher order joint-photon moments; these numbers are consistent with the predicted number of single-shot measurements required from the statistical analysis presented in Ref. [230]. This corresponded to measurement times of 6 hours and 24 hours, respectively; and due to the presence of slow qubit frequency drifts of ~ 0.5 MHz in our experimental setup, we recalibrated the qubit flux bias every hour during these long measurements. We expect that the use of GPU or FPGA based methods for data processing would significantly reduce these measurement times. Nevertheless, we note that full tomography of a photonic state of five itinerant microwave photons has hitherto never been demonstrated until now.

F.2 Process Tomography of the Time-Delayed Feedback Operation

QPT Experiment Design

In order to characterize the qubit-photon CZ gate implemented with our time-delayed feedback protocol, we perform full quantum process tomography (QPT) of the qubit-photon interaction. We again limit the Hilbert space of the bosonic

mode representing the itinerant photon to the single-excitation subspace, so the implemented CZ gate can be considered as a quantum process mapping the Hilbert space of an effective two qubit system to itself.

With this in mind, in characterizing our CZ implementation we are interested in the set of quantum processes that maps two-qubit states to two-qubit states. Such processes (outside of certain cases in which we are not concerned here, e.g., projective measurements) are described by the set of completely-positive trace-preserving (CPTP) linear maps from two-qubit density matrices to two-qubit density matrices. [87].

Performing quantum process tomography requires identifying a complete set of "fiducial" input states of the system and an "informationally complete" set of measurement operators [87, 231]. A complete fiducial set of input states on a d-dimensional Hilbert space $\mathcal{H}$ is a set of d^2 states whose density matrices span the space of density matrices on $\mathcal{H}$. An informationally complete set of measurement operators $\{M_j\}$ is a set of $d^2 - 1$ operators on $\mathcal{H}$ whose expectation values given a state ρ, $\{\mathrm{Tr}(M_j\rho)\}$, uniquely determine ρ.

As our set of d^2 fiducial input states we select all 16 possible unentangled states of the form $|\psi_q\rangle \otimes |\phi_p\rangle$ where $|\psi_q\rangle \in \{|+z\rangle_q, |-z\rangle_q, |+x\rangle_q, |+y\rangle_q\}$ and $|\psi_p\rangle \in \{|+z\rangle_p, |-z\rangle_p, |+x\rangle_p, |-y\rangle_p\}$ (where we are using the conventional names for eigenstates of the Pauli spin operators σ_x, σ_y, σ_z). For our informationally complete set of measurement operators we select the 15 non-identity joint qubit-photon correlators of the form $\sigma_i \otimes a^{\dagger n} a^m$ (where $n, m \in \{0, 1\}$ and $\sigma_i \in \{\mathbb{I}, \sigma_x, \sigma_y, \sigma_z\}$). The expectations of these operators can be shown to uniquely specify any of the joint qubit-photon states we are considering in our effective two-qubit Hilbert space [227]. To measure the expectations of these operators for a given prepared state, we perform single-shot heterodyne measurements of the microwave field in conjunction with single-shot measurements of the qubit polarization (after rotation to the appropriate basis). This allows us, on a shot-by-shot basis, to compute the correlations between the microwave field moments and the qubit polarization operators.

The experimental sequence of our QPT implementation can be seen in Figure F.6. We begin with Q_E and the photonic qubit in their respective ground states, after which we prepare the state of the photonic qubit by performing an X_π^{ge} pulse on Q_E, followed by one of an X_π^{ef} pulse, an $X_{\pi/2}^{ef}$ pulse, an $Y_{\pi/2}^{ef}$ pulse, or no pulse ($\mathbb{I}^{ef}$), following which we use a flux modulation tone to induce shaped emission of the photonic time-bin qubit from Q_E. This results in the initialized photonic time-bin

qubit state to be conditioned on the choice of ef pulse, resulting in the states $|1\rangle$, $|-y\rangle$, $|+x\rangle$, or $|0\rangle$ respectively, while Q_E ends in state $|e\rangle$ after flux modulation.

Before the photonic qubit finishes its propagation through one round trip of the waveguide, we prepare Q_E in one of its four above specified cardinal states. When the photonic qubit finally returns to Q_E, both subsystems have been properly prepared and the CZ gate between the two proceeds by way of our time-delayed feedback interaction. After the CZ is completed the photonic time-bin qubit leaves the waveguide where it is amplified, and its two independent I and Q quadratures are measured via heterodyne detection. The Q_E state is also measured along one of the three chosen polarization axes defining which qubit polarization operator σ_i we are measuring. Note that the emitter state preparation is deferred until immediately prior to the onset of time-delayed feedback, after the itinerant photon has travelled almost the entire round-trip length of the SLWG, in order to minimize the amount of dephasing suffered by Q_E before the CZ gate.

We perform the above control sequence for all 16×3 combinations of prepared states and possible values of σ_i. Note that, for example, while the experimental sequence corresponding to measuring $\sigma_x a$ and $\sigma_y a$ require different qubit basis rotation pulses, the nature of heterodyne measurement of the microwave field means a single experiment can be used to measure all four quantities $\{\sigma_x, \sigma_x a, \sigma_x a^\dagger, \sigma_x a^\dagger a\}$. We thus perform 48 different experiments (each repeated many times) to compute the $16 \times 15 = 240$ different expectations of the form $\langle \sigma_i \otimes a^{\dagger n} a^m \rangle$ that uniquely specify each output state of the implemented CZ gate for each input state.

MLE

Once this data is collected, we perform a maximum-likelihood reconstruction of the time-delayed feedback operation to find the most likely quantum process approximating it. To do this we represent the quantum process $\mathcal{E}$ underlying the time-delayed feedback operation as its χ matrix in the Pauli Product basis of 2 qubits, whereby its action on a general input state is given by:

$$\mathcal{E}(\rho) = \sum_{n,m} \chi_{n,m} P_n \rho P_m^\dagger. \tag{F.6}$$

The quantity χ is a 16×16 Hermitian, positive-semidefinite matrix, and $\{P_j\}$ is some enumeration of the 2 qubit Pauli group. With this representation of the time-delayed feedback process, we use the python library CVXPY [228] to minimize the negative

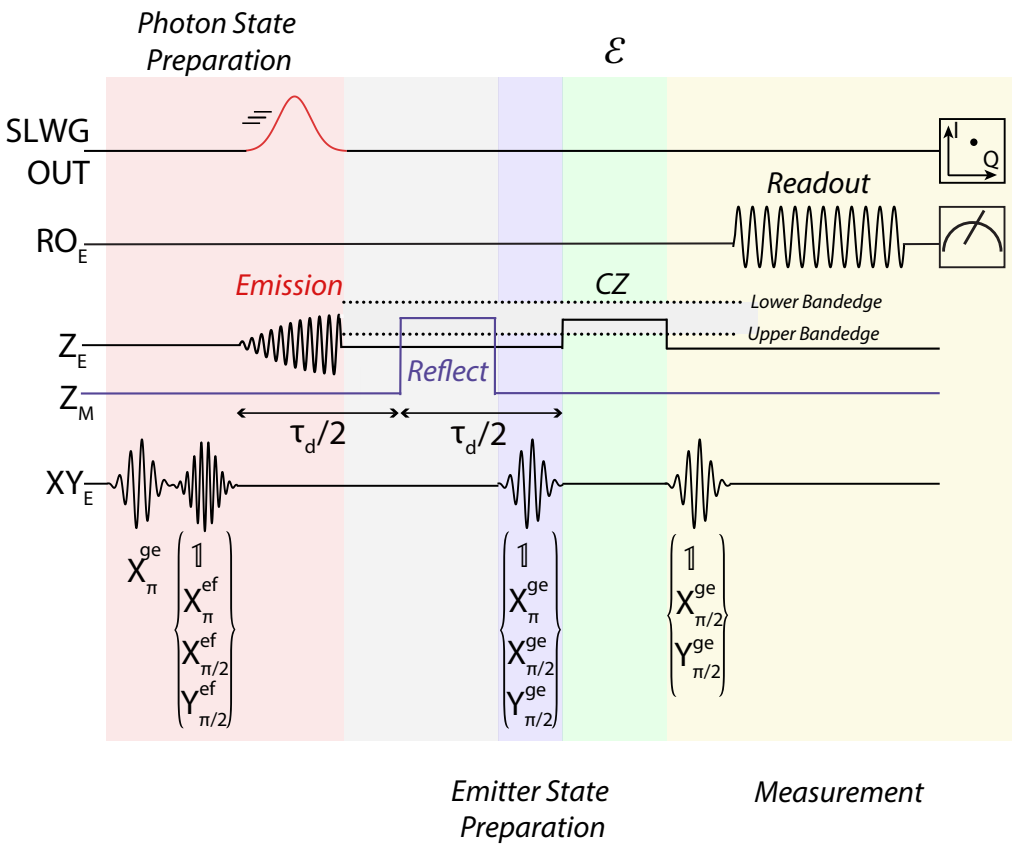

Figure F.6: **Experimental Pulse Sequence for QPT.** A schematic for the pulse sequences that implement the QPT protocol for characterizing our CZ implementation. The shaded regions of different coloration represent different subsequences of the QPT protocol indicated by the italic text above or below the figure (the grey region is time during which the photonic qubit propagates through one round-trip of the waveguide). The bracketed lists of gates below the pulses on the $\mathrm{XY_E}$ line represent variable pulses corresponding to different photonic qubit state preparations (red region), Q_E state preparations (blue region), and Q_E measurement basis rotations (yellow region).

log-likelihood functional of the dataset of qubit-photon correlator expectations given the CZ process $\mathcal{E}$:

$$-\log \mathcal{L}(D|\chi) = \sum_{i=1,j=1}^{i=15,j=16} |\langle \bar{M}_{ij} \rangle - \mathrm{Tr}\big(M_j \; \mathcal{E} \circ \mathcal{B}_i(\rho_0)\big)|^2 / v_{i,j}, \tag{F.7}$$

where $\rho_0 = |0\rangle\langle 0|_q \otimes |0\rangle\langle 0|_p$ is the initial state of the joint qubit-photon system, assumed to be the ground state of both systems, M_j is the j^{th} qubit-photon correlator, $\mathcal{B}_i$ is the i^{th} generalized state preparation superoperator (explained in more detail below), $\langle \bar{M}_{ij} \rangle$ is the measured sample mean of M_j given state preparation $\mathcal{B}_i$, and $\bar{v}_{i,j}$ is the sample variance of $\langle \bar{M}_{i,j} \rangle$. The free parameters available to the optimization are the elements of χ implicitly contained in the computation of $\mathcal{E} \circ \mathcal{B}_i(\rho_0)$ above.

The choice of this log-likelihood follows from exactly the same arguments as the state tomography log-likelihood functional Equation (F.4) given in Appendix F.1, extended to the case of 16 simultaneous sets of state tomography data for the 16 states $\mathcal{E} \circ \mathcal{B}_i(\rho_0)$. Enforcing the CPTP physicality constraints on $\mathcal{E}$ defines the quadratic programming optimization problem for finding the most-likely Pauli-Product representation of $\mathcal{E}$, $\hat{\chi}$:

$$\begin{aligned} \min_{\chi} \quad & -\log \mathcal{L}(D|\chi) \\ \text{s.t.} \quad & \sum_{n,m} \chi_{n,m} P_m^\dagger P_n = \mathbb{I} \\ & \chi \succ 0. \end{aligned} \tag{F.8}$$

After the χ matrix representing our CZ implementation has been reconstructed we find the CZ gate that it most closely approximates modulo any simultaneous local Z operations on either Q_E or the photonic time-bin qubit. These local Z gates can be removed in software and do not quantitatively alter the entangling nature of the CZ gate we are implementing, and thus have no impact on the $\mathrm{Tr}\left(\sqrt{\sqrt{\chi_{\mathrm{CZ}}}\chi_{\mathrm{ideal}}\sqrt{\chi_{\mathrm{CZ}}}}\right)^2$ figure of merit we use to characterize the gate.

Generalized state-preparation superoperator

It is well-documented that QPT can suffer significantly from so-called state preparation and measurement (SPAM) errors, wherein errors during preparation of the QPT input states and errors during measurement are interpreted by the tomographic reconstruction method as errors on the process itself. We find two sources of state-preparation error that we are able to correct for systematically by substituting idealized state preparation unitaries for more general state preparation superoperators. These sources of error are the initial thermal population of Q_E prior to the application of any state preparation control pulses, which by gate set tomography of Q_E (we use the Python library pyGSTi [232] for this) we estimate to be $\sim 1\%$, and the round trip loss of $\sim 13\%$ that the itinerant microwave photon suffers between emission and reinteraction with Q_E.

To account for these errors we define the generalized state-preparation super operators $\{\mathcal{B}_i\}$, each of which we factorize as the composition of three different processes:

$$\mathcal{B}_i = \mathcal{R} \circ \mathcal{U}_i \circ \mathcal{P}. \tag{F.9}$$

The process $\mathcal{U}_i$ corresponds to the i^{th} ideal state preparation, the process $\mathcal{P}$ models the 1% initial thermal population of Q_E, and the process $\mathcal{R}$ models the 13% round

trip loss of the itinerant microwave photon. $\mathcal{P}$ can be implemented by a pin map on the emitter qubit's Hilbert space: $\mathcal{P}(\rho_q) = 0.99\,|0\rangle\langle 0| + 0.01\,|1\rangle\langle 1|$ for all ρ_q. $\mathcal{R}$ can be modeled by a relaxation channel on the photonic qubit's Hilbert space with loss parameter $l = 0.13$. The preparation process $\mathcal{U}_i$ is given by the ideal processes implementing the pulse sequences in the red and blue shaded regions of Figure F.6 (ie: photonic qubit state preparation and Q_E state preparation).

Readout Error Correction

In the same way that it is possible to correct for certain characterized state preparation errors, it is also possible to correct for qubit readout measurement errors that obey certain assumptions. By computing the confusion matrix of the single-shot Q_E state measurement, we can correct for identifiable readout misclassification errors that give rise to erroneous values for qubit-photon correlator expectations.

Consider the quantity $\langle \sigma_z a \rangle$. This expectation can be computed from measured data in the following way:

$$\langle \sigma_z a \rangle = \tilde{p}(+1)\langle \tilde{a} \rangle|_{\sigma_z=+1} - \tilde{p}(-1)\langle \tilde{a} \rangle|_{\sigma_z=-1}, \tag{F.10}$$

where $\tilde{p}(+1)$ denotes the proportion of single-shot measurements for which the qubit polarization along the z quantization axis was found to be +1, and $\langle \tilde{a} \rangle|_{\sigma_z=+1}$ denotes the average value of the single shot field measurements in these same cases; with a similar computation for the -1 case.

Due to the fact that there are probabilities of mismeasurement of the qubit polarization, which we characterize in Appendix E.1, the quantity $\tilde{p}(+1)\langle \tilde{a} \rangle|_{\sigma_z=+1}$ itself should be written as:

$$\begin{aligned} \tilde{p}(+1)\langle \tilde{a} \rangle|_{\sigma_z=+1} = {} & p(+1|+1)p(+1)\langle a \rangle|_{\sigma_z=+1} \\ & + p(+1|-1)p(-1)\langle a \rangle|_{\sigma_z=-1}, \end{aligned} \tag{F.11}$$

where $p(+1|+1)$ corresponds to the probability of measuring a qubit polarization of +1 when the polarization was in fact +1, $p(+1)$ is the actual probability that an ideal measurement would have yielded a polarization of +1, and $\langle a \rangle|_{\sigma_z=+1}$ is the actual expected value of the field conditioned on the qubit polarization along z being +1. There is a similar expression for $\tilde{p}(-1)\langle \tilde{a} \rangle|_{\sigma_z=-1}$:

$$\begin{aligned} \tilde{p}(-1)\langle \tilde{a} \rangle|_{\sigma_z=-1} = {} & p(-1|+1)p(+1)\langle a \rangle|_{\sigma_z=+1} \\ & + p(-1|-1)p(-1)\langle a \rangle|_{\sigma_z=-1}. \end{aligned} \tag{F.12}$$

These two expressions can be combined into a simple linear relationship between the measured quantities $\tilde{p}(+1)\langle\tilde{a}\rangle|_{\sigma_z=+1}$ and $\tilde{p}(-1)\langle\tilde{a}\rangle|_{\sigma_z=-1}$ and the "premeasurement" undistorted quantities $p(+1)\langle a\rangle|_{\sigma_z=+1}$ and $p(-1)\langle a\rangle|_{\sigma_z=-1}$:

$$\begin{pmatrix} \tilde{p}(+1)\langle\tilde{a}\rangle|_{\sigma_z=+1} \\ \tilde{p}(-1)\langle\tilde{a}\rangle|_{\sigma_z=-1} \end{pmatrix} = C \begin{pmatrix} p(+1)\langle a\rangle|_{\sigma_z=+1} \\ p(-1)\langle a\rangle|_{\sigma_z=-1} \end{pmatrix}, \tag{F.13}$$

where C is given by the confusion matrix

$$C = \begin{pmatrix} p(+1|+1) & p(+1|-1) \\ p(-1|+1) & p(-1|-1) \end{pmatrix}. \tag{F.14}$$

This confusion matrix can be measured under the assumption of perfect state preparation by preparing the qubit many times in the ground or excited state, performing a single-shot measurement of Q_E's state, and counting the relative proportions of ground and excited measurements given a particular state preparation. This matrix C can then be inverted and applied to the erroneous conditional photon moments to give the correct moments:

$$\begin{pmatrix} p(+1)\langle a\rangle|_{\sigma_z=+1} \\ p(-1)\langle a\rangle|_{\sigma_z=-1} \end{pmatrix} = C^{-1} \begin{pmatrix} \tilde{p}(+1)\langle\tilde{a}\rangle|_{\sigma_z=+1} \\ \tilde{p}(-1)\langle\tilde{a}\rangle|_{\sigma_z=-1} \end{pmatrix}, \tag{F.15}$$

from which the correct qubit photon correlators can be computed.

State Fidelity Confidence Intervals

The 70% state reconstruction fidelity relative to an ideal target cluster state is quoted with a 95% confidence interval [69.1%, 70.4%] in Chapter 5. We computed this confidence interval using a parametric bootstrapping protocol [233] that involved fitting the distributions of the measured photonic correlations and resampling the fit distributions to reconstruct 1000 bootstrap states. Each distribution of a measured photonic correlation contains 5000 points, where each point is computed from an average of 100,000 single-shot field measurements. Thus corresponding to each moment was an approximately normal histogram of these 5000 values. These histograms could be fit and resampled to reconstruct bootstrapped versions of the generated cluster state. We reconstructed 1000 bootstrap copies this way, and for each copy we computed the fidelity relative to the target cluster state. Then we sorted these fidelities and approximated the 95% confidence interval by taking the 25^{th} element of this sorted list fidelity as the lower bound of the 95% confidence interval and the 975^{th} element as the upper bound.

Appendix G

HETERODYNE MEASUREMENT OF ITINERANT MICROWAVE PHOTONS - ADDITIONAL DETAILS

In this appendix section we expand on the discussion of heterodyne measurement of itinerant microwave photons discussed in Appendix F.1. Note that in the entire following discussion, we refrain from using the “hat symbol" in equations involving quantum operators.

G.1 Heterodyne Measurement

Basics

In our experiment, itinerant photons are generated via emission of the emitter qubit Q_E into the output mode of the slow-light waveguide a_{out}. This emission will consist of a traveling wavepacket, which is a multi-mode state that in general may be written as $|\psi\rangle = \int d\omega f(\omega) a^\dagger_{\text{out}}(\omega) |\text{vac}\rangle$, where $|\text{vac}\rangle$ is the vacuum state with no excitation in any of the modes. We may define a photon wavepacket creation operator $a^\dagger$, where [234]

$$a^\dagger = \int f(\omega) a^\dagger_{\text{out}}(\omega) d\omega = \int f(t) a_{\text{out}}(t) dt, \tag{G.1}$$

and the equivalence of the frequency and time-dependent forms is easily established by use of the Fourier transforms of the functions in the integrands. Note that the time-dependent field $a_{\text{out}}(t)$ is what is continuously sampled in the experiment after quantum-limited amplification. The functions in the integrand are normalized, such that the commutation relation $[a, a^\dagger] = 1$ is satisfied when $\int |f(t)|^2 dt = 1$ (note that the commutation relation of the output field is $[a_{\text{out}}(t), a^\dagger_{\text{out}}(t')] = \delta(t - t')$). As discussed in Appendix F.1, we obtain the *time-independent* statistics associated with a via integration of the measured field against $f(t)$, which is given by the temporal shape of the traveling wavepacket. Finally, we point out to the reader that although quantum optical theory is typically described in the context of distinct single-frequency modes, one may equivalently consider a basis of distinct time-dependent “wavepacket" modes, and the mapping between the two is achieved simply by change of basis transformation given by a unitary matrix; for more information on multi-mode quantum optics, we refer the reader to Refs. [234, 235].

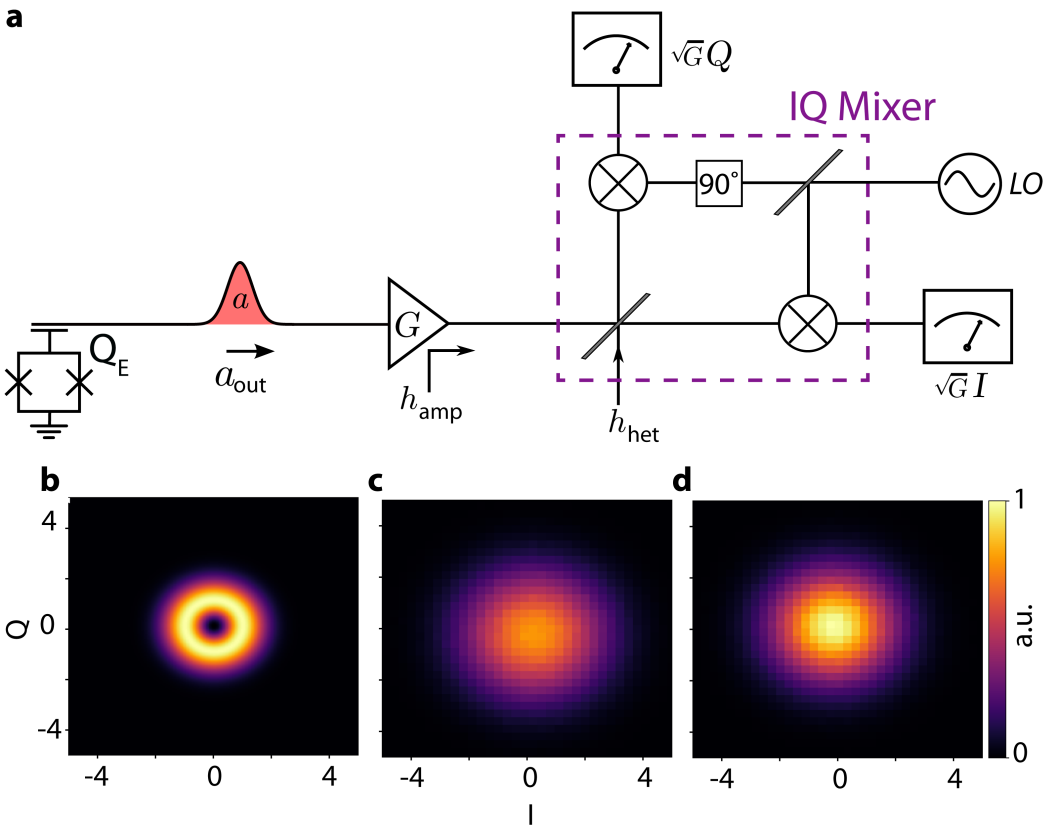

Figure G.1: **Heterodyne Detection of Microwave Fields a** Schematic of heterodyne detection as is typically performed in circuit QED experiments. Emitted fields are amplified by an amplification chain (here represented as a single amplifier) that imparts added noise h_{amp} to the output mode a_{out}. The resultant signal then enters an IQ mixer, where it is split and subsequently mixed with an LO signal. This splitting imparts 1/2 photon of additional noise h_{det} to the measured signal through the unused splitter port; however the added amplifier noise will tend to dominate h_{det}. This measurement allows both quadratures of the field to be measured. **b** Ideal Husimi Q-function of a single-photon Fock state $|1\rangle$. **c** Experimentally measured phase-space distribution for the prepared state $|1\rangle$, where the heterodyne measurement suffered from added noise corresponding to a thermal population of $n_{\text{noise}} \approx 3.5$ noise photons. **d** Experimentally measured phase-space distribution for the prepared state $|0\rangle$, corresponding to the "dark measurement" of the noise mode h; see Appendix text for further details.

We measure the output field $a_{\text{out}}(t)$ through heterodyne detection, which allows us to measure both quadratures of the field. Heterodyne measurement consists of splitting the output field via a beam-splitter (or its microwave equivalent), and "mixing" the output field on both arms of the beam splitter with a detuned strong local oscillator field; see Figure G.1a. By having the phase of the local oscillator field used for mixing differ by 90° for the outputs of each beam splitter arm, we can measure both conjugate quadratures of the field. However, the output field measured will consist of the emitted wavepacket as well as added noise: $a_{\text{out}}(t) + h^{\dagger}_{\text{out}}(t)$.

Noise in Heterodyne Detection

In general, there are three main contributions to added noise in heterodyne detection. The first contribution is the vacuum noise that enters through the unused port of the beam splitter, referred to as h_{het} in Figure G.1a. This will add $1/2$ quanta of added noise to the signal. Fundamentally, one may consider this additional "vacuum noise" h_{het} as the "physical source" of the additional measurement uncertainty associated with the simultaneous detection of two non-commuting conjugate variables, as per Heisenberg's uncertainty principle.

The second contribution to $h^{\dagger}_{\text{out}}(t)$ is the noise added from amplification of the signal. For a generic phase-insensitive linear amplifer with gain G, the input signal is transformed according the following relation [236]:

$$a_{\text{out}} \rightarrow \sqrt{G}a_{\text{out}} + \sqrt{G-1}h^{\dagger}_{\text{amp}}, \tag{G.2}$$

where h_{amp} is an additional bosonic mode accounting for the noise added by the amplifier. For a quantum limited amplifier, h_{amp} will be in the vacuum state, thus corresponding to an additional $1/2$ quanta of added noise to the signal. However, we stress that the magnitude of the quantum-limited amplifier added noise is $1/2$ quanta *when referred to the input of the amplifier*, and it is much larger (by a factor of $\sqrt{G-1}$) when finally reaching the heterodyne measurement stage. Thus, for a signal that is both amplified and undergoes heterodyne detection, the total added noise, referred to the input of the amplifier, will be

$$h_{\text{out}} = \sqrt{\frac{G-1}{G}}h_{\text{amp}} + \sqrt{\frac{1}{G}}h_{\text{het}}. \tag{G.3}$$

In the limit of large gain $G \gg 1$, the contribution to the added noise from h_{amp} overwhelmingly dominates the added noise intrinsic to heterodyne detection h_{het}, and thus we may neglect h_{het} when the measured field is substantially amplifed (phase-insensitively) before heterodyne detection. Naturally, this implies that if a phase-insensitive amplifier is used, measurement of either one or both quadratures of the field will effectively have the same signal-to-noise ratio; thus both quadratures of the field may be measured at no additional cost of added noise. Thus, heterodyne detection of an emitted field will have *at a minimum* $1/2$ quanta of added noise (whether the field is amplified or not).

The third contribution to the added noise will be detection inefficiencies of the measurement; where for the measurement of amplified fields this detection inefficiency primarily consists of loss before the first amplifier of the output chain. Theoretically, it can be shown that heterodyne measurement with sub-unit detection efficiency is equivalent to heterodyne measurement with added (thermal) noise beyond the aforementioned $1/2$ quanta added noise lower bound [237]. One can gain a practical intuition for this fact by considering the data processing for our experiment described in Appendix F.1. The output field is continuously sampled at the digitizer, and we convert voltage at the digitizer to field amplitude at the qubit via a conversion scaling factor G, which is measured via an absolute power calibration experiment such as AC-Stark Shift measurements of the qubit frequency. The key point is that the obtained G will be affected by losses before the first amplifier (because this loss will lower the measured digitizer voltage commensurate with a given field amplitude at the qubit), but the *physical* amount of amplifier added noise will not be affected by losses before the first amplifier (because this noise is added from the amplifier itself). However, because we apply the scaling factor G to measured digitizer voltages that simultaneously consist of emitted fields as well as added noise fields, by "scaling out" the detection inefficiency loss of the measured emitted fields, this scaling effectively increases the magnitude of measured added noise fields (which did not suffer this loss before the first amplifier). Thus in this manner, the added noise measured during heterodyne detection is higher due to sub-unit detection efficiency. Moreover, note that the inverse relationship is also true: heterodyne measurement with added (thermal) noise is equivalent to heterodyne measurement with sub-unit detection efficiency [237].

Another contribution to detection inefficiency is mode-matching inefficiency. As shown in Equation G.1, time-independent statistics associated with the itinerant mode a are obtained from a measured time-dependent field via the mode matching function $f(t)$. Ideally, $f(t)$ is given by the temporal shape of the itinerant mode, and is experimentally obtained through measurement of $\langle a_{\text{out}}(t)\rangle$. However, if this measurement is imperfect, or if for practical reasons part of the emitted field is outside of the measurement time-bin window (as discussed in Appendix E.1), then an imperfect or truncated $f(t)$ will lead to an effective "mode-matching loss" of the itinerant mode when used in the data processing discussed. This "mode-matching loss" will have the same effect as loss before the first amplifier, as discussed above.

The detection efficiency η_{meas} of the heterodyne measurement is thus given by

$\eta_{\text{meas}} = (1 + n_{\text{noise}})^{-1}$, where n_{noise} consists of physical added noise beyond the $1/2$ noise quanta lower bound, as well as "effective" added noise due to losses before the first amplifier and mode-matching inefficiency. The factor of "1" in the denominator reflects the minimum "uncertainty" in the heterodyne measurement of a field, which is comprised of intrinsic vacuum fluctuations of the field, as well the additional $1/2$ quanta of added noise intrinsic to quantum limited amplification or measurement of two non-commuting quadratures.

Correspondence to Quasi-Probability Distribution of the Field

In practice, in order to perform tomography of an itinerant photon through heterodyne detection, we have to obtain its phase-space distribution in the IQ plane, from which we can extract the quantum statistics of the field. We obtain this phase-space distribution through many single-shot heterodyne measurements of the field (via preparing multiple copies of the field). For every single-shot measurement of the measured field $S_{\text{out}}(t) = a_{\text{out}}(t) + h^{\dagger}_{\text{out}}(t)$, we integrate the measured time-dependent field against the emitted photon's mode-matching function $f(t)$. This integration $\int f(t) S_{\text{out}}(t) dt = I + iQ = S$ can be shown to yield single-shot measurements of the complex quantity $S = a + h^{\dagger}$, where a is the wavepacket mode of interest. By collecting many such measurements, we obtain the phase-space distribution in the IQ plane of S, which we henceforth refer to as $D(S)$. An example of an experimentally measured $D(S)$ is shown in Fig G.1c.

In the limiting case of ideal heterodyne detection where we have $\eta_{\text{meas}} = 1$, it can be shown that the measured IQ plane phase space distribution $D(S)$ is given by the Husimi-Q function[237]

$$Q(\alpha) = \frac{1}{\pi} \langle \alpha | \rho | \alpha \rangle, \tag{G.4}$$

where $|\alpha\rangle = e^{-|\alpha|^2/2} \sum_n \frac{\alpha^n}{n!} |n\rangle$, $\alpha = I + iQ$, and ρ is the density matrix of the itinerant microwave photon. The Husimi-Q function is non-negative and normalized to 1, and for a given radiation field state ρ, $Q(\alpha)$ is the probability of measuring α when performing a heterodyne measurement of the state ρ. Nevertheless, it is still considered a "quasi-probability" because since different coherent states are not orthogonal, measurement of two different α do not represent two mutually exclusive measurements.

For further insight into the properties of the Husimi Q-function, consider the func-

tional forms of $Q(\alpha)$ in the IQ plane for the vacuum state $|0\rangle$, the Fock state $|1\rangle$, and the coherent state $|\beta\rangle$. Calculation via formula G.4 yields $e^{-(I^2+Q^2)}$, $e^{-(I^2+Q^2)}(I^2+Q^2)$, and $e^{-\left((I-I_\beta)^2+(Q-Q_\beta)^2\right)}$ respectively, where $\beta = I_\beta + iQ_\beta$. Inspection of these functional forms reveals that $Q(\alpha)$ for the vacuum state becomes a two-dimensional Gaussian distribution with variance equal to 1 centered around the origin, while for the coherent state its $Q(\alpha)$ is simply the vacuum Husimi function displaced by β in the IQ plane. Half of this variance is due to the intrinsic vacuum fluctuations of the field of the $|0\rangle$ and $|\beta\rangle$ states, while the other half is due to the minimal added measurement "uncertainty" when measuring the two conjugate quadratures of the field. Likewise, Fock states also have intrinsic vacuum fluctuations of their field ($\langle n|E|n\rangle = 0$, $\langle n|E^2|n\rangle \sim \hbar\omega(n+\frac{1}{2})$, where E is the electric field operator). Thus, the functional form of $Q(\alpha)$ for the Fock state $|1\rangle$ consists of the functional form of a *ring* broadened by the same Gaussian with variance 1, where the ring shape in the IQ plane is reflective of the fact that Fock states have a well defined photon number (i.e., a well-defined field "intensity") but complete phase uncertainty. As a final example, consider a squeezed state, which for one quadrature will have field fluctuations smaller than those of a coherent state/vacuum state. The $Q(\alpha)$ of a squeezed state $|\zeta\rangle$ with a real valued squeezing parameter $\zeta = r$ can be shown to be $\sim \exp\left[-\left(\frac{I^2}{0.5(e^{-2r}+1)} + \frac{Q^2}{0.5(e^{2r}+1)}\right)\right]$ [238]. In the limit of large squeezing (large r), we find that $Q(\alpha)$ of $|\zeta\rangle$ is a two-dimensional Gaussian with infinite variance in the Q quadrature, and variance equal to $1/2$ in the I quadrature. The $1/2$ variance in the I quadrature is reflective of the fact that although large squeezing with $\zeta = r$ completely removes intrinsic fluctuations of the field in the I quadrature, the minimal added measurement "uncertainty" when measuring the two conjugate quadratures persists.

In practice, our amplification output chain won't be perfectly quantum limited, and we will have sub-unit detection efficiency η_{det}. In that realistic scenario, the measured IQ phase space distribution will differ from the Husimi Q-function. In order to understand the resulting phase space distribution, consider the fact that heterodyne measurement yields the quantity $S = a + h^\dagger$, where the noise mode h is in a thermal state. If the noise mode h is uncorrelated to the signal mode a (which is typically the case, and can be experimentally verified), then the probability distribution for the sum of two independent random variables a and h is equal to the convolution of the probability distributions for the two random variables. Furthermore, the total noise mode h will have contributions from various sources (see Equation G.3 for example), such as the minimal added "vacuum" noise for

heterodyne detection, as well as additional field fluctuations of a thermal field associated with an added noise photon number n_{noise}. Thus, we can identify the measured phase space distribution in the IQ plane $D(S)$ to be the following two-dimensional convolution involving $Q(\alpha)$ [225]:

$$D(S) = \int_{\alpha} d\alpha Q(\alpha) e^{-|S-\alpha|^2/n_{\text{noise}}} / \pi n_{\text{noise}}, \tag{G.5}$$

where n_{noise} is the added noise photon number, $n_{\text{noise}} = 0$ corresponds to ideal heterodyne detection, and $e^{-|\alpha|^2/n_{\text{noise}}}$ is the Gaussian associated with the additional field fluctuations from a thermal population of n_{noise} noise photons in the noise mode h. Note that in the $n_{\text{noise}} \to 0$ limit, this Gaussian becomes a delta function, and we have $D(S) = D(\alpha)$ as expected. Finally, we observe that although we arrived at Equation G.5 through a probabilistic argument, one may also arrive at this equation through standard theoretical quantum optical methods [237, 238]. Indeed, it can be shown that this phase space IQ distribution $D(S)$, as well as the Husumi Q-function, the Wigner function, the Glauber-Sudarshan P function, etc., are all related to each other by a Gaussian convolution, where each distribution corresponds to a phase-space distribution with a particular amount of “fluctuations" that are contained in the distribution; for more information, we refer the reader to Refs. [225, 237, 238].

In Figure G.1b,we plot the theoretical Husumi Q-function of a $|1\rangle$ Fock state, while in Figs. G.1c, d we plot the experimentally obtained IQ phase-space distributions of the prepared $|1\rangle$ and $|0\rangle$ states, which were measured via heterodyne detection with $n_{\text{noise}} \approx 3.5$. It is evident that while Figure G.1b shows the expected broadened ring shape of the Husimi Q-function, this ring shape is no longer discernible in Figure G.1c due to additional noise photons in mode h. However, it is also clear that the phase space distribution in Figure G.1c is meaningfully different than the one in Figure G.1d for the vacuum state $|0\rangle$. In the next section we discuss how one may isolate the statics of a from the statistics of h given the measurements shown in Figs.G.1c, d.

G.2 Obtaining Field Moments from Noisy Heterodyne Measurements

Generally in statistics, important characteristics of a probability distribution can be described by its moments, and under certain typical conditions a probability distribution is uniquely specified by its moments. In a similar vein, we can perform tomography of radiation field states by experimentally obtaining expectation values of the moments of their measured phase space distributions, because the moments

hold the all the relevant information of the phase space distribution that is necessary for tomography [239]. For a single-mode field, the density matrix is given by

$$\langle m|\rho|n\rangle = \frac{1}{\sqrt{n!m!}} \sum_{l=0}^{\infty} \frac{(-1)^l}{l!} \langle (a^\dagger)^{n+l} a^{m+l} \rangle, \tag{G.6}$$

where $\langle (a^\dagger)^n a^m \rangle$ are the expectation values of different moments of the field. Note that, practically, the signal-to-noise ratio for determining a moment of the field degrades exponentially with order of the moment; thus moment-based tomography is only well suited for states that either have finite photon number contributions (satisfying $\langle m|\rho|n\rangle = 0$ for $m, n \geqq N$), or Gaussian states (coherent, thermal, and squeezed states) for which moments up to second order determine all higher order moments [225]. Equation G.6 can be straightforwardly extended to multipartite photonic states with multiple modes; for example, for a two-mode photonic state, the density matrix is given by

$$\langle ml|\rho|nk\rangle = \frac{1}{\sqrt{n!m!k!l!}} \sum_{i,j=0} \frac{(-1)^{i+j}}{i!j!} \langle (a^\dagger)^{n+j} a^{m+j} (b^\dagger)^{k+i} a^{l+i} \rangle, \tag{G.7}$$

where a and b are the lowering operators for two distinct photonic modes.

However, because in heterodyne detection we experimentally measure $S = a + h^\dagger$ rather than exclusively a, we cannot directly obtain expectation values of a from measurements of S. Nevertheless, given that the signal mode a is uncorrelated to the noise mode h, the moments of the measured distribution $D(S)$ are related to the moments of a and h through the following algebraic relation:

$$\langle (S^\dagger)^n S^m \rangle = \langle (a^\dagger + h)^n (a + h^\dagger)^m \rangle = \sum_{i,j=0}^{m,n} \binom{m}{j} \binom{n}{i} \langle (a^\dagger)^i a^j \rangle \langle h^{n-i} (h^\dagger)^{m-j} \rangle, \tag{G.8}$$

where the right-hand side of the equation is simply obtained through the binomial theorem and by assuming that products of a are uncorrelated with products of h. Consequently, Equation G.8 can be inverted to obtain algebraic relations that yield the moments of a via the moments of S and the moments of h. Additionally, the moments of h can simply be measured through a “dark measurement" where no signal is generated through qubit emission or other means, i.e., through heterodyne measurement of the noise of the output chain. For this dark measurement, the signal

mode a will be in the vacuum state, and thus all moments of a will be zero valued except for the trivial moment $\langle (a^\dagger)^0 (a)^0 \rangle$. Thus, for this "dark measurement, via Equation G.8 we have $\langle (S^\dagger)^n S^m \rangle_{\text{dark}} = \langle h^n (h^\dagger)^m \rangle$.

Consequently, we can invert Equation G.8 in order to calculate the moments of a from the measured moments of S and h. Furthermore, calculating the moments of a via the moments of S and h can be simplified by assuming that complex-valued moments of the noise h are zero valued, which is true for thermal states (because single-shot measurements of these moments will always have a random phase, which will lead to zero-valued expectation values when measurement results are averaged). Below, we give some examples of such calculations for a single-mode field:

$$\begin{aligned} \langle S \rangle &= \langle a \rangle + \cancel{\langle h^\dagger \rangle} = \langle a \rangle \\ \implies \langle a \rangle &= \langle S \rangle \end{aligned}$$

$$\begin{aligned} \langle S^\dagger S \rangle &= \langle (a^\dagger + h)(a + h^\dagger) \rangle = \langle a^\dagger a + a^\dagger h^\dagger + ha + hh^\dagger \rangle \\ &= \langle a^\dagger a \rangle + \langle a^\dagger \rangle \cancel{\langle h^\dagger \rangle} + \langle a \rangle \cancel{\langle h \rangle} + \langle hh^\dagger \rangle \\ &= \langle a^\dagger a \rangle + \langle hh^\dagger \rangle \\ \implies \langle a^\dagger a \rangle &= \langle S^\dagger S \rangle - \langle hh^\dagger \rangle = \langle S^\dagger S \rangle - \langle S^\dagger S \rangle_{\text{dark}} \end{aligned}$$

$$\begin{aligned} \langle (S^\dagger)^2 S \rangle &= \langle (a^\dagger + h)^2 (a + h^\dagger) \rangle = \langle ((a^\dagger)^2 + 2a^\dagger h + h^2)(a + h^\dagger) \\ &= \langle (a^\dagger)^2 a + (a^\dagger)^2 \cancel{h^\dagger} + 2a^\dagger \cancel{h} a + 2a^\dagger h h^\dagger + \cancel{h^2} a + \cancel{h^2 h^\dagger} \rangle \\ &= \langle (a^\dagger)^2 a \rangle + 2 \langle a \rangle \langle hh^\dagger \rangle \\ \implies \langle (a^\dagger)^2 a \rangle &= \langle (S^\dagger)^2 S \rangle - 2 \langle a \rangle \langle hh^\dagger \rangle. \end{aligned}$$

And below we give some examples for multipartite photonic states where we have two distinct itinerant wavepacket modes a and b, with their individual measurements given by $S_a = a + h_a^\dagger$ and $S_b = b + h_b^\dagger$, and we further assume that the noises of the individual modes $h_a^\dagger$ and $h_b^\dagger$ are uncorrelated:

$$\begin{aligned} \langle S_a^\dagger S_b \rangle &= \langle (a^\dagger + h_a)(b + h_b^\dagger) \rangle = \langle a^\dagger b \rangle + \cancel{\langle h_a \rangle} \langle b \rangle + \langle a^\dagger \rangle \cancel{\langle h_b^\dagger \rangle} + \cancel{\langle h_a \rangle} \cancel{\langle h_b^\dagger \rangle} \\ &= \langle a^\dagger b \rangle \\ \implies \langle a^\dagger b \rangle &= \langle S_a^\dagger S_b \rangle \end{aligned}$$

$$
\begin{aligned}
\langle S_a^\dagger S_a S_b^\dagger S_b\rangle &= \langle (a^\dagger a + a^\dagger h_a^\dagger + h_a a + h_a^\dagger h_a)(b^\dagger b + b^\dagger h_b^\dagger + h_b b + h_b^\dagger h_b)\rangle \\
&= \langle a^\dagger a b^\dagger b + a^\dagger a b^\dagger \cancel{h_b^\dagger} + a^\dagger a \cancel{h_b} b + a^\dagger a h_b h_b^\dagger \\
&+ a^\dagger \cancel{h_a^\dagger} b^\dagger b + a^\dagger \cancel{h_a^\dagger} b^\dagger \cancel{h_b^\dagger} + a^\dagger \cancel{h_a^\dagger} \cancel{h_b} b + a^\dagger \cancel{h_a^\dagger} h_b h_b^\dagger \\
&+ \cancel{h_a} a b^\dagger b + \cancel{h_a} a \cancel{h_b^\dagger} b^\dagger + \cancel{h_a} a \cancel{h_b} b + \cancel{h_a} a h_b h_b^\dagger \\
&+ h_a^\dagger h_a b^\dagger b + h_a^\dagger h_a b^\dagger \cancel{h_b^\dagger} + h_a^\dagger h_a \cancel{h_b} b + h_a^\dagger h_a h_b h_b^\dagger \rangle \\
&= \langle a^\dagger a b^\dagger b\rangle + \langle a^\dagger a\rangle\langle h_b h_b^\dagger\rangle + \langle b^\dagger b\rangle\langle h_a h_a^\dagger\rangle + \langle h_a^\dagger h_a\rangle\langle h_b h_b^\dagger\rangle \\
\implies \langle a^\dagger a b^\dagger b\rangle &= \langle S_a^\dagger S_a S_b^\dagger S_b\rangle - \left(\langle a^\dagger a\rangle\langle h_b h_b^\dagger\rangle + \langle b^\dagger b\rangle\langle h_a h_a^\dagger\rangle + \langle h_a^\dagger h_a\rangle\langle h_b h_b^\dagger\rangle\right).
\end{aligned}
$$

In Figs. G.1c, d we show the experimentally measured IQ phase space distributions of the prepared $|1\rangle$ and $|0\rangle$ states, which were measured via heterodyne detection with $n_{\text{noise}} \approx 3.5$. By obtaining the moments of S from the data in Figure G.1c, and obtaining the moments of h from the data in Figure G.1d, we were able to calculate the moments of a via the methods outlined above, and reconstructed the density matrix of the single-photon Fock state $|1\rangle$ shown in Figure F.3a, achieving a 97 % fidelity to the ideal state.

We point out to the reader that, given our discussed assumptions about h and by further assuming that each signal mode only has a maximum photon occupancy of 1, only the moments $\langle h_i h_i^\dagger\rangle$ for each noise mode were necessary to measure to the obtain field moments $\left\langle (a_1^\dagger)^{n_1} a_1^{m_1} (a_2^\dagger)^{n_2} a_2^{m_2} ... (a_N^\dagger)^{n_N} a_N^{m_N}\right\rangle \ \forall\ n_i, m_i \in \{0, 1\}$. Moreover, in practice, after obtaining field moments for single-mode fields or joint field moments for multipartite photonic states, instead of using equations such as G.6, G.7 to obtain density matrices, we instead reconstructed the density matrix of generated photonic states via a maximum-likelihood estimation (MLE) algorithm that uses the moments as input; see Appendix F.1 for more detail. We found that although equations such as G.6 and G.7 reconstructed density matrices with reasonable accuracy, numerical and SPAM errors could result in these equations yielding unphysical density matrix outputs.

G.3 Insights on Heterodyne Measurement Data for Multipartite Entangled Photonic States

While a straightforward recipe for reconstructing the density matrix of multipartite photonic states through expectation values of joint field moments has been presented, here we seek to give the reader some additional insights into some properties of the

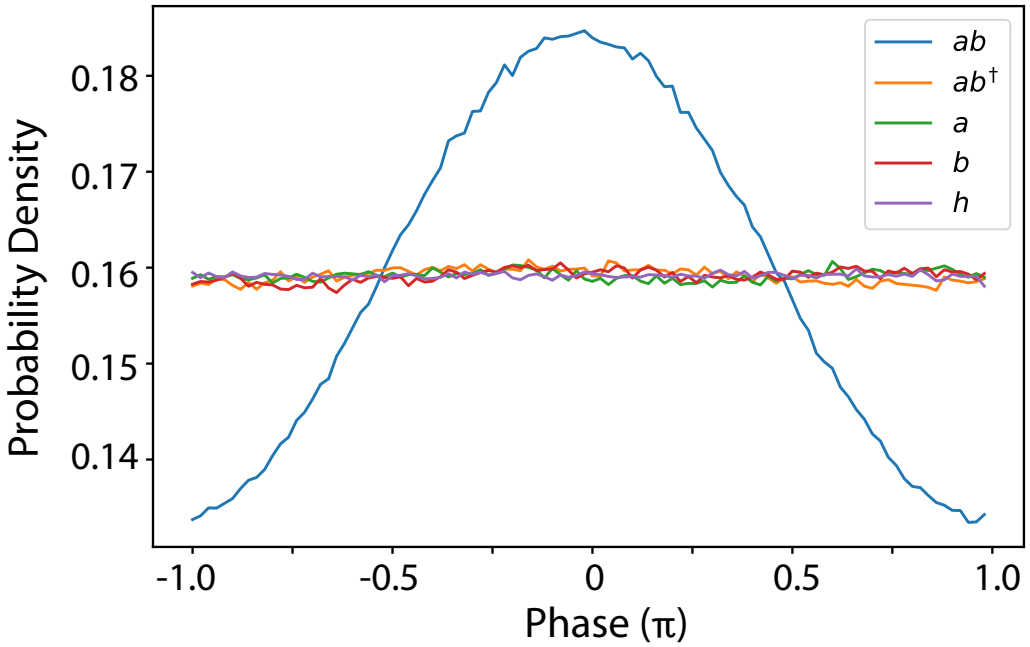

Figure G.2: **Probability Distribution Of Phases of Measured Moments. a** Normalized histograms of phases of experimentally measured moments of the prepared state $|\psi\rangle = \frac{1}{\sqrt{2}}(|00\rangle + |11\rangle)$. For each single-shot measurement, the two distinct itinerant modes a and b are measured via heterodyne detection as discussed in the thesis text, and the measured values are used to calculate the moments for each single shot. The histograms plotted are normalized such that the plotted values represent probability densities.

collected raw data. These insights were often helpful in further understanding our experiment, and aided in debugging.

Measuring Entanglement Through Phase Correlations of Single-Shot Field Measurements

While it is straightforward to visualize properties of phase space distributions of single mode radiation fields, as shown in Figs. G.1b, c, d, visualizing phase space distributions of multiple entangled photonic modes is difficult due to their high dimensionality. Thus, in order to visually ascertain properties of the raw data, it is instead helpful to plot histograms of the phases from single-shot measurements of complex-valued joint field moments. We elucidate this claim by discussing a specific example: the entangled two mode state GHz state $|\psi\rangle = \frac{1}{\sqrt{2}}(|00\rangle + |11\rangle)$. We plot the histograms of measured phases for different field moments in in Figure G.2 for the prepared state, where the data used to generate these plots was directly used in the reconstruction of the density matrix shown in Figure F.3b.

From inspection of Figure G.2, it is evident that the probability distribution of

measured phases for single-shot measurements of the complex-valued moments $ab^\dagger$, a, b, and h follows an uniform distribution; thus each single-shot measurement of these moments will have a completely random phase. However, the probability distribution for the moment ab is peaked at 0 phase (mod 2π); thus shot-to-shot measurements of this moment have phase coherence. These properties of these probability distributions will result in expectation values (obtained from averaging all the single-shot data) of the moments $\langle ab^\dagger \rangle$, $\langle a \rangle$, $\langle b \rangle$, and $\langle h \rangle$ to be zero-valued, while the expectation value of the moment $\langle ab \rangle$ will be finite. This is consistent with the density matrix $\rho = |\psi\rangle\langle\psi| = \frac{1}{2}(|00\rangle\langle 00| + |00\rangle\langle 11| + |11\rangle\langle 00| + |11\rangle\langle 11|)$ and Equation G.7; according to Equation G.7 the density matrix element $\langle 11|\rho|00\rangle$ is equal to $\langle ab \rangle$ and the density matrix element $\langle 10|\rho|01\rangle$ is equal to $\langle ab^\dagger \rangle$. Hence, for the prepared GHz state we expect $\langle ab \rangle$ to be finite-valued, and thus expect to see phase coherence in the probability distribution of measured phases for the moment ab. Likewise, for the GHz state we expect $\langle ab^\dagger \rangle$ to be zero-valued, and thus expect to see a uniform distribution in the measured phases for the moment $ab^\dagger$ (i.e., completely random measured phases). Note that in general, complex valued field moments will yield off-diagonal density matrix elements, while real-valued moments will yield on-diagonal density matrix elements.

Furthermore, we point out to the reader that the expectation values $\langle a \rangle, \langle b \rangle = 0$ are consistent with the fact that $|\psi\rangle$ is a fully entangled state; the reduced density matrix of either the a or b mode is equal to a fully mixed state, and thus single-mode measurements by themselves should contain no information on the entanglement of the state. Hence, we expect single-shot measurements of a or b to have completely random phase consistent with a fully mixed state, as is seen in Figure G.2. Thus, these properties of the moments of $|\psi\rangle$ imply that we may heuristically understand single-shot measurement results of ab as being equal to $|a||b|e^{i(\phi_a+\phi_b)}$, where the statistics $\phi_a + \phi_b$ is given by the plot in Figure G.2, and where single-shot measurement results of a are $|a|e^{i\phi_a}$ and of b are $|b|e^{i\phi_b}$. When writing the moments in this manner, it is evident that although ϕ_a and ϕ_b are completely random on a shot-by-shot basis, their *correlation* is deterministic on a shot-by-shot basis, and it is given by $\phi_a = -\phi_b + \phi_{\text{noise}}$, where ϕ_{noise} encapsulates the (Gaussian) noise of heterodyne detection that is responsible for the width of the phase distribution of ab in Figure G.2. Essentially, for every single-shot measurement, ϕ_a is random and ϕ_b is random, but ϕ_a is equal to the negative of ϕ_b up to detection noise, i.e., their values have a deterministic correlation. Thus, when obtaining single-shot measurement results of $ab = |a||b|e^{i(\phi_a+\phi_b)}$, the shot-to-shot randomness of ϕ_a and ϕ_b cancel out, and the

moment on average has a deterministic phase. Moreover, this heuristic description also explains why $\langle ab^\dagger \rangle = 0$ as well. We may write single-shot measurement results of $ab^\dagger$ as $|a||b|e^{i(\phi_a - \phi_b)}$; in this case $\phi_a - \phi_b = 2\phi_a + \phi_{\text{noise}}$ and thus the randomness of ϕ_a and ϕ_b does *not* cancel out on average, and the $ab^\dagger$ moment also has random phase for every single-shot measurement.

Thus, through this specific example we see that in general the properties of entanglement of a specific multipartite photonic state leads to specific phase correlations in the single-shot heterodyne measurements of these fields, which are obtained through measurement of complex-valued joint-field moments. On the other hand, real valued moments will hold information on $\text{Tr}\,(\rho\,|i\rangle\,\langle i|)$ where $\{|i\rangle\}$ are the basis states of the Hilbert space of the multipartite photonic state, thus yielding the diagonal elements of the density matrix.

Effect of Field Overlap Between Different Itinerant Photonic Modes

One source of measurement error in our heterodyne-based tomography of multipartite photonic states is the overlap of fields of different itinerant photonic modes. While in our experiment we do not have overlapping measurement windows for different itinerant photonic modes, fields of one mode can bleed into the measurement windows of other modes, due to either dispersion-induced pulse distortion and broadening (particularly for broader bandwidth photons), or finite reflections at the "tapered boundary" of the slow-light waveguide overlapping with emission at a later time. Thus, there was a need to understand and measure such overlap's effect on our measurement results in our experiment. In order to understand this effect further, we again consider the two mode GHz state $|\psi\rangle = \frac{1}{\sqrt{2}}(|00\rangle + |11\rangle)$. As discussed in the last section, only the joint moment $\langle ab \rangle$ has phase coherence, and other moments like $\langle ab^\dagger \rangle$ do not have phase coherence and are zero-valued. Moreover, we may heuristically understand single-shot measurement results of a to be $|a|e^{i\phi_a}$, and likewise for b.

Consider the scenario where some of the field from mode a overlaps with the measurement window of mode b, which we define to be $[t_i^b, t_f^b]$. We may heuristically write $S_b = \int_{t_i^b}^{t_f^b} dt\, f_b(t)(b_{\text{out}}(t) + a_{\text{out}}(t)) = |b|e^{i\phi_b} + |\overline{a}|e^{i\overline{\phi}_a}$, where $|\overline{a}|$ is the magnitude of overlap between mode a and the mode-matching function $f_b(t)$ over the measurement window $[t_i^b, t_f^b]$, and $\overline{\phi}_a$ is the phase from the mode-matching integral. Upon calculation of moments, we then have $ab^\dagger = |a||b|e^{i(\phi_a - \phi_b)} + |a||\overline{a}|e^{i(\phi_a - \overline{\phi}_a)}$. As discussed in the previous section, for the two-mode GHz state we have the fol-

lowing deterministic correlation $\phi_a - \phi_b \sim 2\phi_a$ up to detection noise, and ϕ_a is completely random shot-to-shot, so ideally $\langle ab^\dagger \rangle$ is calculated to be zero-valued. However, in the scenario of mode overlap, there will be some deterministic correlation between ϕ_a and $\overline{\phi}_a$, and their difference $\phi_a - \overline{\phi}_a$ will always be some deterministic value up to detection noise. Thus, the term $|a||\overline{a}|e^{i(\phi_a - \overline{\phi}_a)}$ will not average out to zero over many single-shot measurements, and $\langle ab^\dagger \rangle$ will not be zero-valued.

Hence, in order to ascertain the degree to which overlap between two itinerant photon modes is affecting measured expectation values of moments, we can prepare a GHz state of the two modes while maintaining their temporal mode shape and emission time. If measured the $\langle ab^\dagger \rangle$ is negligible, then one may conclude that the effect of mode overlap is minimal. However, if one finds that the $\langle ab^\dagger \rangle$ moment is non-negligible and depends on the emission time of the second mode (increasing if emission happens earlier, and decreasing if emission happens later), then this is a clear sign that the overlap between the two itinerant modes is leading to spurious expectation values of moments, and thus to measurement error. In that scenario, it is recommended to increase separation in time between the modes if possible. In our experiment, we used this method to determine if there was too much overlap between the second and third photons in the 4-photon cluster state prepared discussed in Chapter 5. We found that due to dispersion-induced broadening, the measured $\langle ab^\dagger \rangle$ was ~ 0.1 with a 20 ns interval between their emissions, ~ 0.042 with a 30 ns interval, and did not decrease further than ~ 0.01 for all intervals 40 ns or longer. We hence used this measurement to conclude that we needed 40 ns spacing between broadband (fast)-emitted photons in order to minimize measurement error from their field overlap.

Analysis of Effect of Detection Inefficiency on Moments of Field

As discussed in Appendix G.1, the detection inefficiency η_{meas} affecting measurement of emitted itinerant photons are taken into account during tomography through the conversion scaling factor G. Because this scaling factor G is applied to the raw measured field S_{out}, a calculated *properly scaled* moment $\langle (a^\dagger)^n a^m \rangle$ will be scaled by a factor $G^{-(m+n)/2}$, where part of this scaling includes the factor $\eta_{\text{meas}}^{-(m+n)/2}$. Below we present some rudimentary analysis that corroborates that this is the appropriate scaling.

Consider the following generic model for loss: a partial swap interaction $\hat{U}_\eta$ between

the itinerant mode a and some environmental degree of freedom, where

$$\begin{aligned}\hat{U}_\eta \left|0\right\rangle_a \left|0\right\rangle_{\text{env}} &= \left|0\right\rangle_a \left|0\right\rangle_{\text{env}} \\ \hat{U}_\eta \left|1\right\rangle_a \left|0\right\rangle_{\text{env}} &= \eta^{1/2} \left|1\right\rangle_a \left|0\right\rangle_{\text{env}} + (1-\eta)^{1/2} \left|0\right\rangle_a \left|1\right\rangle_{\text{env}} .\end{aligned}$$

Moreover, consider an initial state of mode a: $\left|\psi\right\rangle_a = \frac{1}{\sqrt{2}}(\left|0\right\rangle_a + \left|1\right\rangle_a)$. After interaction with the environment loss channel, we have:

$$\begin{aligned}\hat{U}_\eta \left|\psi_a\right\rangle \left|0\right\rangle_{\text{env}} &= \frac{1}{\sqrt{2}} \left|0\right\rangle_a \left|0\right\rangle_{\text{env}} + \frac{1}{\sqrt{2}} \left(\eta^{1/2} \left|1\right\rangle_a \left|0\right\rangle_{\text{env}} + (1-\eta)^{1/2} \left|0\right\rangle_a \left|1\right\rangle_{\text{env}}\right) \\ &= \frac{1}{\sqrt{2}} \left(\left|0\right\rangle_a + \eta^{1/2} \left|1\right\rangle_a\right) \left|0\right\rangle_{\text{env}} + \frac{1}{\sqrt{2}} \left((1-\eta)^{1/2} \left|0\right\rangle_a\right) \left|1\right\rangle_{\text{env}} .\end{aligned}$$

Now, by tracing out the environmental degrees of freedom, we arrive at the following reduced density matrix:

$$\begin{aligned}\text{Tr}\left(\hat{U}_\eta \left|\psi_a\right\rangle \left|0\right\rangle_{\text{env}} \left\langle 0\right| \left\langle\psi_a\right| \hat{U}_\eta^\dagger\right) &= \frac{1}{2} \left(\left|0\right\rangle_a + \eta^{1/2} \left|1\right\rangle_a\right) \left(\left\langle 0\right|_a + \eta^{1/2} \left\langle 1\right|_a\right) + \frac{1}{2}(1-\eta) \left|0\right\rangle_a \left\langle 0\right| \\ &= \frac{1+\eta}{2} \left(\frac{\left|0\right\rangle_a + \eta^{1/2} \left|1\right\rangle_a}{\sqrt{1+\eta}}\right) \left(\frac{\left\langle 0\right|_a + \eta^{1/2} \left\langle 1\right|_a}{\sqrt{1+\eta}}\right) + \frac{1}{2}(1-\eta) \left|0\right\rangle_a \left\langle 0\right| .\end{aligned}$$

We may thus identify the resultant state of the itinerant mode a after the loss to be a mixed state that is composed of the following pure states $\left|\phi\right\rangle = \frac{\left|0\right\rangle_a + \eta^{1/2} \left|1\right\rangle_a}{\sqrt{1+\eta}}$ and $\left|\phi'\right\rangle = \left|0\right\rangle_a$ with probabilities $\frac{1+\eta}{2}$ and $\frac{1-\eta}{2}$, respectively. Thus, it is evident that the moments $\langle (a^\dagger)^n a^m \rangle$ will be scaled by a factor $\eta^{-(m+n)/2}$ for the state $\left|\psi_a\right\rangle$ (as well as any generic superposition state) relative to their value in the hypothetical scenario of unit detection efficiency. Finally, note that the resultant partial density matrix is *not* equal to the following density matrix one might naively expect: $\rho_a = (1-\eta) \left|0\right\rangle_a \left\langle 0\right| + \eta \rho_{\text{other}}$, i.e., a mixed state where the vaccum state has probability $(1-\eta)$ and a complimentary state has probability η; one may prove that there is no ρ_{other} that would lead to a valid, physical density matrix.

BIBLIOGRAPHY

Bibliography

[1] Jon Gertner. *The idea factory: Bell Labs and the great age of American innovation*. Penguin, 2012.

[2] Arthur L Schawlow and Charles H Townes. Infrared and optical masers. *Physical Review*, 112(6):1940, 1958.

[3] Theodore H Maiman et al. Stimulated optical radiation in ruby. 1960.

[4] Roy J Glauber. Coherent and incoherent states of the radiation field. *Physical Review*, 131(6):2766, 1963.

[5] Roy J Glauber. The quantum theory of optical coherence. *Physical Review*, 130(6):2529, 1963.

[6] H Jeff Kimble, Mario Dagenais, and Leonard Mandel. Photon antibunching in resonance fluorescence. *Physical Review Letters*, 39(11):691, 1977.

[7] S Haroche, JA Paisner, and AL Schawlow. Hyperfine quantum beats observed in cs vapor under pulsed dye laser excitation. *Physical Review Letters*, 30 (20):948, 1973.

[8] David J Wineland and Wayne M Itano. Laser cooling of atoms. *Physical Review A*, 20(4):1521, 1979.

[9] Arthur Ashkin. Acceleration and trapping of particles by radiation pressure. *Physical review letters*, 24(4):156, 1970.

[10] Serge Haroche and Daniel Kleppner. Cavity quantum electrodynamics. *Phys. Today*, 42(1):24–30, 1989.

[11] H Jeff Kimble. Strong interactions of single atoms and photons in cavity qed. *Physica Scripta*, 1998(T76):127, 1998.

[12] J Hsu. Google's quantum tech milestone excites scientists and spurs rivals. *IEEE Spectrum*, 2019.

[13] Samuel K Moore and Amy Nordrum. Intel's new path to quantum computing. *IEEE Spectrum*, 2018.

[14] Davide Castelvecchi. Ibm's quantum cloud computer goes commercial. *Nature News*, 543(7644):159, 2017.

[15]

[16] Alexandre Blais, Ren-Shou Huang, Andreas Wallraff, Steven M Girvin, and R Jun Schoelkopf. Cavity quantum electrodynamics for superconducting electrical circuits: An architecture for quantum computation. *Phys. Rev. A*, 69(6):062320, 2004.

[17] Long B Nguyen, Yen-Hsiang Lin, Aaron Somoroff, Raymond Mencia, Nicholas Grabon, and Vladimir E Manucharyan. High-coherence fluxonium qubit. *Phys. Rev. X*, 9(4):041041, 2019.

[18] AVEEK DUTTA, Alexander Place, Kevin Crowley, Xuan Hoang Le, Youqi Gang, Xin Gui, Lila Rodgers, Trisha Madhavan, Nishaad Khedkar, Ignace Jarrige, et al. Study of two-level-system losses in tantalum superconducting microwave coplanar waveguide resonators. *Bulletin of the American Physical Society*, 2022.

[19] Michael Tinkham. *Introduction to superconductivity*. Courier Corporation, 2004.

[20] Dibyendu Roy, Christopher M Wilson, and Ofer Firstenberg. Colloquium: Strongly interacting photons in one-dimensional continuum. *Reviews of Modern Physics*, 89(2):021001, 2017.

[21] DE Chang, JS Douglas, Alejandro González-Tudela, C-L Hung, and HJ Kimble. Colloquium: Quantum matter built from nanoscopic lattices of atoms and photons. *Reviews of Modern Physics*, 90(3):031002, 2018.

[22] Alexandra S Sheremet, Mihail I Petrov, Ivan V Iorsh, Alexander V Poshakinskiy, and Alexander N Poddubny. Waveguide quantum electrodynamics: collective radiance and photon-photon correlations. *arXiv preprint arXiv:2103.06824*, 2021.

[23] Ying Dong, J Taylor, Youn Seok Lee, HR Kong, and KS Choi. Waveguide-qed platform for synthetic quantum matter. *Physical Review A*, 104(5):053703, 2021.

[24] Sahand Mahmoodian, Giuseppe Calajó, Darrick E Chang, Klemens Hammerer, and Anders S Sørensen. Dynamics of many-body photon bound states in chiral waveguide qed. *Physical Review X*, 10(3):031011, 2020.

[25] Pierre Türschmann, Hanna Le Jeannic, Signe F Simonsen, Harald R Haakh, Stephan Götzinger, Vahid Sandoghdar, Peter Lodahl, and Nir Rotenberg. Coherent nonlinear optics of quantum emitters in nanophotonic waveguides. *Nanophotonics*, 8(10):1641–1657, 2019.

[26] Susana F Huelga, Angel Rivas, and Martin B Plenio. Non-markovianity-assisted steady state entanglement. *Phys. Rev. Lett.*, 108(16):160402, 2012.

[27] Jiong Cheng, Wen-Zhao Zhang, Ling Zhou, and Weiping Zhang. Preservation macroscopic entanglement of optomechanical systems in non-markovian environment. *Sci. Rep.*, 6:23678, 2016.

[28] Bruno Bellomo, R Lo Franco, and Giuseppe Compagno. Non-markovian effects on the dynamics of entanglement. *Phys. Rev. Lett.*, 99(16):160502, 2007.

[29] Bruno Bellomo, Rosario Lo Franco, Sabrina Maniscalco, and Giuseppe Compagno. Entanglement trapping in structured environments. *Phys. Rev. A*, 78 (6):060302, 2008.

[30] C Gonzalez-Ballestero, Francisco J García-Vidal, and Esteban Moreno. Non-markovian effects in waveguide-mediated entanglement. *New J. Phys.*, 15(7): 073015, 2013.

[31] H Jeff Kimble. The quantum internet. *Nature*, 453(7198):1023–1030, 2008.

[32] Robert Raussendorf, Daniel E Browne, and Hans J Briegel. Measurement-based quantum computation on cluster states. *Phys. Rev. A*, 68(2):022312, 2003.

[33] A Goban, C-L Hung, S-P Yu, JD Hood, JA Muniz, JH Lee, MJ Martin, AC McClung, KS Choi, Darrick E Chang, et al. Atom–light interactions in photonic crystals. *Nat. Comm.*, 5(1):1–9, 2014.

[34] Neil V Corzo, Jérémy Raskop, Aveek Chandra, Alexandra S Sheremet, Baptiste Gouraud, and Julien Laurat. Waveguide-coupled single collective excitation of atomic arrays. *Nature*, 566(7744):359–362, 2019.

[35] M Baur, Stefan Filipp, R Bianchetti, JM Fink, M Göppl, L Steffen, Peter J Leek, Alexandre Blais, and Andreas Wallraff. Measurement of autler-townes and mollow transitions in a strongly driven superconducting qubit. *Physical review letters*, 102(24):243602, 2009.

[36] Io-Chun Hoi, CM Wilson, Göran Johansson, Joel Lindkvist, Borja Peropadre, Tauno Palomaki, and Per Delsing. Microwave quantum optics with an artificial atom in one-dimensional open space. *New Journal of Physics*, 15(2): 025011, 2013.

[37] Arjan F Van Loo, Arkady Fedorov, Kevin Lalumière, Barry C Sanders, Alexandre Blais, and Andreas Wallraff. Photon-mediated interactions between distant artificial atoms. *Science*, 342(6165):1494–1496, 2013.

[38] Mohammad Mirhosseini, Eunjong Kim, Xueyue Zhang, Alp Sipahigil, Paul B Dieterle, Andrew J Keller, Ana Asenjo-Garcia, Darrick E Chang, and Oskar Painter. Cavity quantum electrodynamics with atom-like mirrors. *Nature*, 569(7758):692, 2019.

[39] Io-Chun Hoi, Tauno Palomaki, Joel Lindkvist, Göran Johansson, Per Delsing, and CM Wilson. Generation of nonclassical microwave states using an artificial atom in 1d open space. *Phys. Rev. Lett.*, 108(26):263601, 2012.

[40] Deniz Bozyigit, C Lang, L Steffen, JM Fink, Christopher Eichler, M Baur, R Bianchetti, Peter J Leek, Stefan Filipp, Marcus P Da Silva, et al. Antibunching of microwave-frequency photons observed in correlation measurements using linear detectors. *Nature Physics*, 7(2):154–158, 2011.

[41] C Lang, Christopher Eichler, L Steffen, JM Fink, Matthew J Woolley, Alexandre Blais, and Andreas Wallraff. Correlations, indistinguishability and entanglement in hong–ou–mandel experiments at microwave frequencies. *Nat. Phys.*, 9(6):345–348, 2013.

[42] Gustav Andersson, Baladitya Suri, Lingzhen Guo, Thomas Aref, and Per Delsing. Non-exponential decay of a giant artificial atom. *Nat. Phys.*, 15: 1123–1127, 2019. doi: 10.1038/s41567-019-0605-6.

[43] Bharath Kannan, Max J Ruckriegel, Daniel L Campbell, Anton Frisk Kockum, Jochen Braumüller, David K Kim, Morten Kjaergaard, Philip Krantz, Alexander Melville, Bethany M Niedzielski, et al. Waveguide quantum electrodynamics with superconducting artificial giant atoms. *Nature*, 583(7818):775–779, 2020.

[44] AM Vadiraj, Andreas Ask, TG McConkey, I Nsanzineza, CW Sandbo Chang, Anton Frisk Kockum, and CM Wilson. Engineering the level structure of a giant artificial atom in waveguide quantum electrodynamics. *Physical Review A*, 103(2):023710, 2021.

[45] Bharath Kannan, Aziza Almanakly, Youngkyu Sung, Agustin Di Paolo, David A Rower, Jochen Braumüller, Alexander Melville, Bethany M Niedzielski, Amir Karamlou, Kyle Serniak, et al. On-demand directional photon emission using waveguide quantum electrodynamics. *arXiv preprint arXiv:2203.01430*, 2022.

[46] Christopher Eichler, Jonas Mlynek, Jonas Butscher, Philipp Kurpiers, Klemens Hammerer, Tobias J Osborne, and Andreas Wallraff. Exploring interacting quantum many-body systems by experimentally creating continuous matrix product states in superconducting circuits. *Phys. Rev. X*, 5(4):041044, 2015.

[47] Bharath Kannan, Daniel L Campbell, Francisca Vasconcelos, Roni Winik, DK Kim, Morten Kjaergaard, Philip Krantz, Alexander Melville, Bethany M Niedzielski, JL Yoder, et al. Generating spatially entangled itinerant photons with waveguide quantum electrodynamics. *Science Advances*, 6(41): eabb8780, 2020.

[48] Jean-Claude Besse, Kevin Reuer, Michele C. Collodo, Arne Wulff, Lucien Wernli, Adrian Copetudo, Daniel Malz, Paul Magnard, Abdulkadir Akin, Mihai Gabureac, Graham J. Norris, J. Ignacio Cirac, Andreas Wallraff, and Christopher Eichler. Realizing a deterministic source of multipartite-entangled photonic qubits. *Nat. Commun.*, 11(4877), 2020.

[49] Yong Lu, Ingrid Strandberg, Fernando Quijandría, Göran Johansson, Simone Gasparinetti, and Per Delsing. Propagating wigner-negative states generated from the steady-state emission of a superconducting qubit. *Physical Review Letters*, 126(25):253602, 2021.

[50] Vladimir P Bykov. Spontaneous emission from a medium with a band spectrum. *Sov. J. Quantum Electron.*, 4(7):861, 1975.

[51] Sajeev John and Jian Wang. Quantum electrodynamics near a photonic band gap: Photon bound states and dressed atoms. *Phys. Rev. Lett.*, 64(20):2418, 1990.

[52] Sajeev John and Jian Wang. Quantum optics of localized light in a photonic band gap. *Phys. Rev. B*, 43(16):12772, 1991.

[53] Eli Yablonovitch. Inhibited spontaneous emission in solid-state physics and electronics. *Phys. Rev. Lett.*, 58(20):2059, 1987.

[54] Sajeev John. Strong localization of photons in certain disordered dielectric superlattices. *Phys. Rev. Lett.*, 58(23):2486, 1987.

[55] Sajeev John and Tran Quang. Spontaneous emission near the edge of a photonic band gap. *Phys. Rev. A*, 50(2):1764, 1994.

[56] HZ Shen, Shuang Xu, HT Cui, and XX Yi. Non-markovian dynamics of a system of two-level atoms coupled to a structured environment. *Phys. Rev. A*, 99(3):032101, 2019.

[57] Alejandro González-Tudela and J Ignacio Cirac. Markovian and non-markovian dynamics of quantum emitters coupled to two-dimensional structured reservoirs. *Phys. Rev. A*, 96(4):043811, 2017.

[58] P Lambropoulos, Georgios M Nikolopoulos, Torben R Nielsen, and Søren Bay. Fundamental quantum optics in structured reservoirs. *Reports on Progress in Physics*, 63(4):455, 2000.

[59] Nipun Vats and Sajeev John. Non-markovian quantum fluctuations and superradiance near a photonic band edge. *Phys. Rev. A*, 58(5):4168, 1998.

[60] Hannes Pichler, Soonwon Choi, Peter Zoller, and Mikhail D Lukin. Universal photonic quantum computation via time-delayed feedback. *PNAS*, 114(43): 11362–11367, 2017.

[61] Philip Krantz, Morten Kjaergaard, Fei Yan, Terry P Orlando, Simon Gustavsson, and William D Oliver. A quantum engineer's guide to superconducting qubits. *Appl. Phys. Rev.*, 6(2):021318, 2019.

[62] Steven M Girvin. Circuit qed: superconducting qubits coupled to microwave photons. *Quantum machines: measurement and control of engineered quantum systems*, pages 113–256, 2014.

[63] Uri Vool and Michel Devoret. Introduction to quantum electromagnetic circuits. *International Journal of Circuit Theory and Applications*, 45(7): 897–934, 2017.

[64] Richard P Feynman, Robert B Leighton, and Matthew Sands. *The Feynman lectures on physics, Vol. III: The new millennium edition*, volume 3. Basic books, 2011.

[65] K Osbourne and JM Martinis. Superconducting qubits and the physics of josephson junctions. In *Les Houches conference proceedings*, 2003.

[66] Jens Koch, Terri M. Yu, Jay Gambetta, A. A. Houck, D. I. Schuster, J. Majer, Alexandre Blais, M. H. Devoret, S. M. Girvin, and R. J. Schoelkopf. Charge-insensitive qubit design derived from the cooper pair box. *Phys. Rev. A*, 76: 042319, oct 2007. doi: 10.1103/PhysRevA.76.042319.

[67] Daniel Sank, Zijun Chen, Mostafa Khezri, J Kelly, R Barends, B Campbell, Y Chen, B Chiaro, A Dunsworth, A Fowler, et al. Measurement-induced state transitions in a superconducting qubit: Beyond the rotating wave approximation. *Phys. Rev. Lett.*, 117(19):190503, 2016.

[68] Theodore Walter, Philipp Kurpiers, Simone Gasparinetti, Paul Magnard, Anton Potočnik, Yves Salathé, Marek Pechal, Mintu Mondal, Markus Oppliger, Christopher Eichler, et al. Rapid high-fidelity single-shot dispersive readout of superconducting qubits. *Phys. Rev. Appl.*, 7(5):054020, 2017.

[69] Agnetta Y. Cleland, Marek Pechal, Pieter-Jan C. Stas, Christopher J. Sarabalis, E. Alex Wollack, and Amir H. Safavi-Naeini. Mechanical purcell filters for microwave quantum machines. *Applied Physics Letters*, 115(26):263504, 2019. doi: 10.1063/1.5111151.

[70] Eun Jong Kim. *Waveguide Quantum Electrodynamics in Superconducting Circuits*. PhD thesis, California Institute of Technology, 2022.

[71] Yao-Lung L Fang. *Waveguide QED: Multiple Qubits, Inelastic Scattering, and Non-Markovianity*. PhD thesis, Duke University, 2017.

[72] Darrick E Chang, Anders S Sørensen, Eugene A Demler, and Mikhail D Lukin. A single-photon transistor using nanoscale surface plasmons. *Nature physics*, 3(11):807–812, 2007.

[73] Io-Chun Hoi. *Quantum optics with propagating microwaves in superconducting circuits*. Chalmers University of Technology, 2013.

[74] Yong Lu, Andreas Bengtsson, Jonathan J Burnett, Emely Wiegand, Baladitya Suri, Philip Krantz, Anita Fadavi Roudsari, Anton Frisk Kockum, Simone Gasparinetti, Göran Johansson, et al. Characterizing decoherence rates of a superconducting qubit by direct microwave scattering. *npj Quantum Information*, 7(1):1–9, 2021.

[75] Félix Beaudoin, Marcus P da Silva, Zachary Dutton, and Alexandre Blais. First-order sidebands in circuit qed using qubit frequency modulation. *Phys. Rev. A*, 86(2):022305, 2012.

[76] JD Strand, Matthew Ware, Félix Beaudoin, TA Ohki, BR Johnson, Alexandre Blais, and BLT Plourde. First-order sideband transitions with flux-driven asymmetric transmon qubits. *Physical Review B*, 87(22):220505, 2013.

[77] MP Silveri, JA Tuorila, EV Thuneberg, and GS Paraoanu. Quantum systems under frequency modulation. *Reports on Progress in Physics*, 80(5):056002, 2017.

[78] Giuseppe Calajó, Francesco Ciccarello, Darrick Chang, and Peter Rabl. Atom-field dressed states in slow-light waveguide qed. *Phys. Rev. A*, 93 (3):033833, 2016.

[79] Nicolas Didier, Eyob A. Sete, Marcus P. da Silva, and Chad Rigetti. Analytical modeling of parametrically modulated transmon qubits. *Phys. Rev. A*, 97: 022330, Feb 2018. doi: 10.1103/PhysRevA.97.022330. URL `https://link.aps.org/doi/10.1103/PhysRevA.97.022330`.

[80] Angel Rivas, Susana F Huelga, and Martin B Plenio. Quantum non-markovianity: characterization, quantification and detection. *Reports on Progress in Physics*, 77(9):094001, 2014.

[81] Heinz-Peter Breuer, Elsi-Mari Laine, Jyrki Piilo, and Bassano Vacchini. Colloquium: Non-markovian dynamics in open quantum systems. *Rev. Mod. Phys.*, 88(2):021002, 2016.

[82] Daniel Manzano. A short introduction to the lindblad master equation. *Aip Advances*, 10(2):025106, 2020.

[83] Jan F Haase, Philipp J Vetter, Thomas Unden, Andrea Smirne, Joachim Rosskopf, Boris Naydenov, Alastair Stacey, Fedor Jelezko, Martin B Plenio, and Susana F Huelga. Controllable non-markovianity for a spin qubit in diamond. *Phys. Rev. Lett.*, 121(6):060401, 2018.

[84] Ulrich Hoeppe, Christian Wolff, Jens Küchenmeister, Jens Niegemann, Malte Drescher, Hartmut Benner, and Kurt Busch. Direct observation of non-markovian radiation dynamics in 3d bulk photonic crystals. *Phys. Rev. Lett.*, 108(4):043603, 2012.

[85] Ludwig Krinner, Michael Stewart, Arturo Pazmiño, Joonhyuk Kwon, and Dominik Schneble. Spontaneous emission of matter waves from a tunable open quantum system. *Nature*, 559(7715):589, 2018.

[86] Bi-Heng Liu, Li Li, Yun-Feng Huang, Chuan-Feng Li, Guang-Can Guo, Elsi-Mari Laine, Heinz-Peter Breuer, and Jyrki Piilo. Experimental control of the transition from markovian to non-markovian dynamics of open quantum systems. *Nat. Phys.*, 7(12):931, 2011.

[87] M Nielsen and I L Chuang. *Quantum Computation and Quantum Information*. Cambridge University Press, 2000.

[88] Heinz-Peter Breuer. Foundations and measures of quantum non-markovianity. *J. Phys. B*, 45(15):154001, 2012.

[89] Tommaso Tufarelli, M. S. Kim, and Francesco Ciccarello. Non-markovianity of a quantum emitter in front of a mirror. *Phys. Rev. A*, 90(1):012113, 2014.

[90] Robert Raussendorf and Hans J Briegel. A one-way quantum computer. *Phys. Rev. Lett.*, 86(22):5188, 2001.

[91] Robert Raussendorf, Jim Harrington, and Kovid Goyal. Topological fault-tolerance in cluster state quantum computation. *New J. Phys.*, 9(6):199, 2007.

[92] Robert Raussendorf. Measurement-based quantum computation with cluster states. *International Journal of Quantum Information*, 7(06):1053–1203, 2009.

[93] Ido Schwartz, Dan Cogan, Emma R Schmidgall, Yaroslav Don, Liron Gantz, Oded Kenneth, Netanel H Lindner, and David Gershoni. Deterministic generation of a cluster state of entangled photons. *Science*, 354(6311):434–437, 2016.

[94] Mikkel V Larsen, Xueshi Guo, Casper R Breum, Jonas S Neergaard-Nielsen, and Ulrik L Andersen. Deterministic generation of a two-dimensional cluster state. *Science*, 366(6463):369–372, 2019.

[95] Pieter Kok, William J Munro, Kae Nemoto, Timothy C Ralph, Jonathan P Dowling, and Gerard J Milburn. Linear optical quantum computing with photonic qubits. *Rev. Mod. Phys.*, 79(1):135, 2007.

[96] Philip Walther, Kevin J Resch, Terry Rudolph, Emmanuel Schenck, Harald Weinfurter, Vlatko Vedral, Markus Aspelmeyer, and Anton Zeilinger. Experimental one-way quantum computing. *Nature*, 434(7030):169–176, 2005.

[97] Jeremy L O'brien, Akira Furusawa, and Jelena Vučković. Photonic quantum technologies. *Nature Photonics*, 3(12):687–695, 2009.

[98] Jeremy L O'brien. Optical quantum computing. *Science*, 318(5856):1567–1570, 2007.

[99] Victor Weisskopf and Eugene Wigner. Berechnung der natürlichen linienbreite auf grund der diracschen lichttheorie. *Zeitschrift für Physik*, 63(1-2): 54–73, 1930.

[100] M Brune, F Schmidt-Kaler, Abdelhamid Maali, J Dreyer, E Hagley, JM Raimond, and S Haroche. Quantum rabi oscillation: A direct test of field quantization in a cavity. *Phys. Rev. Lett.*, 76(11):1800, 1996.

[101] Edward M Purcell, Henry Cutler Torrey, and Robert V Pound. Resonance absorption by nuclear magnetic moments in a solid. *Phys. Rev.*, 69(1-2):37, 1946.

[102] Yanbing Liu and Andrew A Houck. Quantum electrodynamics near a photonic bandgap. *Nat. Phys.*, 13(1):48, 2017.

[103] Neereja M Sundaresan, Rex Lundgren, Guanyu Zhu, Alexey V Gorshkov, and Andrew A Houck. Interacting qubit-photon bound states with superconducting circuits. *Phys. Rev. X*, 9(1):011021, 2019.

[104] Mohammad Mirhosseini, Eunjong Kim, Vinicius S Ferreira, Mahmoud Kalaee, Alp Sipahigil, Andrew J Keller, and Oskar Painter. Superconducting metamaterials for waveguide quantum electrodynamics. *Nat. Commun.*, 9, 2018.

[105] Amnon Yariv, Yong Xu, Reginald K Lee, and Axel Scherer. Coupled-resonator optical waveguide: a proposal and analysis. *Opt. Lett.*, 24(11): 711–713, 1999.

[106] Masaya Notomi, Eiichi Kuramochi, and Takasumi Tanabe. Large-scale arrays of ultrahigh-q coupled nanocavities. *Nat. Phot.*, 2:741–747, nov 2008. doi: 10.1038/nphoton.2008.226.

[107] Diederik S Wiersma, Paolo Bartolini, Ad Lagendijk, and Roberto Righini. Localization of light in a disordered medium. *Nature*, 390(6661):671, 1997.

[108] Steven M Girvin. Circuit qed: superconducting qubits coupled to microwave photons. In Michel Devoret, Benjamin Huard, Robert Schoelkopf, and Leticia F. Cugliandolo, editors, *Quantum Machines: Measurement and Control of Engineered Quantum Systems*, chapter 3, pages 113–256. Oxford University Press, Oxford, UK, 2011.

[109] David M Pozar. *Microwave engineering*. John Wiley & Sons, 2009.

[110] H Gersen, TJ Karle, RJP Engelen, Wim Bogaerts, Jeroen P Korterik, NF Van Hulst, TF Krauss, and L Kuipers. Direct observation of bloch harmonics and negative phase velocity in photonic crystal waveguides. *Phys. Rev. Lett.*, 94(12):123901, 2005.

[111] Youzhen Wang, Yewen Zhang, Li He, Fuqiang Liu, Hongqiang Li, and Hong Chen. Direct observation of negative phase velocity and positive group velocity in time domain for composite right/left-handed transmission lines. *J. Appl. Phys.*, 100(11):113503, 2006.

[112] Jonathan Woodley and Mohammad Mojahedi. Backward wave propagation in left-handed media with isotropic and anisotropic permittivity tensors. *J. Opt. Soc. Am. B*, 23(11):2377–2382, 2006.

[113] Federico Lombardo, Francesco Ciccarello, and G Massimo Palma. Photon localization versus population trapping in a coupled-cavity array. *Phys. Rev. A*, 89(5):053826, 2014.

[114] YP Zhong, H-S Chang, KJ Satzinger, M-H Chou, Audrey Bienfait, CR Conner, É Dumur, Joel Grebel, GA Peairs, RG Povey, et al. Violating bell's inequality with remotely connected superconducting qubits. *Nat. Phys.*, page 1, 2019.

[115] Yi Wang, Hieng Tiong Su, Frederick Huang, and Michael J Lancaster. Wideband superconducting coplanar delay lines. *IEEE Trans. Microw. Theory Tech.*, 53(7):2348–2354, 2005.

[116] Michael Sumetsky and Benjamin J Eggleton. Modeling and optimization of complex photonic resonant cavity circuits. *Opt. Express*, 11(4):381–391, 2003.

[117] Seymour B Cohn. Direct-coupled-resonator filters. *Proceedings of the IRE*, 45(2):187–196, 1957.

[118] *Sonnet, Sonnet Suites, Version 16.52*.

[119] Jiansong Gao. *The physics of superconducting microwave resonators*. PhD thesis, California Institute of Technology, 2008.

[120] Alain Aspect and Massimo Inguscio. Anderson localization of ultracold atoms. *Phys. Today*, 62(8):30, 2009.

[121] Devin L Underwood, Will E Shanks, Jens Koch, and Andrew A Houck. Low-disorder microwave cavity lattices for quantum simulation with photons. *Phys. Rev. A*, 86(2):023837, 2012.

[122] Kristian Høeg Madsen, Serkan Ates, Toke Lund-Hansen, A Löffler, S Reitzenstein, A Forchel, and Peter Lodahl. Observation of non-markovian dynamics of a single quantum dot in a micropillar cavity. *Phys. Rev. Lett.*, 106(23): 233601, 2011.

[123] Daniel M Reich, Nadav Katz, and Christiane P Koch. Exploiting non-markovianity for quantum control. *Sci. Rep.*, 5:12430, 2015.

[124] B Bylicka, D Chruściński, and Sci Maniscalco. Non-markovianity and reservoir memory of quantum channels: a quantum information theory perspective. *Sci. Rep.*, 4:5720, 2014.

[125] DTH Tan, K Ikeda, RE Saperstein, B Slutsky, and Y Fainman. Chip-scale dispersion engineering using chirped vertical gratings. *Opt. Lett.*, 33(24): 3013–3015, 2008.

[126] Christophe Caloz. Metamaterial dispersion engineering concepts and applications. *Proceedings of the IEEE*, 99(10):1711–1719, 2011.

[127] A Säynätjoki, M Mulot, Jouni Ahopelto, and H Lipsanen. Dispersion engineering of photonic crystal waveguides with ring-shaped holes. *Opt. Express*, 15(13):8323–8328, 2007.

[128] Hannes Pichler and Peter Zoller. Photonic circuits with time delays and quantum feedback. *Phys. Rev. Lett.*, 116(9):093601, 2016.

[129] I-C Hoi, AF Kockum, L Tornberg, A Pourkabirian, G Johansson, Per Delsing, and CM Wilson. Probing the quantum vacuum with an artificial atom in front of a mirror. *Nat. Phys.*, 11(12):1045, 2015.

[130] Yao-Lung L Fang, Francesco Ciccarello, and Harold U Baranger. Non-markovian dynamics of a qubit due to single-photon scattering in a waveguide. *New J. Phys.*, 20(4):043035, 2018.

[131] Tommaso Tufarelli, Francesco Ciccarello, and MS Kim. Dynamics of spontaneous emission in a single-end photonic waveguide. *Phys. Rev. A*, 87(1): 013820, 2013.

[132] Dmitry O Krimer, Matthias Liertzer, Stefan Rotter, and Hakan E Türeci. Route from spontaneous decay to complex multimode dynamics in cavity qed. *Physical Review A*, 89(3):033820, 2014.

[133] Alexander Carmele, Julia Kabuss, Franz Schulze, Stephan Reitzenstein, and Andreas Knorr. Single photon delayed feedback: a way to stabilize intrinsic quantum cavity electrodynamics. *Phys. Rev. Lett.*, 110(1):013601, 2013.

[134] Lingzhen Guo, Anton Frisk Kockum, Florian Marquardt, and Göran Johansson. Oscillating bound states for a giant atom. *Phys. Rev. Research*, 2(4): 043014, 2020.

[135] Fatih Dinc. Diagrammatic approach for analytical non-markovian time evolution: Fermi's two-atom problem and causality in waveguide quantum electrodynamics. *Phys. Rev. A*, 102:013727, Jul 2020. doi: 10.1103/PhysRevA.102.013727. URL https://link.aps.org/doi/10.1103/PhysRevA.102.013727.

[136] Giuseppe Calajó, Yao-Lung L Fang, Harold U Baranger, Francesco Ciccarello, et al. Exciting a bound state in the continuum through multiphoton scattering plus delayed quantum feedback. *Phys. Rev. Lett.*, 122(7):073601, 2019.

[137] Savannah Garmon, Kenichi Noba, Gonzalo Ordonez, and Dvira Segal. Non-markovian dynamics revealed at a bound state in the continuum. *Phys. Rev. A*, 99(1):010102, 2019.

[138] Fatih Dinc and Agata M Brańczyk. Non-markovian super-superradiance in a linear chain of up to 100 qubits. *Phys. Rev. Research*, 1(3):032042, 2019.

[139] Kanupriya Sinha, Pierre Meystre, Elizabeth A Goldschmidt, Fredrik K Fatemi, Steven L Rolston, and Pablo Solano. Non-markovian collective emission from macroscopically separated emitters. *Phys. Rev. Lett.*, 124(4): 043603, 2020.

[140] Huaixiu Zheng and Harold U Baranger. Persistent quantum beats and long-distance entanglement from waveguide-mediated interactions. *Phys. Rev. Lett.*, 110(11):113601, 2013.

[141] Alexander Carmele, Nikolett Nemet, Victor Canela, and Scott Parkins. Pronounced non-markovian features in multiply excited, multiple emitter waveguide qed: Retardation induced anomalous population trapping. *Phys. Rev. Research*, 2(1):013238, 2020.

[142] Tomás Ramos, Benoît Vermersch, Philipp Hauke, Hannes Pichler, and Peter Zoller. Non-markovian dynamics in chiral quantum networks with spins and photons. *Phys. Rev. A*, 93(6):062104, 2016.

[143] R. J. Schoelkopf and S. M. Girvin. Wiring up quantum systems. *Nature*, 451: 664–669, feb 2008. doi: 10.1038/451664a.

[144] M. H. Devoret and R. J. Schoelkopf. Superconducting circuits for quantum information: An outlook. *Science*, 339:1169–1174, mar 2013. doi: 10.1126/science.1231930.

[145] Kevin Lalumiere, Barry C Sanders, Arjan F van Loo, Arkady Fedorov, Andreas Wallraff, and Alexandre Blais. Input-output theory for waveguide qed with an ensemble of inhomogeneous atoms. *Phys. Rev. A*, 88(4):043806, 2013.

[146] E Vetsch, D Reitz, G Sagué, R Schmidt, ST Dawkins, and A Rauschenbeutel. Optical interface created by laser-cooled atoms trapped in the evanescent field surrounding an optical nanofiber. *Phys. Rev. Lett.*, 104(20):203603, 2010.

[147] S-P Yu, JD Hood, JA Muniz, MJ Martin, Richard Norte, C-L Hung, Seán M Meenehan, Justin D Cohen, Oskar Painter, and HJ Kimble. Nanowire photonic crystal waveguides for single-atom trapping and strong light-matter interactions. *Appl. Phys. Lett.*, 104(11):111103, 2014.

[148] Alisa Javadi, I Söllner, Marta Arcari, S Lindskov Hansen, Leonardo Midolo, Sahand Mahmoodian, G Kiršanskė, Tommaso Pregnolato, EH Lee, JD Song, et al. Single-photon non-linear optics with a quantum dot in a waveguide. *Nat. Commun.*, 6:8655, 2015.

[149] Mihir K Bhaskar, Denis D Sukachev, Alp Sipahigil, Ruffin E Evans, Michael J Burek, Christian T Nguyen, Lachlan J Rogers, Petr Siyushev, Mathias H Metsch, Hongkun Park, et al. Quantum nonlinear optics with a germanium-vacancy color center in a nanoscale diamond waveguide. *Phys. Rev. Lett.*, 118(22):223603, 2017.

[150] Audrey Bienfait, Kevin J Satzinger, YP Zhong, H-S Chang, M-H Chou, CR Conner, É Dumur, J Grebel, GA Peairs, RG Povey, et al. Phonon-mediated quantum state transfer and remote qubit entanglement. *Science*, 364(6438):368–371, 2019.

[151] C Eichler, C Lang, JM Fink, J Govenius, S Filipp, and A Wallraff. Observation of entanglement between itinerant microwave photons and a superconducting qubit. *Phys. Rev. Lett.*, 109(24):240501, 2012.

[152] R. Barends, J. Kelly, A. Megrant, D. Sank, E. Jeffrey, Y. Chen, Y. Yin, B. Chiaro, J. Mutus, C. Neill, P. O'Malley, P. Roushan, J. Wenner, T. C. White, A. N. Cleland, and John M. Martinis. Coherent josephson qubit suitable for scalable quantum integrated circuits. *Phys. Rev. Lett.*, 111:080502, aug 2013. doi: 10.1103/PhysRevLett.111.080502.

[153] Andrew J Keller, Paul B Dieterle, Michael Fang, Brett Berger, Johannes M Fink, and Oskar Painter. Al transmon qubits on silicon-on-insulator for quantum device integration. *Appl. Phys. Lett.*, 111(4):042603, 2017.

[154] SN Shevchenko, Sahel Ashhab, and Franco Nori. Landau–zener–stückelberg interferometry. *Phys. Rep.*, 492(1):1–30, 2010.

[155] Elsi-Mari Laine, Jyrki Piilo, and Heinz-Peter Breuer. Measure for the non-markovianity of quantum processes. *Phys. Rev. A*, 81(6):062115, 2010.

[156] Govind S Agarwal. Vacuum-field rabi oscillations of atoms in a cavity. *J. Opt. Soc. Am. B*, 2(3):480–485, 1985.

[157] Yimin Wang, Jiří Minář, Lana Sheridan, and Valerio Scarani. Efficient excitation of a two-level atom by a single photon in a propagating mode. *Phys. Rev. A*, 83(6):063842, 2011.

[158] Magdalena Stobińska, Gernot Alber, and Gerd Leuchs. Perfect excitation of a matter qubit by a single photon in free space. *EPL*, 86(1):14007, 2009.

[159] Jian Li, MP Silveri, KS Kumar, J-M Pirkkalainen, A Vepsäläinen, WC Chien, J Tuorila, MA Sillanpää, PJ Hakonen, EV Thuneberg, et al. Motional averaging in a superconducting qubit. *Nat. Commun.*, 4:1420, 2013.

[160] Sean Barrett, Klemens Hammerer, Sarah Harrison, Tracy E Northup, and Tobias J Osborne. Simulating quantum fields with cavity qed. *Phys. Rev. Lett.*, 110(9):090501, 2013.

[161] C Eichler, D Bozyigit, C Lang, L Steffen, J Fink, and A Wallraff. Experimental state tomography of itinerant single microwave photons. *Phys. Rev. Lett.*, 106 (22):220503, 2011.

[162] Shingo Kono, Kazuki Koshino, Yutaka Tabuchi, Atsushi Noguchi, and Yasunobu Nakamura. Quantum non-demolition detection of an itinerant microwave photon. *Nat. Phys.*, 14(6):546–549, 2018.

[163] Jean-Claude Besse, Simone Gasparinetti, Michele C Collodo, Theo Walter, Philipp Kurpiers, Marek Pechal, Christopher Eichler, and Andreas Wallraff. Single-shot quantum nondemolition detection of individual itinerant microwave photons. *Phys. Rev. X*, 8(2):021003, 2018.

[164] Arne L Grimsmo, Baptiste Royer, John Mark Kreikebaum, Yufeng Ye, Kevin O'Brien, Irfan Siddiqi, and Alexandre Blais. Quantum metamaterial for broadband detection of single microwave photons. *Phys. Rev. Appl.*, 15: 034074, mar 2021.

[165] William K Wootters. Quantum entanglement as a quantifiable resource. *Phil. Trans. R. Soc. A.*, 356(1743):1717–1731, 1998.

[166] Ryszard Horodecki, Paweł Horodecki, Michał Horodecki, and Karol Horodecki. Quantum entanglement. *Rev. Mod. Phys.*, 81(2):865, 2009.

[167] Charles H Bennett. Quantum information. *Phys. Scr.*, 1998(T76):210, 1998.

[168] Richard Jozsa. Entanglement and quantum computation, appearing in geometric issues in the foundations of science, huggett s et. al., eds, 1997.

[169] Nicolas Gisin and Rob Thew. Quantum communication. *Nat. Phot.*, 1(3): 165–171, 2007.

[170] Julia Kempe. Multiparticle entanglement and its applications to cryptography. *Phys. Rev. A*, 60(2):910, 1999.

[171] Hans J Briegel, David E Browne, Wolfgang Dür, Robert Raussendorf, and Maarten Van den Nest. Measurement-based quantum computation. *Nat. Phys.*, 5(1):19–26, 2009.

[172] Nicolai Friis, Davide Orsucci, Michalis Skotiniotis, Pavel Sekatski, Vedran Dunjko, Hans J Briegel, and Wolfgang Dür. Flexible resources for quantum metrology. *New J. Phys.*, 19(6):063044, 2017.

[173] Nathan Shettell and Damian Markham. Graph states as a resource for quantum metrology. *Phys. Revi. Lett.*, 124(11):110502, 2020.

[174] Hans J Briegel and Robert Raussendorf. Persistent entanglement in arrays of interacting particles. *Phys. Rev. Lett.*, 86(5):910, 2001.

[175] Sreraman Muralidharan and Prasanta K Panigrahi. Quantum-information splitting using multipartite cluster states. *Physical Review A*, 78(6):062333, 2008.

[176] Dirk Schlingemann and Reinhard F Werner. Quantum error-correcting codes associated with graphs. *Phys. Rev. A*, 65(1):012308, 2001.

[177] BA Bell, DA Herrera-Martí, MS Tame, Damian Markham, WJ Wadsworth, and JG Rarity. Experimental demonstration of a graph state quantum error-correction code. *Nat. Comm.*, 5(1):1–10, 2014.

[178] Michael A Nielsen. Optical quantum computation using cluster states. *Phys. Rev. Lett.*, 93(4):040503, 2004.

[179] Daniel E Browne and Terry Rudolph. Resource-efficient linear optical quantum computation. *Phys. Rev. Lett.*, 95(1):010501, 2005.

[180] Netanel H Lindner and Terry Rudolph. Proposal for pulsed on-demand sources of photonic cluster state strings. *Phys. Rev. Lett.*, 103(11):113602, 2009.

[181] Kianna Wan, Soonwon Choi, Isaac H Kim, Noah Shutty, and Patrick Hayden. Fault-tolerant qubit from a constant number of components. *PRX Quant.*, 2 (4):040345, 2021.

[182] Yu Shi and Edo Waks. Deterministic generation of multidimensional photonic cluster states using time-delay feedback. *Phys. Rev. A*, 104(1):013703, 2021.

[183] Yuan Zhan and Shuo Sun. Deterministic generation of loss-tolerant photonic cluster states with a single quantum emitter. *Phys. Rev. Lett.*, 125(22):223601, 2020.

[184] Shanshan Xu and Shanhui Fan. Generate tensor network state by sequential single-photon scattering in waveguide qed systems. *APL Photonics*, 3(11): 116102, 2018.

[185] Vinicius S Ferreira, Jash Banker, Alp Sipahigil, Matthew H Matheny, Andrew J Keller, Eunjong Kim, Mohammad Mirhosseini, and Oskar Painter. Collapse and revival of an artificial atom coupled to a structured photonic reservoir. *Phys. Rev. X*, 11(4):041043, 2021.

[186] Jung-Tsung Shen and Shanhui Fan. Coherent single photon transport in a one-dimensional waveguide coupled with superconducting quantum bits. *Phys. Rev. Lett.*, 95(21):213001, 2005.

[187] Marek Pechal, Lukas Huthmacher, Christopher Eichler, Sina Zeytinoğlu, AA Abdumalikov Jr, Simon Berger, Andreas Wallraff, and Stefan Filipp. Microwave-controlled generation of shaped single photons in circuit quantum electrodynamics. *Phys. Rev. X*, 4(4):041010, 2014.

[188] Pol Forn-Diaz, CW Warren, CWS Chang, AM Vadiraj, and CM Wilson. On-demand microwave generator of shaped single photons. *Phys. Rev. Appl.*, 8 (5):054015, 2017.

[189] Jesper Ilves, Shingo Kono, Yoshiki Sunada, Shota Yamazaki, Minkyu Kim, Kazuki Koshino, and Yasunobu Nakamura. On-demand generation and characterization of a microwave time-bin qubit. *npj Quantum Inf.*, 6(1):1–7, 2020.

[190] Kevin Reuer, Jean-Claude Besse, Lucien Wernli, Paul Magnard, Philipp Kurpiers, Graham J Norris, Andreas Wallraff, and Christopher Eichler. Realization of a universal quantum gate set for itinerant microwave photons. *Phys. Rev. X*, 12(1):011008, 2022.

[191] Anthony Megrant, Charles Neill, Rami Barends, Ben Chiaro, Yu Chen, Ludwig Feigl, Julian Kelly, Erik Lucero, Matteo Mariantoni, Peter JJ O'Malley, et al. Planar superconducting resonators with internal quality factors above one million. *Appl. Phys. Lett.*, 100(11):113510, 2012.

[192] Greg Calusine, Alexander Melville, Wayne Woods, Rabindra Das, Corey Stull, Vlad Bolkhovsky, Danielle Braje, David Hover, David K Kim, Xhovalin Miloshi, et al. Analysis and mitigation of interface losses in trenched superconducting coplanar waveguide resonators. *Appl. Phys. Lett.*, 112(6): 062601, 2018.

[193] Wayne Woods, Greg Calusine, Alexander Melville, Arjan Sevi, Evan Golden, David K Kim, Danna Rosenberg, Jonilyn L Yoder, and William D Oliver. Determining interface dielectric losses in superconducting coplanar-waveguide resonators. *Phys. Rev. Appl.*, 12(1):014012, 2019.

[194] MA Yurtalan, J Shi, GJK Flatt, and A Lupascu. Characterization of multilevel dynamics and decoherence in a high-anharmonicity capacitively shunted flux circuit. *Phys. Rev. Appl.*, 16(5):054051, 2021.

[195] Fei Yan, Youngkyu Sung, Philip Krantz, Archana Kamal, David K Kim, Jonilyn L Yoder, Terry P Orlando, Simon Gustavsson, and William D Oliver. Engineering framework for optimizing superconducting qubit designs. *arXiv preprint arXiv:2006.04130*, 2020.

[196] Abigail Shearrow, Gerwin Koolstra, Samuel J Whiteley, Nathan Earnest, Peter S Barry, F Joseph Heremans, David D Awschalom, Erik Shirokoff, and David I Schuster. Atomic layer deposition of titanium nitride for quantum circuits. *Appl. Phys. Lett.*, 113(21):212601, 2018.

[197] Lukas Grünhaupt, Nataliya Maleeva, Sebastian T Skacel, Martino Calvo, Florence Levy-Bertrand, Alexey V Ustinov, Hannes Rotzinger, Alessandro Monfardini, Gianluigi Catelani, and Ioan M Pop. Loss mechanisms and quasiparticle dynamics in superconducting microwave resonators made of thin-film granular aluminum. *Phys. Rev. Lett.*, 121(11):117001, 2018.

[198] É Dumur, KJ Satzinger, GA Peairs, M-H Chou, A Bienfait, H-S Chang, CR Conner, J Grebel, RG Povey, YP Zhong, et al. Quantum communication with itinerant surface acoustic wave phonons. *npj Quantum Inf.*, 7(1):1–5, 2021.

[199] MD Hutchings, Jared B Hertzberg, Yebin Liu, Nicholas T Bronn, George A Keefe, Markus Brink, Jerry M Chow, and BLT Plourde. Tunable superconducting qubits with flux-independent coherence. *Phys. Rev. Appl.*, 8(4): 044003, 2017.

[200] Yu Chen, C Neill, Pedram Roushan, Nelson Leung, Michael Fang, Rami Barends, Julian Kelly, Brooks Campbell, Z Chen, Benjamin Chiaro, et al. Qubit architecture with high coherence and fast tunable coupling. *Phys. Rev. Lett.*, 113(22):220502, 2014.

[201] Fei Yan, Philip Krantz, Youngkyu Sung, Morten Kjaergaard, Daniel L Campbell, Terry P Orlando, Simon Gustavsson, and William D Oliver. Tunable coupling scheme for implementing high-fidelity two-qubit gates. *Phys. Rev. Appl.*, 10(5):054062, 2018.

[202] Robert I Killey, Philip M Watts, Madeleine Glick, and Polina Bayvel. Electronic dispersion compensation by signal predistortion. In *2006 Optical Fiber Communication Conference and the National Fiber Optic Engineers Conference*, pages 3–pp. IEEE, 2006.

[203] Siddharth Ramachandran. *Fiber based dispersion compensation*, volume 5. Springer Science & Business Media, 2007.

[204] Zhoushen Huang, Aashish Clerk, and Ivar Martin. Nondispersing wave packets in lattice floquet systems. *Physical Review Letters*, 126(10):100601, 2021.

[205] Sihao Huang, Benjamin Lienhard, Greg Calusine, Antti Vepsäläinen, Jochen Braumüller, David K Kim, Alexander J Melville, Bethany M Niedzielski, Jonilyn L Yoder, Bharath Kannan, et al. Microwave package design for superconducting quantum processors. *PRX Quant.*, 2(2):020306, 2021.

[206] Nicholas T Bronn, Vivekananda P Adiga, Salvatore B Olivadese, Xian Wu, Jerry M Chow, and David P Pappas. High coherence plane breaking packaging for superconducting qubits. *Quantum Sci. Technol.*, 3(2):024007, 2018.

[207] Sara Bartolucci, Patrick Birchall, Hector Bombin, Hugo Cable, Chris Dawson, Mercedes Gimeno-Segovia, Eric Johnston, Konrad Kieling, Naomi Nickerson, Mihir Pant, et al. Fusion-based quantum computation. *arXiv preprint arXiv:2101.09310*, 2021.

[208] Alexander PM Place, Lila VH Rodgers, Pranav Mundada, Basil M Smitham, Mattias Fitzpatrick, Zhaoqi Leng, Anjali Premkumar, Jacob Bryon, Andrei Vrajitoarea, Sara Sussman, Guangming Cheng, Trisha Madhavan, Harshvardhan K Babla1, Xuan H Le, Youqi Gang, Berthold Jäck, András Gyenis, Nan Yao, Robert J Cava, Nathalie P de Leon, and Andrew A Houck. New material platform for superconducting transmon qubits with coherence times exceeding 0.3 milliseconds. *Nat. Commun.*, 12:1779, 2021.

[209] J Wenner, Yi Yin, Yu Chen, R Barends, B Chiaro, E Jeffrey, J Kelly, A Megrant, JY Mutus, C Neill, et al. Catching time-reversed microwave coherent state photons with 99.4% absorption efficiency. *Phy. Rev. Lett.*, 112 (21):210501, 2014.

[210] Philipp Kurpiers, Paul Magnard, Theo Walter, Baptiste Royer, Marek Pechal, Johannes Heinsoo, Yves Salathé, Abdulkadir Akin, Simon Storz, J-C Besse, et al. Deterministic quantum state transfer and remote entanglement using microwave photons. *Nature*, 558(7709):264–267, 2018.

[211] Christian Schön, Enrique Solano, Frank Verstraete, J Ignacio Cirac, and Michael M Wolf. Sequential generation of entangled multiqubit states. *Phys. Rev. Lett.*, 95(11):110503, 2005.

[212] Sebastian Krinner, Simon Storz, Philipp Kurpiers, Paul Magnard, Johannes Heinsoo, Raphael Keller, Janis Luetolf, Christopher Eichler, and Andreas Wallraff. Engineering cryogenic setups for 100-qubit scale superconducting circuit systems. *EPJ Quantum Technol.*, 6(1):2, 2019.

[213] C. Macklin, K. O'Brien, D. Hover, M. E. Schwartz, V. Bolkhovsky, X. Zhang, W. D. Oliver, and I. Siddiqi. A near–quantum-limited josephson traveling-wave parametric amplifier. *Science*, 350:307–310, oct 2015. doi: 10.1126/science.aaa8525.

[214] Jen-Hao Yeh, Jay LeFebvre, Shavindra Premaratne, FC Wellstood, and BS Palmer. Microwave attenuators for use with quantum devices below 100 mk. *J. Appl. Phys.*, 121(22):224501, 2017.

[215] Ho Trung Dung and Kikuo Ujihara. Analytic solution for retardation in two-atom systems. *Phys. Rev. A*, 59(3):2524, 1999.

[216] R.J.P. Engelen, Y. Sugimoto, Y. Watanabe, J.P. Korterik, N. Ikeda, N.F. van Hulst, K. Asakawa, and L. Kuipers. The effect of higher-order dispersion on slow light propagation in photonic crystal waveguides. *Opt. Express*, 14(4):1658–1672, Feb 2006. doi: 10.1364/OE.14.001658. URL `http://opg.optica.org/oe/abstract.cfm?URI=oe-14-4-1658`.

[217] Paul Adrien Maurice Dirac. The quantum theory of the emission and absorption of radiation. *Proceedings of the Royal Society of London. Series A, Containing Papers of a Mathematical and Physical Character*, 114(767): 243–265, 1927.

[218] Rami Barends, Julian Kelly, Anthony Megrant, Daniel Sank, Evan Jeffrey, Yu Chen, Yi Yin, Ben Chiaro, Josh Mutus, Charles Neill, et al. Coherent josephson qubit suitable for scalable quantum integrated circuits. *Phys. Rev. Lett.*, 111(8):080502, 2013.

[219] Evan Jeffrey, Daniel Sank, J. Y. Mutus, T. C. White, J. Kelly, R. Barends, Y. Chen, Z. Chen, B. Chiaro, A. Dunsworth, A. Megrant, P. J. J. O'Malley, C. Neill, P. Roushan, A. Vainsencher, J. Wenner, A. N. Cleland, and John M. Martinis. Fast accurate state measurement with superconducting qubits. *Phys. Rev. Lett.*, 112:190504, May 2014. doi: 10.1103/PhysRevLett.112.190504. URL https://link.aps.org/doi/10.1103/PhysRevLett.112.190504.

[220] Eyob A. Sete, John M. Martinis, and Alexander N. Korotkov. Quantum theory of a bandpass purcell filter for qubit readout. *Phys. Rev. A*, 92:012325, Jul 2015. doi: 10.1103/PhysRevA.92.012325. URL https://link.aps.org/doi/10.1103/PhysRevA.92.012325.

[221] Michiel A Rol, Livio Ciorciaro, Filip K Malinowski, Brian M Tarasinski, Ramiro E Sagastizabal, Cornelis Christiaan Bultink, Yves Salathe, Niels Haandbæk, Jan Sedivy, and Leonardo DiCarlo. Time-domain characterization and correction of on-chip distortion of control pulses in a quantum processor. *Appl. Phys. Lett.*, 116(5):054001, 2020.

[222] Blake Robert Johnson. *Controlling photons in superconducting electrical circuits*. Yale University, 2011.

[223] Jonas Bylander, Simon Gustavsson, Fei Yan, Fumiki Yoshihara, Khalil Harrabi, George Fitch, David G Cory, Yasunobu Nakamura, Jaw-Shen Tsai, and William D Oliver. Noise spectroscopy through dynamical decoupling with a superconducting flux qubit. *Nat. Phys.*, 7(7):565–570, 2011.

[224] Line Hjortshøj Pedersen, Niels Martin Møller, and Klaus Mølmer. Fidelity of quantum operations. *Physics Letters A*, 367(1-2):47–51, 2007.

[225] Christopher Eichler. *Experimental characterization of quantum microwave radiation and its entanglement with a superconducting qubit*. PhD thesis, ETH Zurich, 2013.

[226] J M Chow, J M Gambetta, A D Córcoles, S T Merkel, J A Smolin, C Rigetti, S Poletto, G A Keefe, M B Rothwell, J R Rozen, M B Ketchen, and M Steffen. Universal quantum gate set approaching fault-tolerant thresholds with superconducting qubits. *Phys. Rev. Lett.*, 109(6):060501, 2012.

[227] C Eichler, D Bozyigit, and A Wallraff. Characterizing quantum microwave radiation and its entanglement with superconducting qubits using linear detectors. *Phys. Rev. A*, 86:032106, 2012.

[228] Steven Diamond and Stephen Boyd. CVXPY: A Python-embedded modeling language for convex optimization. *Journal of Machine Learning Research*, 17(83):1–5, 2016.

[229] David C McKay, Christopher J Wood, Sarah Sheldon, Jerry M Chow, and Jay M Gambetta. Efficient z gates for quantum computing. *Phys. Rev. A*, 96 (2):022330, 2017.

[230] Marcus P da Silva, Deniz Bozyigit, Andreas Wallraff, and Alexandre Blais. Schemes for the observation of photon correlation functions in circuit qed with linear detectors. *Phys.Rev. A*, 82(4):043804, 2010.

[231] E Nielsen, J K Gamble, K Rudin, T Scholten, Young K, and R Blume-Kohout. Gate set tomography. *Quantum*, 5:557, 2021.

[232] E Nielsen, R Blume-Kohout, L Saldyt, J Gross, T Scholten, K Rudinger, T Proctor, J K Gamble, and A Russo. *PyGSTi version 0.9.9.1*. 2020. doi: 10.5281/zenodo.3675466.

[233] Adam C. Keith, Charles H. Baldwin, Scott Glancy, and E. Knill. Joint quantum-state and measurement tomography with incomplete measurements. *Phys. Rev. A*, 98:042318, Oct 2018. doi: 10.1103/PhysRevA.98.042318.

[234] Rodney Loudon. *The quantum theory of light*. OUP Oxford, 2000.

[235] Brian J Smith and MG Raymer. Photon wave functions, wave-packet quantization of light, and coherence theory. *New J. Phys.*, 9(11):414, 2007.

[236] Carlton M Caves. Quantum limits on noise in linear amplifiers. *Physical Review D*, 26(8):1817, 1982.

[237] U Leonhardt and H Paul. Realistic optical homodyne measurements and quasiprobability distributions. *Phys. Rev. A*, 48(6):4598, 1993.

[238] Stephen Barnett and Paul M Radmore. *Methods in theoretical quantum optics*, volume 15. Oxford University Press, 2002.

[239] Ulrike Herzog. Generating-function approach to the moment problem for the density matrix of a single mode. *Physical Review A*, 53(4):2889, 1996.